

Budker Institute of Nuclear Physics  
Siberian Branch Russian Academy of Sciences  
(BINP SB RAS)

*Super Charm – Tau Factory*

CONCEPTUAL DESIGN REPORT  
PART TWO  
(collider, injector)

[very preliminary draft]

Novosibirsk – 2018

This document is focused on a project of the Super Charm – Tau factory in the Budker Institute of Nuclear Physics (Novosibirsk, Russia). An electron-positron collider will operate in the range of center-of-mass energies from 2 to 5 GeV with unprecedented peak luminosity of about  $10^{35} \text{ cm}^{-2}\text{s}^{-1}$  and longitudinally polarized electrons at interaction point.

V.V. Anashin, A.V. Anisenkov, V.M. Aulchenko, E.M. Baldin, A.K. Barladyan, A.Yu. Barnyakov, I.Yu. Basok, E.A. Bekhtenev, O.L. Beloborodova, D.E. Berkaev, A.E. Blinov, V.E. Blinov, A.V. Bobrov, V.S. Bobrovnikov, A.G. Bogdanchikov, A.V. Bogomyagkov, A.E. Bondar, A.A. Borodenko, A.V. Bragin, A.R. Buzykaev, V.L. Chernyak, V.Ya. Chudaev, I.N. Churkin, N.S. Dikansky, T.V. Dimova, A.M. Dolgov, V.P. Druzhinin, F.A. Emanov, S.I. Eidelman, Yu.I. Eidelman, D.A. Epifanov, L.B. Epshteyn, E.S. Ershov, V.S. Fadin, N.I. Gabyshev, A.Yu. Garmash, S.A. Glukhov, V.B. Golubev, D.N. Grigoriev, V.R. Groshev, G.I. Gusev, S.E. Karnaev, G.V. Karpov, S.V. Karpov, P.V. Kasyanenko, V.F. Kazanin, E.K. Kengebulatov, **B.I. Khazin**, S.V. Khrushchev, V.A. Kiselev, V.I. Kokoulin, V.V. Kolmogorov, S.A. Kononov, I.A. Koop, A.A. Korol, E.A. Kravchenko, A.A. Krasnov, P.P. Krokovny, V.N. Kudryavtsev, A.S. Kuzmin, V.S. Kuzminykh, V.F. Kulikov, G.N. Kulipanov, E.A. Kuper, G.Ya. Kurkin, A.E. Levichev, E.B. Levichev, R.N. Li, P.V. Logachev, P.V. Martyshkin, D.V. Matvienko, A.S. Medvedko, O.I. Meshkov, N.A. Mezentsev, A.I. Milstein, A.A. Morozov, N.Yu. Muchnoi, S.A. Nikitin, I.B. Nikolaev, I.N. Okunev, A.P. Onuchin, S.B. Oreshkin, A.A. Osipov, A.S. Osipov, A.V. Otboev, A.V. Petrenko, M.V. Petrichenkov, V.M. Petrov, V.V. Petrov, P.A. Piminov, A.O. Poluektov, A.V. Polyanski, V.G. Prisekin, Yu.A. Pupkov, V.A. Rodiakin, G.A. Savinov, Yu.M. Schatunov, S.I. Serednyakov, D.N. Shatilov, V.E. Shebalin, L.I. Shekhtman, S.V. Shiyankov, V.A. Shkaruba, S.N. Shmakov, D.A. Shtol, A.I. Shusharo, B.A. Shwartz, I.V. Sidorov, S.V. Sinyatkin, K.Yu. Skovpen, A.N. Skrinsky, V.V. Smaluk, A.V. Sokolov, E.V. Starostina, A.M. Sukharev, A.A. Talyshev, V.I. Telnov, Yu.A. Tikhonov, V.M. Titov, A.G. Tribendis, Yu.V. Usov, A.N. Vinokurova, P.D. Vobly, G.V. Vodnev, A.I. Vorobiov, V.S. Vorobiev, Yu.V. Yudin, A.N. Yushkov, A.S. Zaytsev, V.N. Zhilich, V.V. Zhulanov, A.N. Zhuravlev, K.V. Zolotarev

**Budker Institute of Nuclear Physics**, *pr. Lavrentieva 11, Novosibirsk 630090, Russia*

A.F. Danilyuk

**Boreskov Institute of Catalysis**, *pr. Lavrentieva 5, Novosibirsk 630090, Russia*

N.N. Achasov, I.F. Ginzburg, G.N. Shestakov

**Sobolev Institute of Mathematic**, *av. Acad. Koptiyug 4, Novosibirsk 630090, Russia*

A.G. Kharlamov, G.L. Kotkin, I.B. Logashenko, D.A. Maksimov, O.I. Meshkov, I.O. Orlov, V.G. Serbo, Yu.I. Skovpen

**Novosibirsk State University**, *st. Pirogova 2, Novosibirsk 630090, Russia*

M.Yu. Barnyakov, S.G. Pivovarov

**Novosibirsk State Technical University**, *pr. K.Marksa 20, Novosibirsk 630090, Russia*

A.V. Arefiev, T.A. Aushev, K.A. Chilikin, R.N. Chistov, M.V. Danilov, D.R. Liventsev, R.V. Mizuk, G.V. Pakhlova, P.N. Pakhlov, V.Yu. Rusinov, E.I. Solovyeva, E.I. Tarkovsky, I.N. Tikhomirov, T.V. Uglov

**State Scientific Center of the Russian Federation – Institute for Theoretical and Experimental Physics**, *st. Bolshaya Cheremushkinskaya 25, Moscow 117218, Russia*

I.R. Boyko, D.V. Dedovich, Yu.A. Nefedov, A.S. Zhemchugov

**Joint Institute for Nuclear Research**, *st. Joliot-Curie 6, Dubna, Moscow region 141980, Russia*

V.A. Chtchegelsky, V.L. Golovtsov, N.V. Gruzinsky, V.I. Iatsura, V.A. Nikonov, A.V. Sarantsev,  
L.N. Uvarov  
**Petersburg Nuclear Physics Institute, Gatchina, Leningrad district 188300, Russia**

A.Yu. Loginov, V.N. Stibunov  
**Tomsk Polytechnic National Research University of Resource-Efficient Technology,**  
*av. Lenin 30, Tomsk 634050, Russia*

D.A. Finogeev, T.L. Karavicheva, E.V. Karpechev, A.B. Kurepin, A.N. Kurepin, V.I. Razin,  
A.I. Reshetin, N.S. Topilskaya, E.A. Usenko  
**Institute for Nuclear Research, pr. 60th October Anniversary prospect 70, Moscow 117312,**  
*Russia*

V. Smakhtin  
**Weizmann Institute of Science, PO Box 26, Rehovot 76100, Israel**

M. Bracko, S. Korpar  
**University of Maribor, Smetanova 17, SI-2000 Maribor, Slovenia**

B. Golob, R. Pestotnik, M. Staric  
**Jozef Stefan Institute, P.O.B. 3000, SI-1001, Ljubljana, Slovenia**

P. Krizan  
**University of Ljubljana, Jadranska 19, SI-1000, Ljubljana, Slovenia**

D. Babusci, G. Venanzoni, M. Zobov  
**Lab. Nazionali di Frascati dell'INFN, CP 13, via E. Fermi 40, I-00044, Frascati Roma,**  
*Italy*

A. Lusiani  
**Scuola Normale Superiore e INFN, Piazza dei Cavalieri 7, I-56126, Pisa, Italy**

M. Mascolo, D. Moricciani  
**University of Rome Tor Vergata, via della Ricerca Scientifica, 1, I-00133, Roma, Italy**

H. Czyż  
**Institute of Physics, University of Silesia in Katowice, Uniwersytecka 4, PL-40-007**  
*Katowice, Poland*

F. Jegerlehner  
**A.Humboldt University, DESY, Platanenallee 6, D-15738, Zeuthen, Germany**

# Contents

<b>Introduction</b>	<b>7</b>
<b>1 Collider</b>	<b>10</b>
1.1 Crab Waist Collision Scheme . . . . .	10
1.2 Parameters . . . . .	13
1.3 Optics . . . . .	19
1.3.1 Experimental section . . . . .	19
1.3.2 Bending arc . . . . .	25
1.3.3 Technical section . . . . .	26
1.3.4 Siberian snake . . . . .	28
1.3.5 Damping wiggler . . . . .	30
1.4 Control of the beam emittance and damping parameters . . . . .	32
1.5 Beam-beam effects and luminosity . . . . .	37
1.6 Polarization . . . . .	40
1.6.1 Closed spin orbit. Spin rotators . . . . .	40
1.6.2 Radiative relaxation of spins . . . . .	42
1.6.3 Time-averaged degree of polarization . . . . .	42
1.7 Collective Effects . . . . .	44
1.7.1 Collective Effects . . . . .	44
1.7.2 Beam lengthening . . . . .	45
1.7.3 Coherent energy losses . . . . .	49
1.7.4 TMC instability (fast head-tail) . . . . .	51
1.7.5 Longitudinal multi-bunch instability . . . . .	52
1.7.6 Transverse multi-bunch instability . . . . .	54
1.7.7 Ion instabilities . . . . .	56
1.7.8 Electron clouds . . . . .	59
1.8 Feedbacks . . . . .	60
1.8.1 Objective of stabilization . . . . .	60
1.8.2 Correction algorithms . . . . .	61
1.8.3 Calculation of transfer functions . . . . .	62
1.8.4 Orbit Stabilization . . . . .	63
1.8.5 Fast feedback systems . . . . .	64
1.9 RF system . . . . .	65
1.9.1 Requirements to RF system . . . . .	65
1.9.2 Accelerating cavities . . . . .	70
1.9.3 RF power supply system . . . . .	70
1.9.4 Procedure for calculating operation of RF system . . . . .	71
1.9.5 Operating modes of the RF system . . . . .	73

1.9.6	Control System . . . . .	73
1.9.7	Estimation of parameters of RF system with superconducting cavities . . . . .	75
1.10	Vacuum system . . . . .	76
1.10.1	Requirements to the vacuum . . . . .	76
1.10.2	Concept of beam vacuum chamber . . . . .	76
1.11	Magnet system . . . . .	80
1.11.1	Dipole magnets . . . . .	80
1.11.2	Quadrupole lenses . . . . .	82
1.11.3	Sextupole lenses . . . . .	83
1.12	Power Supply System . . . . .	85
1.12.1	Power supplies for dipole magnets . . . . .	85
1.12.2	Power supplies for quadrupole lenses . . . . .	87
1.12.3	Power supplies of sextupole lenses . . . . .	88
1.12.4	Power supplies of correctors . . . . .	88
1.13	Superconducting magnets . . . . .	88
1.13.1	Final focus . . . . .	88
1.13.2	Damping wiggler . . . . .	93
1.13.3	Solenoid of Siberian Snake . . . . .	111
1.14	Beam Diagnostics . . . . .	114
1.14.1	Beam Energy Measurement Systems . . . . .	114
1.14.2	Beam position system . . . . .	116
1.14.3	The optical diagnostics . . . . .	118
<b>2</b>	<b>Injector</b>	<b>134</b>
2.1	Acceleration module . . . . .	134
2.2	Source of operation electrons . . . . .	138
2.2.1	Laser system . . . . .	143
2.2.2	Photocathode . . . . .	143
2.3	Injection of positrons . . . . .	143
2.3.1	Electron source . . . . .	148
2.4	Source of polarized electrons . . . . .	149
2.4.1	Photocathode . . . . .	150
2.4.2	High-voltage unit . . . . .	152
2.4.3	Activation of photocathodes . . . . .	154
2.4.4	Magneto-optical system. Spin rotator . . . . .	155
2.4.5	Mott Polarimeter . . . . .	157
2.4.6	Beam bunching, pre-acceleration, and injection of beam into linac . . . . .	157
2.4.7	Conclusion . . . . .	158

# Introduction

Several laboratories engaged in the research on high-energy physics discussed projects of  $c\tau$  factories in the nineties of the last century. Those installations were planned for a beam energy of  $1 \div 3$  GeV and a peak luminosity of about  $10^{33} \text{ cm}^{-2}\text{s}^{-1}$  [1, 2, 3, 4, 5, 6, 7]. In connection with study of narrow resonances, various options of monochromatization of the particle collision energy were considered, as well as the possibility of obtaining transversely polarized particles (for accurate energy calibration). The only implemented project from the “family” of the  $c\tau$  factories of the 90s is the BEPC-II collider, which was commissioned at the IHEP laboratory in Beijing in 2009 [8]. BEPC-II reached the projected peak luminosity of  $1 \cdot 10^{33} \text{ cm}^{-2}\text{s}^{-1}$  at a beam energy of 1.89 GeV in 2016.

The revival of interest in the subject under consideration and commencement of work on the project of the Super Charm–Tau factory at Budker INP SB RAS is due to, first, the outstanding results that were obtained at B-factories at the laboratories of KEK (Japan) and SLAC (USA). These works culminated in the awarding of the 2008 Nobel Prize in Physics to Y. Nambu, M. Kobayashi, and T. Maskawa. Although the high luminosity of the B-factories and the initial radiation state method (proposed and developed at BINP) yielded interesting results in the low-energy region, the creation of a collider factory specialized on studying the physics of charmed particles and tau lepton is still an extremely topical issue.

Secondly, the growing interest in creating a next-generation Super Charm–Tau factory was caused by the appearance of a fundamentally new scheme of beam collision in electron-positron colliders. This scheme (*Crab Waist*, CW) allows raising the luminosity by one or two orders of magnitude without significant increase in the intensity of the beams or the dimensions of the installation or decrease in the bunch length. The idea was offered by the Italian physicist Pantaleo Raimondi in 2006 in connection with the study of the possibility of creating a B-factory with high luminosity [9]. Later, the method was rigorously substantiated in the joint works by P. Raimondi, M. Zobov (INFN LNF, Frascati), and D. Shatilov (BINP, Novosibirsk) [10, 11]. Since 2008, the CW scheme has been successfully applied at the  $\Phi$ -factory DAΦNE (INFN LNF, Frascati); the results of the experiments show the method to be promising and are in good agreement with the theory [12, 13]. In addition to the Super Charm–Tau factory in Novosibirsk, the projects of the  $e^+e^-$  colliders for ultra-high energy FCC-ee (CERN) and CEPC (IHEP, China) are also based on the new approach.

Based on the tasks discussed in detail in the section devoted to the physical program of the Super Charm–Tau factory, the following basic requirements to the accelerator complex were formulated.

- The beam energy must vary from 1 GeV to 2.5 GeV, which will enable conduction of experiments from the threshold of production of nucleons and antinucleons to the region of the family of  $\psi$  mesons and charmed baryons. In addition, due to such a wide energy range it will be possible to use the results obtained on the VEPP-2000 and VEPP-4 colliders at BINP.

- The luminosity of the factory must be not less than  $10^{35} \text{ cm}^{-2}\text{s}^{-1}$  in the high-energy region and not less than  $10^{34} \text{ cm}^{-2}\text{s}^{-1}$  in the low-energy region.
- The electron beam must be longitudinally polarized at the interaction point [14, 15].
- No asymmetry of the energies of the colliding beams is required.
- The known methods of monochromatization of the beam collision energy reduce the luminosity, and thus it was decided to abandon monochromatization. The high luminosity in the CW collision scheme makes it possible to effectively study narrow resonance states without monochromatization.
- The energy calibration will be carried out using the reverse Compton scattering of laser radiation on the particles of the circulating beam. This technique was implemented in recent years at VEPP-4M [16] and demonstrated a relative measurement accuracy of better than  $10^{-4}$ , which seems sufficient for the objectives of the new Super Charm–Tau factory. Transversely polarized beams are not required.

So, the main features of the new electron-positron collider in Novosibirsk, that make it a unique world-class facility are the wide range of energies, high luminosity, and the possibility of conducting experiments with a longitudinally polarized electron beam.

In addition to experiments on particle physics and fundamental interactions, the creation of such an advanced facility will result in substantial progress in technologies for application of charged particle beams (including high-field superconducting magnetic systems, high-power and efficient RF generators, precision beam diagnostic devices, control systems, data collection and processing, etc.). These technologies can be successfully used for development and creation of particle accelerators for applied tasks, including sources of synchrotron radiation, installations for therapy of cancer with proton and ion beams, and other types of accelerators for industrial and medical applications.

# Bibliography

- [1] A. N. Skrinsky, “Studies for a Tau-Charm Factory”, SLAC-Report-451, October, 1994.
- [2] “C-Tau in Novosibirsk: Conceptual Design Report”, BINP, Novosibirsk, 1995.
- [3] E. Perelshtein et al, Proc. of the 3rd Workshop on the TC Factory, Marbella, Spain, 1-6 Jun 1993, 557-570.
- [4] M. V. Danilov et al, Int. J. Mod. Phys. A, Proc. Suppl. 2A (1993) 455-457.
- [5] E. Berger et al, ANL-HEP-TR-94-12, Feb 1994.
- [6] Yu. Aleksahin, A. Dubrovin, A. Zholents, in EPAC-90 Proc., vol. 1, 398-400.
- [7] He-Sheng Chen, Nucl. Phys. Proc. Suppl. 59: 316-323, 1997.
- [8] J. Q. Wang, L. Ma, Q. Qin, C. Zhang, “Status and performance of BEPC II”, Proceedings of IPAC-10, Kyoto, Japan, 2010, WEXMH01, p. 2359.
- [9] P. Raimondi, “Status of the SuperB Effort”, presentation at the 2nd Workshop on SuperB Factory, LNF-INFN, Frascati, March 2006.
- [10] P. Raimondi, D. Shatilov, M. Zobov, “Beam-Beam Issues for Colliding Schemes with Large Piwinski Angle and Crabbed Waist”, LNF-07-003-IR, 2007, e-Print: physics/0702033.
- [11] P. Raimondi, D. Shatilov, M. Zobov, “Suppression of beam-beam resonances in Crab Waist collisions”, EPAC08-WEPP045, Proc. of EPAC-2008, Genoa, Italy, 23–27 June 2008.
- [12] M. Zobov for DAFNE Collaboration Team, “DAFNE Operation Experience with Crab Waist Collision”, arXiv:0810.2211v1.
- [13] M. Zobov et al., “Test of crab-waist collisions at DAFNE Phi factory”, Phys.Rev.Lett.104:174801, 2010.
- [14] Ya. S. Derbenev, A. M. Kondratenko, A. N. Skrinsky, “On the spin motion of particles in storage rings with arbitrary field”, BINP preprint 2-70, 1970.
- [15] Ya. S. Derbenev, A. M. Kondratenko, A. N. Skrinsky, Soviet Doklady (Physics) vol. 192, 6, pp. 1255-1258, 1970 (in Russian). Soviet Physics “Doklady”, 15, pp 583-586, 1970 (translation).
- [16] V. E. Blinov et al., “Beam energy and energy spread measurement by Compton backscattering of laser radiation at the VEPP-4M collider”, ICFA Beam Dyn. Newslett., vol. 48, pp. 195–207, 2009.

# Chapter 1

## Collider

### 1.1 Crab Waist Collision Scheme

For flat beams, the luminosity dependence on the main parameters can be written as follows:

$$L = \frac{\gamma f_0}{2r_e} \cdot \frac{N_b \xi_y}{\beta_y^*}, \quad (1.1)$$

where  $\gamma$  is the relativistic factor,  $r_e$  is the classical radius of electron,  $f_0$  is the collision frequency,  $N_b$  is the number of particles in a bunch,  $\xi_y$  is the vertical beam-beam parameter and  $\beta_y^*$  is the beta function at the interaction point. In traditional collision schemes with a small or zero angle, because of the beam divergence (the so called *hour-glass* effect),  $\beta_y^*$  is limited by the bunch longitudinal dimension  $\sigma_z$ , which cannot be made very small for intense beams because of the collective effects. Decreasing  $\beta_y^*$  (and thus  $\sigma_z$ ) requires, in the first approximation, a proportional reduction in  $N_b$ , i. e., there is a certain limit on the ratio  $N_b/\beta_y^*$ . In addition, there is a restriction  $\xi_y \leq (0.07 \div 0.1)$  because of the beam-beam effects. These two conditions determine the maximum luminosity of the traditional electron-positron colliders.

The Crab Waist collision scheme [1] in the case of “standard” (i. e., previously achieved) currents and bunch length makes it possible to increase  $N_b/\beta_y^*$  by more than an order of magnitude, and  $\xi_y$  by a factor of two to three. The former is achieved by arranging the crossing of two beams at an angle  $2\theta$  in a horizontal plane so that the value of Piwinski angle

$$\phi = \frac{\sigma_z}{\sigma_x} \tan \theta \approx \frac{\sigma_z}{\sigma_x} \theta \quad (1.2)$$

is quite large, see Fig. 1.1. In this case, the length of the interaction area (overlapping of the beams)

$$L_i = \frac{\sigma_z}{\sqrt{1 + \phi^2}} \approx \frac{\sigma_x}{\theta} \quad (1.3)$$

becomes approximately  $\phi$  times (for  $\phi \gg 1$ ) less than  $\sigma_z$ , and  $\beta_y^*$  can be reduced by the same factor without amplification of the hour-glass effect. In addition, this scheme is absolutely free of the problem of parasitic crossings because the beams are separated by several transverse dimensions already at a distance of the bunch length.

The need for crossing angle arose long ago, with the advent of a new generation of colliders, the so-called factories. Their main difference is that the electron and positron beams circulate in separate rings, which intersect only at the Interaction Point (IP). This enables operation in a multibunch regime [almost] without parasitic crossings. However, for rapid trajectory separation

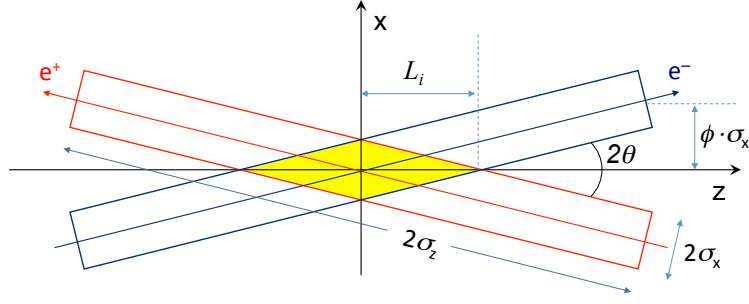


Figure 1.1. Crossing scheme with large Piwinski angle.

the beams have to intersect at the IP at some angle. In this case, the synchro-betatron coupling resonances intensify (see, for example, [2, 3]), and the main criterion here is not the geometric angle, but Piwinski angle. Therefore, the first generation of factories (DAΦNE, PEP-II, KEKB, BEPC-II) meets the condition  $\phi < 1$ , which was considered necessary for a long time. However, in collision schemes with  $\phi \gg 1$  and  $\beta_y^* \sim \sigma_z/\phi$ , the mechanism of excitation of coupling resonances becomes different, and the main role here belongs to the modulation of the vertical betatron phase [at the moment of a kick from the counter bunch] by the horizontal betatron oscillations. This problem turned out to have an elegant solution [1, 4, 5] by means of two sextupole magnets located symmetrically on both sides of the IP at the azimuths with the certain betatron phase advance (see Fig. 1.2) and the integral strength

$$K_2L = \frac{1}{2\theta\beta_y^*\beta_y} \cdot \sqrt{\frac{\beta_x^*}{\beta_x}}, \quad (1.4)$$

where  $\beta^*$  and  $\beta$  denote the beta functions at the IP and at the azimuth of the sextupoles.

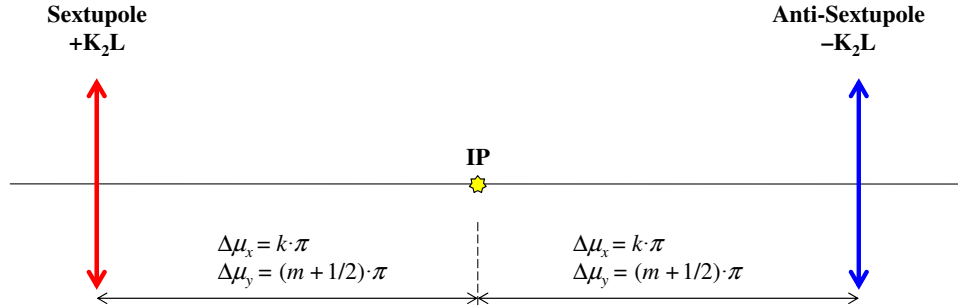


Figure 1.2. Scheme of arrangement of CW sextupoles ( $k$  and  $m$  are integers).

The essence of this transformation is to make the vertical betatron phase of the particle at the point where it intersects the axis of the counter beam independent on its horizontal coordinate. In this case, the betatron and synchro-betatron coupling resonances are suppressed [5, 6], which makes it possible to obtain a record  $\xi_y$ , several times larger than in head-on collision. It can be shown that such a transformation leads to rotation of the bunch waist (line of minimum  $\beta_y$ ) and makes it parallel to the axis of the counter beam, as shown in Fig. 1.3. Namely this rotation of the waist gave the name to the whole scheme, and the sextupoles involved in it got the name of “crab sextupoles”.

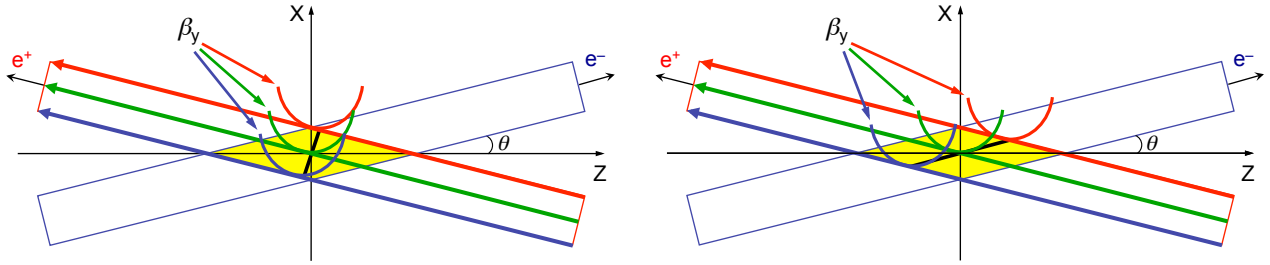
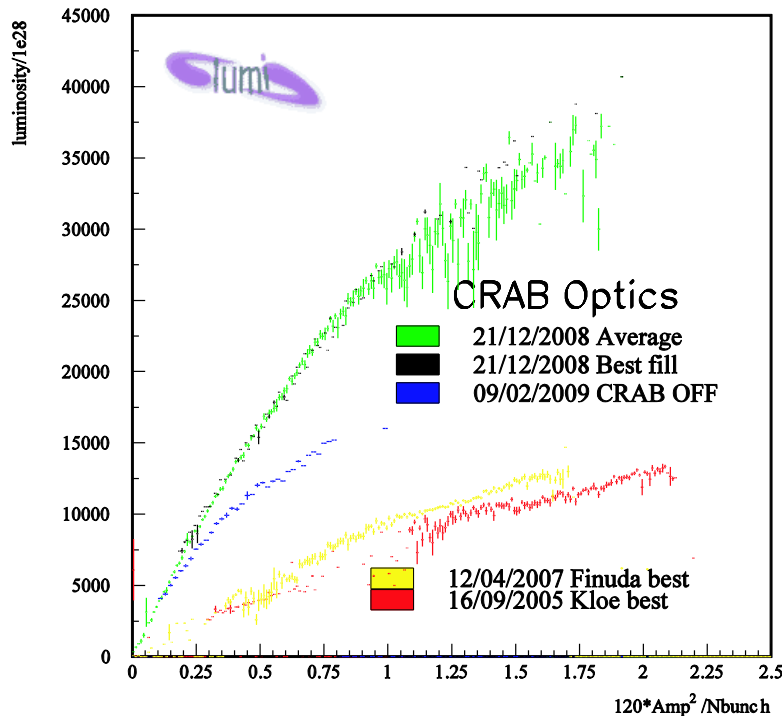


Figure 1.3. Minimum of vertical beta function in conventional (left) and Crab Waist (right) schemes.

The Crab Waist collision scheme was experimentally tested at the  $\Phi$ -factory DAΦNE (Frascati, Italy) [7, 8]. Via relatively small alterations, they enlarged the crossing angle  $\theta$  and reduced the emittances, which led to increase in  $\phi$  and allowed decreasing  $\beta_y^*$  approximately 2.5 times. Fig. 1.4 [9] shows the peak luminosity at DAΦNE under different conditions, and the advantages of the new approach are clearly visible. The blue dots correspond to the new scheme but with the crab sextupoles turned off. At the same currents, the luminosity is much higher here than in the old configuration (red and yellow dots), due to the smaller  $\beta_y^*$ . On the other hand, the stronger beam-beam effects (coupling resonances) hinder reaching high currents, so the blue dots vanish early. When the crab sextupoles are turned on (green and black dots), the coupling resonances are suppressed and the luminosity is higher. The gap between the green and blue points increases with increasing the beam current, which is quite natural: with small  $\xi_y$  the resonances are fewer and weaker, and thus their suppression is not so noticeable. However, the main CW effect is that the ultimate current from the beam-beam effects is several times higher and so is the luminosity.



Red and yellow dots: results in previous configuration (without CW).

Figure 1.4. Measured peak luminosity at DAΦNE vs. intensity of colliding beams.

It should be noted that initially, DAΦNE was designed for the old collision scheme, and one could not expect that minor modifications would realize the full potential of the new scheme. Besides, the luminosity there is now limited not by the beam-beam effects. But the operability of CW has been demonstrated convincingly, and all the experimental results are in good agreement with the theory and simulation.

## 1.2 Parameters

The physical program of the Super Charm–Tau factory implies collider operation in two regimes. The first regime is scanning in the entire beam energy range ( $1 \div 2.5$  GeV) with a step of several MeV. No longitudinal beam polarization is required for this experiment. The second regime is acquisition of statistics at certain points of the beam energy.

**1.00 GeV** Nucleon production threshold. Longitudinal polarization is required.

**1.12 GeV**  $\Lambda$  hyperon production threshold. Polarization is required.

**1.55 GeV**  $J/\psi$  peak. Polarization is desirable to study the damping of  $J/\psi \rightarrow \Lambda\bar{\Lambda}$ .

**1.78 GeV**  $\tau$  lepton production threshold. Polarization is required.

**1.84 GeV**  $\psi(2S)$  peak. Polarization is desirable to study the  $\tau$  lepton.

**1.89 GeV**  $\psi(3770)$  peak. Polarization is desirable to study the  $\tau$  lepton.

**2.10 GeV**  $D_s$  meson production threshold. Polarization is desirable to study the  $\tau$  lepton.

**2.29 GeV**  $\Lambda_c$  baryon production threshold. Polarization is required.

The main integral (the main running time of the Super Charm–Tau factory) will be acquired in the  $J/\psi$ ,  $\psi(2S)$ ,  $\psi(3770)$  peaks and at the threshold of production of  $D_s$  mesons and  $\Lambda_c$  baryons. So, the optimization of the installation, including the luminosity, is carried out in the energy range of 1.5 GeV to 2.5 GeV. In the  $\psi(2S)$  and  $\psi(3770)$  peaks and at the threshold of production of  $D_s$  mesons and  $\Lambda_c$  baryons, the cross section of  $\tau$  lepton is large, and thus longitudinal polarization at these points is highly desirable for study of the physics of  $\tau$ . Thus, polarization is needed at a low energy ( $\sim 1$  GeV), in the  $J/\psi$  peak, and over the entire energy range above the threshold of  $\tau$  lepton production if it does not lead to luminosity drop.

The collider has the following features:

- high single-bunch luminosity due to the Crab Waist collision scheme with large Piwinski angle and submillimeter vertical beta function at the interaction point;
- multi-bunch regime, which implies the use of the double ring scheme;
- the final focus on the basis of superconducting quadrupole lenses, providing a small beta function;
- small horizontal and vertical beam emittances;
- high intensity of a short bunch ( $\sim 10$  mm);
- effective control of the damping parameters (emittance, damping time, etc.) to ensure maximum luminosity in the entire energy range;

- high level of longitudinal polarization of the electron beam in the entire energy range;
- continuous injection at the energy of the experiment, ensuring maintenance of high current, and obtaining a high integral luminosity;
- simultaneous operation of two high-performance injectors: the source of positrons and the source of polarized electrons.

The following considerations were taken into account when choosing the collider parameters:

**Luminosity.** The high luminosity of the Super Charm–Tau factory is achieved due to the multi-bunch regime and the Crab Waist collision scheme (see p. 1.1). From (1.1) one can see that in this scheme the luminosity grows because of two factors: (a) vertical beta function reduction at the interaction point (which becomes possible due to the shortening of the beam interaction area) and (b) increase in  $\xi_y$ , the dependence of which on the main parameters can be written as follows [10, 11]:

$$\xi_y \propto \frac{N_b}{\sigma_x} \cdot \sqrt{\frac{\beta_y^*}{\varepsilon_y(1 + \phi^2)}}. \quad (1.5)$$

We need at a “standard” bunch population  $N_b$  to make  $\phi \gg 1$ , reduce  $\beta_y^*$  (by about  $\phi$  times), and increase  $\xi_y$  several-fold. Obviously, this is possible only with a significant decrease in the transverse dimensions of the beam. This implies the requirement of small emittance for collider with the CW scheme. In addition, decrease in  $\sigma_x$  allows us to fulfil the condition  $\phi \gg 1$  at a relatively small crossing angle  $\theta \sim 30$  mrad.

The following strategy was chosen to maintain high luminosity in the entire energy range. The design of the final focus depends on the angle  $\theta$  and the beta functions at the interaction point, which remain unchanged at all energies. The number of bunches, the number of particles in a bunch, the emittances and the damping decrements also remain constant throughout the energy range. The parameters of the collider are chosen so as to obtain a luminosity of  $10^{35} \text{ cm}^{-2} \text{ s}^{-1}$  at a beam energy of 1.9 GeV. With increasing energy, the luminosity will remain constant, and the parameters  $\xi_{x,y}$  become smaller, i.e., the beam-beam effects will weaken. At energies lower than 1.9 GeV,  $\xi_y$  will remain constant due to the increase in the bunch length, and the luminosity will go down linearly with the energy. Note that the bunch lengthening is a positive factor in terms of collective effects and intrabeam scattering, which grows with diminishing energy. The luminosity and the beam-beam effects are discussed in more detail in p. 1.5.

**The arrangement of the final focus (FF).** The final focus in colliders with the CW scheme is one of the most difficult and critical areas. A submillimeter  $\beta_y^*$  leads to a large value of the vertical beta function in the first quadrupole (defocusing) lens of the FF, which causes a number of negative effects on the dynamics of the beam: increase in the chromaticity of the IP, which needs local compensation by strong sextupole lenses; increase in the influence of the edge nonlinear fields of the FF lenses; nonparaxiality of the motion; etc. For these reasons, we have to place the doublet of the FF quadrupole lenses as close as possible to the interaction point (in our case, in a distance of 60 cm) and make the lenses strong (in our case, the maximum gradient is 10.7 kG/cm). The in-detector placement of the FF lenses, solenoids compensating for the effect of the detector longitudinal field on the beam, the vacuum chamber of the two intersecting rings, the elements of the cryogenic system, etc., makes the designing of the final focus area a technical challenge. BINP has suggested a compact superconducting two-aperture lens with an iron magnetic core, which meets the complex requirements of the FF. The prototype lens was manufactured and tested at the rated current. The small lens aperture and the large beta function determine the mechanical acceptance of the accelerator.

**Damping time and beam emittance.** In the entire energy range, the beam emittance and damping time are assumed to be constant. The damping decrement of horizontal betatron oscillations because of synchrotron radiation has the following form:

$$\alpha_x = \tau_x^{-1} = C_a E^3 \frac{I_2}{\Pi}, \quad (1.6)$$

where  $C_a = 2113.1 \text{ m}^2/\text{GeV}^3/\text{s}$ ,  $\Pi$  is the perimeter of the storage ring,  $I_2$  is the second radiation integral (the dimensionless damping decrement is  $J_x = 1$ ), which includes the contribution from the magnetic lattice of the ring  $I_{2,R}$  and from the damping wigglers  $I_{2,W}$ :

$$I_2 = I_{2,R} + I_{2,W}, \quad I_{2,W} = \frac{1}{2} h_W^2 L_W, \quad (1.7)$$

where  $h_W = B_W/BR$ ,  $B_W$  is the peak value of the field in a wiggler,  $BR$  is the magnetic rigidity,  $L_W = \lambda_W N_W$  is the total length of the wigglers,  $\lambda_W$  is the field period, and  $N_W$  is the number of periods. For maintaining a constant damping time in the entire energy range, superconducting wigglers (damping wigglers) are installed in the magnetic lattice of the storage ring, which makes it possible to effectively tune the integral  $I_2$ . Note that the energy loss to synchrotron radiation per revolution is uniquely tied with the damping time,

$$U_0 = C_a \gamma^2 \frac{\Pi}{\tau_x}. \quad (1.8)$$

Decrease in the damping time leads to increase in the power of the radiation losses, which is to be compensated for by the accelerating RF system,

$$P = U_0 I, \quad (1.9)$$

where  $I$  is the beam current.

In addition, the superconducting wigglers enable control of the horizontal emittance ( $I_{5,R}$  and  $I_{5,W}$  denote the contribution of the ring and the damping wigglers, respectively) according to the following expression:

$$\varepsilon_x = C_q \gamma^2 \frac{I_5}{I_2}, \quad I_5 = I_{5,R} + I_{5,W}, \quad I_{5,W} = \frac{1}{15\pi^3} h_W^3 \lambda_W^2 \left( \bar{\beta}_x + \frac{20\pi^2 \eta_0^2}{\bar{\beta}_x h_W^2 \lambda_W^2} \right), \quad (1.10)$$

where  $C_q = 3.83 \cdot 10^{-13} \text{ m}$ ,  $\bar{\beta}_x$  is the average value of the horizontal beta function over the length of the wiggler, and  $\eta_0$  is the dispersion function in the center of a wiggler. The expression for  $I_{5,W}$  was derived in a wiggler model approximation with a sinusoidal field distribution. It is desirable to install the superconducting wigglers in places with a small beta function, in order to minimize their influence on the beam. Varying  $\eta_0$ , or if necessary  $\bar{\beta}_x$ , it is possible to change the emittance of the beam.

A beam emittance of  $8 \text{ nm}\cdot\text{rad}$  was chosen for the Super Charm–Tau factory, which is a compromise between the small beam size at the interaction point, required for luminosity, and the intrabeam scattering intensity, which can determine particle losses and requirements to the injector, especially at a low energy. The technologies for obtaining such emittance are well known and tested on SR sources. The vertical emittance of the beam is determined by the coupling of the betatron oscillations. To estimate the luminosity at the Super Charm–Tau factory, we use betatron coupling at a level of  $\varepsilon_y/\varepsilon_x \sim 0.005$ . In modern SR sources, the value of this parameter reaches  $\varepsilon_y/\varepsilon_x \sim 1 \div 2 \cdot 10^{-3}$ . However, given the complex structure of the final focus, the presence of Siberian snakes, etc., we apply a more conservative value.

**Number of particles and bunch length.** The maximum number of particles in one bunch is determined by the *fast head-tail instability*. The threshold current of this effect is proportional to the bunch length and must be taken into account when choosing the latter. A large bunch charge distorts the potential well of the accelerating RF field (*potential well distortion*) and increases the bunch length. In addition, microwave instability may lead to increase in the beam energy spread when the threshold current is exceeded, as well as in the bunch length. This effect has a threshold character, and it is advantageous to work at beam current values below the threshold. At this stage, the current and bunch length values for the Super Charm–Tau factory are chosen based on the values already achieved at B-factories. A number of particles of  $7 \cdot 10^{10}$  at a bunch length of 1 cm seems to be a reasonable value.

**Number of bunches.** The number of bunches (total current) is determined by the power of the accelerating RF system. The number of bunches determines the parameters of the system for suppressing the multi-bunch instabilities. Suppression of multi-turn ion instability in the electron ring requires a  $5 \div 10\%$  gap in the bunch repetition. *Fast ion instability* in the electron ring can lead to enlarging of the vertical size of the bunches along the train, which imposes restrictions on the pressure of the residual gas. In the positron ring, increase in the vertical dimension can be observed due to interaction with electron clouds (*e-cloud instability*), which arise from secondary particles near the beam axis. The instability threshold is proportional to the beam current and inversely proportional to the distance between the bunches. To suppress the e-cloud instability, it is recommended to use an anti-chamber, grooves, incisions, and special coating of the vacuum chamber surface in order to reduce the yield of secondary electrons, as well as applying electrodes and solenoids to suppress the clouds, etc.

In our project, the following structure of bunch repetition is used: 406 bunches in each 3rd separatrix (train) and 138 empty separatrices (train gap). A total of 1356 separatrices (harmonic number).

**Loss of particles.** Two effects dominate at the Super Charm–Tau factory, leading to loss of particles: intrabeam scattering (the Touschek effect) and single bremsstrahlung. The second effect is practically independent of the energy of the particles and is determined by the luminosity, which goes down with decreasing energy. Respectively, the single bremsstrahlung losses will also fall. The “Touschek” losses increase with decreasing beam energy, but bunch lengthening partially suppresses this effect.

**Injection.** To provide a high integral luminosity it is necessary to maintain an appropriate average current. So, “continuous” particle injection (*top-up* injection) is planned. The choice of the injection rate is determined by the efficiency of data recording (the ratio between the dead time of the detector and the background load). The maximum injection rate is 50 Hz.

**Polarization.** One of the key aspects of the Super Charm–Tau factory is the longitudinal polarization of the electron beam at the interaction point. To this end, a source of polarized electrons will be used. At the exit of the source, any spin direction can be obtained. So, all further rotations taken into account, the injected beam will have the correct spin direction at the injection point.

Two options to obtain longitudinal polarization at the interaction point were considered: a scheme with restoration of polarization and a scheme using “Siberian snakes”. In the first variant, two spin rotators are placed in the vicinity of the IP, which rotate the spin in a small longitudinal interval so that in the rest of the ring the motion of the spin is not perturbed. The spin rotators are compact, and the integral of the longitudinal field is small, but this scheme has a drawback of the presence of (three) spin resonances in the working energy region, one of which is at the threshold of production of  $\tau$  lepton, and the other in the region of  $\Lambda$  baryon. For these reasons, we have chosen a scheme using five Siberian snakes, which is free of this shortcoming. For reduction

in the spin-orbit coupling, the superconducting damping wigglers are placed between the Siberian snakes.

**Measurement of beam energy and polarization level.** The physical program of the Super Charm–Tau factory does not require very precise measurement of the beam energy; it is enough to provide a relative precision of  $\sim 10^{-4}$ , which can be done using the Compton back scattering [84]. This method also makes it possible to measure the energy spread in the beam within 10%, as well as the beam polarization level.

**General scheme of facility.** The Super Charm–Tau factory consists of the following installations (see Fig. 1.5):

- the positron injector with the cooling storage ring;
- the injector of polarized electrons;
- the linear accelerator, which accelerates/decelerates the beams to the energy of the experiment;
- the double ring collider.

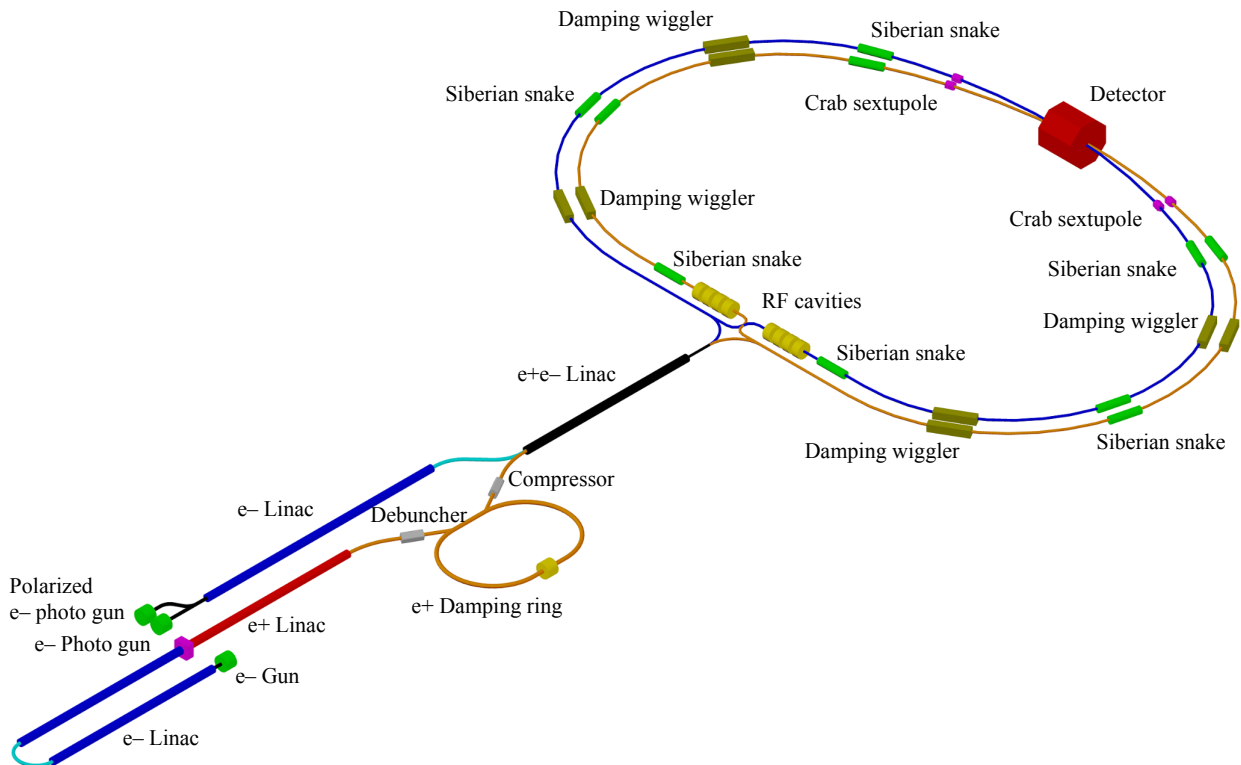


Figure 1.5. Scheme of Super Charm–Tau factory complex.

The two independent injectors (of electrons and positrons) make it possible to efficiently produce particles without losing time to change the polarity of the magnets, as well as realizing the scheme of simultaneous two-bunch acceleration. The linear accelerator (in contrast to the synchrotron one) makes it possible to accelerate the polarized particles without losing the degree of polarization, as well as accelerating large particle charges with smaller losses and a higher frequency.

The main parameters of the collider are given in Table 1.1.

Table 1.1. Table parameters of Super Charm – Tau factory.

<b>Energy</b>	<b>1.0</b>	<b>1.5</b>	<b>2.0</b>	<b>2.5</b>	<b>GeV</b>
Perimeter, $\Pi$	813.1				m
Time of revolution, $\tau_0$	2.712				$\mu\text{s}$
Revolution frequency, $f_0$	368.7				kHz
RF frequency, $f_{\text{RF}}$	499.95				MHz
Harmonic number, $h$	1356				
Betatron tunes, $\nu_x/\nu_y$	43.545 / 40.58				
Synchrotron tune, $\nu_z$	$4.62 \cdot 10^{-3}$	$1.17 \cdot 10^{-2}$	$9.98 \cdot 10^{-3}$	$8.19 \cdot 10^{-3}$	
Compaction factor, $\alpha$	$8.73 \cdot 10^{-4}$	$8.81 \cdot 10^{-4}$	$8.82 \cdot 10^{-4}$	$8.83 \cdot 10^{-4}$	
Wiggler field, $B_{\text{W}}$	50.0	50.0	34.8	10.2	kG
Bending field, $B_0$	3.85	5.78	7.71	9.63	kG
Energy loss per turn, $U_0$	107	271	361	452	keV
RF voltage, $U_{\text{RF}}$	0.156	1.106	1.108	0.988	MV
RF separatrix, $\Delta E/E_{\text{max}}$					
Hor. damping time, $\tau_x$	50.5	30			ms
Ver. damping time, $\tau_y$	50.5	30			ms
Long. damping time, $\tau_z$	25.4	15			ms
Coupling, $k$	0.5%				
Hor. emittance, $\varepsilon_x$	8.0				nm·rad
Ver. emittance, $\varepsilon_y$	0.04				nm·rad
Energy spread, $\sigma_{\Delta E/E}$	$8.7 \cdot 10^{-4}$	$1.1 \cdot 10^{-3}$	$9.3 \cdot 10^{-4}$	$7.2 \cdot 10^{-4}$	
Energy spread, $\sigma_E$	0.87	1.65	1.86	1.79	MeV
Bunch length, $\sigma_z$	2.13	1.2	1.0	1.0	cm
Hor. admittance, $A_x$	$1.1 \cdot 10^{-4}$				cm·rad
Ver. admittance, $A_y$	$4.6 \cdot 10^{-6}$				cm·rad
Number of particles per bunch, $N_b$	$7.1 \cdot 10^{10}$				
Bunch current, $I_b$	4.19				mA
Number of bunches, $n_b$	406				
Train gap	138 (10%)				
Time between bunches, $\tau_b$	6				ns
Total number of particles, $N$	$2.88 \cdot 10^{13}$				
Total current, $I$	1.7				A
Hor. beta functions at IP, $\beta_x$	4				cm
Ver. beta functions at IP, $\beta_y$	0.08				cm
Hor. beam size at IP, $\sigma_x$	17.8				$\mu\text{m}$
Ver. beam size at IP, $\sigma_y$	0.178				$\mu\text{m}$
Crossing angle, $2\theta$	60				mrاد
Piwinski angle, $\phi$	35.9	20.2	16.8	16.8	
Hour-glass factor	0.9066	0.9067	0.9068	0.9068	
Hor. beam-beam parameter, $\xi_x$	0.0016	0.0033	0.0036	0.0029	
Ver. beam-beam parameter, $\xi_y$	0.114	0.135	0.121	0.097	
Single-bunch luminosity, $L_b$	$1.17 \cdot 10^{32}$	$2.08 \cdot 10^{32}$	$2.50 \cdot 10^{32}$	$2.50 \cdot 10^{32}$	$\text{cm}^{-2}\text{s}^{-1}$
<b>Luminosity, <math>L</math></b>	<b><math>0.47 \cdot 10^{35}</math></b>	<b><math>0.86 \cdot 10^{35}</math></b>	<b><math>1.02 \cdot 10^{35}</math></b>	<b><math>1.02 \cdot 10^{35}</math></b>	<b><math>\text{cm}^{-2}\text{s}^{-1}</math></b>

## 1.3 Optics

The collider of the Super Charm–Tau factory consists of two (electron and positron) storage rings (see Fig. 1.6), lying in the horizontal plane and crossing at two places: at the main one, where the detector is located, and in a half a turn. The collider is mirror-symmetrical with respect to the straight line passing through the crossing places. The storage rings are identical except for the fact that the electron ring comprises five Siberian snakes to control the particle spin direction (see p. 1.6). The Siberian snake consists of two superconducting solenoids, between which a group of quadrupole lenses is placed. The similar sections of the positron ring have the same structure, but without solenoids, which can be established if necessary. The half-rings between the Siberian snakes accommodate four superconducting damping wigglers, which control the beam emittance and the damping time of the oscillations (see p. 1.4). The Siberian snakes and the damping wigglers are placed in dispersion free sections.

Each ring consists of two bending arcs, the experimental section, and the technical section. The distance between the rings, except for the section near the main crossing place and the rings separation section in the technical section, is 1 m. The outer half of ring has a length of 408.26 m, and the inner of 404.85 m. The dimensions of whole ring are as follows: the minor axis (from the crossing place to the intersection of the rings in the technical section) is 197.9 m, and the major axis (from the outer arc to the inner one) is 302.6 m.

Figure 1.7 shows the optical functions of a half-ring of the Super Charm–Tau factory. Here and below, under the figure with optical functions, the sequence of the magnets is shown: black is for the bending magnets, blue is for the quadrupole lenses, green is for the sextupole lenses, and magenta is for the solenoids.

### 1.3.1 Experimental section

The experimental section is to ensure crossing of the beams at an angle of 60 mrad in the center of the detector, parameters corresponding to the maximum luminosity. The optical functions of the experimental section include focusing of the beams at the intersection point to the required dimensions, correction of chromatic and geometric aberrations, crab transformation, matching of the optical functions of the final focus with the arcs, etc. Sections with large betatron and dispersion functions can accommodate collimators to suppress the background of the detector.

The experimental section consists of (1) the final telescope, which includes the final focus system, (2) the vertical and horizontal chromaticity correction sections, (3) the crab sextupole section, and (4) the matching section. The section from the interaction point to the matching cell also forms a telescope (see below about the concept of telescope). For separation of the electron and positron rings from the interaction point, as well as controlling the dispersion function inside the chromaticity correction section, the experimental section contains dipole magnets. The total bending angle and the length of the section are, respectively,  $45^\circ$  and 197.87 m (in the outer arc,  $24.2^\circ$  and 99.61 m; in the inner arc,  $20.8^\circ$  and 98.25 m). Figure 1.8 presents a schematic image of the experimental section, and Fig. 1.9 shows the optical functions of this section.

The first (final) telescope consists of two doublets of quadrupole lenses separated by a long section, containing a bending magnet. The first doublet of quadrupole lenses, which are also called the final focus lenses, should be placed as close as possible to the collision point inside the detector, since the beta functions increase quadratically: from very small values to the maximum values over the entire ring. For the required focusing of the beams at the interaction point, the final focus lenses have a large field gradient, which can only be realized by means of superconducting technology. The final focus lenses have two apertures for both the incoming and outgoing beam

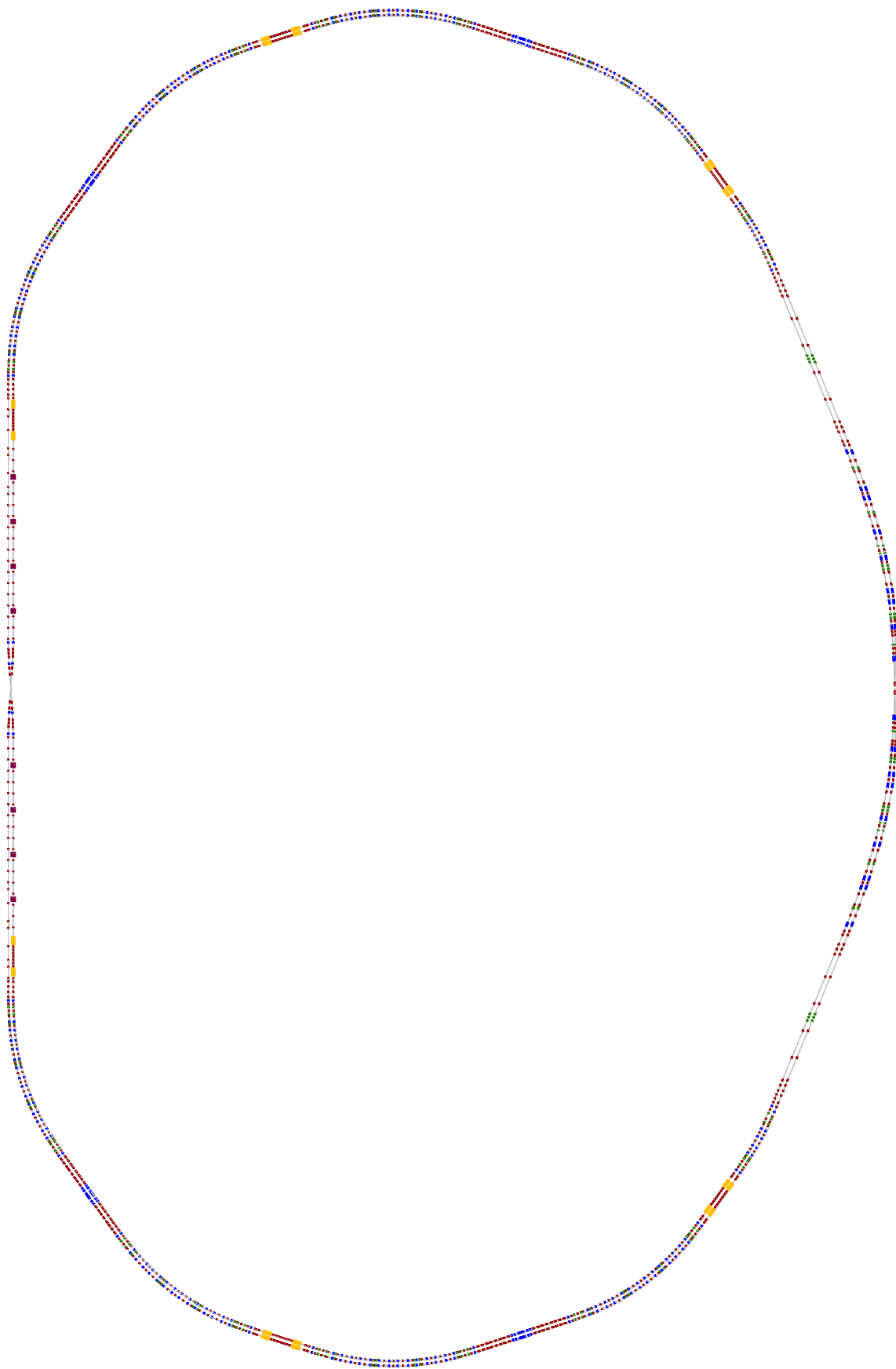


Figure 1.6. Scheme of ring of Super Charm – Tau factory.

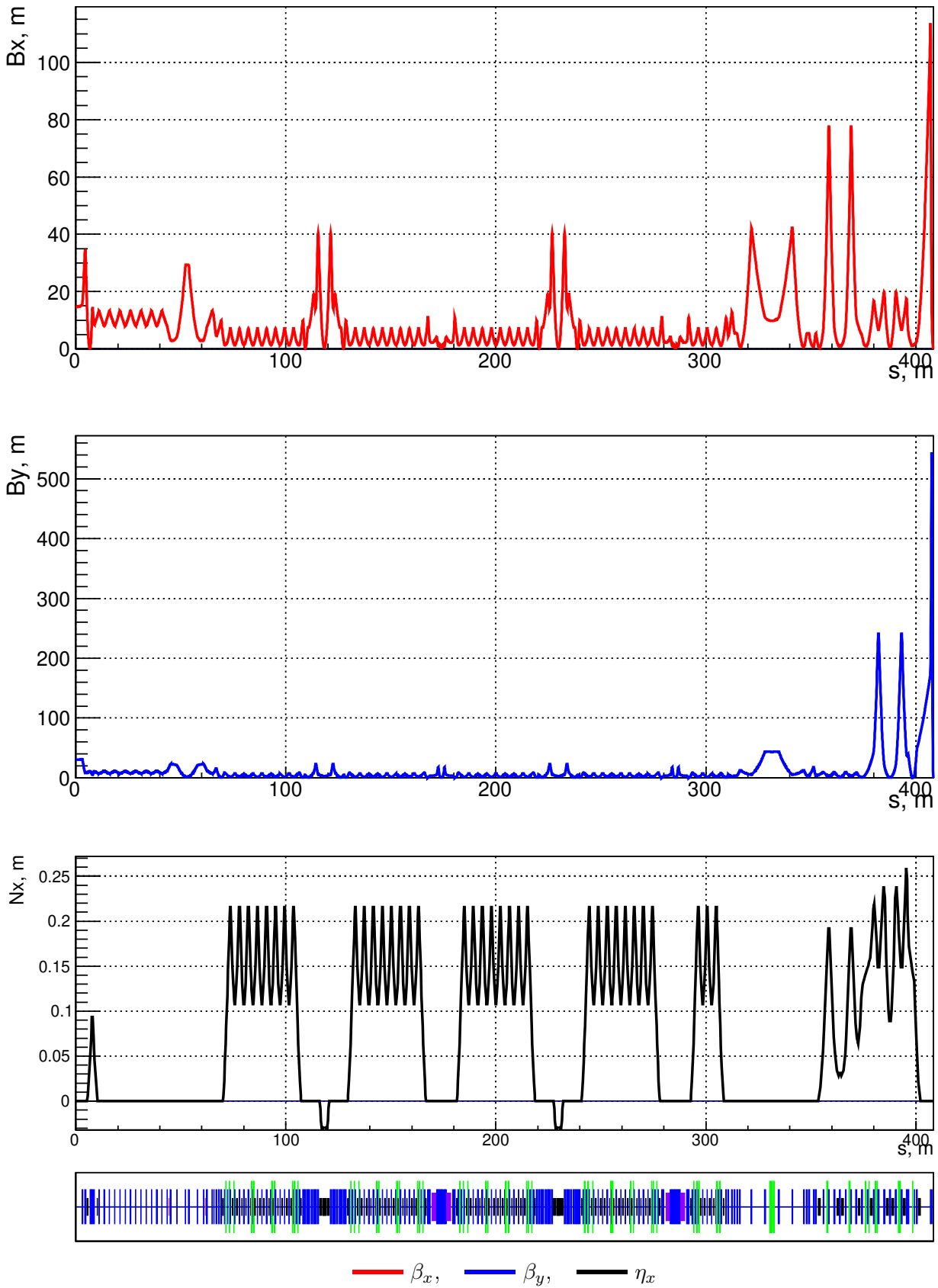


Figure 1.7. Optical functions of half-ring of Super Charm–Tau factory.

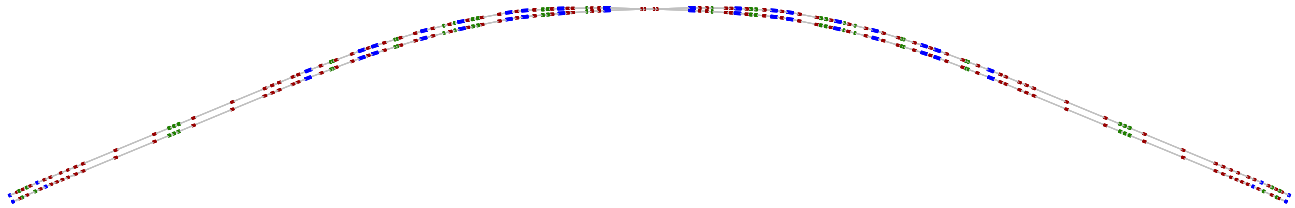


Figure 1.8. Scheme of experimental section.

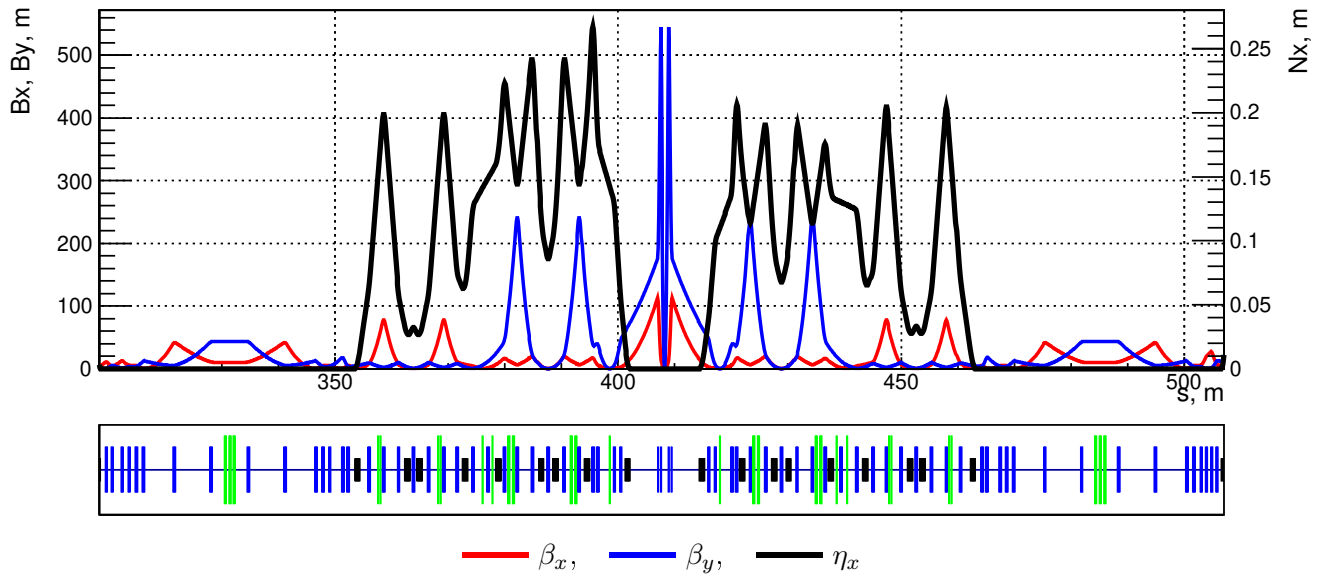


Figure 1.9. Optical functions of experimental section.

to pass through the center of its aperture and to not experience the dipole field, which generates synchrotron radiation, which creates a substantial background load on the detector. The crossing angle was chosen such that it is possible to create a double aperture lens and attain the required beam sizes at the interaction point.

In front of the final focus lenses there is placed a superconducting anti-solenoid, which compensates for the integral of the longitudinal field of the main detector solenoid from the IP to the end of the anti-solenoid. After the anti-solenoid, the longitudinal field is made equal to zero by compensating solenoidal windings placed above the yoke of the quadrupole lenses and the section between them. Thus, the motion of a particle outside the main solenoid and anti-solenoid will be uncoupled. The entire system of the solenoids has a common axis. It should be noted that when the beam energy changes, the gradient of the quadrupole lenses will vary proportionally, whereas the anti-solenoid and compensating solenoids will remain constant, and their field will be determined only by the field of the main solenoid.

The entire structure of the final focus, including the compensating solenoids and the anti-solenoid, is placed inside one cryostat. The technical implementation of the final focus system is set out in p. 1.13.1. Parameters of the magnets of the final focus section and of the beam in them are given in Table 1.2.

Table 1.2. Parameters of final focus magnets and beam sizes in them.

Azimuth cm	Magnet	Aperture* cm	Length cm	Field	$\Delta x$ cm	$\sigma_x$ $\mu\text{m}$	$\sigma_y$ $\mu\text{m}$
0	detector solenoid	$\varnothing 5.3$	45	10 kG**	0	17.8	0.178
40	Beginning of cryostat						
45	anti- solenoid	$\varnothing 5.3$	10	45 kG**	2.7	201.6	100.4
55					3.3	246.1	122.7
Empty section of 5 cm							
60	defocusing quadrupole lens – EQ0	$\varnothing 2.0$	20	$-10.7 \text{ kG/cm}^{***}$	3.6	268.3	133.9
72					4.3	348.5	147.7
80					4.8	436.8	142
Empty section of 20 cm							
110	focusing quadrupole lens – EQ1	$\varnothing 4.2$	20	$6.6 \text{ kG/cm}^{***}$	6.6	830	98.4
129					7.7	952.5	83.7
130					7.8	951.6	83.6
135	End of cryostat						

\* Internal size of the vacuum chamber.

\*\* Regardless of the beam energy.

\*\*\* Corresponding to a beam energy of 2.5 GeV.

Each of the subsequent magnets has a single aperture and affects only one beam. The second doublet of the final telescope lenses is located in 4.8 m. This distance is necessary for both the beta functions, which reach the maximum values in the quadrupole lenses of the final focus, to decrease to “acceptable” values. Before the second doublet of the lenses there is a bending magnet, which has different angles for incoming and outgoing beams, i. e., for the inner and outer arcs. Its purpose is to separate the beams and excite the dispersion that is required in the chromaticity correction sections after the final telescope. The field of the magnet was chosen small to reduce the synchrotron radiation directed to the detector.

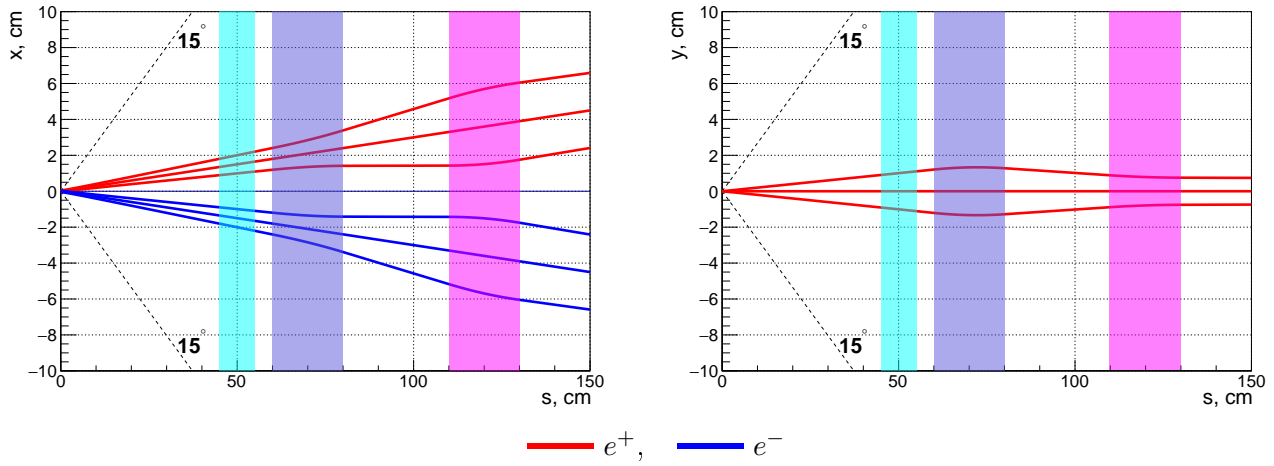


Figure 1.10. Orbit and beam dimensions in final focus system.

After the final telescope, the chromaticity correction sections are located: the vertical one and then the horizontal one. These sections are intended for local compensation of the chromaticity of the final focus lenses. For example, both final doublets produce a chromaticity equal to  $\xi_x = -19.5$  and  $\xi_y = -161.6$ , which is 17% and 60% as compared with the whole ring. For the purpose of compensation for the chromaticity of the beta functions, the sextupole lenses of the chromaticity correction sections are spaced from the final focus lenses by  $n\pi$  in the betatron phase. For higher efficiency of the sextupole lenses, the beta functions in them attain high values (with respect to the ring),  $\beta_x/\beta_y = 9/177\text{ m}$  in the vertical sextupole and  $\beta_x/\beta_y = 61/3\text{ m}$  in the horizontal one. As a result, these sextupole lenses produce large geometric aberrations. For their compensation, we use a scheme with sextupole pairs with a spacing of  $-I$  and sextupole compensators placed next to the main ones [12].

After the chromaticity correction sections, the section of the crab sextupole is located. At the beginning of this section, the dispersion function becomes equal to zero. The quadrupole lenses of this section allow tuning of the beta functions in the crab sextupole with preservation of the condition for the phase advance before the interaction point:  $\Delta\mu_x = 7/2\pi$  and  $\Delta\mu_y = 11/4\pi$ . After the crab sextupole, the group of quadrupole lenses is located, which turn the entire section to the interaction point into a telescope. The experimental section is ended with the matching section, which is necessary to obtain the required values of the optical functions at the entry to the super-period of the bending arc.

The telescope is the name for an optical section the transformation matrix of which is represented in the following form [13]:

$$M_{x,y} = \begin{bmatrix} K_{x,y} & 0 \\ 0 & \frac{1}{K_{x,y}} \end{bmatrix},$$

where  $K_{x,y}$  is the conversion factor of the telescope. The phase advance in this section will be equal to  $n\pi$ . The beta functions at the beginning  $s_0$  and at the end  $s_1$  of the telescope will be

$$\beta_{x,y}(s_1) = K_{x,y}^2 \beta_{x,y}(s_0),$$

and the beam sizes will be

$$\sigma_{x,y}(s_1) = K_{x,y} \sigma_{x,y}(s_0).$$

The telescope enables tuning of the beta functions at the IP by means of the quadrupole lenses in the matching cell of the experimental section. In so doing, all the other elements (inside the telescope) will remain constant, and all the phase relationships necessary for the chromaticity and crab sextupoles will be performed automatically. This will greatly simplify the tuning of the optics, correction of errors, etc.

### 1.3.2 Bending arc

The half-rings accommodate four Siberian snakes with four superconducting damping wigglers between them. The Siberian snakes and the damping wigglers are installed in the dispersion free sections. These sections are connected by four super-periods of bending arc with a bending angle of  $36^\circ$ . The length of the super-period of the outer arc is 37.53 m, and of the inner one 36.89 m. The optical functions of the super-period are depicted in Fig. 1.11. Each super-period contains two cells, located at the edges and intended to nullify the dispersion function, and seven FODO cells.

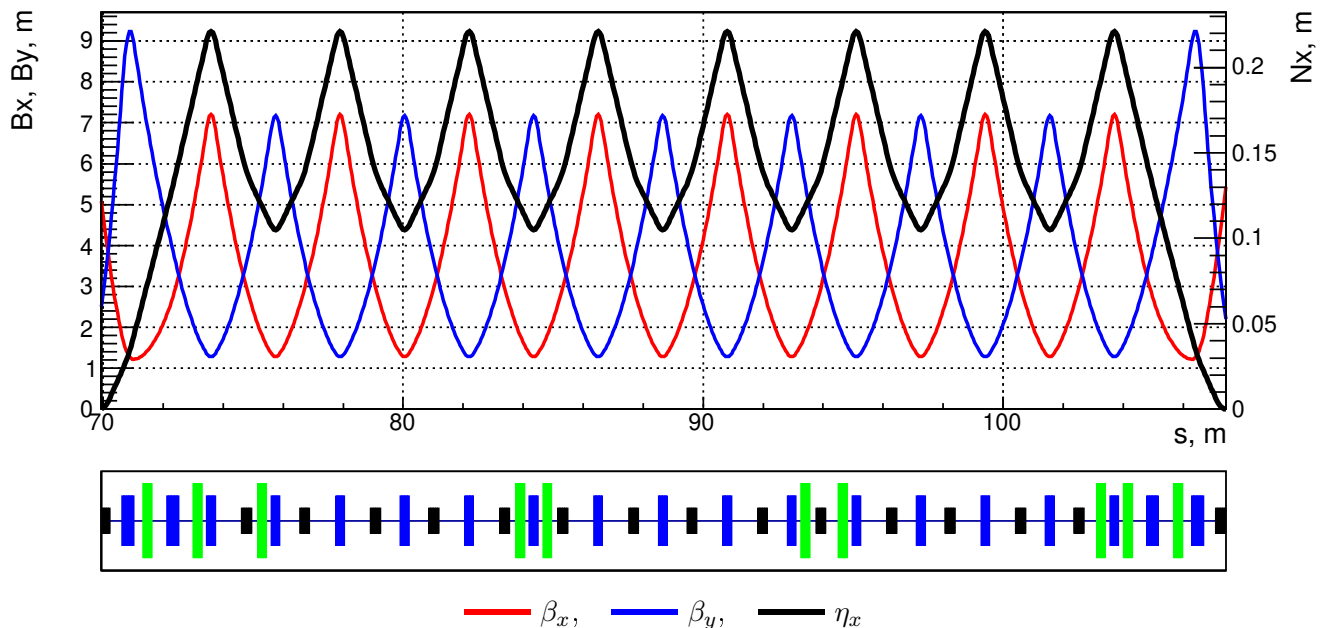


Figure 1.11. Optical functions of super period of bending arc.

The dispersion matching cell contains two quadrupole lenses and one bending magnet, at the output of which the dispersion function and its derivative are zero. Besides that, the dispersion matching cells contain two sextupole lenses for optimization of the dynamic aperture.

The FODO cell contains two bending magnets and two quadrupole lenses. The length of the FODO cell is 4.30 m and 4.22 m in the outer and inner arcs, respectively. The advance of the betatron phases in the FODO cells in both arcs is  $\Delta\nu_{x,y} = 0.25$ . Thus, the matrix of transformation through two FODO cells is  $-I$ , due to which the sextupole lenses used to compensate for the natural chromaticity can be arranged as sextupole pairs [13] to suppress the second order of geometric aberrations.

Both in the matching cells and in the FODO cells, the same bending magnets 34 cm long with a bending angle of  $2.25^\circ$  are used. The field of bending magnet is chosen from the condition of the damping time of the betatron oscillations  $\tau_{x,y} \sim 30$  sec at a beam energy of 2.5 GeV (see p. 1.4).

The length and number of the FODO cells are selected from the consideration of formation of beam emittance  $\varepsilon_x \sim 8$  nm-rad and creation of three sextupole pairs in one super period of the bending arc (one horizontal and two vertical pairs).

Since the experimental section has a total bending angle of  $45^\circ$ , the matching of the geometry of the ring between the experimental section and a Siberian snake is performed using a short super-period consisting of two dispersion matching cells and two standard FODO cells, in which one horizontal sextupole pair is located. The bending angle of this super-period is  $13.5^\circ$ ; the length in the outer arc is 16 m; the length in the inner arc is 16.74 m. The optical functions of the super-period are depicted in Fig. 1.12.

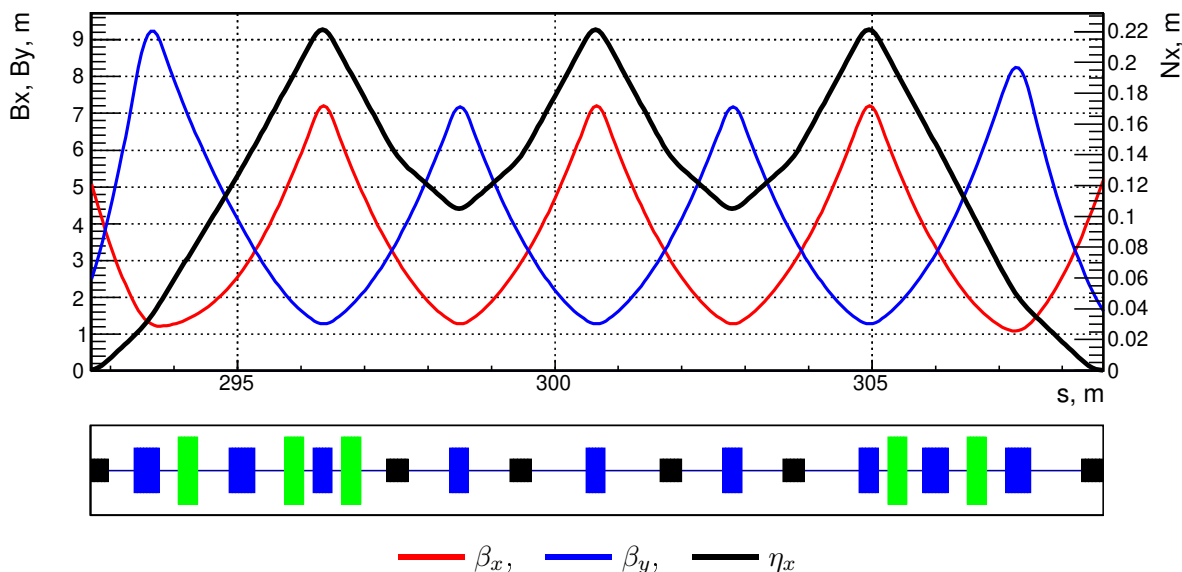


Figure 1.12. Optical functions of short super-period of bending arc.

### 1.3.3 Technical section

The technical section is located in a half-turn from the main interaction point and is intended for placement of the RF system, one Siberian snake, the ring separation segment, and the injection segment. The total length of the technical section, which is 139.74 m, is chosen so as to match the geometry of the entire ring, which is determined by the experimental section and the bending arcs. The technical section consists of the internal straight section 58.81 m long, the separation section 22.1 m long, and the outer straight section 69.83 m long. The technical section is shown in Fig. 1.13, and the optical functions are shown in Fig. 1.14.

The main part of the long segments of the technical section are FODO cells 5 m long and empty segments 2.25 m long. The advance of the betatron phases on one cell is  $\Delta\nu_x \approx 0.08$  and  $\Delta\nu_y \approx 0.09$ . Tuning of the betatron tunes of the entire ring is performed by means of change in the phase advance of the FODO cells. On the edges of the technical section, there are matching cells, which are to match the periodic behavior of the beta functions of the FODO cells with the super-period of the bending arcs.

On the edge of the inner segment adjacent to the bending arcs, there is one of the Siberian snakes. The inner segment also accommodates RF cavities, which are powered from the RF generator behind the inner wall of the tunnel of the Super Charm – Tau factory.



Figure 1.13. Technical section.

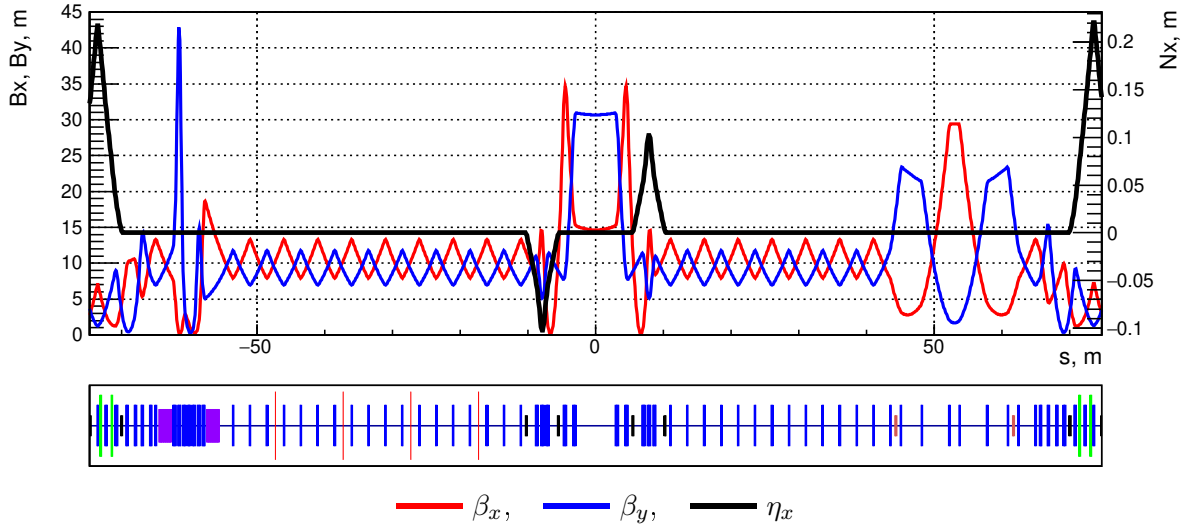


Figure 1.14. Optical functions of technical section.

The 22.1 m long ring separation segment is located in the middle of the technical section and consists of two achromatic bends, between them two doublets of quadrupoles spaced by a gap 5.8 m long are placed, where the two rings intersect. The achromatic bends carry out parallel transfer of the axis of the ring (the beam orbit) 1 m apart. Each achromatic bend consists of two dipole magnets of different polarity with a bending angle of  $2^\circ$ ; between the magnets there is a triplet of quadrupole lenses. The magnets are powered from the main field power source. The quadrupole doublets form a parallel beam in the long section of the crossing of the rings. The optical functions of the ring-separation segment are shown in Fig. 1.15.

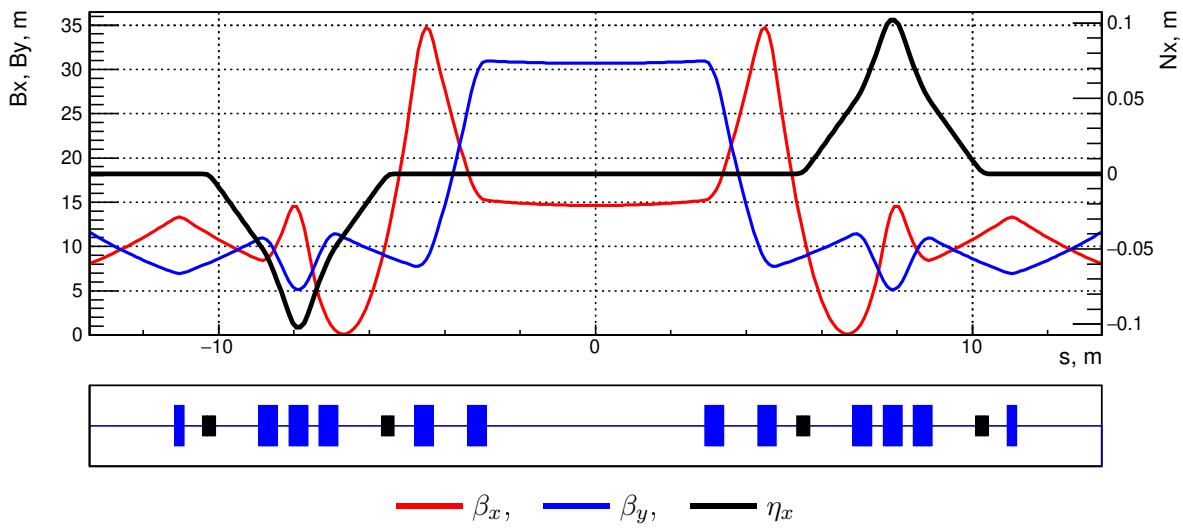


Figure 1.15. Optical functions of ring-separation segment in technical section.

The injection segment is in the external part of the technical section. The optical functions of

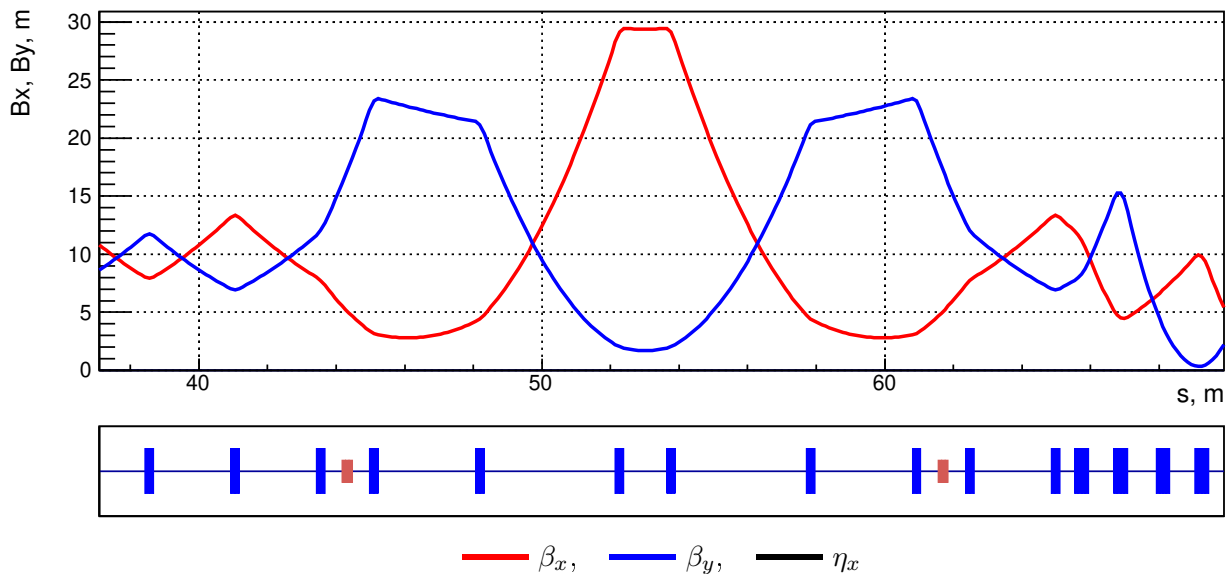


Figure 1.16. Optical functions of injection segment in technical section.

this segment are shown in Fig. 1.16. The beta functions at the injection point are  $\beta_x = 29.4$  m,  $\beta_y = 1.68$  m. Before and after the injection point there are a pre-inflector and inflector.

### 1.3.4 Siberian snake

Longitudinal polarization at the interaction point is created using five Siberian snakes (see p. 1.6), located azimuthally in the storage ring with a spacing of  $72^\circ$ . A Siberian snake consists of two superconducting solenoids, each 1.85 m long, between them seven quadrupole lenses (four focusing and three defocusing) are placed in a straight section 5.23 m long. The total length of Siberian snake is 8.93 m. All the Siberian snakes are located in the dispersion-free sections. Figure 1.17 shows the optical functions of the bending arc segment containing a Siberian snake. The behavior of the optical functions is symmetrical with respect to the middle of the Siberian snake. The main parameters of the magnetic elements and the distance between them are represented in Table 1.3, where the following notation is used:

$$N = \frac{B_z}{BR}, \quad K_1 = \frac{1}{BR} \frac{\partial B_y}{\partial x},$$

where  $BR$  is the magnetic rigidity and  $B_y$  and  $B_z$  are the vertical and longitudinal components of the field.

The transport matrix of Siberian snake (from the beginning of the first solenoid to the end of the second one) is

$$M = \begin{bmatrix} I & 0 \\ 0 & -I \end{bmatrix},$$

where  $I$  is the  $2 \times 2$  unitary matrix. This condition is met due to use of seven quadrupole lenses and empty sections between them, the solenoids either switched on or off.

The issue of the field of tolerances for the permissible deviations of the lens gradients from the nominal values was investigated. No too strict limitations on the exactness of the control of the lens currents were found. In fact, field deviations in the lenses and solenoids of up to 10% do not result in a significant increase in the vertical emittance.

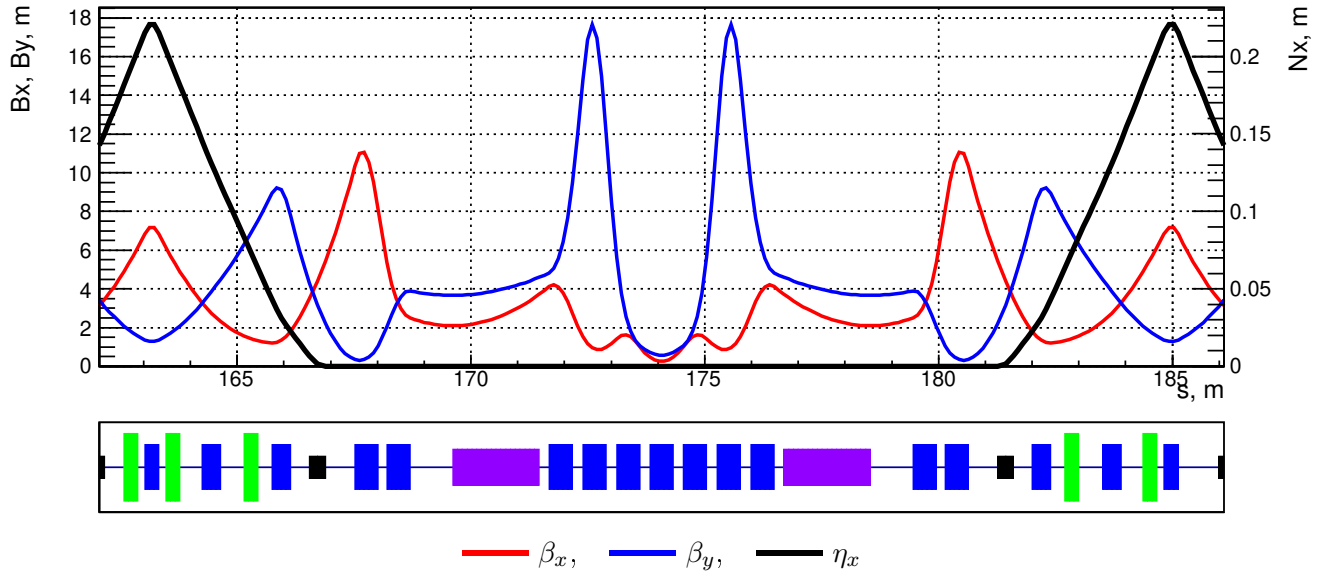


Figure 1.17. Optical functions of segment with Siberian snake (solenoids switched off).

Table 1.3. Siberian snake parameters.

Element	Notation	Length	Strength	Value	
<i>Snake</i>				<i>On</i>	<i>Off</i>
Solenoid	SOL	1.85 m	$N$	$0.849 \text{ m}^{-1}$	$0 \text{ m}^{-1}$
Section	DSP0	0.50 m			
Quadrupole	QSP0	0.50 m	$K_1$	$2.03 \text{ m}^{-2}$	$2.37 \text{ m}^{-2}$
Section	DSP1	0.20 m			
Quadrupole	QSP1	0.65 m	$K_1$	$-2.21 \text{ m}^{-2}$	$-2.89 \text{ m}^{-2}$
Section	DSP2	0.20 m			
Quadrupole	QSP2	0.65 m	$K_1$	$2.78 \text{ m}^{-2}$	$3.04 \text{ m}^{-2}$
Section	DSP3	0.30 m			
Quadrupole	QSP3	0.50 m	$K_1$	$-2.57 \text{ m}^{-2}$	$0.62 \text{ m}^{-2}$

### 1.3.5 Damping wiggler

Control of the radiation parameters of the beam in each ring of the Super Charm–Tau factory is performed using four superconducting damping wigglers. The choice of parameters for the damping wigglers is described in detail in p. 1.4, and the technical realization of superconducting wiggler — in p. 1.13.2. For reduction in the effect of the damping on the dynamics of the spin in the ring, the damping wigglers are placed in the bending arcs between the Siberian snakes, i. e., with a spacing of an angle of  $36^\circ$ . The total length of the section is 21.9 m. Figure 1.18 shows the optical functions of the damping wiggler segment. The behavior of the optical functions is symmetric with respect to the middle of the section.

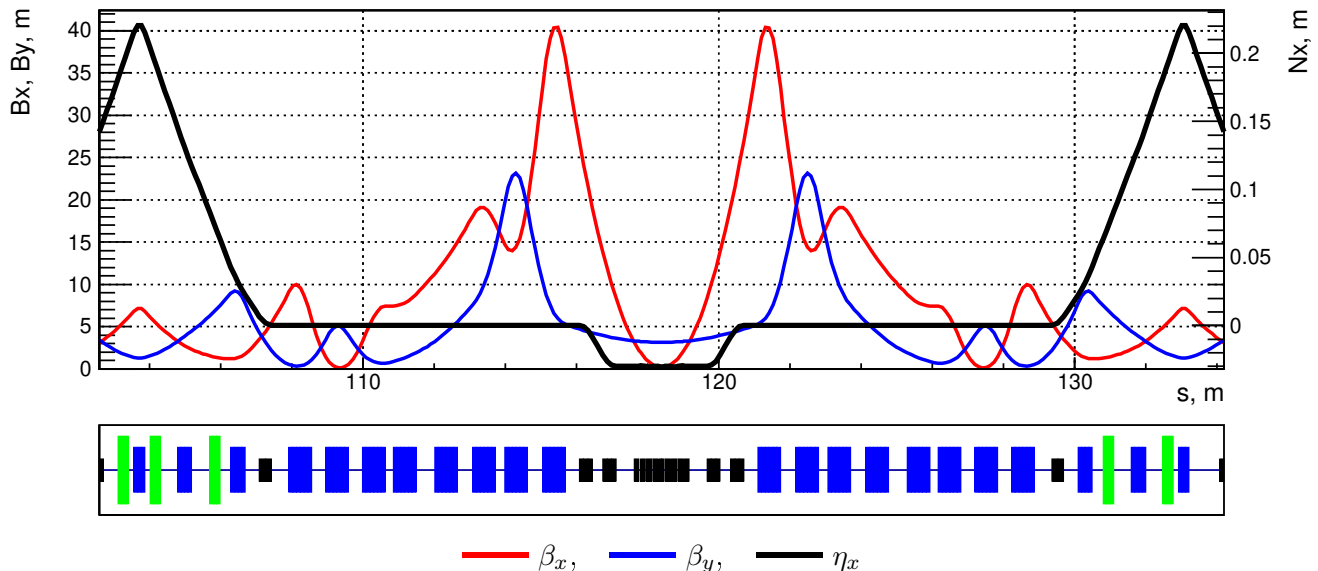


Figure 1.18. Optical functions of damping wiggler section at 2.5 GeV.

A damping wiggler with a (magnetic) length of 1.875 m is placed in the middle of section. On both sides of the wiggler there are two bending magnets 34 cm long with an empty gap 50 cm long between them, which are used for creation of a local bump to the orbit (with zero bending angle) and, thus, a change in the dispersion in the wiggler. Further, between the bending magnets and the super-period of the bending arc, in a straight section 8.62 m long, there are 8 quadrupole lenses to focus the optical functions in the center of the wiggler to small values, which is required to reduce the emittance growth at high energies, as well as diminishing the influence of wiggler focusing at low energies. With the help of these lenses, the effect of the wiggler field on the optics of the storage ring is compensated for. So, the values of the optical functions at the entry to and exit from the section and the phase advances in the section do not depend on the wiggler field in the entire energy range.

For due account of the effect of damping wiggler field on the optics and radiation parameters of the beam, we used an approximate wiggler modeling based on considerations stated below. The field of a wiggler with infinitely wide poles is described as follows [14]:

$$\begin{aligned}
 B_x &= 0, \\
 B_y &= B_W \cosh(k_W y) \sin(k_W z), \\
 B_z &= -B_W \sinh(k_W y) \cos(k_W z),
 \end{aligned}
 \tag{1.11}$$

where  $k_W = 2\pi/\lambda_W$ ,  $\lambda_W$  is the field period, and  $B_W$  is the maximum (peak) value of the field. The

wiggler model used at the Super Charm–Tau factory is built on a periodic sequence of rectangular magnets. One half-period of the field is represented by a set of three magnets of the same polarity but of different lengths and field amplitudes (see Fig. 1.19). From the symmetry condition, the first and last magnets are identical. Parameters of these magnets are chosen from three conditions: the angle of bending in a half-period and the second  $I_2$  and third  $I_3$  radiation integrals,

$$\theta_W = \frac{1}{\pi} h_W \lambda_W, \quad I_{2,W} = \frac{1}{4} h_W^2 \lambda_W, \quad I_{3,W} = \frac{2}{3\pi} h_W^3 \lambda_W.$$

Thus, the field  $B_m$  and the lengths  $L_m$  of the equivalent magnets are

$$B_{m_0} = B_W \frac{K-2\pi}{6(\pi^2-8)}, \quad L_{m_0} = \lambda_W \frac{\pi K - 2(5\pi^2 - 48)}{8\pi K}, \quad (1.12)$$

$$B_{m_1} = B_W \frac{K+2\pi}{6(\pi^2-8)}, \quad L_{m_1} = \lambda_W \frac{\pi K + 2(5\pi^2 - 48)}{4\pi K},$$

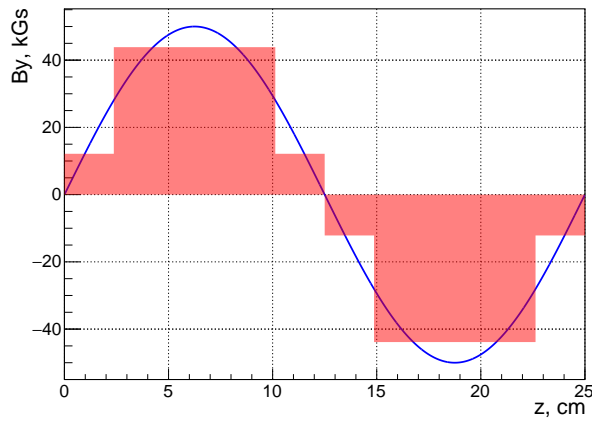
where  $m_0$  and  $m_1$  denote the side magnet and the central magnet on the field half-period, and the constant  $K$  is equal to

$$K = \sqrt{2(768 - 166\pi^2 + 9\pi^4)}.$$

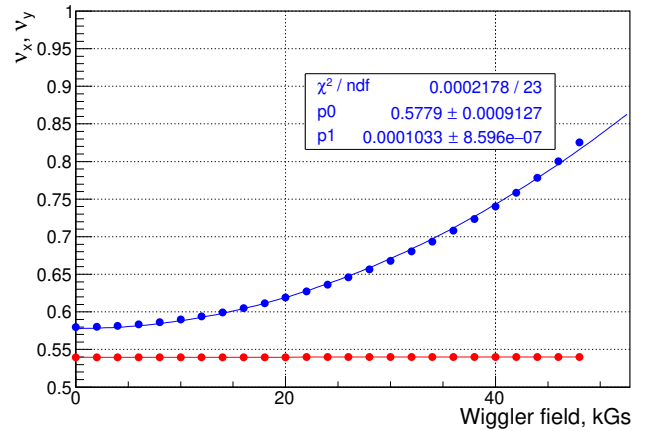
This model will also give a correct contribution to the focusing. For example, the betatron tune shift introduced by the wiggler field is

$$\Delta\nu_x = 0, \quad \Delta\nu_y = \frac{1}{8\pi} h_W^2 L_W \bar{\beta}_y, \quad (1.13)$$

where  $L_W = N_W \lambda_W$  is the total length of the wigglers, and  $\bar{\beta}_y$  is the vertical beta function averaged over the length of the wiggler. The dependence of the betatron tunes on the amplitude of the damping wiggler, obtained from the simulation, is shown in Fig. 1.20.



— model, — field



—  $\nu_x$ , —  $\nu_y$

Figure 1.19. Wiggler model (one field period).

Figure 1.20. Dependence of betatron tunes on damping wiggler field.

## 1.4 Control of the beam emittance and damping parameters

To attain the maximum luminosity at the Super Charm–Tau factory in the whole energy range (see p. 1.2), it is necessary to effectively control the radiation damping parameters of the accelerator in order to maintain the horizontal emittance ( $\varepsilon_x = 8 \text{ nm-rad}$ ) and the damping time ( $\tau_{x,y} = 30 \text{ ms}$ ,  $\tau_z = 15 \text{ ms}$ ) constant. For this purpose, it is planned to place superconducting wigglers in both rings. The parameters of the magnet lattice of the main ring (without damping wigglers) are chosen so that at the maximum energy (2.5 GeV) they meet the requirement  $\varepsilon_x \approx 8 \text{ nm-rad}$  and  $\tau_{x,y} \approx 30 \text{ ms}$ . Table 1.4 presents the radiation integrals [15] of the main lattice of the Super Charm–Tau factory, i. e., without damping wigglers. The technical aspects of the realization of superconducting wigglers are discussed in p. 1.13.2.

All calculations of this section are performed without taking into account the intrabeam scattering, whose effect is significant at low beam energies.

Table 1.4. Radiation integrals of Super Charm–Tau factory without damping wigglers.

Integral	Value
$I_1$	0.727 m
$I_2$	$0.687 \text{ m}^{-1}$
$I_3$	$0.077 \text{ m}^{-2}$
$I_{4,x}$	$-9.17 \cdot 10^{-5} \text{ m}^{-1}$
$I_5$	$4.88 \cdot 10^{-4} \text{ m}^{-1}$

The parameters of the wigglers can be estimated from the considerations below. The dependence of the damping time on the energy and magnet lattice of the circular accelerator looks as follows [15]:

$$\tau_{x,y,z} = \frac{\Pi}{C_a E^3 J_{x,y,z} I_2}, \quad (1.14)$$

where  $C_a = 2113.1 \text{ m}^2/\text{GeV}^3/\text{s}$ ,  $\Pi$  is the perimeter of the storage ring,  $E$  is the beam energy,  $J_{x,y,z}$  are dimensionless damping decrements for which the condition  $J_{x,y} = 1$  and  $J_z = 2$  is met (since at the Super Charm–Tau factory all the bending magnets have no field gradient), and  $I_2$  is the second radiation integral, which is calculated as follows:

$$I_2 = \int h(s)^2 ds = I_{2,R} + I_{2,W}. \quad (1.15)$$

The integral  $I_2$  has two components:  $I_{2,R}$ , which is formed by the main lattice of the ring without damping wigglers (only the bending magnets) and is a constant of the beam energy, and  $I_{2,W}$ , which is an adjustable contribution from the damping wigglers. In the case of a sinusoidal field behavior along the wiggler axis, the latter component can be calculated as

$$I_{2,W} = \frac{1}{2} h_W^2 L_W, \quad (1.16)$$

where  $h_W = B_W/BR$ ,  $B_W$  is the peak value of the field in the wiggler,  $BR$  is the magnetic rigidity,  $L_W = \lambda_W N_W$  is the total length of all wigglers,  $\lambda_W$  is the field period, and  $N_W$  is the number of periods.

Let us express (1.15) in terms of (1.14), taking  $\tau_x = \tau_y = \text{const}$  and  $I_{2,R} = \text{const}$ , i.e., independent of the beam energy,

$$I_{2,W} = \frac{\Pi}{C_a \tau_x} E^{-3} - I_{2,R} \quad (1.17)$$

and use (1.16) to find the dependence of the field in the damping wiggler on the beam energy:

$$B_W = 33.36E \sqrt{\frac{2}{L_W} \left( \frac{\Pi}{C_a \tau_x} E^{-3} - I_{2,R} \right)}. \quad (1.18)$$

So, changing the field of the wiggler, we can control the time of radiation damping. Let us now consider the contribution of the wigglers to the emittance of the beam, which is expressed as follows [15]:

$$\varepsilon_x = C_\varepsilon \frac{I_5}{J_x I_2} E^2, \quad (1.19)$$

where  $C_\varepsilon = C_q/m^2/c^4 = 1.467 \cdot 10^{-6} \text{ m/GeV}$ , and  $I_5$  is the radiation integral determined by the optical functions in the storage ring ( $H_x = \beta_x \eta_x'^2 + 2\alpha_x \eta_x' \eta_x + \gamma_x \eta_x^2$ )

$$I_5 = \int |h(s)|^3 H_x(s) ds = I_{5,R} + I_{5,W}, \quad (1.20)$$

where  $I_{5,R} = \text{const}$  is the contribution of the bending magnets of the ring, and  $I_{5,W}$  is the contribution of the damping wigglers, which in the case of a sinusoidal wiggler field is calculated as follows:

$$I_{5,W} = \frac{1}{15\pi^3} h_W^3 \lambda_W^2 \left( \bar{\beta}_x + \frac{20\pi^2 \eta_0^2}{\beta_x h_W^2 \lambda_W^2} \right), \quad (1.21)$$

where  $\bar{\beta}_x$  is the mean value of the horizontal beta function over the length of the wiggler, and  $\eta_0$  is the dispersion function at the entry to the wiggler. In this expression, we neglected the effect of the wiggler field on the focusing. However, the contribution from the intrinsic dispersion function excited by the wiggler field is taken into account. This contribution is especially important at low energies of the Super Charm–Tau factory. Then

$$I_{5,W} = \frac{1}{C_\varepsilon} \frac{I_2(E) \varepsilon_x}{E^2} - I_{5,R}, \quad (1.22)$$

where the dependence of  $I_2$  on the energy can be expressed through (1.15) and (1.17).

The dependence of the integrals  $I_{2,W}$  and  $I_{5,W}$  in the energy range of the Super Charm–Tau factory is shown in Fig. 1.21 under the condition that  $\tau_x = 30 \text{ ms}$ ,  $\varepsilon_x = 8 \text{ nm-rad}$ , and  $\Pi = 813.1 \text{ m}$ , the integrals  $I_{2,R}$  and  $I_{5,R}$  taken from Table. 1.4.

Thus, varying  $B_W$ , we can control  $I_2$  and, in turn,  $\tau_x$ . With a given  $I_2$  we can attain a required  $\varepsilon_x$  via changing the dispersion,

$$\eta_0 = \frac{\bar{\beta}_x h_W^2 \lambda_W^2}{20\pi^2} \left[ \frac{15\pi^3}{h_W^3 \lambda_W^2} \left( \frac{1}{C_\varepsilon} \frac{I_2(E) \varepsilon_x}{E^2} - I_{5,R} \right) - \bar{\beta}_x \right]. \quad (1.23)$$

To ensure dependencies (1.17) and (1.22) we use four damping wigglers with a maximum field of 50 kG, a length of 1.875 m, and a field period  $\lambda_W = 25 \text{ cm}$ . Variation in the dispersion in a damping wiggler is achieved using four dipole magnets with a zero total bending angle, which are placed near the wiggler and create local distortion of the orbit inside the wiggler (bump). The

dependence of the wiggler field and dispersion in it on the beam energy is shown in Fig. 1.23. For comparison (here and below), presented are the dependences for the lattice with the damping wigglers switched off (red dots), with the damping wigglers without field limitation (green dots), and with a 50 kG damping wiggler. These dependences were obtained from calculation of the actual lattice of the Super Charm–Tau factory considering compensation for the influence of the damping wigglers on the optics of the collider. Table 1.5 presents radiation integrals of the whole ring of the Super Charm–Tau factory at different beam energies. The table also shows the regular bending field  $B_0$ , the wiggler field  $B_W$ , the field  $B_b$  of the bending magnet that creates dispersion inside the wiggler and the field  $B_e$  of the bending magnet in front of the IP (detector).

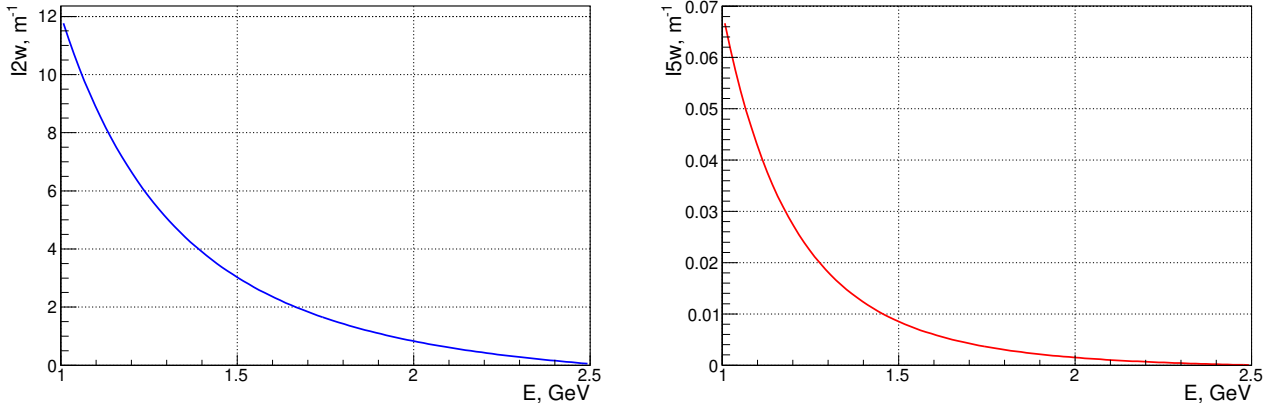


Figure 1.21. Integrals  $I_{2,W}$  and  $I_{5,W}$  vs. beam energy.

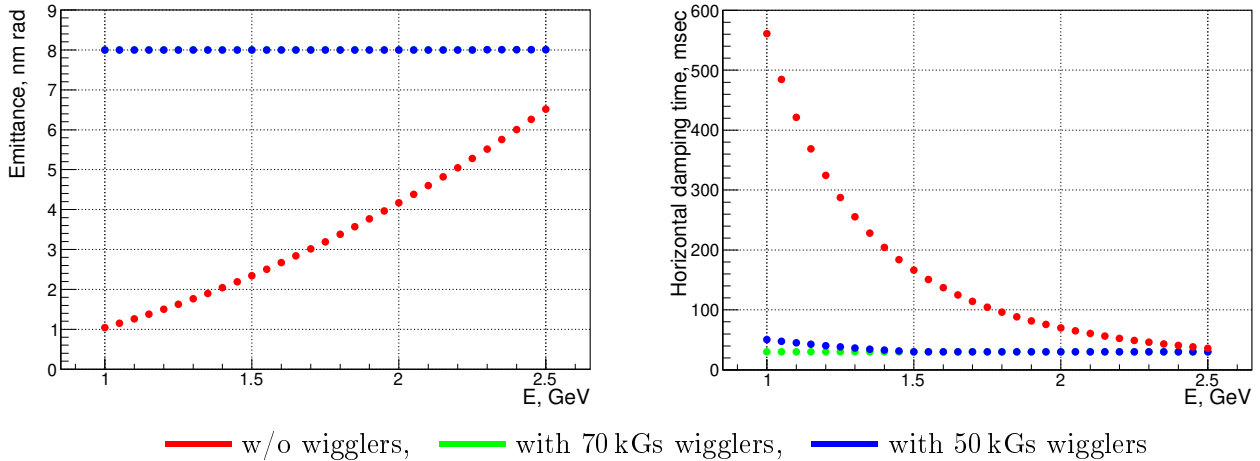


Figure 1.22. Beam emittance and decay time vs. beam energy.

Unfortunately, because of technical difficulties in implementing the superconducting wiggler (see p. 1.13.2), we failed to obtain a field of above 50 kG and, therefore, did not meet the conditions  $\varepsilon_x = 8 \text{ nm}\cdot\text{rad}$  and  $\tau_{x,y} = 30 \text{ ms}$  in the entire energy range. However, the main energy range (where the basic acquisition of the luminosity integral will be realized) is 1.5 GeV to 2.5 GeV. Thus, at energies below 1.5 GeV, the wiggler field will remain constant (maximal), 50 kG. In this case it is possible to keep the emittance of the beam constant,  $\varepsilon_x = 8 \text{ nm}\cdot\text{rad}$ , due to varying the dispersion in the wiggler, and the damping time will increase (see Fig. 1.22). It is worth noting that the damping time at 1 GeV is  $\tau_x \sim 50 \text{ ms}$ , whereas with the damping wigglers switched off  $\tau_x \sim 550 \text{ ms}$ .

Table 1.5. Radiation integrals and field of magnets of Super Charm – Tau factory at different beam energies.

Energy	1.0	1.5	2.0	2.5		GeV
$B_0$	3.85	5.78	7.71	9.63	9.63	kG
$B_e$	1.47	2.2	2.94	3.67	3.67	kG
$B_W$	50	50	34.8	10.2	0	kG
$B_b$	3.42	4.82	7.91	10.3	0	kG
$I_1$	0.710	0.716	0.717	0.718	0.727	m
$I_2$	7.63	3.80	1.61	0.822	0.687	$\text{m}^{-1}$
$I_3$	7.94	2.41	0.419	0.092	0.077	$\text{m}^{-2}$
$I_{4,x}$	$-9.79 \cdot 10^{-4}$	$-7.37 \cdot 10^{-4}$	$-1.9 \cdot 10^{-4}$	$-1.02 \cdot 10^{-4}$	$-9.17 \cdot 10^{-5}$	$\text{m}^{-1}$
$I_5$	$4.16 \cdot 10^{-2}$	$9.21 \cdot 10^{-3}$	$2.19 \cdot 10^{-3}$	$7.17 \cdot 10^{-4}$	$4.88 \cdot 10^{-4}$	$\text{m}^{-1}$

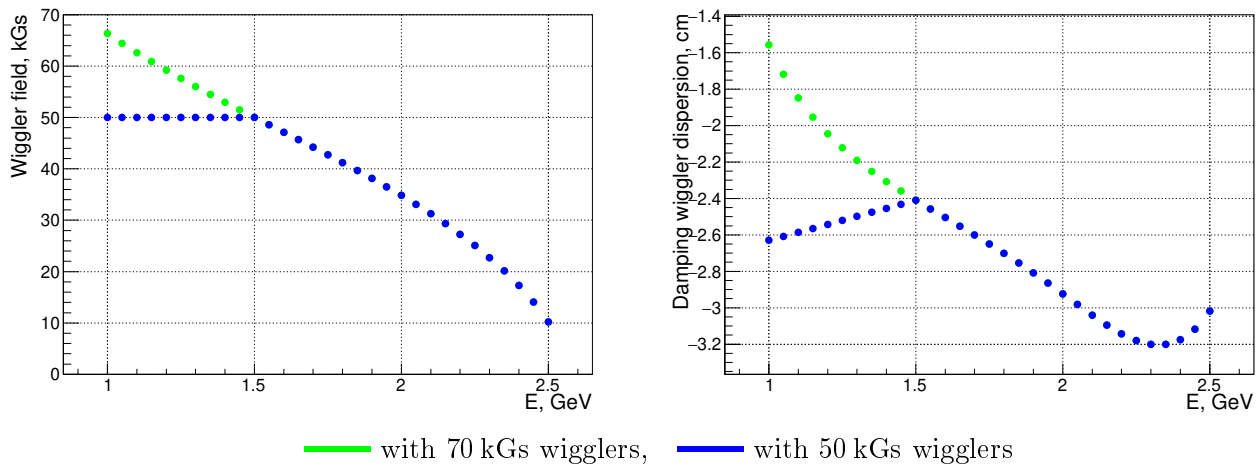


Figure 1.23. Damping wiggler field and dispersion in it vs. beam energy.

As a consequence, the use of the damping wigglers to increase the radiation with decreasing the beam energy changes the dependence of the energy spread on the energy:

$$\sigma_{\Delta E/E} = E \sqrt{C_\varepsilon \frac{I_3}{J_z I_2}} = E \sqrt{\frac{C_\varepsilon I_3}{2 I_2}}. \quad (1.24)$$

In the case of a ring without damping wigglers, the expression under the square root is a constant. The dependence of the relative and absolute energy spread in the beam is shown in Fig. 1.24 (blue dots). For comparison, the dependence of the energy spread for the lattice without the damping wigglers is given (red points).

In turn, the dependence of the energy loss to the synchrotron radiation and the loss power per turn changes (see Fig. 1.25)

$$U_0 = c C_a I_2 E^4 = \frac{2c\Pi}{\tau_x} E, \quad P_0 = U_0 I,$$

where  $c$  is the speed of light, and  $I$  is the total beam current. For comparison, the dependences without the damping wigglers are also given (red dots).

Let us estimate the power of synchrotron radiation for different types of magnets.

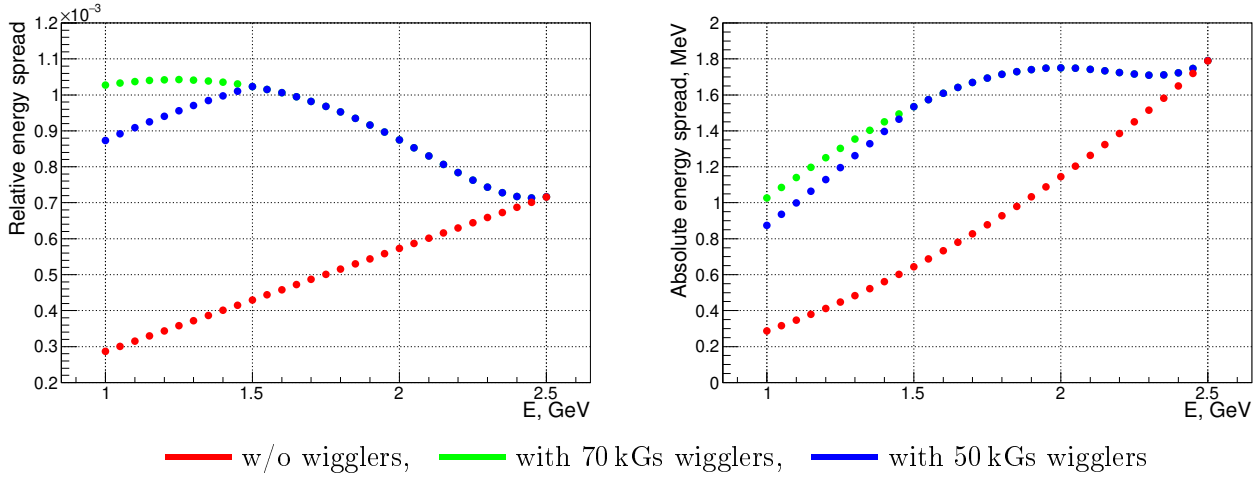


Figure 1.24. Relative and absolute energy spread in beam vs. beam energy.

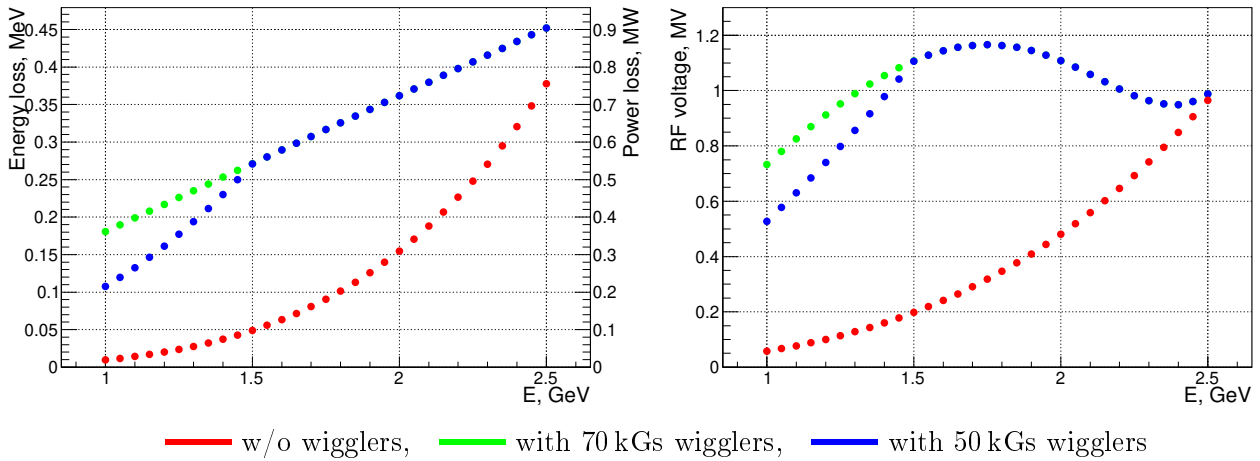


Figure 1.25. Energy loss and power of loss (beam current of 2 A) to synchrotron radiation and RF voltage ( $\sigma_z = 1$  cm) vs. beam energy.

Table 1.6. Radiation power of different types of magnets of Super Charm–Tau factory.

Energy	1.0	1.5	2.0	2.5	GeV
Regular bending	0.13	0.65	2.04	4.99	kW
Final bending	0.05	0.28	0.87	2.13	kW
Damping wiggler	48.4	109	94.1	12.6	kW
Bump bending	0.10	0.49	2.34	6.16	kW

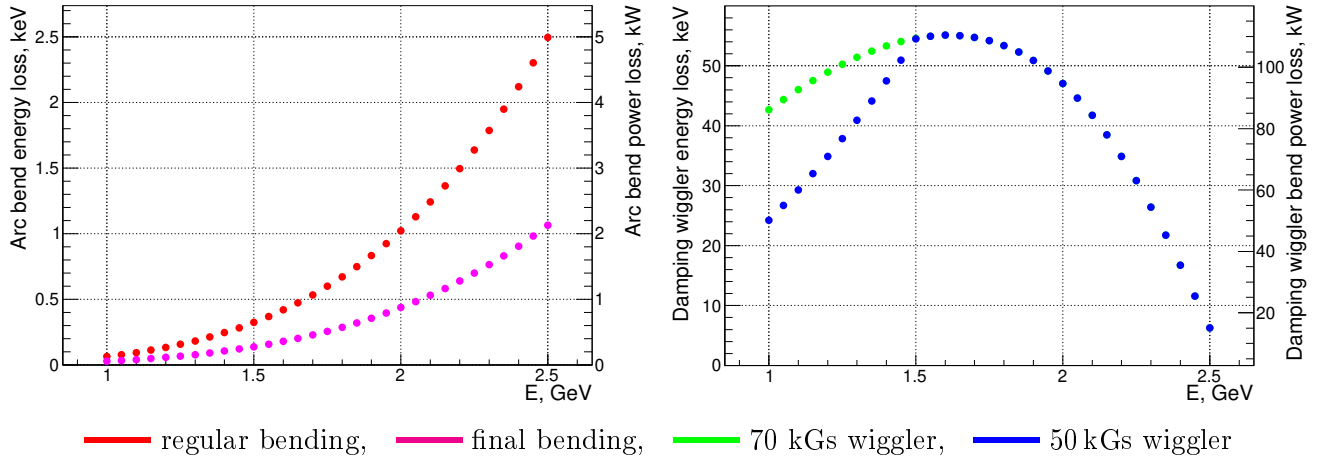


Figure 1.26. Energy loss and power of loss (beam current of 2 A) to synchrotron radiation vs. beam energy for different types of magnets.

As noted above, the effect of the damping wigglers on the radiation parameters of the beam was estimated without taking into account the intrabeam scattering, which at low beam energies will lead to increase in the phase space volume in dependence on the beam current. The increment of the emittance of the beam because of this effect can be compensated for by reducing the dispersion function in the damping wigglers in comparison with dependence (1.23). In addition, the process of intrabeam scattering will lead to increase in the energy spread in comparison with (1.24), and this increment can not be compensated for. However, the use of the damping wigglers, with which it is possible to keep the emittance of the beam constant throughout the energy range, enables substantial weakening of the effect of the intrabeam scattering.

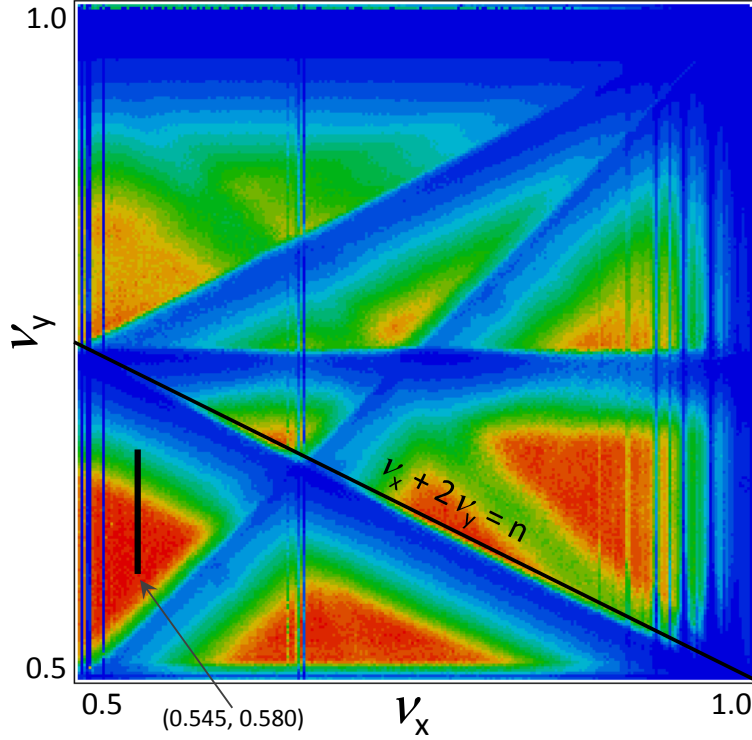
## 1.5 Beam-beam effects and luminosity

The beam-beam parameters for  $\sigma_y \ll \sigma_x$  and  $\theta \neq 0$  become [10, 11]:

$$\begin{aligned} \xi_x &= \frac{N_b r_e}{2\pi\gamma} \cdot \frac{\beta_x^*}{\sigma_x^2 (1 + \phi^2)} \quad \Rightarrow \quad \frac{N_b r_e}{2\pi\gamma} \cdot \frac{\beta_x^*}{(\sigma_z \theta)^2} \\ \xi_y &= \frac{N_b r_e}{2\pi\gamma} \cdot \frac{\beta_y^*}{\sigma_x \sigma_y \sqrt{1 + \phi^2}} \quad \Rightarrow \quad \frac{N_b r_e}{2\pi\gamma} \cdot \frac{\beta_y^*}{\sigma_y \sigma_z \theta} \end{aligned} \quad (1.25)$$

The expressions after arrows correspond to  $\phi \gg 1$  and  $\theta \ll 1$ . Note that  $\xi_x \propto 1/\varepsilon_x$  (in head-on collision) transforms to  $\xi_x \propto \beta_x^*$  when  $\phi \gg 1$ , and the  $\xi_y$  dependence on  $\sigma_x$  vanishes.

To find the area of good working points, we performed numerical simulations using the beam-beam code `Lifetrac` [17]. At the first stage, a simplified model was applied: linear lattice without explicit betatron coupling, weak-strong approximation. The fractional parts of betatron tunes were scanned in the range from 0.5 to 1.0, all other parameters are taken from Table 1.1 at 2 GeV; the results are presented in Fig. 1.27. Since  $\xi_x \ll \xi_y$ , the footprint looks like a narrow vertical strip, the bottom edge resting on the working point. Particles with small vertical betatron amplitudes have maximum tune shifts and are in the upper part of the footprint, so the resonances in Fig. 1.27 seem to be shifted down.



The color scale from zero (blue) to  $10^{35} \text{ cm}^{-2} \text{ s}^{-1}$  (red). The black narrow rectangle shows the footprint at  $(0.545, 0.580)$ .

Figure 1.27. Luminosity at 2 GeV as a function of betatron tunes.

In collision schemes with large Piwinski angle, the bunches rotate in the horizontal plane due to beam-beam interaction; so we have some kind of crab crossing without crab cavities. In the weak-strong model, rotation of the “weak” bunch is compensated by the crab sextupoles and does not lead to negative consequences. However, rotation of the “strong” bunch can disrupt the operation of Crab Waist scheme; so the rotation angle should be much less than  $\theta$ . The former depends on  $\nu_x$ : it is minimal near the half-integer resonance and is maximal near the integer one; hence the red regions on the right-hand side of Fig. 1.27 should be excluded from consideration. Another point: to achieve the design luminosity it is necessary to obtain a small vertical emittance, and here the distance from the working point (and the whole footprint) to the main coupling resonance  $\nu_x = \nu_y$  is important. If we consider good regions near this resonance, it is better to stand above it, since beam-beam effects shift the bunch core upward, thereby increasing the distance to the resonance.

In view of the foregoing, the good region is reduced to the red triangle in the lower left corner, bounded from below by the main coupling resonance, from above by the sextupole resonance  $\nu_x + 2\nu_y = n$ , and from the left by the half-integer resonance  $2\nu_x = 1$  with its synchrotron satellites. All other higher-order coupling resonances are suppressed by the Crab Waist, and therefore are not visible. However, the synchro-betatron resonances  $2\nu_x - 2k\nu_z = n$  turned out to be more dangerous than it may seem from Fig. 1.27. A new phenomenon has recently been discovered in collisions with  $\phi \gg 1$ : coherent  $X$ - $Z$  instability [18], which leads to a disruption in the operation of Crab Waist scheme and multiple growth of the horizontal emittance. The increase in  $\sigma_x$  itself does not have a noticeable impact on the luminosity, but this leads to a proportional increase in  $\sigma_y$  due to the betatron coupling; so eventually the luminosity decreases several times.

The instability does not cause dipole oscillations and therefore cannot be suppressed by feedback. We need to look for conditions under which it does not arise.

As shown in [19], the problem is related to synchrotron satellites of half-integer betatron resonance, so  $\nu_x$  and the relation between  $\xi_x$  and  $\nu_z$  are of great importance. Fig. 1.28 shows the growth of  $\varepsilon_x$  because of the instability, and synchro-betatron resonances of high orders are clearly visible. As a consequence, in contrast to a head-on collision, the limit on  $\xi_x$  is now determined by the synchrotron tune. In our case  $\xi_x$  is less than  $\nu_z$  approximately 3 times; precisely because of this there are regions between resonances that are free of instability. In this connection, it is important that  $\beta_x^*$  be small enough: besides that  $\xi_x \propto \beta_x^*$ , the bunch rotation angle mentioned above is also proportional to  $\beta_x^*$ .

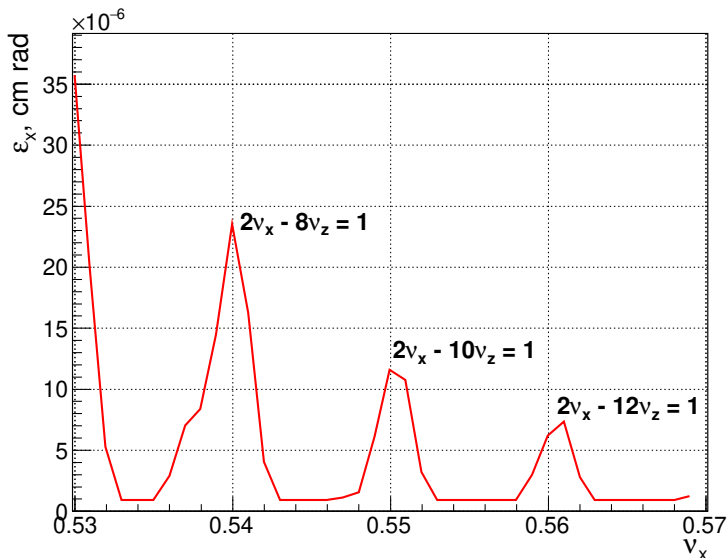


Figure 1.28. Growth of  $\varepsilon_x$  due to coherent X-Z instability, as a function of  $\nu_x$ .

As is seen from Fig. 1.28, with the growth of  $\nu_x$  the order of resonances increases, their strength weakens and the free gaps become wider. However, moving the working point to the right, it is also necessary to increase  $\nu_y$  to keep the distance to the main coupling resonance. Both these actions lead to a decrease in the distance between the upper edge of the footprint and the resonance  $\nu_x + 2\nu_y = n$  (see Fig. 1.27). Thus, for  $\nu_x$  there are two suitable options: 0.545 and 0.555, while  $\nu_y$  should be selected from the requirement  $\nu_y - \nu_x > 0.03$  to provide sufficient distance to the coupling resonance. This determines our choice of the working point.

It should be noted that the design value  $\xi_y = 0.12$  is well below the limit. The margin can be estimated by the distance from the footprint top edge to the line  $\nu_x + 2\nu_y = n$  or, which is almost the same, from the footprint bottom edge to the point where it crosses the border of the red area. There are several ways to raise  $\xi_y$ : increasing the bunch current, reducing the bunch length, and decreasing the vertical emittance (betatron coupling). But all this also leads to decrease in the lifetime due to intrabeam scattering (Touschek effect) and enhancement of collective effects. This means that  $\xi_y$  is not limited by beam-beam interaction, which, consequently, will not have a significant impact on the equilibrium distribution of particles in a bunch.

In colliders with a large total current and a large number of bunches, one of the important parameters is their permissible longitudinal displacement. The parameters and cost of RF system depend on this, and the tolerance is determined by its influence on beam-beam effects and luminosity. In head-on collision, a longitudinal displacement of bunches implies a displacement of the

IP azimuth; so it should be much smaller than  $\beta_y^*$ . Otherwise, because of the hour-glass effect,  $\beta_y$  will grow at the actual collision point, which means that  $\xi_y$  will increase (and may exceed the threshold), while the luminosity falls due to the geometric factor. However, in collision with  $\phi \gg 1$ , everything looks different. As is seen from Fig. 1.1, a longitudinal displacement of bunches now *does not lead* to a shift in the IP azimuth, and  $\xi_y$  does not grow but even falls slightly. The only drawback is a slight decrease in luminosity due to the geometric factor. So, a displacement of one of the bunches by  $0.3\sigma_z$  leads to a drop in the luminosity by  $2 \div 3\%$ , which is quite acceptable.

## 1.6 Polarization

Polarized electrons are produced on the photocathode of the source with an energy of 100 keV to 200 keV and then they are accelerated in a linear accelerator to the energy required for the experiment, 1 GeV to 2.5 GeV. The spin manipulator of the source can set any desired direction of the electron spin at the point of their injection into the ring. It remains only to make a closed spin trajectory along the perimeter of the ring such that the spin is longitudinal at the point of the collision of electrons with positrons.

### 1.6.1 Closed spin orbit. Spin rotators

For this, it is proposed to install five spin rotators on the electron storage ring, the so-called Siberian snakes [20], each rotating the spin by  $180^\circ$  around the longitudinal axis of the accelerating coordinate system. Each such snake consists of two superconducting solenoids separated by a mirror-symmetric optical system of seven quadrupole lenses, see Fig. 1.29. The total field integral of the two solenoids is

$$\int B dl = \pi B \rho = 26.15 \text{ T} \cdot \text{m}, \quad \text{for } E = 2.5 \text{ GeV}.$$

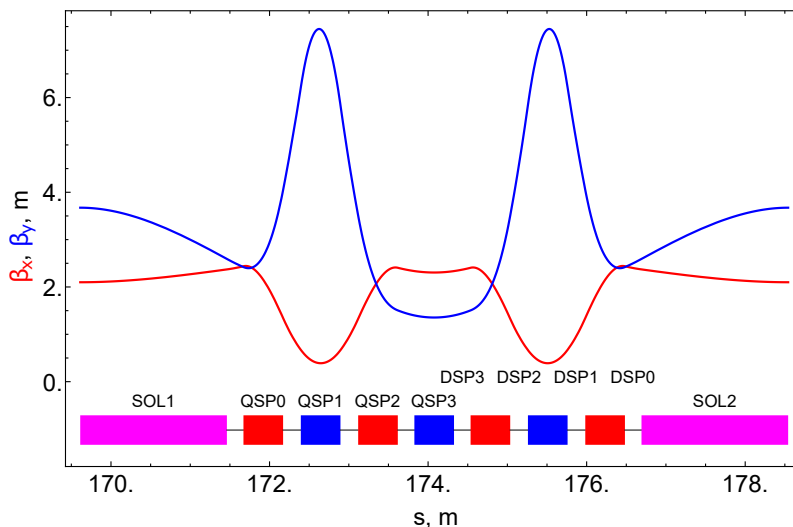


Figure 1.29. Optical scheme of spin rotator, full Siberian snake rotating spin by  $180^\circ$  around solenoid axis.

The transport matrix of the spin rotator, including the solenoids, must satisfy two conditions: first, it is to have zero off-diagonal  $2 \times 2$  blocks; second, it is to meet the condition of spin

transparency. For a full Siberian snake, both these requirements are met simultaneously if we set that [21]

$$M_x = -M_y = \begin{pmatrix} -\cos(2\phi) & -2r \sin(2\phi) \\ (2r)^{-1} \sin(2\phi) & -\cos(2\phi) \end{pmatrix} = \begin{pmatrix} 1 & 0 \\ 0 & 1 \end{pmatrix},$$

where  $\phi$  is the angle of spin rotation by one solenoid. In the case of full snake,  $\cos(2\phi) = -1$ . In the case of  $\phi < \pi/2$ , the snake is called partial. Unfortunately, it is considerably inferior to a full snake in the rate of depolarization of the beam and will not be considered further.

A method for compensating for betatron oscillations introduced by solenoids by means of inserting between them a certain optical system that satisfies the condition  $M_x = -M_y$  was proposed in [22]. A great advantage of the discussed option of compensation for the coupling is the absence of necessity to use any skew lenses. In this scheme, the field of solenoids can vary within wide limits without change in the strength of the quadrupole lenses and, in particular, their complete switching-off is allowed, the coupling remaining zero. However, if we want to do without changing the betatron phase advance throughout the insert, then we need to slightly adjust the gradients of the fields in the lenses. The main advantage is that the lens does not need to be rotated around the longitudinal axis, as it should be done in some alternative coupling compensation schemes, also considered in [22].

With an odd number of snakes, the spin in the arcs of the ring is everywhere in the median plane and is exactly longitudinal in the middle of the arcs between the snakes. Schematically this is depicted in Fig. 1.30, where the equilibrium direction of the spins is shown (a closed spin trajectory) in a ring with five snakes spaced uniformly in the azimuth. The depolarizing effect of the damping wigglers is minimal if they are set at places where the spin is longitudinal.

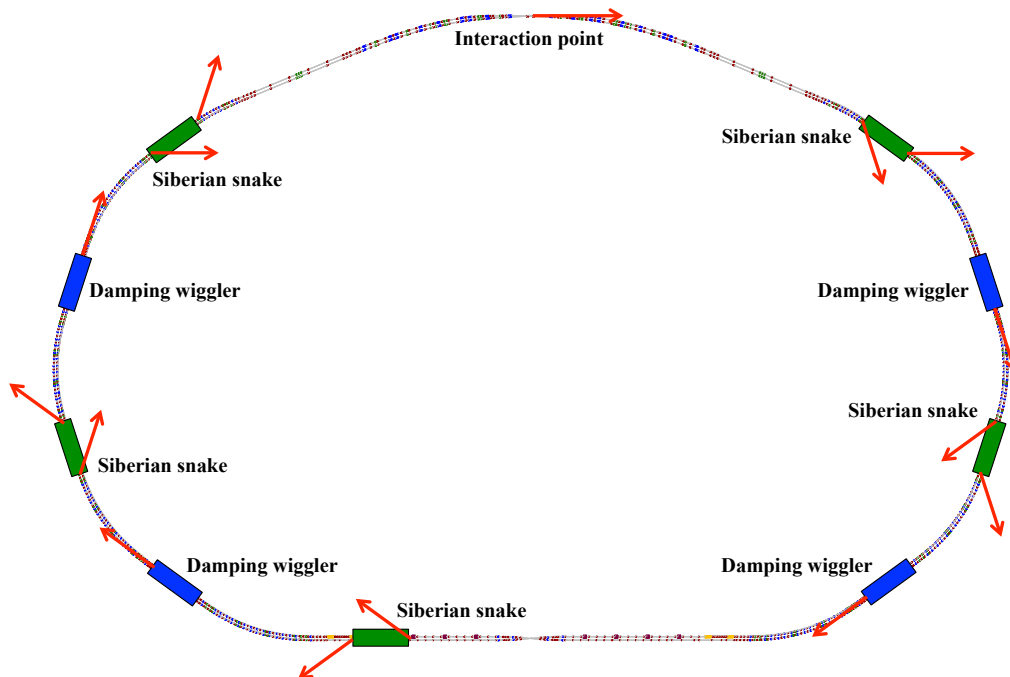


Figure 1.30. Equilibrium closed spin trajectory in ring with five Siberian snakes.

## 1.6.2 Radiative relaxation of spins

The depolarization time grows in proportion to the square of the number of the snakes. We chose five snakes, which ensures reliable preservation of the polarization of the electron beam in the entire energy range. When working at a low energy, we can use fewer snakes. Analytical estimates of the azimuth-averaged squared modulus of the spin-orbit coupling vector for the ring with  $n_{\text{snk}}$  Siberian snakes give the following result:

$$\langle \mathbf{d} \rangle = \mathbf{d}^2(0) + \frac{\pi^2}{3} \frac{\nu^2}{n_{\text{snk}}^2}$$

$$\mathbf{d}^2(0) = \frac{\pi^2}{4} \sin^2 \frac{\pi\nu}{n_{\text{nsk}}}.$$

Here  $\mathbf{d}$  is the spin-orbit coupling vector,  $\mathbf{d}^2(0)$  is the square of its modulus at the minimum point,  $\langle \mathbf{d} \rangle$  is its mean value over the entire length of the arc, and  $\nu = E(\text{MeV})/440.652$  is the spin tune. Figure 1.31 depicts the  $d(\theta) = |\gamma(\partial\mathbf{n}/\partial\gamma)|$  dependence graph calculated by the program `ASPIRRIN` [23, 24] for this number of Siberian snakes ( $n_{\text{snk}} = 5$ ) at an energy  $E = 2.5 \text{ GeV}$ . Knowing the behavior of  $\mathbf{d}$  in the ring, it is easy to calculate the time of radiative spin relaxation and the equilibrium degree of radiative polarization. They are determined by the well-known Derbenev and Kondratenko formulae [25]:

$$\xi_{\text{rad}} = -\frac{8}{5\sqrt{3}} \frac{\langle |r|^{-3} \mathbf{b}(\mathbf{n} - \mathbf{b}) \rangle}{\langle |r|^{-3} \left( 1 - \frac{2}{9}(\mathbf{n}\mathbf{v})^2 + \frac{11}{18}\mathbf{d}^2 \right) \rangle}$$

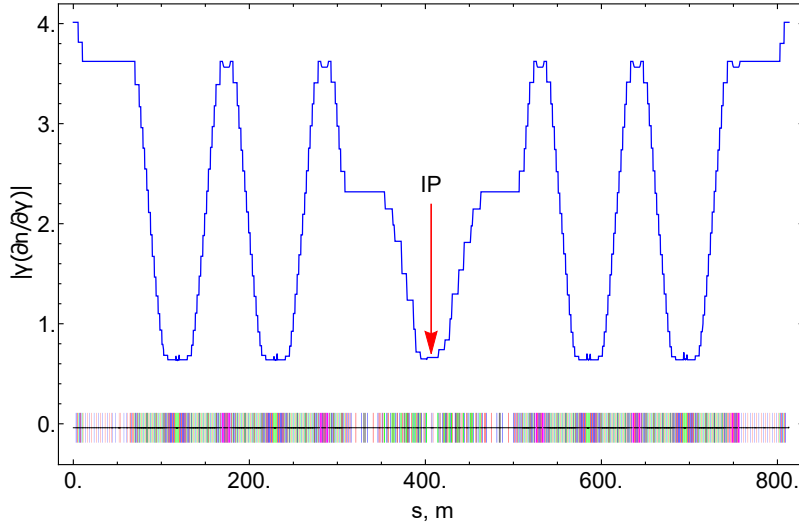
$$\tau_{\text{rad}}^{-1} = \frac{5\sqrt{3}}{8} \lambda_e r_e c \gamma^5 \left\langle |r|^{-3} \left( 1 - \frac{2}{9}(\mathbf{n}\mathbf{v})^2 + \frac{11}{18}\mathbf{d}^2 \right) \right\rangle.$$

Here  $r$  is the radius of curvature of the orbit in the dipole magnets,  $\mathbf{b}$  is a unit vector directed along the field in these magnets,  $\mathbf{n}$  is a unit vector indicating the equilibrium direction of spin,  $\mathbf{v}$  is a unit vector directed along the velocity, and the rest notations have a usual meaning.

At the Super Charm–Tau factory it is planned to use the wigglers to adjust the radiation damping decrements, namely, to maintain the damping time at a level of about 30 ms in the entire energy range of the operation. At a low energy, the wigglers are switched on to the maximum field, and in the case of operation at the maximum energy near 2.5 GeV, the wigglers are almost completely turned off. When calculating the depolarization time in the storage ring, it is necessary to take into account the influence of the wigglers on this process. As can be seen from Fig. 1.31, their contribution depends heavily on their place. If they are in the sections of the ring where the modulus of the spin-orbit coupling vector is minimal (in the middle of the arcs separating the snakes), their influence is insignificant. If they are evenly distributed over the ring, their influence becomes quite tangible. So, naturally, we placed all the four damping wigglers at the places where the modulus of the spin-orbit coupling vector is minimal. The basic parameters of the wigglers are given in the general list of parameters of the collider.

## 1.6.3 Time-averaged degree of polarization

The equilibrium degree of radiative polarization of the beams almost turns to zero in the presence of the Siberian snakes, see Fig. 1.32. And this is good, since a non-zero degree of beam polarization can lead to systematic errors in analysis of the spin asymmetry of the processes of interest to us. It



Crossing of beams is in azimuth  $s = 406.55$  m

Figure 1.31. Dependence of modulus of spin-orbit coupling vector on azimuth for 2.5 GeV with five Siberian snakes.

is proposed to inject in some random way bunches of polarized electrons into different separatrices (there are about 400 separatrices) and to mark all the events recorded with the number of the separatrix they correspond to.

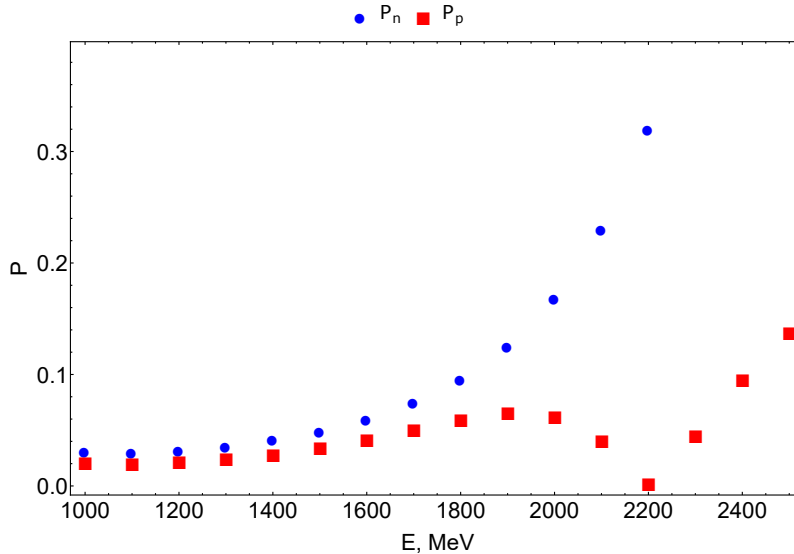
The loss of particles, mainly from the bremsstrahlung on the counter beam, must, of course, be replenished with fresh polarized electrons. As a result, some equilibrium degree of polarization gradually sets, determined by the balance of the number of particles that have lived in the ring for different times. It is easy to show that the equilibrium degree of polarization is

$$\xi = \xi_{\text{beam}} \frac{\tau_{\text{rad}}}{\tau_{\text{beam}} + \tau_{\text{rad}}} + \xi_{\text{rad}} \frac{\tau_{\text{beam}}}{\tau_{\text{beam}} + \tau_{\text{rad}}}.$$

Here  $\xi_{\text{beam}} = 90\%$  is the degree of polarization of fresh beam,  $\xi_{\text{rad}} = 0\%$  is the degree of radiative self-polarization of electrons in the ring,  $\tau_{\text{beam}} = 1000$  s is the lifetime of particles in the ring, and  $\tau_{\text{rad}}$  is the time of radiative spin relaxation.

Figure 1.33 presents graphs of the dependence of the time-averaged longitudinal polarization of the electron beam for the option of the Super Charm–Tau factory with five snakes in the top-up mode with a degree of polarization of 90%. The beam lifetime in these calculations is set equal to 750 s. It can be seen from the graphs that the basic option with five Siberian snakes provides a level of polarization of the order of 80% practically in the entire energy range of the accelerator, except for only 2.5 GeV, where it decreases to a level of  $-66\%/ +72\%$ . The equilibrium degree of polarization can be increased due to reduction in the time of replacement of a partially depolarized beam with a new one with a 90% polarization. So, transition to a cycle with an effective lifetime of 300 s increases the degree of polarization at an energy of 2.5 GeV to  $-79\%/ +82\%$ . The regime of faster replacement of a partially depolarized old beam with a fresh one is easily accomplished through partially knocking out the stored beam during the injection of each new portion. We must, of course, bear in mind that decreasing the effective beam lifetime to 300 s will require increasing the rate of production of polarized electrons to at least  $10^{11}$  particle/s.

The technical aspects of the implementation of spin rotators are presented in p. 1.3.4, and of superconducting solenoids in p. 1.13.3.



Dependence of equilibrium degree of radiative polarization with five Siberian snakes (red squares) and with solenoids turned off (blue circles). In the first case, the polarization vector is everywhere perpendicular to field in dipole magnets, while in the second case it is always vertical.

Figure 1.32. Dependence of equilibrium radiative polarization degree on electron energy.

## 1.7 Collective Effects

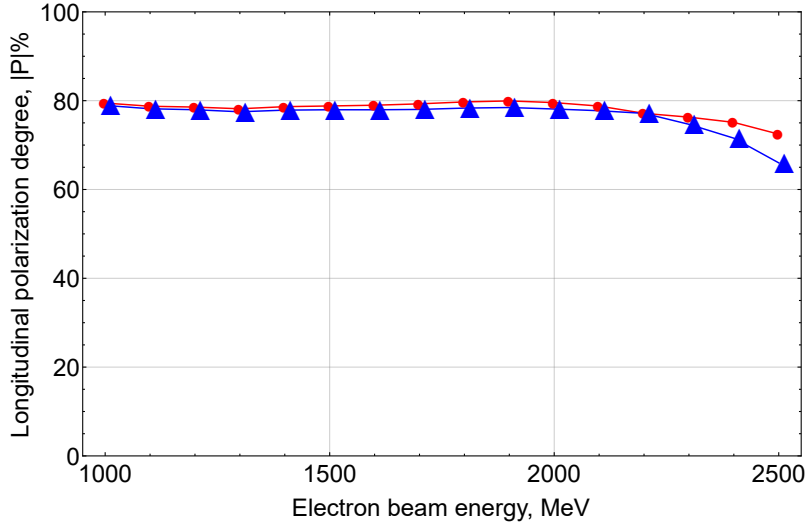
### 1.7.1 Collective Effects

The interaction of an intense beam of charged particles with the electromagnetic fields induced by it in the vacuum chamber (wake fields) leads to various collective effects in the beam dynamics. These effects depend on the beam intensity and become noticeable when the number of particles in the beam is large. The most significant consequence of collective effects is the motion instability. When the resonance conditions are satisfied, small deviations in the position or energy of the beam can increase because of the beam interaction with the wake fields. Such a positive feedback leads to instability of the oscillations and, as a consequence, to loss of the beam or its degradation.

In the frequency domain, the interaction of the beam with the components of the vacuum chamber via the wake fields is described by frequency-dependent coupling impedances. The presence of narrow-band impedance sections in the accelerator (for example, parasitic higher modes of accelerating cavities) can lead to appearance of multi-bunch instability, and broadband impedance can cause intrabunch instability of the beam. Fundamentals of the theory of collective effects, instabilities, and coupling impedances are presented in [26, 27, 28].

To analyse single-bunch stability of the beam, the vacuum chamber of the accelerator as a whole is usually represented in the form of a broadband impedance, resulting from summing of the broadband impedances of all the components of the chamber. The broadband impedance is generally assumed to be additive because the wake fields rapidly decay, and the interference of the wake fields excited by the beam in different components of the vacuum chamber can be practically neglected. The value of the total broadband impedance is used to estimate the stability of the intrabunch motion of the beam. It is also a measure of the quality of the design and fabrication of the vacuum chamber.

To assess the permissible coupling impedances of the projected collider, it would be useful to consider the experience of previous B-factories: KEKB and PEP-II. It makes sense to compare



The red and blue colors correspond to opposite signs of projection of the polarization vector on the longitudinal axis. The beam lifetime is set equal to 750 s.

Figure 1.33. Degree of longitudinal polarization of electrons with 5 snakes switched on in top-up mode (90%).

the parameters of storage rings, the beam energy in which is close to a value of 2.5 GeV, chosen for the projected Super Charm–Tau factory. These are the installations KEKB LER with an energy of 3.5 GeV and PEP-II LER with an energy of 3.1 GeV. The energy of the KEKB HER and PEP-II HER storage rings, 8 GeV and 9 GeV, respectively, significantly exceeds the design energy of the Super Charm–Tau factory.

The main parameters of the KEKB LER and PEP-II LER accelerators and the Super Charm–Tau factory that are of interest for the analysis of collective effects, as well as the results of estimates of the instabilities, are given in Tables 1.7 and 1.8.

## 1.7.2 Beam lengthening

The electromagnetic fields induced by the beam change the shape of the acceleration RF field acting on the beam. This effect results in distortion of the longitudinal propagation of particles and bunch lengthening, while the energy spread does not change. The bunch lengthening caused by the potential well distortion is approximately described by Eq. [29],

$$\left(\frac{\sigma_t}{\sigma_{t0}}\right)^3 - \frac{\sigma_t}{\sigma_{t0}} = \frac{I_b \alpha}{\sqrt{2\pi} \nu_z^2 (\omega_0 \sigma_{t0})^3 E/e} \operatorname{Im} \left( \frac{Z_{\parallel}}{n} \right)_{\text{eff}}, \quad (1.26)$$

where  $I_b$  is the beam current,  $\sigma_{t0} = \sigma_{z0}/c$ , and  $\sigma_{z0}$  is the bunch length at zero current,  $\alpha$  is the momentum compaction factor, and  $\nu_z$  is the synchrotron tune (in the units of the revolution frequency  $\omega_0$ ). The effective impedance  $(Z_{\parallel}/n)_{\text{eff}}$ , used for estimates of beam stability, is a weighted normalized impedance averaged over the spectrum of the beam frequencies [30]:

$$\left( \frac{Z_{\parallel}}{n} \right)_{\text{eff}} = \frac{\sum_{p=-\infty}^{\infty} Z_{\parallel}(\omega_p) \frac{\omega_0}{\omega_p} h_m(\omega_p)}{\sum_{p=-\infty}^{\infty} h_m(\omega_p)}, \quad (1.27)$$

Table 1.7. KEKB, PEP-II, and Super Charm–Tau factory parameters.

	KEKB LER	KEKB HER	PEP-II LER	PEP-II HER	Super $c\tau$
Energy, GeV	3.5	8.0	3.1	9.0	2.0
Perimeter, m	3016.26	3016.26	2199.3	2199.3	813.1
Bunch length, mm	4	4	11	11	10
Energy spread	$7.1 \cdot 10^{-4}$	$6.7 \cdot 10^{-4}$	$8.1 \cdot 10^{-4}$	$6.1 \cdot 10^{-4}$	$9.3 \cdot 10^{-4}$
Distance between bunches, m	0.59	0.59	1.26	1.26	1.8
Horizontal emittance, nm	18	18	50		8
Vertical emittance, nm	0.36	0.36	2		0.04
Synchrotron tune	$0.01 \div 0.02$	$0.01 \div 0.02$	0.03	0.05	0.01
Betatron tune (hor.)	45.52	47.52	36.57	24.57	43.54
Betatron tune (ver.)	45.08	43.08	34.64	23.64	40.57
Average beta function (hor.), m	10	10	10.84	14.5	6.3
Average beta function (ver.), m	10	10	9.95	13.84	9.5
Orbit coupling	$1 \div 2 \cdot 10^{-4}$	$1 \div 2 \cdot 10^{-4}$	$1.31 \cdot 10^{-3}$	$2.41 \cdot 10^{-3}$	$8.82 \cdot 10^{-4}$
Radius of bend in magnets, m	16.3	104.5			8.25
Bending magnet length, m	0.915	5.86			0.454
RF voltage, MV	$5 \div 10$	$10 \div 20$	5.12	18.5	1.24
RF frequency, MHz	508.887	508.887	476	476	500
Harmonic number	5120	5120	3492	3492	1356
Revolution frequency, kHz	99.4	99.4	136.3	136.3	368.7
Rad. damping time (longit.), ms	43/23	23	40	37	15
SR energy loss/ revolution, MeV	0.81/1.5	3.5	0.87	3.57	0.361
Total radiation power, MW	2.1/4.0	3.8			0.586
Number of particles in bunch	$3.3 \cdot 10^{10}$	$1.4 \cdot 10^{10}$	$6 \cdot 10^{10}$	$2.7 \cdot 10^{10}$	$7.1 \cdot 10^{10}$
Bunch current, mA	0.52	0.22	1.3	0.59	4.19
Bunch peak current, A	158	67	104.5	47	136
Total beam current, A	2.6	1.1	2.1	1.0	1.7
Vacuum chamber	Cu * $\varnothing$ 94 mm NEG inserts	Cu racetrack** $104 \times$ $50\text{mm}^2$ $\varnothing$ 50 mm NEG stripes	sections: stainless steel $\varnothing$ 94 mm arcs: Al ellipt. $95 \times 59\text{mm}^2$ antichamber	1300 m: copper, 900 m: stainless steel	Copper- plated aluminum $100 \times$ $50\text{mm}^2$

\* Low photodesorption coefficient, high thermal conductivity, possibility of X-ray shielding.

\*\* For minimization of gap in dipole magnets.

Table 1.8. Estimates of instabilities of KEKB, PEP-II and Super Charm–Tau factory.

	KEKB LER	KEKB HER	PEP-II LER	PEP-II HER	Super $c\tau$
Microwave instability	$I_{th} = 0.1 \text{ mA} @$ $Z/n =$ 72 mOhm $I_{th} = 0.5 \text{ mA}^*$ $I_b = 0.52 \text{ mA}$	$I_{th} = 0.2 \text{ mA} @$ $Z/n =$ 76 mOhm $I_b = 0.22 \text{ mA}$	$I_{th} = 3.0 \text{ mA} @$ $Z/n =$ 80 mOhm $I_b = 1.3 \text{ mA}$	$I_{th} = 9.0 \text{ mA}$ $@ Z/n =$ 80 mOhm $I_b = 0.6 \text{ mA}$	$I_{th} = 2.2 \text{ mA} @$ $Z/n =$ 100 mOhm $I_b = 4.2 \text{ mA}$
Bunch lengthening	25%	7%	20%	6%	50%
TMC instability	$I_{th} = 1.4 \text{ mA}^*$	$I_{th} = 2.4 \text{ v}^*$	$I_{th} = 1.9 \text{ mA}$	$I_{th} = 2.7 \text{ mA}^*$	$I_{th} = 6 \text{ mA} @$ $Z_y = 100 \text{ kOhm/m},$ 1 GeV
Longitudinal multi-bunch instability – higher modes of cavities	60 ms	150 ms	1 ms	2 ms	
Transverse multi-bunch instability—higher modes of cavities	30 ms	80 ms	0.5 ms	1 ms	
Transverse multi-bunch instability—wall resistance (resistive-wall CBI)	5 ms (feedbacks suppress.)		hor: 1.4 ms, ver: 0.9 ms; feedbacks damping time 0.31 ms	hor: 5.6 ms, ver: 3.8 ms	hor: 4 ms, ver: 1.5 ms @ 1 GeV, 1 A
Multi-bunch instability—ions		1 ms (calculation)	solenoids with field of 30 G		>10 ms
Multi-bunch instability—electronic clouds	>0.4 ms solenoids + feedbacks				0.16 ms at $\xi = 1$

\* According to measurements.

where  $Z_{\parallel}(\omega)$  is the frequency-dependent longitudinal impedance,  $n = \omega/\omega_0$  is the number of the harmonic of the revolution frequency,  $E$  is the beam energy, and  $\omega_p = p\omega_0 + m\omega_s$  is the set of frequencies of a single bunch. For a Gaussian beam, the normalized spectral power density  $h_m(\omega) = C_m \tilde{\lambda}_m(\omega) \tilde{\lambda}_m^*(\omega)$  of the  $m$ th oscillation mode is described by the equation

$$h_m(\omega) = (\omega\sigma_t)^{2m} e^{-\omega^2\sigma_t^2}, \quad (1.28)$$

where  $\sigma_t = \sigma_z/c$ ,  $\sigma_z$  is the length of the bunch. The  $m = 0$  mode corresponds to bunch lengthening because of potential well distortion.

If the beam current exceeds a certain threshold value, then the interaction of the beam with the longitudinal impedance leads to microwave instability of the longitudinal motion. Above the instability threshold, both the bunch length and the energy spread of the beam grow with increasing current. The value of the amplitude of the bunch threshold current  $I_p$  for a relativistic beam can be estimated from the following formula [31, 32]:

$$I_p^{\text{mwi}} = \frac{\alpha E/e}{|Z_{\parallel}/n|_{\text{eff}}} \left( \frac{\Delta p}{p} \right)_{\text{FWHM}}^2, \quad (1.29)$$

where  $\Delta p/p = \gamma^2/(\gamma^2 - 1)\Delta E/E$  is the spread of the longitudinal beam momentum, equivalent to the energy spread  $\Delta E/E$  for ultrarelativistic ( $\gamma \gg 1$ ) particles. For a bunch with a Gaussian density distribution and mean-square length  $\sigma_z$ , the amplitude current value  $I_p$  is tied with the average current  $I_b$  by the following relation:

$$I_p = I_b \frac{\sqrt{2\pi}R}{\sigma_z}, \quad (1.30)$$

where  $R$  is the average radius of the accelerator. The average threshold current of microwave instability for a Gaussian beam is given by the following expression [32]:

$$I_b^{\text{mwi}} = \frac{\sigma_{s0} \sqrt{2\pi} \alpha E/e}{R |Z_{\parallel}/n|_{\text{eff}}} \left( \frac{\sigma_E}{E} \right)^2. \quad (1.31)$$

Figure 1.34 shows graphs of the threshold current of microwave instability vs. the normalized longitudinal impedance for four beam energies: 1, 1.5, 2, and 2.5 GeV. It can be seen that a design bunch current of 4.4 mA will not exceed the instability threshold at a normalized impedance of not more than 70 mOhm.

It should be noted that formulae (1.29 and 1.31) were derived for long proton beams and for short bunches in modern electron storage rings, such as the third generation SR sources. These formulae give highly overestimated values of the threshold instability current. For more accurate estimates, numerical simulation using a realistic impedance model is required.

The microwave instability is usually restricted by the nonlinearity and does not lead to beam losses. However, it causes turbulent lengthening of bunch and increase in the energy spread with growing beam intensity. Above the threshold of microwave instability, the bunch lengthening as a function of the current for a relativistic electron or positron beam with a Gaussian distribution of the linear density is approximately described by the following cubic equation [33, 34]:

$$\sigma_t^3 = \frac{I_b \alpha}{\sqrt{2\pi} \nu_z^2 (\omega_0 \sigma_{t0})^3 E/e} \left| \frac{Z_{\parallel}}{n} \right|_{\text{eff}}. \quad (1.32)$$

It should be noted that the results of measurements of the bunch length as a function of current do not show a noticeable change in the function describing the bunch lengthening above the

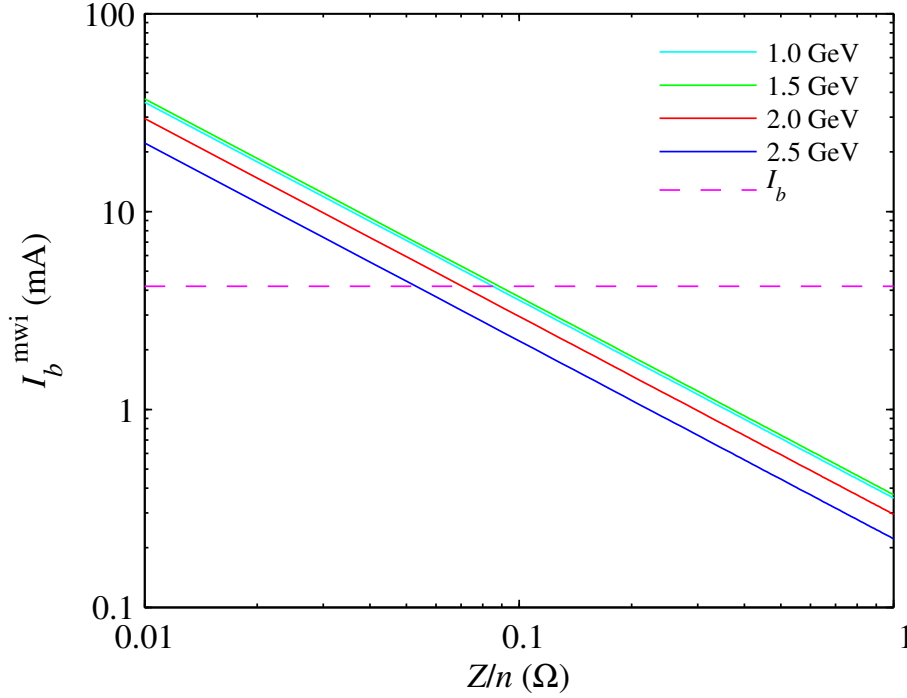


Figure 1.34. Threshold current of microwave instability.

microwave instability threshold, although the threshold is clearly visible in the measurements of the energy spread [34, 35, 36].

Figure 1.35 shows the bunch length as a function of the beam current for three values of the normalized longitudinal impedance (0.05, 0.1, and 0.2 Ohm) at 2 GeV and at fixed accelerating voltage  $V_{RF}=0.99$  MV. For comparison, the measured bunch lengthening at KEKB LER [38] at a working bunch current of 0.5 mA is about 25% ( $Z/n \simeq 0.07$  Ohm) and at PEP-II LER [39] about 20% at a bunch current of 1.3 mA ( $Z/n \simeq 0.08$  Ohm).

If it is necessary to maintain the longitudinal beam size at any current, then to compensate for the lengthening it is necessary to increase the accelerating RF voltage, see Fig. 1.36. It can be seen that a significant excess of the microwave instability threshold is undesirable since it leads to a significant increase in the RF voltage required to compensate for the bunch lengthening.

### 1.7.3 Coherent energy losses

The interaction of the beam with the longitudinal impedance leads to coherent energy losses, which depend quadratically on the beam charge  $q$  [27]:

$$\Delta E = k_{\parallel} q^2. \quad (1.33)$$

The coefficient of proportionality  $k_{\parallel}$  is called the coherent loss factor (longitudinal loss factor). It depends both on the properties of the vacuum chamber, characterized by the impedance  $Z_{\parallel}$ , and on the longitudinal density distribution of the beam:

$$k_{\parallel} = \frac{\omega_0}{2\pi} \sum_{p=-\infty}^{\infty} Z_{\parallel}(\omega_p) h_0(\omega_p), \quad (1.34)$$

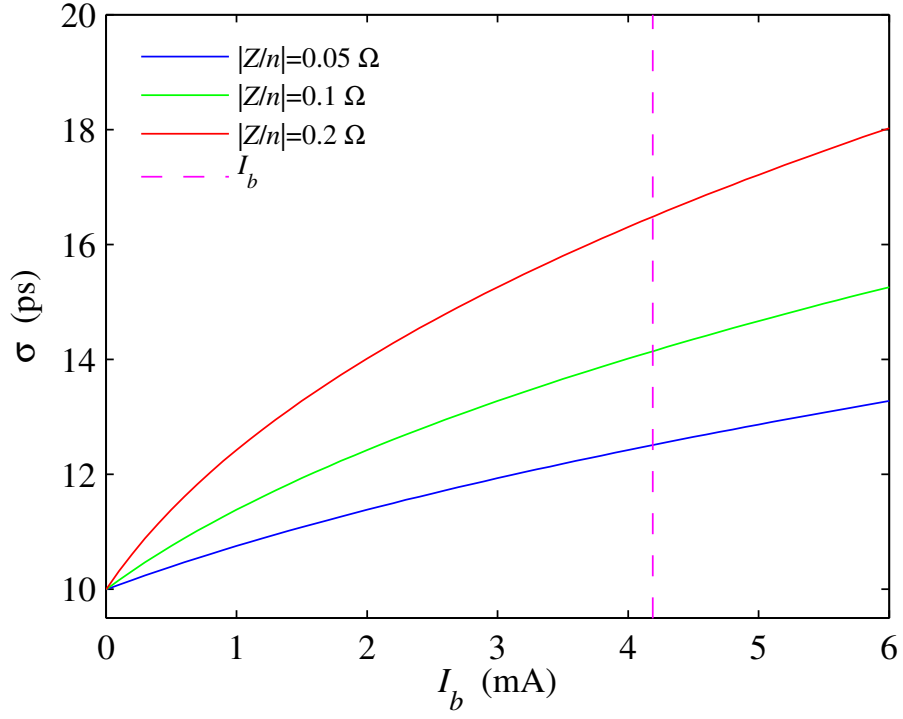


Figure 1.35. Bunch lengthening vs. current ( $E = 2 \text{ GeV}$ ).

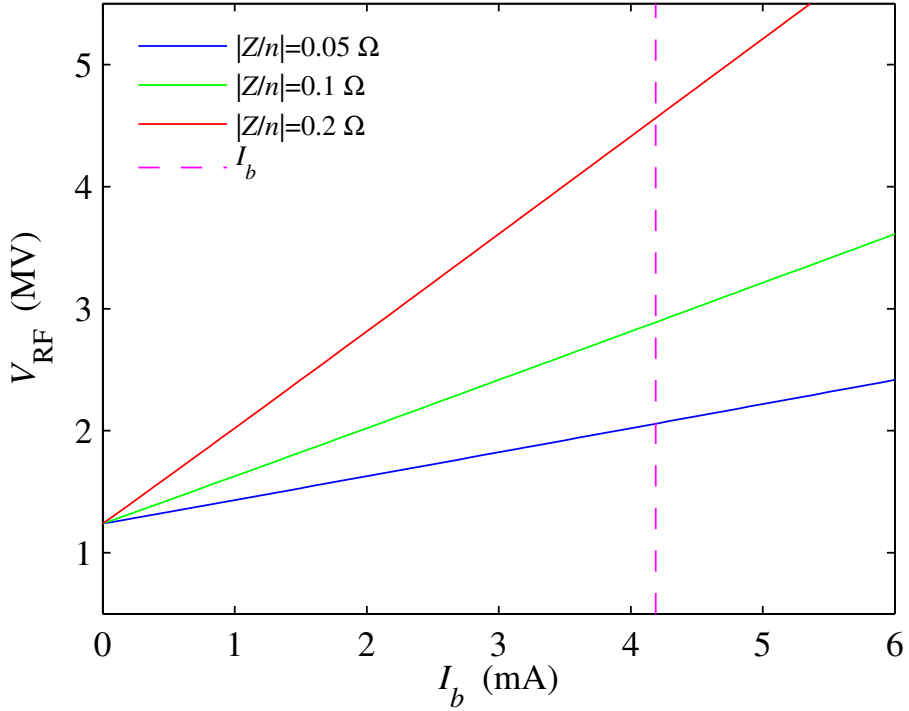


Figure 1.36. Compensation for bunch lengthening ( $E = 2 \text{ GeV}$ ,  $\sigma_{z0} = 10 \text{ mm}$ ).

where  $h_0(\omega_p)$  is the normalized density of the spectral power of the 0th mode of oscillations of Gaussian beam (1.28). If  $\sigma_t \omega_0 \ll 1$ , then the sum can be replaced with the integral:

$$k_{\parallel} = \frac{1}{2\pi} \int_{-\infty}^{\infty} Z_{\parallel}(\omega) h_0(\omega) d\omega. \quad (1.35)$$

Like losses to synchrotron radiation, the coherent energy losses are compensated for in the accelerating cavities at each beam revolution.

### 1.7.4 TMC instability (fast head-tail)

The resonant interaction between the beam and short-lived transverse wake fields, characterized by the transverse broadband impedance, is the cause of the instability of the transverse coupled modes (transverse mode coupling, TMC, or fast head-tail). The wake fields induced by the head of the bunched beam act on the particles of its tail part (the head-tail effect). Because of synchrotron oscillations, the head and tail of the beam periodically change places; when the resonance conditions are met, unlimited increase in the amplitude of the betatron oscillations takes place, which leads to losses of beam particles down to the threshold intensity.

For a vacuum chamber of a circular cross-section, the relationship between the longitudinal  $Z_{\parallel}(\omega)$  and transverse dipole  $Z_{\perp}(\omega)$  impedances is described by the following formula (a consequence of the Panofsky-Wenzel theorem) [37, 27]):

$$Z_{\perp}(\omega) \approx \frac{2c}{b^2\omega} Z_{\parallel}(\omega), \quad (1.36)$$

where  $b$  is the chamber radius. In the case of inductive impedance,

$$Z_{\perp}(\omega) \approx \frac{2R}{b^2} \frac{Z_{\parallel}}{n}, \quad (1.37)$$

where  $R$  is the average radius of the accelerator. This formula can also be used for rough estimates in the case of a chamber of varying cross section,  $b$  assumed to be equal to the average half-height of the chamber.

The interaction of the beam with the dipole transverse impedance results in the coupling of the head-tail modes of the transverse oscillations of the bunch. The rise/damping time increases rapidly with the mode number  $m$ , and thus modes with large  $m$  usually are not dangerous for the stability of the beam since they are suppressed by the radiation damping. Since only a few lower modes are essential for analysis of the transverse bunch stability, the problem can be reduced to solving the eigenvalue problem [26]. The coupling of the oscillation modes of the bunch leads to a coherent shift of the betatron tune, which is linearly dependent on the beam current at low currents [26]:

$$\Delta\nu_{\beta} = -\frac{I_b}{4\sqrt{\pi}\sigma_t\omega_0 E/e} \sum_j \beta_j \text{Im} Z_{\perp j}^{\text{eff}}, \quad (1.38)$$

where  $Z_{\perp j}^{\text{eff}}$  is the effective transverse impedance, summation performed over all local impedances, and  $\beta_j$  is the beta function at the place of localization of the  $j$ th impedance. Figure 1.37 shows graphs of coherent shift of the betatron tune vs. the beam current for three transverse impedance values (19.5, 39, and 78 Ohm/m), calculated using formula (1.37), applied to the respective values of the normalized longitudinal impedance (0.05, 0.1, and 0.2 Ohm). The energy is 2 GeV; the accelerating voltage is 0.99 MV. The solid lines show the calculation results with allowance for the bunch lengthening, and the dashed lines show the calculation results without the lengthening.

As can be seen in Fig. 1.37, the dependence (1.38) of the betatron tune on the beam current remains linear only if the lengthening of the bunch is neglected. For more accurate estimates of the tune shift and the instability threshold, the beam length in (1.38) must take the lengthening into account. For comparison, the measured coherent shift of the vertical betatron tune in the case of KEKB LER is about  $3.5 \text{ A}^{-1}$  [40], and in the case of PEP-II LER—about  $12 \text{ A}^{-1}$  [41].

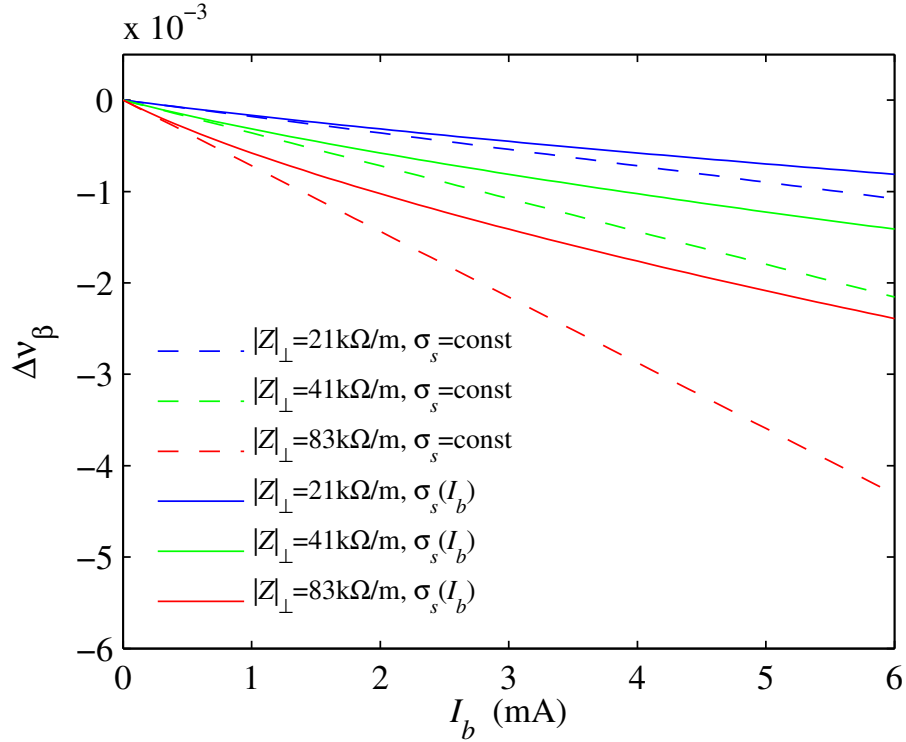


Figure 1.37. Coherent shift of vertical betatron tune vs. current ( $E = 2$  GeV).

At zero beam current, the tune of the  $-1$ th mode of bunch oscillations is less than the tune of the  $0$ th mode by the synchrotron tune value. With increasing current, the tunes of these modes shift towards each other and the instability of the transverse coupled modes arises when the tune of the  $0$ th oscillation mode coincides with the tune of the  $-1$ th mode. Defining the instability threshold current as the current at which the tune of the  $0$ th mode shifts by half the synchrotron tune, we can write the formula for the threshold current:

$$I_b^{\text{tmci}} = \frac{4\sqrt{\pi} \sigma_t \nu_z \omega_0 E/e}{\sum_j \beta_j \text{Im} Z_{\perp j}^{\text{eff}}}. \quad (1.39)$$

Figure 1.38 presents graphs of the TMC instability threshold current with allowance for the bunch lengthening vs. the transverse impedance for four beam energy values: 1, 1.5, 2, and 2.5 GeV. It can be seen that a design bunch current of 4.4 mA will not exceed the instability threshold at a transverse impedance value of not more than 150 kOhm/m at a minimum energy of 1 GeV.

### 1.7.5 Longitudinal multi-bunch instability

The interaction of the beam with the higher modes of the accelerating cavities (narrowband impedance) leads to the excitation of long-lived wake fields, which, acting on subsequent bunches, can cause longitudinal instability in the multi-bunch regime [42]. A beam consisting of  $N_b$  bunches evenly distributed over the perimeter of the accelerator can be considered as a system of coupled oscillators with  $N_b$  degrees of freedom and thus  $N_b$  oscillation modes with the phase shift  $\Delta\varphi = 2\pi n/N_b$ ,  $n = 0, 1, \dots, N_b - 1$ . The interaction of such a beam with the higher mode of cavity leads to resonance excitation of the  $n$ th oscillation mode when the higher mode frequency  $\omega_r$  coincides

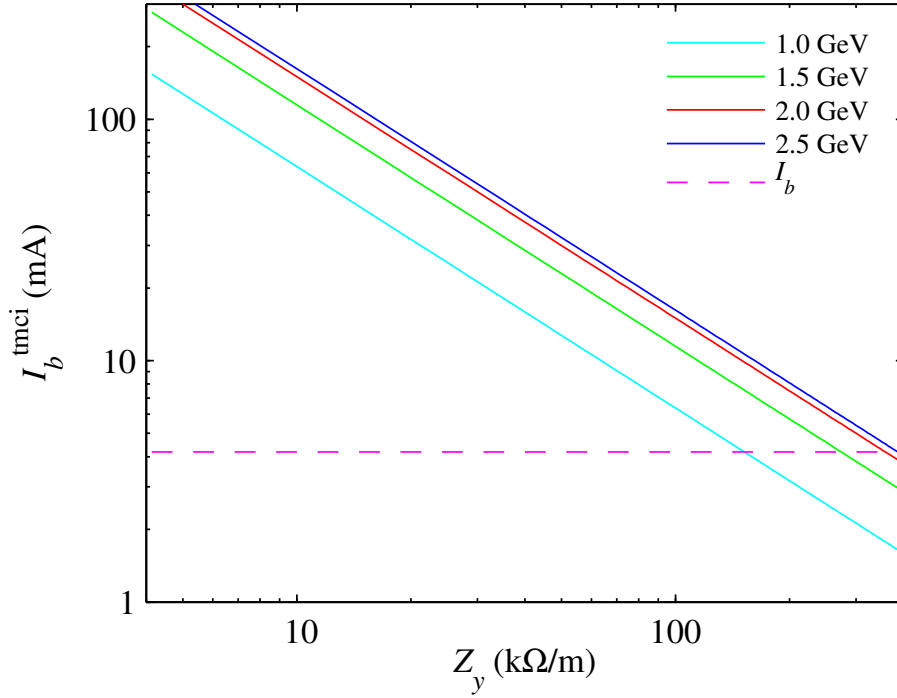


Figure 1.38. TMC instability threshold current.

with any of the frequencies  $\omega_{np}$  of the beam spectrum:

$$\omega_{np} = (pN_b + n + m\nu_z)\omega_0, \quad (1.40)$$

where  $p$  is an integer,  $\nu_z$  is the synchrotron tune in units of the frequency of revolution  $\omega_0$ , and  $m$  is the coherent mode of oscillations (dipole:  $m = 1$ , quadrupole:  $m = 2$  and so on).

If the  $n$ th oscillation mode is excited by any of the higher modes of the accelerating cavity, whose impedance has the following form:

$$Z_{\parallel\text{HOM}}(\omega) = \frac{R_s}{1 + iQ_{\text{HOM}}\left(\frac{\omega}{\omega_r} - \frac{\omega_r}{\omega}\right)}, \quad (1.41)$$

where  $\omega_r$  is the resonance frequency,  $R_s$  is the shunt impedance, and  $Q_{\text{HOM}}$  is the Q factor, then the rise time can be estimated using the following formula [43, 44]:

$$\frac{1}{\tau_{\parallel n}} = \frac{\alpha N_b I_b}{4\pi \nu_z E/e} \omega_{np} \text{Re} Z_{\parallel\text{HOM}}(\omega_{np}). \quad (1.42)$$

If the frequency of the  $n$ th oscillation mode  $\omega_{np}$  is close to the resonance frequency of the higher mode  $\omega_r$ , then the impedance  $\text{Re} Z_{\parallel\text{HOM}}$  can be expressed in terms of the characteristic impedance  $\rho = R_s/Q_{\text{HOM}}$ , and the Q factor  $Q_{\text{HOM}}$  of the higher mode by the following approximate formula:

$$\text{Re} Z_{\parallel\text{HOM}}(\Delta\omega) \approx \frac{\rho Q_{\text{HOM}}}{1 + 4Q_{\text{HOM}}^2 \left(\frac{\Delta\omega}{\omega_r}\right)^2}, \quad (1.43)$$

where  $\Delta\omega = \omega_{np} - \omega_r$  is the frequency detuning ( $\Delta\omega \ll \omega_r$ ).

In electron-positron storage rings the main mechanism for suppressing longitudinal oscillations is radiation damping. For a stable motion, the characteristic time  $\tau_z$  of the radiation damping must be less than the rise time  $\tau_{\parallel n}$  (1.42) of any mode in the operating range of the beam current. Since the impedance of each of the higher modes is characterized by its resonance frequency, shunt impedance, and the  $Q$  factor, the instability rise time must be estimated for each mode. Taking into account the radiative damping, it is possible to estimate the minimum shift of the frequency of the higher mode from the resonance that is required for stabilization of the  $n$ th oscillation mode [44]:

$$|\Delta\omega| \geq \frac{\omega_r}{2Q_{\text{HOM}}} \sqrt{N_b I_b \frac{\alpha \tau_z}{4\pi \nu_z E/e} \omega_{np} \rho Q_{\text{HOM}} - 1}. \quad (1.44)$$

The detuning of higher modes from the resonance with the frequencies  $\omega_{np} = (pN_b + n + \nu_z)\omega_0$  can be carried out by adjusting the temperature of the cavity, which changes its geometric dimensions, which results in a shift of the resonance frequencies of the higher modes. In principle, certain temperature ranges corresponding to detuning of higher-mode frequencies from resonances can be found. The use of modern systems of auto-regulation makes it possible to stabilize the cavity temperature within  $0.05^\circ\text{C}$  and thereby maintain beam stability during the experiment.

### 1.7.6 Transverse multi-bunch instability

The interaction of beam with higher modes of accelerating cavities, the resistive impedance of the walls of the vacuum chamber, as well as with residual gas ions and electron clouds (in positron storage devices), can lead to excitation of transverse multi-bunch instabilities. When a bunch flies through a narrow-band impedance structure, it excites long-lived wake fields, which affect the subsequent bunches. When resonance conditions are fulfilled, all the bunches start coherent oscillations with a certain phase shift between the bunches.

The interaction of a beam consisting of  $N_b$  bunches uniformly distributed over the perimeter of the accelerator, with any of the higher modes of the cavity the frequency of which  $\omega_r$  coincides with one of the frequencies

$$\omega_{np} = (pN_b + n + m\nu_\beta)\omega_0, \quad (1.45)$$

leads to excitation of the  $n$ th mode of oscillations. Here  $p$  is an integer, and  $\nu_\beta$  is the fractional part of the betatron tune in units of the revolution frequency  $\omega_0$ .

The transverse impedance of the higher mode of the accelerating cavity can be written in the following form:

$$Z_{\perp\text{HOM}}(\omega) = \frac{\omega_r}{\omega} \frac{R_s}{1 + iQ_{\text{HOM}} \left( \frac{\omega}{\omega_r} - \frac{\omega_r}{\omega} \right)}, \quad (1.46)$$

where  $\omega_r$  is the resonance frequency,  $R_s$  is the shunt resistance, and  $Q_{\text{HOM}}$  is the  $Q$  factor. If the  $n$ th oscillation mode is excited by a higher mode of the cavity with a frequency close to  $\omega_{np}$ , then the rise time can be estimated using a formula similar to (1.42) [45, 44]:

$$\frac{1}{\tau_{\perp n}} = \frac{\omega_0 \beta_c N_b I_b}{4\pi E/e} \text{Re } Z_{\perp\text{HOM}}(\omega_{np}). \quad (1.47)$$

The instability will not be excited if the rise time  $\tau_{\perp n}$  (1.47) of any mode in the operating range of the beam current is greater than  $\tau_{\perp}$ , the time of damping of the transverse oscillations of the beam by the radiative and other mechanisms. To stabilize the transverse motion of the beam, it

is necessary to detune the unstable  $n$ th transverse oscillation mode from the resonance by a value not less than[44]

$$|\Delta\omega| \geq \frac{\omega_r}{2Q_{\text{HOM}}} \sqrt{N_b I_b \frac{\omega_0 \beta_c \tau_{\perp}}{4\pi E/e} \rho Q_{\text{HOM}} - 1}, \quad (1.48)$$

where  $\rho = R_s/Q_{\text{HOM}}$  is the characteristic impedance.

In addition to the higher modes of the cavities, the transverse multi-bunch instability can be excited by the interaction of the beam with the resistive impedance of the vacuum chamber walls. The image current induced by the flying relativistic beam in the walls of the chamber with a finite conductivity excites electromagnetic fields, which, acting on subsequent bunches, can lead to development of instability. The frequency dependence of the impedance of the walls of a cylindrical vacuum chamber of radius  $b$  and length  $L$  is described by the following expression:

$$Z_{\perp\text{rw}}(\omega) = (1 + i) \frac{L}{2\pi} \frac{Z_0 \delta_z(\omega)}{b^3}, \quad (1.49)$$

where  $Z_0 = 120\pi \text{ Ohm}$  is the impedance of free space,  $\delta_z(\omega) = \sqrt{\frac{2}{\mu\sigma\omega}}$  is the thickness of the skin layer, and  $\sigma$  and  $\mu$  are the conductivity and magnetic permeability of the wall material, respectively. Since the value of impedance (1.49) is inversely proportional to the square root of the frequency, the interaction with the resistive impedance at the lowest frequency of the transverse spectrum of the beam (1.45)  $\omega_{\min} = \nu_{\beta}\omega_0$  or  $\omega_{\min} = (1 - \nu_{\beta})\omega_0$  is the most dangerous in terms of beam instability. The formula for estimating the rise time of this instability has the following form:

$$\frac{1}{\tau_{\perp\text{rw}}} = \frac{\beta_{\text{aver}}\omega_0}{4\pi E/e} N_b I_b \sum_{p=-\infty}^{\infty} \text{Re} Z_{\perp\text{rw}}(\omega_{np}). \quad (1.50)$$

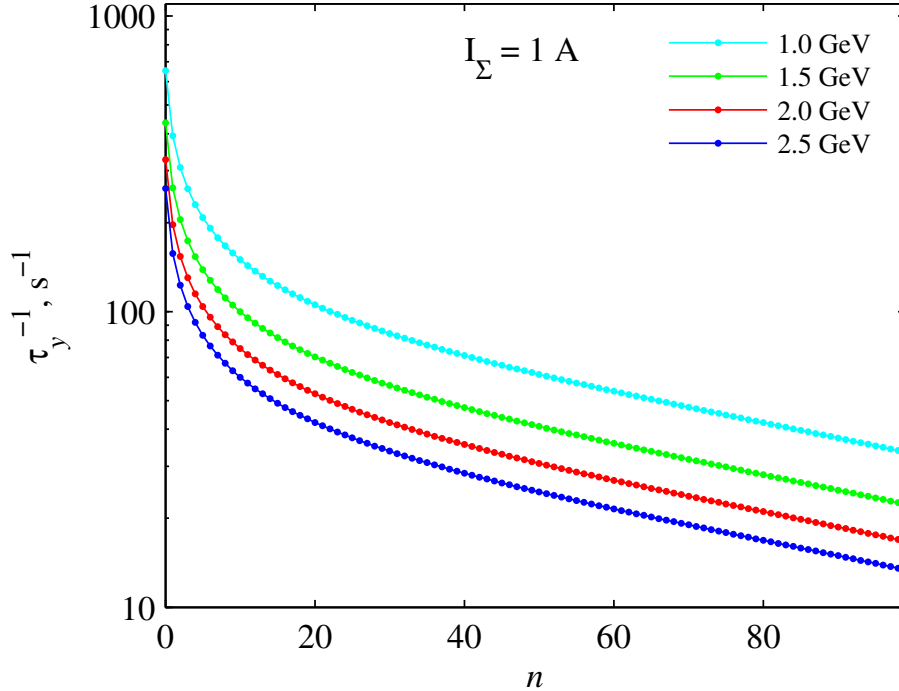


Figure 1.39. Instability increment vs. mode number  $n$ .

Figure 1.39 shows graphs of the instability increment  $1/\tau_{y_{rw}}$  of the lowest (the most dangerous) modes in dependence on the mode number  $n$  for four values of the beam energy: 1, 1.5, 2, and 2.5 GeV; the total beam current  $N_b I_b = 1$  A.

### 1.7.7 Ion instabilities

In electron storage rings with intense beams, multi-bunch instabilities can be excited at the interaction of beam particles with the residual gas ions, which can accumulate in a potential well of the electron beam. The ultimate current of electron beam limited by a multi-turn electron-ion instability can be estimated roughly through comparison of the linear densities of ions and electrons. The instability arises when the number of ions trapped in a potential well of the beam approaches the number of electrons in the beam. The linear density of ions can be estimated using the following formula:

$$\lambda_i = \frac{N_e N_b}{k_B T_{\text{gas}}} \sigma_i P_{\text{gas}} , \quad (1.51)$$

where  $T_{\text{gas}}$  and  $P_{\text{gas}}$  are the temperature and pressure of the residual gas, respectively,  $\sigma_i$  is the ionization cross section,  $k_B$  is Boltzmann's constant,  $N_b$  is the number of bunches,  $N_e = I_b T_0 / e$  is the number of electrons per bunch, and  $T_0 = 1/f_0$  is the revolution period. Neglecting the recombination processes and assuming that the instability arises at  $\lambda_i \approx \lambda_e$ , we can estimate the characteristic time of development of the instability as  $\tau \approx T_0 \lambda_e / \lambda_i$ , where  $\lambda_e$  is the linear density of electrons.

Within the framework of the linear theory of the interaction of an electron beam with ions, which is valid for oscillation amplitudes not exceeding the transverse size of the beam, the frequency of the ion oscillations in a potential well of the electron beam is described by the following expression [46]:

$$\omega_i = \sqrt{\frac{2(q_i/q_p) N_e r_p c^2}{A_i L_{\text{sep}} \sigma_y (\sigma_x + \sigma_y)}} , \quad (1.52)$$

where  $q_i/q_p$  is the charge of ion in the proton charge units,  $A_i$  the mass of ion in a.m.u.,  $r_p$  is the classical proton radius, and  $L_{\text{sep}}$  is the distance between bunches. Ions can cause only multi-bunch instabilities, since the  $c/\omega_i$  value exceeds 10 m at most installations. The nonlinearity of the interaction taken into account, the Q factor is small in most cases,  $Q_i < 10$ . In the case of  $N_b$  uniformly distributed bunches, ions accumulate in the beam if their atomic mass exceeds the critical value  $A_{\text{crit}}$ :

$$A_i \geq A_{\text{crit}} = \frac{(q_i/q_p) N_e r_p L_{\text{sep}}}{2\sigma_y (\sigma_x + \sigma_y)} . \quad (1.53)$$

For the Super Charm–Tau factory, the minimum bunch current at which the accumulation of ions is possible is 0.24 mA ( $\text{H}_2$ ), 2.2 mA ( $\text{H}_2\text{O}$ ), 3.5 mA ( $\text{CO}$ ), and 5.5 mA ( $\text{CO}_2$ ). A fairly effective means of control of multi-turn accumulation of ions is a gap in a sequence of bunches.

The intensity of the electron-ion interaction can be characterized by the magnitude of the coherent shift of the horizontal  $\nu_x$  and vertical  $\nu_y$  betatron tunes [46]:

$$\Delta\nu_x = \frac{\langle\beta_x\rangle (q_i/q_p) r_e \lambda_i P}{4\pi\gamma\sigma_x(\sigma_x + \sigma_y)} \quad \Delta\nu_y = \frac{\langle\beta_y\rangle (q_i/q_p) r_e \lambda_i P}{4\pi\gamma\sigma_y(\sigma_x + \sigma_y)} , \quad (1.54)$$

where  $\langle\beta_{x,y}\rangle$  is the average beta function,  $\gamma = E/m_e c^2$  is the Lorentz factor, and  $E$  is the beam energy. Taking into account the spread of ion frequencies  $\Delta\omega_i$ , caused by the variation of the

transverse dimensions of the beam along the perimeter of the ring, we can express the instability rise time  $\tau$  through the coherent shift (1.54):

$$\frac{1}{\tau} = \frac{\pi}{2} \frac{\Delta\nu\omega_0}{(\Delta\omega_i/\omega_i)_{\text{FWHM}}}. \quad (1.55)$$

Figure 1.40 shows graphs of the rise time of vertical multi-turn ion instability (1.55) vs. residual gas pressure  $P_{\text{gas}}$  at a nominal total beam current of 1.7 A in  $N_b = 406$  bunches.

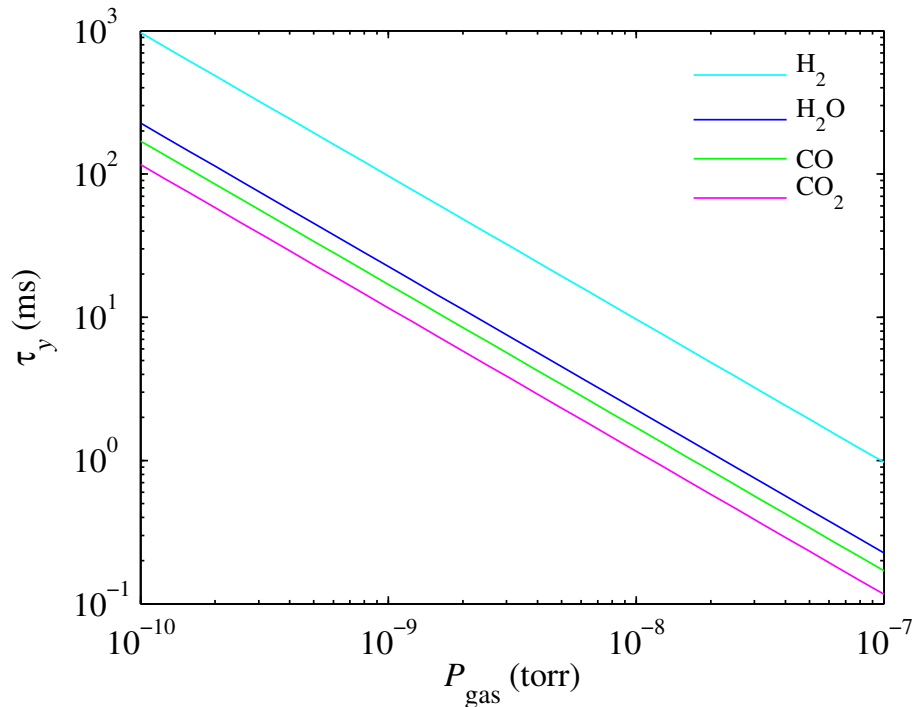


Figure 1.40. Time of rise of vertical multi-turn ion instability.

In installations with very large (several amperes) beam currents and small emittances, such as the modern B-factories or linear accelerators, the accumulation of ions in a single beam flight may be sufficient to excite fast ion-beam instability. The density of the ions of the residual gas increases along a train of electron bunches, which leads both to excitation of coherent oscillations of individual bunches and to growth of the emittance of the beam. Unlike multi-turn ion instability, this effect is one-turn and is not suppressed by a gap in a train of bunches. Evidences of fast ion instability were observed in the electron rings of the KEKB [47] and PEP-II B-factories at the beginning of their work. The possible cause of instability is inadequate vacuum. The instability was successfully suppressed by means of systems of bunch-to-bunch transverse feedback.

Within the framework of the linear theory of the interaction of an electron beam with ions, which is valid for oscillation amplitudes not exceeding the beam transverse dimension, the growth of the amplitude of the oscillations is proportional to  $\exp(\sqrt{t/\tau_c})$ , and asymptotic estimates of the time constant  $\tau_c$  can be made using the formula [48] (for singly charged ions),

$$\frac{1}{\tau_c} = \frac{4n_{\text{gas}}\sigma_i\langle\beta_y\rangle N_e^{3/2} N_b^2 r_e r_p^{1/2} L_{\text{sep}}^{1/2} c}{3\sqrt{3}\gamma\sigma_y^{3/2}(\sigma_x + \sigma_y)^{3/2} A_i^{1/2}}. \quad (1.56)$$

The linear model is based on the assumption that the ions are produced due to impact ionization of the atoms of the residual gas by the beam particles, and the captured particles have small initial velocities. The linear theory does not take into account the following effects:

- non-linearity of the electron-ion interaction: the oscillation build-up stops at amplitudes of the order of the transverse beam size, after which filamentation and a slower growth of the instability occur;
- the beta function beating, which leads to a spread in the ion frequencies;
- the synchrotron motion;
- electron beam halo formation.

The modified linear theory, taking into account the loss of coherence because of the beta function beating, which leads to a spread in the frequencies  $\Delta\omega_i$ , results in an exponential instability growth proportional to  $\exp(t/\tau_e)$  with the characteristic time [49]:

$$\frac{1}{\tau_e} \approx \frac{1}{\tau_c} \frac{c}{2\sqrt{2}N_b L_{\text{sep}}(\Delta\omega_i)_{\text{rms}}} . \quad (1.57)$$

Figure 1.41 shows graphs of the rise time of vertical fast ion instability (1.57) vs. the residual gas pressure  $P_{\text{gas}}$  at a nominal total beam current of 1.7 A in  $N_b = 406$  bunches,  $\langle\beta_x\rangle = 6.3$  m,  $\langle\beta_y\rangle = 9.5$  m,  $\sigma_x = \sqrt{\varepsilon_x\beta_x} = 224 \mu\text{m}$ ,  $\sigma_y = \sqrt{\varepsilon_x\beta_x} = 20 \mu\text{m}$ , and  $L_{\text{sep}} = 1.8$  m.

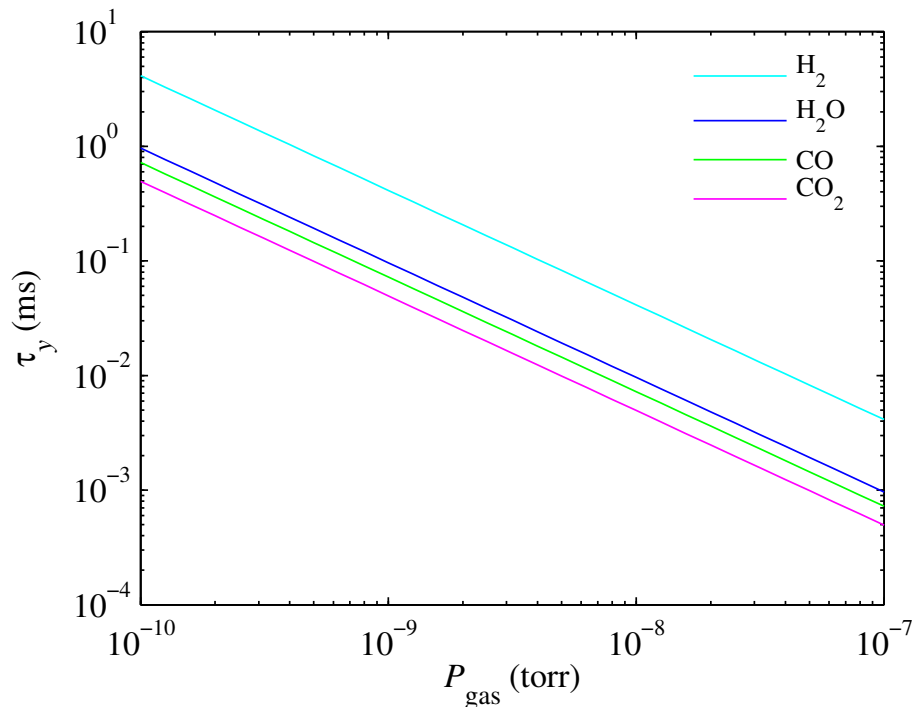


Figure 1.41. Rise time of vertical fast ion instability.

In [50] it is shown that fast ion instability may increase the beam emittance. Because of the relationship between the longitudinal and transverse motion of the beam (head-tail), the ion cloud produced by the beam head particles is displaced relative to the tail particles, and the electric field of the ions deflects the tail particles. The perturbation theory applied to a simple linear interaction model gives in the first order the perturbation of the emittance over the train length  $L_{\text{train}}$ :

$$\Delta\varepsilon_y \approx \frac{1}{2\pi\langle\beta_y\rangle} \left( \hat{y} \frac{L_{\text{train}}\langle\beta_y\rangle\lambda_i r_e}{2\gamma\sigma_y(\sigma_x + \sigma_y)} \right)^2 , \quad (1.58)$$

where  $\lambda_i \approx 6N_e N_b P_{\text{gas}}$  is the linear ion density at the end of the train, and  $\hat{y}$  is the amplitude of the Fourier components of the longitudinal distribution of the beam at the beginning of the train at the frequency  $\omega_i$ . This initial amplitude can be determined by, for example, the shot noise (Schottky noise) or vertical dispersion.

### 1.7.8 Electron clouds

The formation and accumulation of electron clouds in positron machines can lead to excitation of both multi-bunch and single-bunch instabilities since the frequency  $\omega_e$  of the electron oscillator is larger than the ion frequency  $\omega_e/\omega_i = \sqrt{m_i/m_e} > 100$  times, and the wavelength of the wake fields  $2\pi c/\omega_e$  is comparable with the bunch length  $\sigma_z$ . Neglecting the motion of the bunch and assuming that the interaction force is linear, we can write the following simple expression for the frequency of the electron oscillator [51]:

$$\omega_e = \sqrt{\frac{2\lambda_p r_e c^2}{\sigma_y(\sigma_x + \sigma_y)}}, \quad (1.59)$$

where  $\lambda_p \approx N_e/(2\sigma_z)$  is the linear density of the beam positrons, and  $r_e$  is the classical radius of electron. Vertical blow-up of the positron beam was observed at the KEKB electron-positron collider [52, 53]. The effect has a threshold character: at a beam current exceeding the threshold value, the vertical beam size began to grow in proportion to the current and almost doubled at a current of 300 mA. This effect was one of the most serious problems limiting the luminosity of KEKB.

The blow-up of the positron beam is characterized by the following features:

- the effect is multi-turn and is not associated with the beam-beam effects;
- the instability threshold is proportional to the beam current and inversely proportional to the distance between the bunches;
- at large vertical chromaticity ( $5 \div 8$ ), no dipole oscillations were observed; at lower chromaticity (about 2) and feedback switched off, dipole oscillations were excited;
- the blow-up of the beam is practically independent of the betatron frequencies, vacuum conditions, or wiggler fields;
- the introduction of vertical collimators (the main source of impedance) does not affect the blow-up of the beam;
- this effect was not observed in the horizontal plane.

A theoretical explanation of the effect is proposed in [51]. The blow-up of the positron beam is attributed to the single-bunch instability, which is caused by the interaction with the electron clouds arising in photoemission or secondary emission. The instability arises in the multi-bunch mode of operation, since an electron cloud is formed in a successive flight of many bunches. Coherent dipole oscillations are excited by the wake-fields of the electron cloud, which manifest themselves as the head-tail effect (strong or weak). The observed increase in the transverse dimension is a result of the head-tail oscillations. The rise time of the instability is determined by the density of the electron cloud near the beam. The distribution of electrons in the cloud was calculated by computer simulation [54].

The results of calculation of the instability increments by a two-particle model are given in [51]. Formulae were derived and were used to make estimates of the increments for KEKB LER, which

are in good agreement with the results of numerical simulation. Within the framework of the two-particle model, the integral of wake fields in one revolution can be written in the form  $W_0 = 8\pi\rho_e P/N_e$ , where  $\rho_e = N_e/\pi h_x h_y L_{\text{sep}}$  is the equilibrium space density of electron cloud with allowance for neutralization,  $h_x$  and  $h_y$  are the vertical and horizontal semi-apertures of the vacuum chamber, and  $L_{\text{sep}}$  is the distance between the positron bunches. Substituting  $W_0$  in the equation for calculating the increment of the head-tail instability [26] with allowance for the chromaticity, we can write down the following expression for the rise time of the dipole head-tail mode:

$$\frac{1}{\tau_1} \approx \frac{64}{3} \frac{\rho_e \langle \beta_y \rangle r_e \sigma_z \xi_y f_0}{\alpha \gamma}, \quad (1.60)$$

where  $\alpha$  is the momentum compaction factor,  $\xi$  is the chromaticity, and  $\sigma_z$  is the length of positron bunch. Evaluation for the Super Charm–Tau factory ( $E = 2 \text{ GeV}$ ):  $\tau_1 \simeq 160 \mu\text{s}$  with a chromaticity  $\xi = 1$  (for KEKB LER  $\tau_1 \simeq 500 \mu\text{s}$  at  $\xi = 8$ ). The two-particle model also makes it possible to calculate the threshold value of the space density of electron cloud above which the fast head-tail instability arises:

$$\rho_e > \frac{2\gamma\nu_s}{\pi r_e P \langle \beta_y \rangle}. \quad (1.61)$$

Evaluation for the Super Charm–Tau factory ( $E = 2 \text{ GeV}$ ):  $\rho_e > 10^{12} \text{ m}^{-3}$ ; this value is close to the estimates made for KEKB LER.

The mathematical model of the head-tail instability caused by electron clouds was published in [55]. The model was developed on the basis of a multimode analysis of the eigenvalue problem with allowance for the chromaticity of the magnetic lattice. The model also shows the results of the analysis of the shift of the frequencies and the increments of the coupled modes in dependence on the density of electron cloud and chromaticity, with and without feedback, for two installations: KEKB LER and CERN SPS. It is shown that increase in chromaticity can significantly rise the instability threshold, the chromaticity effect being more pronounced at higher  $Q$  factors of the model electron oscillator.

To reduce the density of electron clouds in KEK, it was proposed to use a magnetic field (about 10 Gs is enough to capture photoelectrons with a characteristic energy of 10 eV), for which purpose solenoids were placed on the free sections of the vacuum chamber.

## 1.8 Feedbacks

### 1.8.1 Objective of stabilization

The effective operation of lepton colliders and synchrotron radiation source is usually associated with high requirements to the stability of beam parameters. The following perturbing factors can decrease the efficiency of the accelerator: deviation of the fields in magnets from calculated values, errors in the alignment of the elements of the magnetic system, seismic vibrations, thermal expansion of magnets and accelerating cavities, temperature drift of parameters, and other dynamic effects. Fully automated control of key beam parameters, such as the orbit, betatron frequencies, coupling of oscillations, chromaticity, energy, etc., with continuous correction of perturbations introduced by the above factors becomes practically an integral part of the modern accelerator control system.

The variety of modern feedback systems is determined by different requirements to feedback parameters in accelerators of different types. Beam stability in colliders is a necessary condition for optimizing luminosity in experiments on high-energy physics. Orbit stabilization is required

to minimize the emittance and ensure stable convergence of the beams at the interaction points. In addition to the orbit, the feedback systems stabilize the betatron tunes to prevent intersection of betatron resonances during acceleration because resonances can cause losses of beam particles.

In dependence on the sources, various perturbations affecting the beam orbit, betatron tunes, betatron coupling, chromaticity, and energy can be conditionally divided into three groups.

1. External perturbations: changes in ambient temperature and atmospheric pressure; mechanical ground motion caused by seismic activity, tidal waves, and human activity (industry and transport). These perturbations come to the particle beam mainly from quadrupoles, the beam focusing in which depends on transverse displacements.
2. The intrinsic perturbations of the accelerator: variation of the fields in the elements of the magnetic lattice, noise caused by the flow of cooling liquids, vibration of ventilation pumps, and eddy currents.
3. Failures of individual elements, which are important for large machines, where failure of one of the tens or even hundreds of correctors can stop the experiment for the time of repair.

The characteristic time scale of the perturbations can be long-term (from several months to several days), medium-term (days or hours) or short-term (from hours to milliseconds). Applicability of feedbacks to correct slow perturbations of the beam is eventually limited by the thermal drift, noise, and systematic errors in the measuring and correcting circuits. Because of the sensitivity of beam to thermal drift, in the modern machines it is necessary to stabilize not only the orbit but also the temperature of the experimental hall, accelerator tunnel, vacuum chamber, and cooling water within about  $\pm 0.1$  °C. The instabilities of longitudinal or transverse motion of beam with fast growth times (multi-bunch and TMC instability) can be suppressed by fast feedback systems whose reaction time is comparable with the period of beam revolution.

External perturbations, beam parameters, and the strengths of correctors are functions of time. Therefore, the feedback systems are designed with a separate analysis of the scheme to correct deviations of beam parameter from a required value for a given constant perturbation (space domain) and time-dependent (time domain) processes describing the operation of the system in real time. This separation makes the operation of the system more flexible, especially at possible failures of individual elements, when fast adjustment of the feedback parameters is required.

## 1.8.2 Correction algorithms

If the effect of the correcting elements on parameters such as the orbit, betatron tunes, betatron coupling, chromaticity and energy can be considered linear in the first approximation, then the matrix formalism can be used to calculate the correction. The relationship between the measured beam parameters and the corrective actions in the linear approximation is described by the following matrix equation:

$$x = Rf, \tag{1.62}$$

where  $x = (x_1, \dots, x_N)$  is the vector of beam parameter values measured by  $N$  pickups,  $f = (f_1, \dots, f_M)$  is the vector of  $M$  corrective actions,  $R$  is the response matrix the elements  $R_{ij}$  of which describe the reaction of the  $i$ th pickup to a change in the force of the  $j$ th corrector. In the case of correction of the closed orbit of the beam,  $x$  is the set of orbital deviations measured by the beam position pickups, and  $f$  are the currents of the dipole correcting magnets.

The correction algorithm essentially consists in the inversion of the response matrix  $R$ . However, in practice, the matrix  $R$  often turns out to be degenerate or almost degenerate, and thus

one of the most widely used algorithms to invert  $R$  is the singular value decomposition, SVD. The response matrix is written down as  $R = U\lambda V^T$ , and the inverse matrix as  $R^{-1} = V\lambda^{-1}U^T$ , where  $U$  is a  $M \times N$  dense unitary matrix,  $\lambda$  is the diagonal matrix consisting of the eigenvalues of the matrix  $R$ , and  $V$  is the orthogonal matrix whose columns are eigenvectors of the matrix  $R$ . To exclude singularities in the calculation of  $R^{-1}$ , the  $\lambda_k^{-1}$  values corresponding to the small eigenvalues  $\lambda_k$  are taken to zero. The number of eigenvalues used to calculate the inverse matrix  $R^{-1}$  is chosen as a compromise between the accuracy of the correction and the reliability of the algorithm: a larger number of eigenvalues provides better convergence, but the correction process becomes more sensitive to measurement errors and electronics noise. In addition, the response matrix used for correction may diverge from the actual matrix of the magnetic lattice. So, the correction process can consist of several successive iterations.

### 1.8.3 Calculation of transfer functions

Analysis of the time-domain processes occurring in the system of beam parameter stabilization makes it possible to optimize the system operation in real time. A scheme of a closed automatic control system with one input and one output is shown in Fig. 1.42.

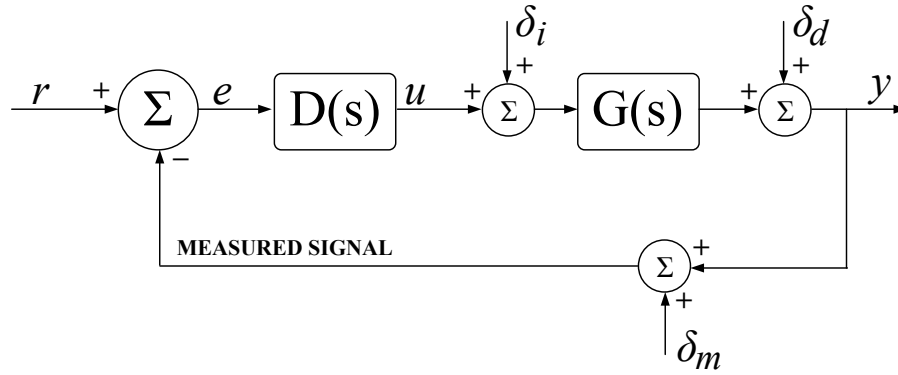


Figure 1.42. First-order automatic control system.

The object to control is characterized by the frequency-dependent transfer function  $G(s)$ , and the control device (controller)—by the function  $D(s)$ . The stability of the system and its sensitivity to perturbations and noise are determined by the following functions:

$$T(s) \equiv \frac{y}{r} = \frac{D(s)G(s)}{1 + D(s)G(s)}, \quad (1.63)$$

$$S_d(s) \equiv \frac{y}{\delta_d} = \frac{1}{1 + D(s)G(s)}, \quad (1.64)$$

$$S_i(s) \equiv \frac{y}{\delta_i} = \frac{G(s)}{1 + D(s)G(s)}, \quad (1.65)$$

$$S_u(s) \equiv \frac{u}{\delta_d} = \frac{D(s)}{1 + D(s)G(s)}, \quad (1.66)$$

where  $T(s)$  is the full transfer function,  $S_d(s)$  is the nominal sensitivity that defines the suppression of perturbations by the feedback scheme,  $S_i(s)$  is the sensitivity to input perturbations, and  $S_u(s)$  is the sensitivity of the control system. The state variables are also indicated in Fig. 1.42:  $r$  is the correction goal;  $y$  is the quantity to correct;  $e$  is the error signal;  $u$  is the corrective effect;  $\delta_m$

is the measurement noise;  $\delta_i$  and  $\delta_d$  are perturbations at the input and output of the object to control. The sensitivity to measurement noise is equal to the nominal transfer function  $T_0(s)$ .

The classical feedback calculation is based on the study of the zeros in the denominator in equations (1.63-1.66) using, for example, the Nyquist stability criterion, formulated as follows: a close-loop system is stable if the hodograph of the transfer function  $D(p)G(p)$  of the open-loop system does not encompass a point with the coordinates  $(-1, 0i)$  on the complex plane. If an open-loop system is unstable, then the closed-loop system is stable if and only if the hodograph of the transfer function  $D(p)G(p)$  of the unstable open-loop system encompasses a point with the coordinates  $(-1, 0i)$   $n/2$  times, where  $n$  is the number of the roots of the characteristic equation of the open-loop system with a positive real part. In this case, a number of conditions must be met, such as providing the necessary bandwidth, minimizing mavericks in the regulatory process, ensuring a wide dynamic range of corrective actions, and achieving maximum reliability with respect to the measurement errors and the model inaccuracies.

As a rule, feedback systems for stabilization of beam parameters in accelerators are developed and put into operation independently of each other, and their interdependence and reduction of parasitic links are not studied properly. Nevertheless, for stable and reliable operation of systems, as early as at the design stage it is necessary to take into account possible cross-links between several parallel and possibly embedded feedback loops.

#### 1.8.4 Orbit Stabilization

Stabilization of the orbit is necessary for effective collision of beams in a collider. Usually, the main cause of distortion of the beam orbit on the short to medium-term time scales is mechanical displacement of the magnets caused by ground vibrations, thermal effects, movement of the cooling liquid, etc. Other sources of instability are the power supply current oscillations containing harmonics of the mains frequency and magnetic fields. Identification and minimization of noise sources at the stage of the accelerator design can significantly improve the situation. However, in many cases the required level of stability can only be achieved through feedback systems. In particular, it is impossible to do without fast feedbacks when the most stringent conditions are imposed on the short-term (milliseconds to seconds) and medium (minutes to days) beam stability [56].

In a typical feedback scheme to stabilize the beam orbit, the input signals come from a set of beam position pickups, and the corrective action is performed using dipole magnetic correctors. Programmable signal processors of various types are commonly used as regulators. In a local scheme, three or four magnetic correctors create a local compensated effect to stabilize the position and angle of the electron beam at a desired point without affecting the rest of the orbit. A global feedback circuit, including all available beam position pickups and correctors, is to minimize the root-mean-square deviation of the orbit from some optimal one.

A correction algorithm is based on the inversion of the response matrix that ties the beam position at the locations of the pickups with the currents of the magnetic correctors. The method of eigenvalue decomposition of the matrix is used for the inversion. With this method, a system of an arbitrary number of pickups and correctors linked together by the response matrix can be imaged in the transformed space, where each pickup is associated with one virtual equalizer via a single coefficient. These coefficients correspond to the eigenvalues of the diagonal response matrix in the transformed space, and thus it is possible to turn from the original MIMO system to a set of independent SISO feedback loops for each transformed correction channel. The dynamics of each channel is determined by the low-frequency characteristic of the corrector, mainly by the eddy currents in the yoke of the magnet and the walls of the vacuum chamber. Another important parameter is the total delay time of the system, determined by the time of the measurement,

processing, and transfer. Thus, each correction channel can be fairly accurately described by a model consisting of a first-order low-pass filter and a delay.

Data processing in systems of fast orbit stabilization is most often realized in field-programmed gate arrays (FPGAs). The control element is a proportional-integral-differential controller (PID controller). At feedback operating frequencies up to 10 kHz, the optimal choice of the PID controller parameters enables effective stabilization of the beam orbit in the frequency band of  $100 \div 150$  Hz. Correctors without magnetic cores can be used to expand the frequency band in local fast-feedback loops, while all available standard orbit correctors are usually included in a slower global feedback. Stable components of the perturbation spectrum, such as the mains frequency and its harmonics, can be effectively suppressed by special narrow-band feedback loops.

### 1.8.5 Fast feedback systems

Modern accelerators are equipped with fast feedback systems for turn-by-turn or bunch-by-bunch suppression of transverse and longitudinal instabilities of beam movement. A block diagram of feedback system for suppressing the transverse oscillations of beam is shown in Fig. 1.43.

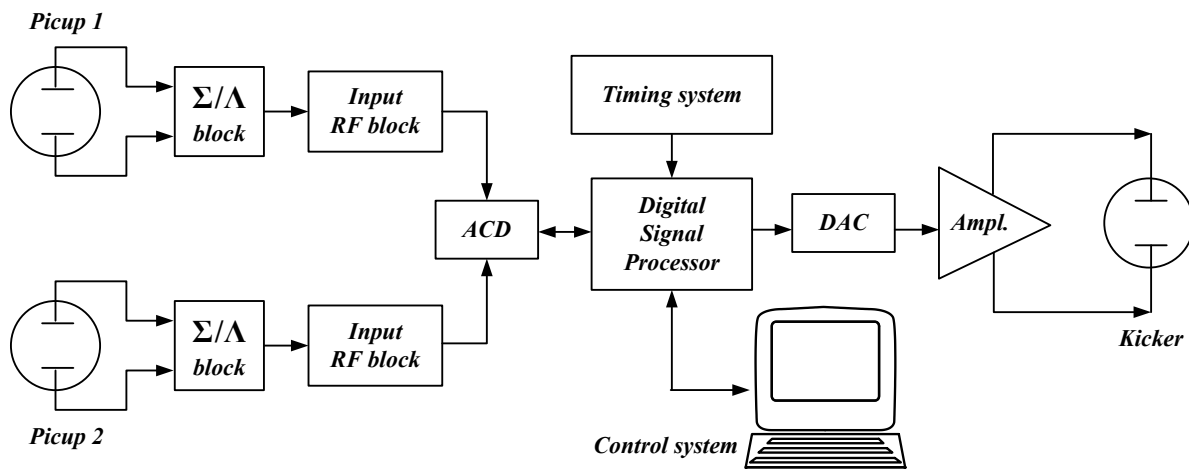


Figure 1.43. Block diagram of feedback system for suppression of transverse oscillations of beam.

The beam position sensors are electrostatic or stripline pickups, whose signals are processed by analogue hybrid circuits, whose output signals are proportional to the vertical and horizontal coordinates of the beam and its intensity. These signals are then detected and digitized. The digital data is processed by a field-programmed gate array (FPGA), which calculates the strength of the pulsed kicker impact on the beam. Filters with finite impulse response (FIR filters) are applied to processing the signals. Stripline pickups and kickers with directivity enable simultaneous stabilization of the motion of opposite-direction electron and positron bunches using the same striplines for both types of particles [57]. Measurement of the beam position with two pickups enables calculation of the transverse position and momentum of the beam in each revolution. Signal processing includes the following operations: measurement of beam deflection in the pickups, calculation of the coordinate and momentum of the beam in the kicker, and calculation of corrective action. In longitudinal feedback systems, the input signal is the deviation of the phase of the beam from the equilibrium signal, and broadband cavities are used as kickers.

For the Super Charm – Tau factory it is necessary to develop a feedback system for suppressing the transverse multi-bunch instability caused by the interaction of the beam with the resistive impedance of the walls of the vacuum chamber. It is also very likely that the threshold current of the TMC instability will be close to the design beam current.

## 1.9 RF system

The project of the Super Charm–Tau factory includes two storage rings: for  $e^+$  and  $e^-$ . The beam energy in each ring is in the range of  $1 \div 2.5$  GeV. For both rings, the parameter values are identical. Table 1.9 presents parameters of one ring of the Super Charm–Tau factory for the maximum regime of the collider.

The beam structure: a train of 406 bunches filling each third separatrix and then 138 empty separatrices.

Table 1.9. Parameters of storage ring of Super Charm–Tau factory.

Energy	1.0	1.5	2.0	2.5	GeV
Revolution frequency, $f_0$	368.7				kHz
RF frequency, $f_{\text{RF}}$	499.954				MHz
Harmonic number, $h$	1356				
Number of particles per bunch, $N_0$	$8.3 \cdot 10^{10}$				
Bunch current, $I_0$	4.93				mA
Number of bunches, $N_b$	406				
Train gap	138 (10%)				
Total number of particles, $N$	$3.39 \cdot 10^{13}$				
Total current, $I$	2.0				A
Damping time, $\tau_x / \tau_y / \tau_z$	30/30/15				ms
Bunch length, $\sigma_z$	1.92	1.28	1	1	cm
Energy spread, $\sigma_{\Delta E/E}$	$1.09 \cdot 10^{-3}$	$1.1 \cdot 10^{-3}$	$9.3 \cdot 10^{-4}$	$7.2 \cdot 10^{-4}$	
Energy spread, $\sigma_E$	1.09	1.65	1.86	1.80	MeV
Compaction factor, $\alpha$	$8.49 \cdot 10^{-4}$	$8.77 \cdot 10^{-4}$	$8.82 \cdot 10^{-4}$	$8.83 \cdot 10^{-4}$	
Synchrotron tune, $\nu_z$	$6.23 \cdot 10^{-2}$	$9.73 \cdot 10^{-3}$	$1.06 \cdot 10^{-2}$	$8.21 \cdot 10^{-3}$	
Energy loss per turn, $U_0$	190	298	397	497	keV
RF voltage, $U_{\text{RF}}$	0.33	0.96	1.5	1.2	MV
Synchronous phase, $\varphi_{s1}^*$	$144.3^\circ$	$162.4^\circ$	$163.0^\circ$	$152.9^\circ$	

\* phase value relative to the zero of growing RF voltage.

### 1.9.1 Requirements to RF system

The operation of the RF system of the Super Charm–Tau factory has the following features:

- heavy beam load (high beam power and reactivity introduced by it);
- need to suppress multibunch instabilities (the feedback system and damping of the higher modes of the RF system) and transient processes associated with the presence of unfilled separatrices (beam load uneven over the period of revolution, which requires a generator power margin).

Since similar requirements were applied to the RF systems of the B-factories at KEKB and PEP-II [58, 59], a preliminary estimation can be made using the parameters of the RF systems of these colliders. Table 1.10 presents the parameters of the accelerating cavities of these factories [60, 61, 62].

Table 1.10. Parameters of accelerating cavities of B-factories at KEKB and PEP-II.

Parameter	s/c, KEKB	ARES, KEKB	PEP-II	
Frequency, $f_{\text{RF}}$	509	509	476	MHz
Characteristic impedance, $\rho$	46.5	7.5	116	Ohm
Q factor, $Q_0$		$1.15 \cdot 10^5$	$3 \cdot 10^4$	
RF voltage, $U_{\text{RF}}$	1.3	0.5	0.59	MV
Power to cavity and to beam	$250 \div 400$	350	350	kW

Comparison of the required maximum RF power, of about 1.2 MW, the losses taken into account, and the maximum RF voltage, 1.5 MV, shows that the RF system of each ring must include at least three accelerating cavities.

The simplest configuration of the RF system is the power supply of each cavity from a separate klystron with a power equal to  $400 \div 500$  kW (continuous wave). The powers of klystrons available in the market are 300, 800, or 1200 kW. In this case, the arrangement of the RF system has several options:

- 4 klystrons (each for 300 kW CW) for 4 cavities;
- 6 klystrons (each for 300 kW CW) for 3 cavities;
- 2 klystrons (each for 800 kW CW) for 4 cavities.

Figure 1.44, a) presents the option of 6 klystrons THALES TH2161B (310 kW) and 3 accelerating cavities. Figure 1.44, b) shows the option with 2 klystrons made by CPI (Microwave Power Products Division) VKP-7958A (800 kW) and 4 accelerating cavities.

To reduce the RF power reflected from the cavity (compensation for the beam-induced reactivity), it is necessary to detuning the eigenfrequency of the RF system and the operating frequency  $f_{\text{RF}}$ . The detuning value can be estimated from the following formula:

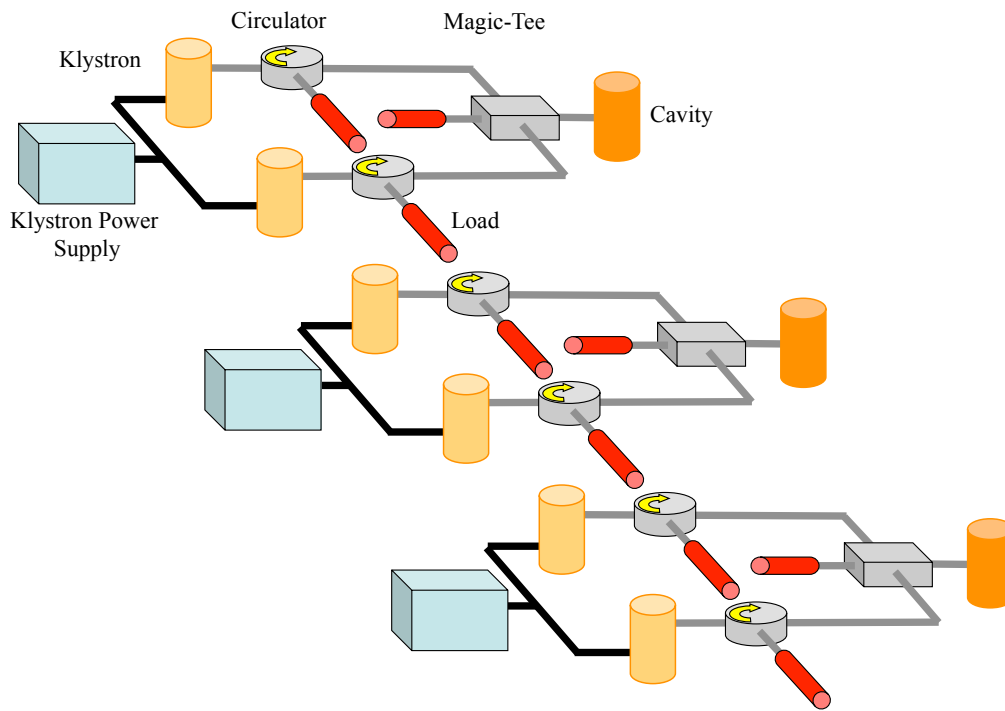
$$df = -\frac{f_{\text{RF}} I \rho \sin\left(\arccos\left(\frac{U_0}{U_{\text{RF}}}\right)\right)}{U_{\text{RF}}},$$

where  $f_{\text{RF}}$ ,  $I$ ,  $U_0$ , and  $U_{\text{RF}}$  are parameters from Tab. 1.9, and  $\rho$  is the total characteristic impedance of the cavities of the RF system.

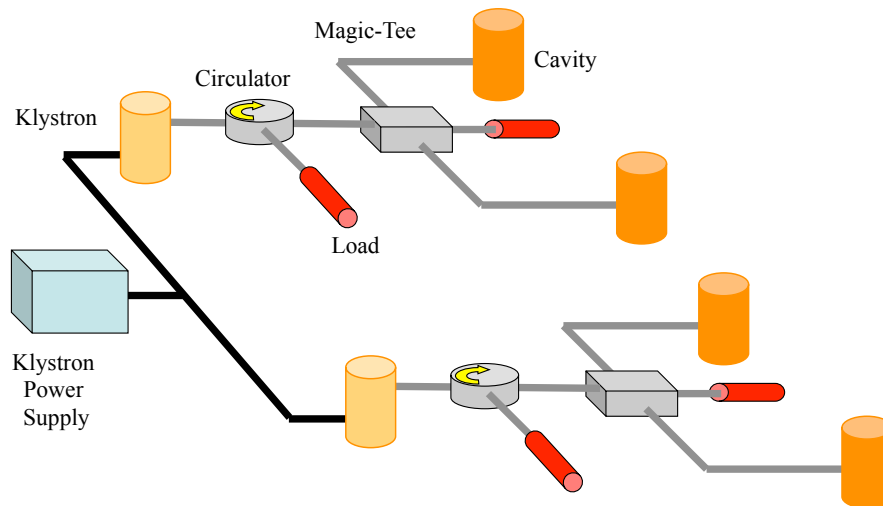
Table 1.11 gives estimates of the impedance of the 3-cavity RF system, obtained using data from Table 1.10. The minimum bandwidth  $\Delta f$  and detuning of the RF system  $df$  occur with the ARES cavities, and the maximum ones occur with the PEP-II cavities. In this case, suppression of the bunch beam instabilities associated with the interaction with the working mode of the RF system may necessitate creation of a feedback system on comb filters. A description of such a system for PEP-II is given in [63]. Fig. 1.45–1.46 shows cavity impedance curves without feedback and with feedback, taken from this article.

The interaction of bunches with higher order modes (HOMs) of the accelerating cavities can also lead to development of multibunch beam instabilities, which will limit the beam current. Therefore, the design of the accelerating cavities should allow for decrease in the Q factors (suppression) of the HOMs.

There is an additional requirement to the operation of the RF system, consisting in ensuring the exactness of bunch arrival at the IP. Since part of the perimeter of the ring is not filled with



(a) Each cavity is powered from two THALES TH2161B klystrons via circulators and hybrid waveguide tee; the klystrons have common power source.



(b) Two klystrons VKP-7958A feed four cavities.

Figure 1.44. Options of RF system of one ring of Super Charm – Tau factory.

Table 1.11. Estimations of impedance of 3-cavity RF system.

Parameter	s/c, KEKB	ARES, KEKB	PEP-II	
Frequency, $f_{\text{RF}}$	500	500	500	MHz
Characteristic impedance, $\rho$	139.5	22.5	348	Ohm
Q factor with load, $Q$ (2.5 GeV)	$5.19 \cdot 10^3$	$25.2 \cdot 10^3$	$1.94 \cdot 10^3$	
Bandwidth, $\Delta f = f_{\text{RF}}/Q$	96.3	19.8	257.3	kHz
Detuning, $df$ (2 GeV, 3 cavities)	-112	-18	-280	kHz
Detuning, $df$ (1 GeV, 1 cavity)	-115	-19	-287	kHz

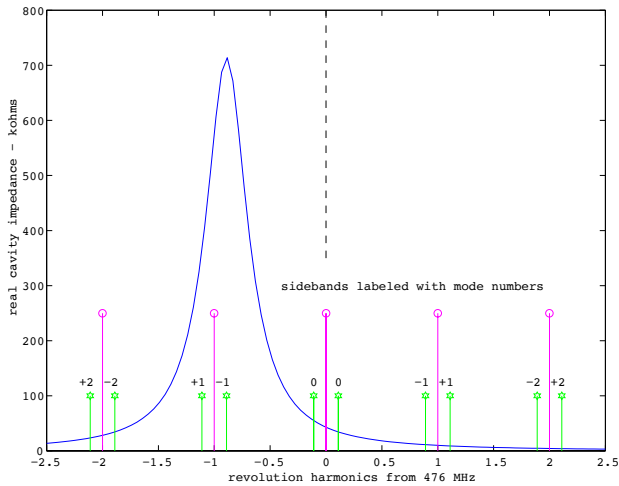


Figure 1.45. Cavity impedance, beam revolution harmonics, synchrotron sidebands — mode numbers labeled [63].

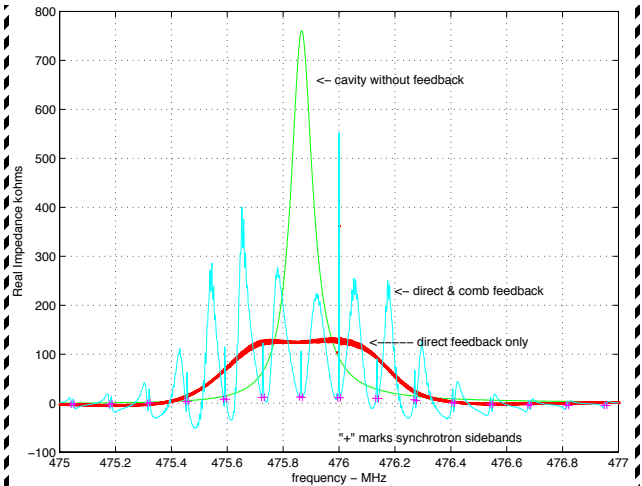


Figure 1.46. Measured real cavity impedance with no feedback, direct RF feedback and also equalized comb feedback. [63].

bunches (a train gap of 10%, see Table 1.9), at the respective time the RF system is not loaded with the beam. This leads to the fact that the amplitude and phase of the accelerating voltage change with a period equal to the period of revolution: during the flight of a train of bunches, the amplitude of the voltage across the cavities decreases (because at this time the load exceeds the average value over the period of the revolution), and during train gap it increases to its initial value (see Fig. 1.47). As a result, each bunch will have its own synchronous phase:

$$\varphi_{s_i} = 180^\circ - \arcsin\left(\frac{U_0}{U_{RF_i}}\right) + \varphi_{RF_i},$$

where  $\varphi_{s_i}$  is the synchronous phase of the  $i$ th bunch,  $U_0$  is the energy loss per turn,  $U_{RF_i}$  is the amplitude of the RF voltage (during the flight of the  $i$ th bunch), and  $\varphi_{RF_i}$  is the value of the RF voltage phase relative to the generator current (during the flight of the  $i$ th bunch).

The value of the voltage  $dU_i$  induced by the passing  $i$ th bunch on the cavities of the RF system can be estimated from the following formula:

$$dU_i = -\frac{q_i}{C} = -q_i\omega_c\rho_c,$$

where  $q_i$  is the bunch charge, and  $C$ ,  $\omega_c$ , and  $\rho_c$  are, respectively, the equivalent capacitance, the cyclic frequency, and the total characteristic impedance of the RF system cavities.

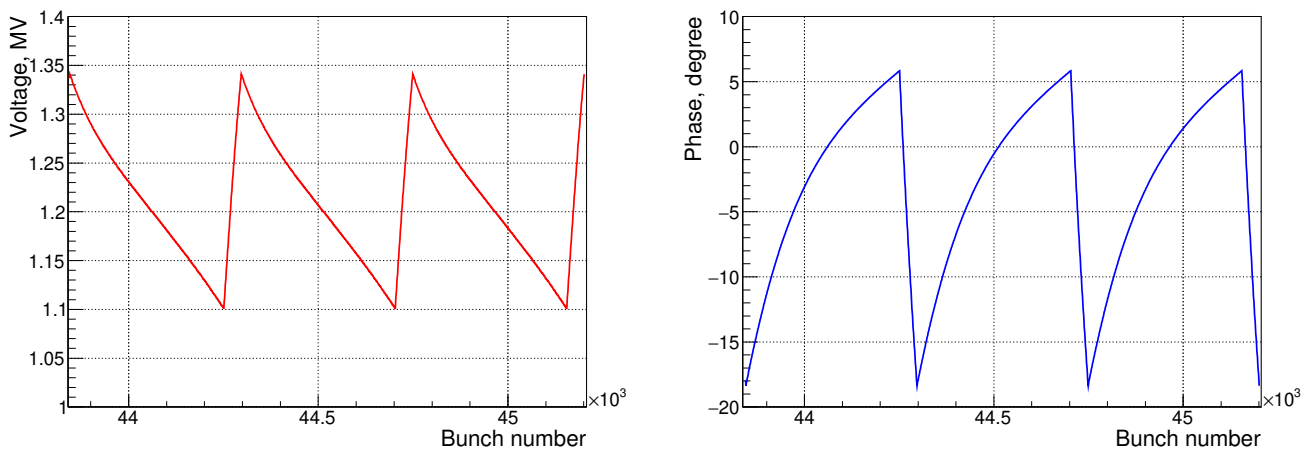


Figure 1.47. Varying amplitude and phase of RF voltage.

If the charge distributions over the bunches in both rings are identical, then the RF voltages in both rings change identically during the time of flight; the synchronous phases for each pair of colliding bunches (with the same number from different rings) are also the same. In this case, the interaction point for each pair of bunch does not move.

If the bunch charges in each ring are varied independently in the range of  $\pm 10\%$  from the average value (this is caused by the need to compensate for the loss of particles by means of additional injection during the factory operation), then the voltages  $dU_i$  induced by them (in the flight through the cavities of the RF system) will also vary within  $\pm 10\%$ . As a result, the amplitudes and phases of the RF voltages in the two rings will differ, and hence the synchronous phases in the pairs of colliding bunches (with the same number from different rings) will also be different, which will cause displacement of the IP from pair to pair.

The value of the difference for synchronous phases  $\varphi_{s_i}$  and hence the value of the displacement of the interaction point are directly proportional to the non-uniformity of the charges in the bunches (in C), as well as to the frequency and the total characteristic impedance of the cavities.

Since the average value of the bunch charge has been set (by the beam current), the inhomogeneity of the bunch charge is also given (and amounts to  $\pm 10\%$  of the average value) and the frequency of the RF system operation is fixed ( $\omega_c = 2\pi \cdot 500$  MHz), the displacement of the IP is entirely determined by the value of the total characteristic impedance  $\rho_c$  of the cavities of the RF system.

Estimates show that to ensure a required accuracy of the beam interaction point of  $1.5 \div 3$  mm, it is necessary to have an RF system with a total characteristic impedance not exceeding 350 Ohm (the estimate is derived from peak-to-peak levels).

### 1.9.2 Accelerating cavities

A more detailed evaluation of the RF system of the Super Charm–Tau factory was made using the data for accelerating cavities at PEP-II [62]. These cavities are made of copper and equipped with a waveguide power input (with a vacuum ceramic RF window), a tuner for adjusting the frequency of the operating mode, and 3 waveguide suppressors of higher order modes. The parameters of cavity are given in Table 1.12.

Table 1.12. Cavity parameters at PEP-II.

Parameter	Value
Length, $L$	$\sim 2$ m
Operating frequency, $f_{\text{RF}}$	476 MHz
Characteristic impedance, $\rho$	116 Ohm
Q factor, $Q$	$3 \cdot 10^4$
Shunt impedance	3.5 MOhm
RF voltage, $U_{\text{RF}}$	0.59 MW
RF power applied at cavity	350 kW
Power of loss in walls	50 kW
Power transmitted to beam	300 kW

The number of accelerating cavities is determined by the maximum required RF power, which is equal to 994 kW to the beam (when operating at 2.5 GeV), and the maximum RF voltage, which is equal to 1.5 MV in operation at 2.0 GeV (see Table 1.9). From comparison of these requirements with the parameters of cavity at PEP-II (see Table 1.12) it follows that each ring of the Super Charm–Tau factory needs three cavities of this type.

### 1.9.3 RF power supply system

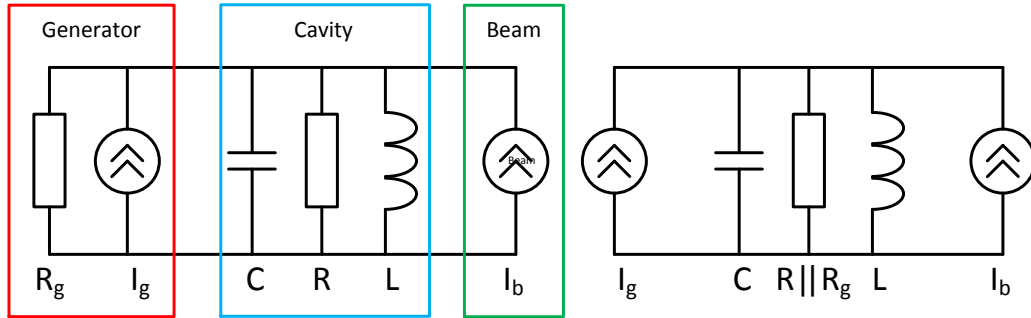
The maximum RF power level of the generator corresponds to operation at 2.5 GeV. This level is determined by the sum of the power transmitted to the beam and the power of loss (in the waveguides and circulators of  $\sim 7\%$  and in the walls of the cavities and in HOMs loads) and is equal to 1.17 MW for each ring of the Super Charm–Tau factory.

The THALES TH2161B (500 MHz, 310 kW) klystrons or the CPI VKP-7958A (800 kW) klystrons can be used as RF power generators (see Fig. 1.44).

Let us make an estimation of the power consumption. Taking the efficiency of the klystrons equal to 64% and the efficiency of the high-voltage power supplies equal to 89%, we find that the total power consumption for the two rings is  $2 \times 1.2 \text{ MW} / 0.89 / 0.64 = 4.2 \text{ MW}$ .

### 1.9.4 Procedure for calculating operation of RF system

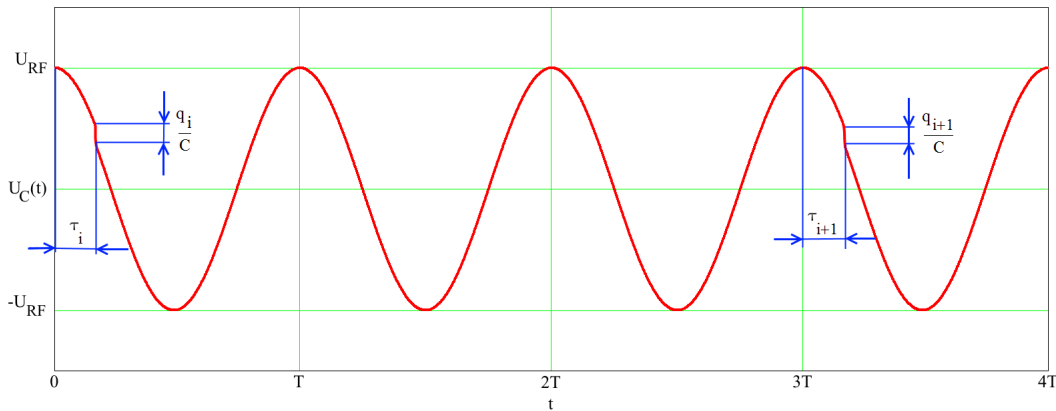
Simulation of the operation of the RF system was carried out using the equivalent circuit shown in Fig. 1.48.



$C$ ,  $R$ , and  $L$  are parameters of equivalent resonant circuit;  $R_g$  is the equivalent impedance of generator, referred to circuit;  $I_g$  is the RF generator current;  $I_b$  is the beam current.

Figure 1.48. Equivalent circuit of RF system.

Figure. 1.49 shows the time dependence of the voltage on the resonant circuit.



$U_{RF}$  is the amplitude of the RF voltage (since the picture is qualitative, for its simplicity we neglect the change in  $U_{RF}$  after the flight of bunches);  $T$  is the generator oscillation period;  $\tau_i$  and  $\tau_{i+1}$  are the moments of flight of the bunches, counted from the moments  $T$  and  $3T$ ;  $q_i/C$  and  $q_{i+1}/C$  are the changes in the voltage after the flight of the bunches with the numbers  $i$  and  $i + 1$ .

Figure 1.49. Voltage  $U_C(t)$  vs. time, shown near moments of flight of bunches with numbers  $i$  and  $i + 1$ .

The oscillatory process in the resonance circuit shown in Fig. 1.48 can be represented as the superposition of the processes caused by the generator current (forced oscillations) and by the beam current (damped free oscillations arising in the circuit after the flight of the next bunch).

The capacitor voltage  $U_C$  and current through inductor  $I_L$  versus time can be written as follows:

$$U_C(t) = U_{C\text{forced}}(t) + U_{C\text{free}}(t),$$

$$I_L(t) = I_{L\text{forced}}(t) + I_{L\text{free}}(t).$$

- for forced oscillations

$$U_{C\text{forced}}(t) = \text{Re} \left[ \frac{I_g \rho Q \exp(j(\omega_g t + \varphi))}{1 + jQ \left( \frac{\omega_g}{\omega_c} - \frac{\omega_c}{\omega_g} \right)} \right],$$

$$I_{L\text{forced}}(t) = \text{Re} \left[ \frac{I_g Q \exp(j(\omega_g t + \varphi))}{j \frac{\omega_g}{\omega_c} \left( 1 + jQ \left( \frac{\omega_g}{\omega_c} - \frac{\omega_c}{\omega_g} \right) \right)} \right],$$

where  $I_g$ ,  $\omega_g$ , and  $\varphi$  are the amplitude, cyclic frequency, and phase of the generator current, and  $\rho$ ,  $\omega_c$ , and  $Q$  are the characteristic impedance, cyclic resonant frequency, and  $Q$  factor of the circuit with load  $R_g$  (see Fig. 1.48, right);

- for free oscillations (after the flight of the next bunch)

$$U_{C\text{free}}(t) = \text{Re} \left[ \left( U_{C\text{free}}(0) + j\rho I_{L\text{free}}(0) \right) \exp \left( \omega_c t \left( j - \frac{1}{2Q} \right) \right) \right],$$

$$I_{L\text{free}}(t) = \frac{1}{\rho} \text{Im} \left[ \left( U_{C\text{free}}(0) + j\rho I_{L\text{free}}(0) \right) \exp \left( \omega_c t \left( j - \frac{1}{2Q} \right) \right) \right],$$

where  $U_{C\text{free}}(0)$  and  $I_{L\text{free}}(0)$  are the voltage and current at the zero time point.

The voltages and currents during the flight of the  $i$ th bunch can be calculated by the following step-by-step algorithm.

1. Suppose that at a moment  $t = 0$ , corresponding to the zero phase of the generator current, the voltage is  $U_C(0)$  (see Fig. 1.49), and the current is  $I_L(0)$ . Then for the voltage and current at an instant  $\tau_i$  we obtain

$$U_C(\tau_i) = \text{Re} \left[ \left[ U_C(0) - U_{C\text{forced}}(0) + j\rho \left( I_L(0) - I_{L\text{forced}}(0) \right) \right] \times \right. \\ \left. \times \exp \left( \omega_c \tau_i \left( j - \frac{1}{2Q} \right) \right) \right] + U_{C\text{forced}}(\tau_i),$$

$$I_L(\tau_i) = \frac{1}{\rho} \text{Im} \left[ \left[ U_C(0) - U_{C\text{forced}}(0) + j\rho \left( I_L(0) - I_{L\text{forced}}(0) \right) \right] \times \right. \\ \left. \times \exp \left( \omega_c \tau_i \left( j - \frac{1}{2Q} \right) \right) \right] + I_{L\text{forced}}(\tau_i).$$

2. Let  $\tau_i$  be the moment of flight of a synchronous particle with a charge  $q_i$ . Then for the values the of voltage and current immediately after the flight we obtain

$$U_C(\tau_i + 0) = U_C(\tau_i - 0) - \frac{q_i}{C},$$

$$I_L(\tau_i + 0) = I_L(\tau_i - 0).$$

3. For the moment  $t = 3T$ , corresponding to the “zero” moment of the next bunch (see

Fig. 1.49), we obtain:

$$\begin{aligned}
 U_C(3T) &= \text{Re} \left[ \left[ U_C(\tau_i + 0) - U_{C\text{forced}}(\tau_i) + j\rho \left( I_L(\tau_i) - I_{L\text{forced}}(\tau_i) \right) \right] \times \right. \\
 &\quad \left. \times \exp \left( \omega_c(3T - \tau_i) \left( j - \frac{1}{2Q} \right) \right) \right] + U_{C\text{forced}}(0), \\
 I_L(3T) &= \frac{1}{\rho} \text{Im} \left[ \left[ U_C(\tau_i + 0) - U_{C\text{forced}}(\tau_i) + j\rho \left( I_L(\tau_i) - I_{L\text{forced}}(\tau_i) \right) \right] \times \right. \\
 &\quad \left. \times \exp \left( \omega_c(3T - \tau_i) \left( j - \frac{1}{2Q} \right) \right) \right] + I_{L\text{forced}}(0).
 \end{aligned}$$

4. For the bunch with the number  $i + 1$  we set that  $t = 0$ :

$$\begin{aligned}
 U_C(0) &= U_C(3T), \\
 I_L(0) &= I_L(3T)
 \end{aligned}$$

and repeat the calculations of steps 1 ÷ 3.

The calculations carried out in this way allow us to determine the values of the voltage  $U_C$  and current  $I_L$  during the entire period of revolution of the beam (for 1356 periods  $T$ ).

Modeling of the tuning of the RF system is reduced to selection of tuning of the cavity frequency and the value of the generator current to provide a stationary process of particle acceleration at a given RF voltage and energy loss per turn.

### 1.9.5 Operating modes of the RF system

Table 1.13 presents the results of modeling of the operating modes of the RF system of the storage ring for parameters corresponding to the data from Table 1.9 (overdesign). To obtain a stable regime when operating at an energy of 1 GeV, we reduce the beam current to 1.25 A, and only one accelerating cavity used (to reduce the characteristic impedance). Operation at a current of 2 A necessitates further reduction in the characteristic impedance (down to  $\sim 15$  Ohm) or application of feedback system.

The calculations for each regime were carried out in two stages.

1. First, we tuned the RF system for a beam with identical charges in the bunches.
2. Then (with these settings of the RF system) we calculated beams with a random variation of charges in the bunches within  $\pm 10\%$  (of the average value). This calculation was carried out twice, modeling regimes for both storage rings of the accelerator. Comparison of the synchronous phases obtained for these two calculations allows estimating the offset of the interaction point.

For each mode of operation, the displacement of the interaction point was estimated from the peak-to-peak levels (the difference between the maximum and minimum values) of three pairs of calculations (see Fig. 1.50).

### 1.9.6 Control System

Figure 1.51 presents the block diagram of the RF system in which each accelerating cavity is fed from a separate klystron.

Table 1.13. Modes of operation of RF system of one ring (with margin in parameters).

Energy	1.0	1.5	2.0	2.5	GeV
Beam current	1.25	2.0	2.0	2.0	A
Loss per turn	190	298	397	497	kV
Power to beam	238	596	794	994	kW
RF voltage	330	960	1500	1200	kV
Number of cavities	1	3	3	3	pc.
Voltage across one cavity	330	320	500	400	kV
Frequency detuning	-185	-349	-224	-273	kHz
RF loss in cavities	16	44	108	69	kW
Power into RF	254	640	902	1063	kW
Power into 1 cavity	254	213	301	354	kW
VSWR in feeder line	1.05	1.06	1.84	1.0	
Generator power	254	704	992	1169	kW
Generator power without frequency tuning	291	1200	1350	1470	kW
RF shift of interaction point (peak-to-peak)	1.79	1.78	0.92	1.5	mm

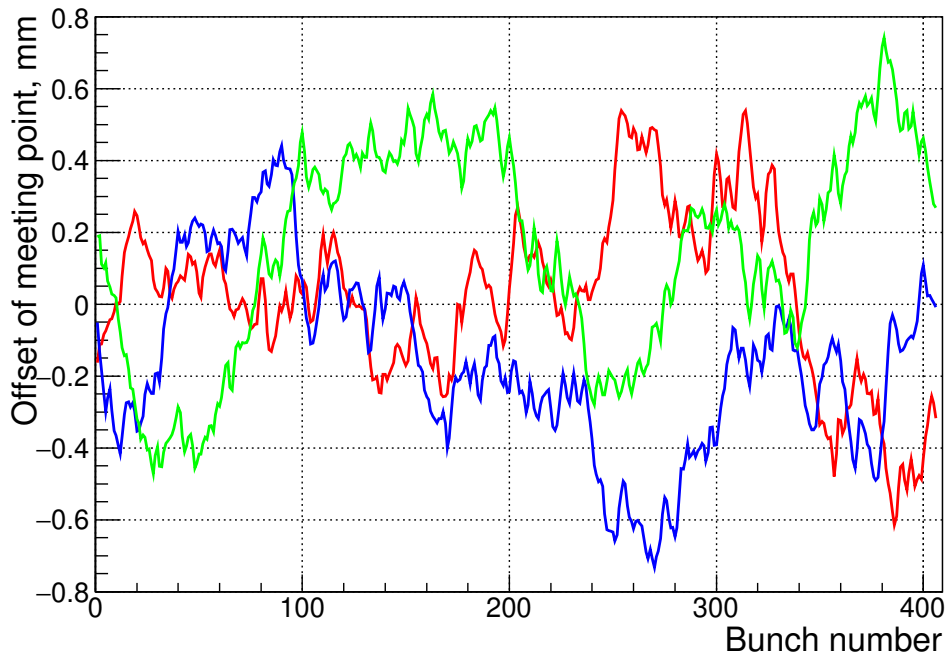


Figure 1.50. Offset of IP.

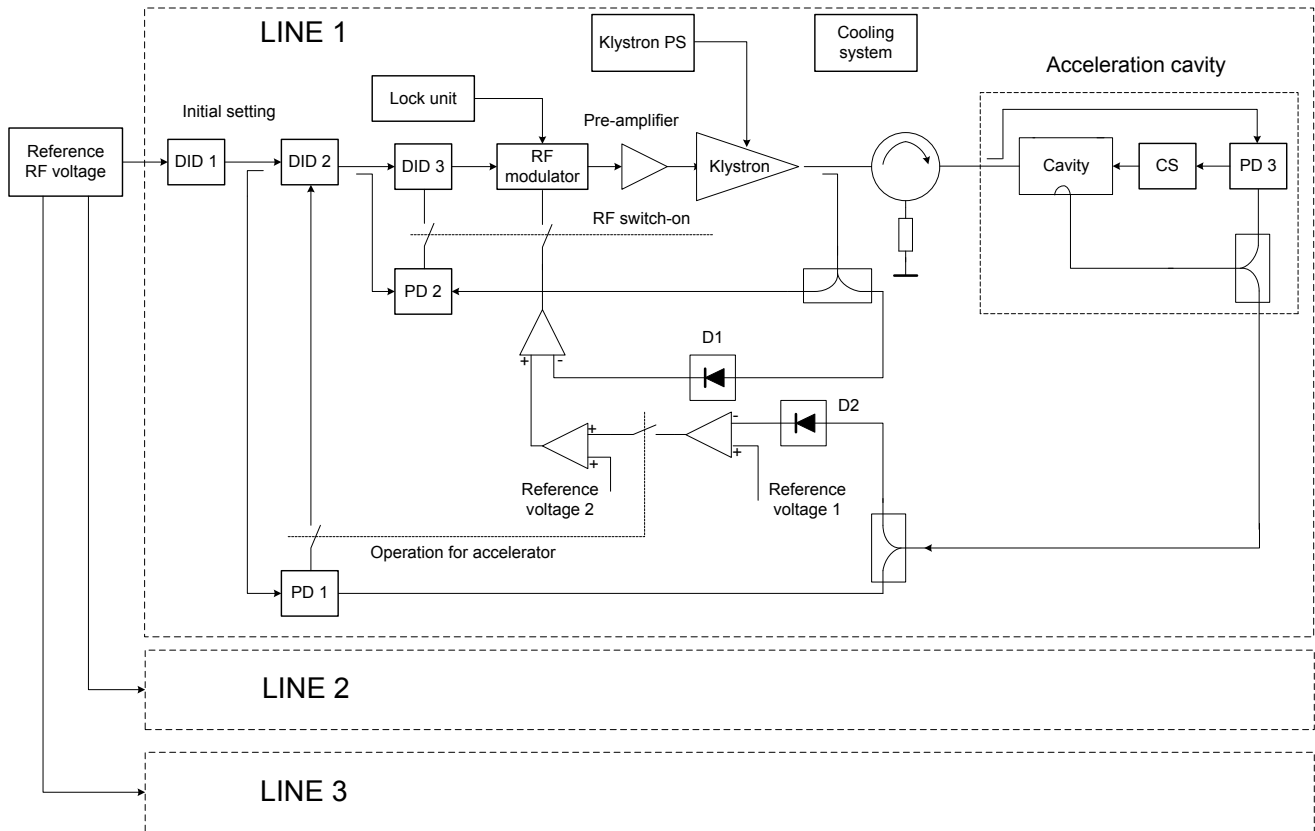


Figure 1.51. Block diagram of RF system of Super Charm–Tau factory.

### 1.9.7 Estimation of parameters of RF system with superconducting cavities

The estimates are based on the parameters of the superconducting cavities with suppression of HOMs at HER SuperKEKB [61, 64] (see Table 1.10).

According to these data, three superconducting cavities are enough for one ring of the Super Charm–Tau factory. The total characteristic impedance of the cavities will be 140 Ohm, which is 2.5 times less than the characteristic resistance of the RF system based on PEP-II cavities. Such a decrease in the characteristic impedance will result in a 2.5-fold decrease in the displacement of the interaction point and a decrease in the detuning of the cavities to 115 kHz (see Table 1.11), which would allow us to abandon the need to create a feedback system.

According to the estimates of the superconducting cavities of the project SuperPEP [65], one cavity with a 1 MW transmission power and an accelerating voltage of 1.5 MV will be enough for the RF system of one ring of the Super Charm–Tau factory.

However, currently there are no manufacturing technologies for superconducting cavities in Russia.

## 1.10 Vacuum system

### 1.10.1 Requirements to the vacuum

The operating vacuum in the electron ring is determined by the dynamics of storage of ionic core as a result of the ionization of the molecules of the residual gas. In p. 1.7.7 it was shown that for the rise time of fast ion instability to exceed the period of revolution of relativistic particles by tens of times, a vacuum at a level of  $10^{-9}$  Torr is required (in the nitrogen equivalent). In the positron ring, the pressure of the residual gases is determined by the requirement to the “vacuum” lifetime of the beam: not less than 3 hours. Inelastic scattering of electrons and positrons with energies of above 0.5 GeV on the molecules of the residual gas is the dominant process, which determines the “vacuum” lifetime of the beam:

- $\sigma_{in} = 4r_e^2\alpha Z_i^2 \left[ \frac{4}{3} \left( \ln \frac{E}{\Delta E} - \frac{5}{8} \right) \ln(183Z_i^{-1/3}) + \frac{1}{9} \left( \ln \frac{E}{\Delta E} - 1 \right) \right]$ , cross-section of inelastic scattering on the nuclei of the residual gas molecules,
- $\sigma_{ie} = 4r_e^2\alpha Z_i^2 \left[ \frac{4}{3} \left( \ln \frac{E}{\Delta E} - \frac{5}{8} \right) \ln(1440Z_i^{-2/3}) + \frac{1}{9} \left( \ln \frac{E}{\Delta E} - 1 \right) \right]$ , cross-section of inelastic scattering on the electrons of the residual gas,
- $\tau = \left[ \sum_i n_i c (\sigma_{in} + \sigma_{ie}) \right]^{-1}$ , beam lifetime,

where  $n_i = P_i/kT$  is the concentration of the residual gas of the  $i$ th component,  $P_i$  is the corresponding residual gas pressure,  $k$  is the Boltzmann constant,  $T$  is the gas temperature,  $c$  is the light velocity,  $\Delta E/E$  is the energy acceptance,  $Z_i$  is the nuclear charge of the  $i$ th component of the residual gas,  $\alpha$  is the fine structure constant, and  $r_e$  is the classical radius of electron.

The main components of residual gases in the presence of synchrotron radiation are molecular hydrogen (about 80%) and carbon monoxide (less than 20%). The remaining significant components (carbon dioxide and saturated hydrocarbons) are less than 5%. Calculations show that the pressure of the residual gases in the positron ring must not exceed  $3 \cdot 10^{-9}$  Torr for the “vacuum” beam lifetime to be three hours at least.

### 1.10.2 Concept of beam vacuum chamber

Table 1.14 presents the main parameters of the collider that determine the geometry and properties of the beam vacuum chamber.

To ensure the maximum smoothness of the beam vacuum chamber and to simplify and reduce the cost of the evacuation system, it is proposed to use the TiZrV getter coating (the technology has been implemented at BINP [66]). Such a solution obviously provides the required level of rarefaction in the presence of intense SR since it transforms the inner surface of the vacuum chamber from a source of gas loading into a distributed vacuum pump [67, 68, 69]. In addition, certain regimes of the TiZrV system getter deposition result in films with a low quantum yield of secondary electrons [70, 71], which makes it possible to reduce the density of electron clouds in the positron ring. To activate the getter, it is necessary to warm up the chamber (up to 220 °C).

Calculation of the maximum possible internal vertical aperture of the chamber in a dipole magnet: the dipole distance gap – 2 mm (doubled technical section) – 2 mm (double clearance for thermal insulation) –  $2h$  (double wall thickness of the vacuum chamber). Thus, with a wall thickness of 2 mm, the inner diameter of the vacuum chamber is 68 mm. It is assumed that the

Table 1.14. Parameters of vacuum chamber of Super Charm–Tau factory.

Parameter	Value
Beam current	2 A
Total SR flux	$\sim 4.5 \cdot 10^{21} \text{ s}^{-1}$
Average SR flux per unit length	$\sim 5.5 \cdot 10^{18} \text{ s}^{-1} \text{ m}^{-1}$
Total SR power	$\sim 900 \text{ kW}$
Maximum SR power of dipole magnet	6.2 kW
Maximum SR power of damping wiggler	109 kW
Bunch repetition period	6 ns
Number of bunches	406
Gap between poles of dipoles*	76 mm
Diameter of inscribed circle of magnetic lenses*	76 mm
Minimum distance between poles of sextupoles**	17 mm

\* Minimum technological gap to the poles is 2 mm.

\*\* Minimum technological gap to the poles is 1 mm.

vacuum chambers will be made of an aluminum alloy (for example, A6063) by extrusion, which allows designing the vacuum chamber with channels for water cooling and installation of heaters.

The most significant potential problem of the positron ring is the formation of dense electron clouds. According to many theoretical estimates and experimental results [72, 73], the threshold density of electron cloud at which coherent beam instabilities arise is as low as  $5 \cdot 10^5 \text{ cm}^{-3}$ . The primary source of low-energy electrons in the beam propagation region are photo electrons resulting from the action of direct, re-reflected, and re-emitted photons of SR on the walls of the vacuum chamber. The simplest and most effective way to suppress the photo electrons in the straight drift section is application of a longitudinal magnetic field of  $20 \div 30 \text{ G}$ , which deflects the electrons back to the walls of the vacuum chamber. In the magnet elements, the photo electrons from the direct SR are also deflected back to the chamber wall. Therefore, the accumulation of electrons in the beam propagation region is because of electrons (moving along the lines of force of the magnetic field) resulting from the action of the re-reflected and scattered SR. For estimates, in a simple circular vacuum chamber the fraction of re-reflected and scattered photons is taken equal to 70% of the direct SR flux [74, 75]. In the first approximation, the vacuum chamber is uniformly illuminated by this photon flux. The averaged quantum yield of photo electrons at photon energies of above 20 eV is  $2 \div 5\%$  [74, 75]. On the average, in a chamber with a diameter of over 40 mm, a time between bunches of 6 ns, and a number of positrons in a bunch of  $7 \cdot 10^{10}$ , the photo electrons have time to accelerate in the field of two bunches (they get two “bumps”) before they reach the wall of the vacuum chamber. Thus, the average lifetime of the photo electrons is 12 ns. Respectively, the average density of the photo electrons can be estimated as

$$n_e = \frac{2\tau \bar{\Gamma}_0 R Y}{\pi r^2} \approx 7 \cdot 10^5 \text{ cm}^{-3},$$

where  $\bar{\Gamma}_0 = 5.5 \cdot 10^{18} \text{ m}^{-1} \text{ s}^{-1}$  is the average photon flux per unit length of the beam chamber,  $\tau = 6 \text{ ns}$  is the period of bunch repetition,  $r = 34 \text{ mm}$  is the radius of the beam vacuum chamber,  $R = 0.7$  is the fraction of the re-reflected and scattered photons, and  $Y = 0.05$  is the quantum yield of photo-electrons.

The obtained estimate of the photo electron density already exceeds the threshold of beam

instability. Therefore, the geometry of the vacuum chamber must be arranged so that the surface interacting with the direct SR flux is beyond the beam propagation region. Possible realizations of the beam vacuum chamber by the method of aluminum alloy extrusion are presented in Figs. 1.52-1.54. The extrusion technology enables simultaneous production of parallel channels for cooling (curly channels) and heating of the chamber (channels with a diameter of 3 mm).

Free electrons are accelerated in the field of the bunches to energies exceeding 100 eV. The interaction of the accelerated (primary) electrons with the walls of the vacuum chamber leads to formation of secondary electrons, which after acceleration in the field of subsequent bunches in turn act as primary electrons. If, on average, the number of the secondary electrons in the process of the secondary electron emission exceeds the number of the primary electrons, this process leads to an avalanche-like increase in the electron density (this phenomenon was called the “multipactor”) in the beam propagation region. Note that the phenomenon of the secondary electron emission can lead to a significant increase in the density of the electron cloud in the beam propagation region even if the average quantum yield of the secondary electrons is less than the unity. Assuming that the average number of the secondary electrons does not exceed the number of the primary electrons, the total density of the electron cloud can be estimated from the following expression:

$$n_e = \frac{Y \cdot s \cdot \bar{\Gamma}_0 \cdot \tau}{(1 - \delta_{\text{eff}}) \cdot \pi r^2},$$

where  $s$  is the fraction of the photon flux interacting with the walls of the vacuum chamber in the beam propagation region,  $\delta_{\text{eff}} = \int_0^{\infty} \delta(E_e) n_e(E_e) dE_e$  is the effective (average) secondary electron emission coefficient,  $\delta(E_e)$  is the quantum yield of secondary electrons as a function of the energy of the primary electrons (the maximum value of  $\delta(E_e)$ , which as a rule exceeds 1, and corresponds to the energy of the primary electrons in the range of 200 ÷ 400 eV),  $n_e(E_e)$  is the energy distribution of the primary electrons, which is most difficult to estimate because of the shielding effect of the space charge of the electron cloud itself on the interaction with the beam. The estimates show that if a certain functional coating or specialized treatment of the vacuum chamber allows reducing  $\delta_{\text{eff}}$  to a value of 0.95 or less, then the requirement to  $s$  is 0.05 or less, which is quite feasible.

Currently, there are three options for processing the inner surface of the chamber that significantly decrease the quantum yield of secondary electrons.

1. TiZrV system getter coating. As already noted, this is the most promising option since it provides distributed pumping of the beam vacuum chamber. It has the following disadvantages: the vacuum chamber is to be warmed up to 220 °C, and a technological study is required for obtaining  $\delta_{\text{max}} < 1$ , which has not yet been implemented in practice.
2. Graphene-like carbon coating [76]. Advantage: no heating of the vacuum chamber is required. Potential disadvantages: significant gas emission because of the SR. A distributed pumping system is required.
3. Laser surface treatment [77]. Advantages: no heating of the vacuum chamber is required. Potential disadvantages: significant gas emission because of the SR. A distributed pumping system is required.

All the three options of processing the inner surface of the beam vacuum chamber require careful study in terms of reliability in operation in the presence of intense SR and requirements to the radio-frequency impedance of the beam vacuum chamber.

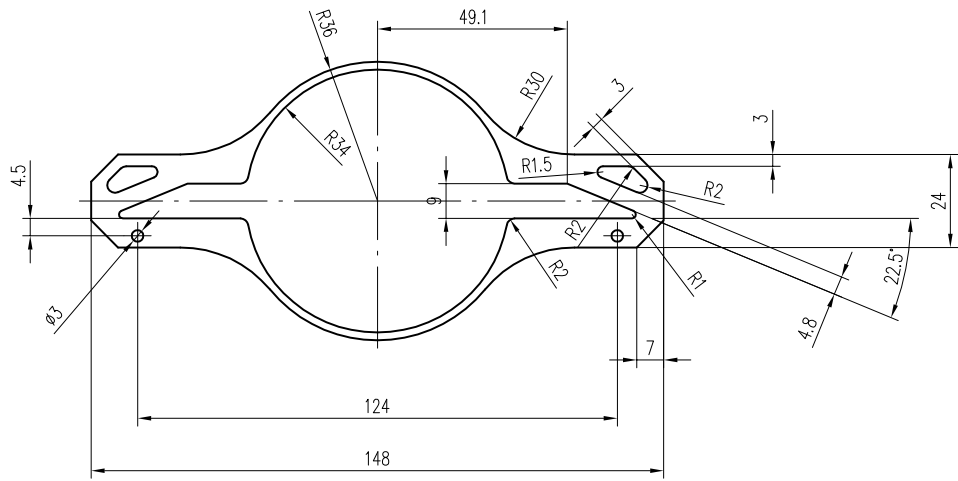


Figure 1.52. Cross section of regular vacuum chamber.

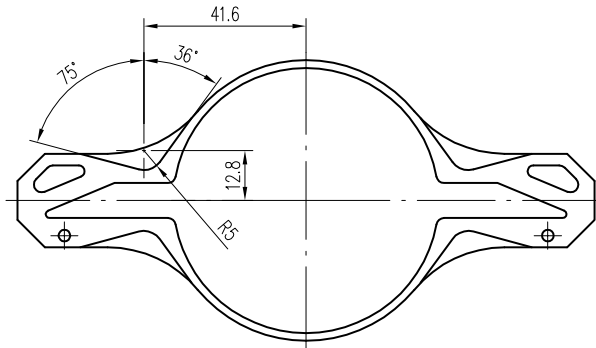


Figure 1.53. Cross section of vacuum chamber in sextupole lenses.

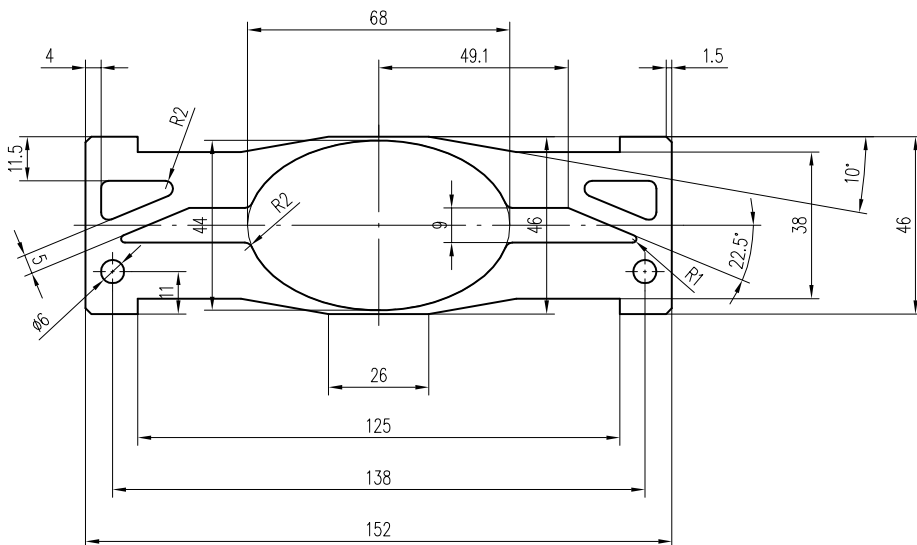


Figure 1.54. Cross section of vacuum chamber in wigglers.

## 1.11 Magnet system

The magnet lattice of the Super Charm–Tau factory consists of two identical storage rings: for positrons<sup>1</sup> and for electrons. The main part of the magnet lattice of each of the rings consists of normally conducting electromagnets. The superconducting devices (final focus, damping wigglers, solenoids of Siberian snakes) are discussed in p. 1.13.

Table 1.15 presents the types of magnetic elements for one ring with the following notation:

$$B_n = \frac{\partial^n B_y}{\partial x^n}(x = 0, y = 0, z),$$

where  $x$  and  $y$  are the horizontal and vertical directions, respectively. That is,  $B_0$  is the dipole field,  $B_1$  is the field gradient,  $B_2$  is the sextupole gradient, and so on.

Table 1.15. Types of magnetic elements of one ring of Super Charm–Tau factory.

N <sup>o</sup>	Magnet type	Length, cm	Apert., mm	Not.	Min	Max	Unit	Q-ty
1	Dipole	34	150 × 76	$B_0$	0.0	10.5	kG	160
2	Dipole	100	150 × 76	$B_0$	1.0	6.0	kG	18
	Total							178
1	Quadrupole	25	∅76	$B_1$	0.2	1.2	kG/cm	41
2	Quadrupole	30	∅76	$B_1$	0.7	2.2	kG/cm	130
3	Quadrupole	40	∅76	$B_1$	0.0	2.6	kG/cm	60
4	Quadrupole	50	∅76	$B_1$	0.0	2.6	kG/cm	97
5	Quadrupole	65	∅76	$B_1$	0.0	2.6	kG/cm	84
	Total							412
1	Sextupole	20	∅76	$B_2$	0.0	1.3	kG/cm <sup>2</sup>	14
2	Sextupole	30	∅76	$B_2$	0.0	1.3	kG/cm <sup>2</sup>	90
3	Sextupole	40	∅76	$B_2$	0.0	1.3	kG/cm <sup>2</sup>	14
	Total							118

The material of the cores of all magnetic elements is stamped sheet electrotechnical steel of grade 21848; the thickness is 1 mm; the filling factor is 98%.

The vacuum chamber cross section has a complex shape, with a ∅68 mm beam area. The thickness of the walls in the minimum size (vertically) is 2 mm. The technical gap to the poles is 2 mm. The vertical aperture of the dipoles (pole gap) is 76 mm; the inscribed diameter in the quadrupoles and sextupoles is ∅76 mm.

The magnetic calculations are performed by the program MERMAID, created by A. N. Dubrovin at BINP SB RAS.

### 1.11.1 Dipole magnets

All the dipole magnets have the same yoke cross section. Field variation occurs due to the current and number of turns in the excitation winding. Since the lengths of the magnets are small in comparison with the radius of curvature of the trajectory of the beam, the magnets are straight (rectangular bending). The vacuum chamber in the dipole magnet aperture has a regular cross section (see p. 1.10, Fig. 1.52). The cross section of 1/4 magnet is shown in Fig. 1.55.

<sup>1</sup>In the positron ring there are no superconducting solenoids of Siberian snakes.

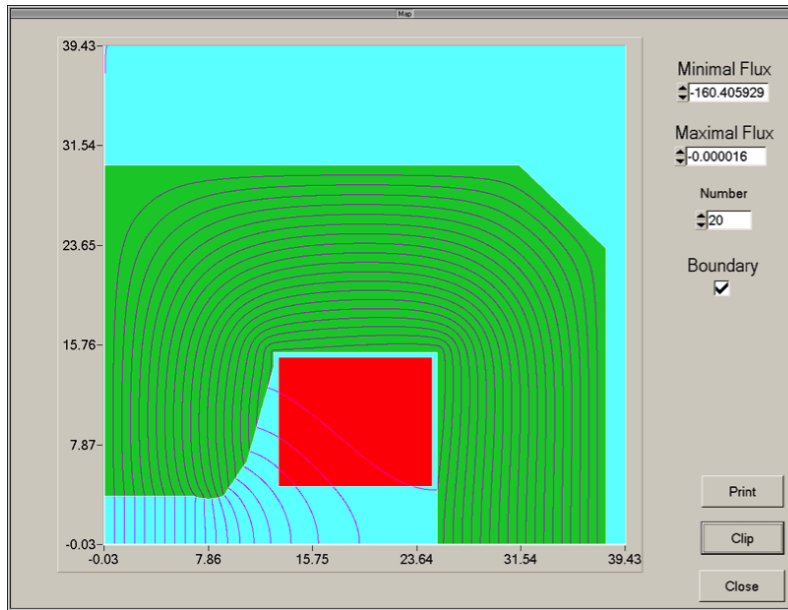
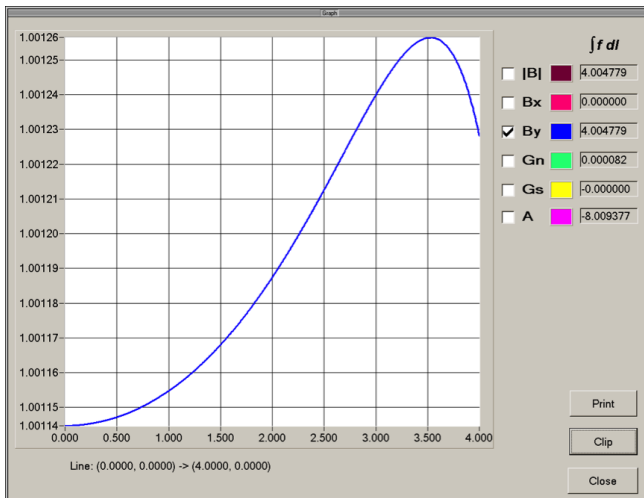


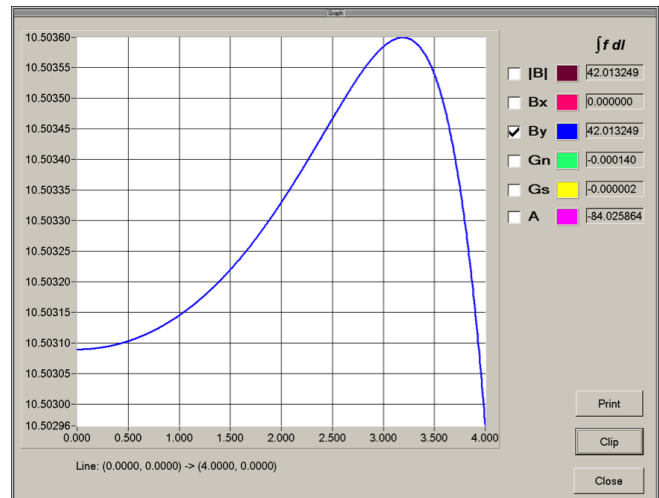
Figure 1.55. Cross section of 1/4 dipole magnet.

The excitation winding consists of two coils: top and bottom ones. The coil is made of a copper hollow conductor with a  $23 \times 15 \times \varnothing 6.55$  mm cross-section. Each coil of the 1st and 2nd type dipoles contains 4 layers of 7 turns, in total 28 turns, and each coil of the type 3 dipoles contains 2 layers of 7 turns, in total 14 turns.

Figure 1.56 shows the distribution in the axis  $x$  ( $y = 0$ ) at small and large field levels. The distribution is similar at intermediate field values. The field quality  $\Delta B/B$  is better than  $\pm 1 \cdot 10^{-4}$  in the area within  $\pm 30$  mm. The shape of the core meets the requirements to the field quality.



(a) 1 kG



(b) 10.5 kG

Figure 1.56. Field distribution in dipole magnet.

Table 1.16 presents the parameters of the dipole magnets.

All types of the dipole magnets are provided with a correction of  $\pm 1\%$ .  $2 \times 2$  mm PSD type tie, current of up to 6 A, 45 turns per coil, two coils per magnet.

The coils are cooled by water. At a pressure difference of 4 atm, the heating of the coils of all

Table 1.16. Parameters of dipole magnets.

Type	Q-ty	$L$ , cm	$B_0$ , kG	$I$ , A	$U$ , V	$P$ , kW	Dimensions, m	Weight, t
1	160	34	10.5	1150	6.8	7.8	$0.6 \times 0.76 \times 0.62$	1.2
2	18	100	6.0	1300	6.8	8.8	$0.6 \times 0.76 \times 1.28$	3.0

Notation:  $L$  is the magnetic length,  $B_0$  is the maximum field,  $I$  is the current in the coil,  $U$  is the voltage drop on one magnet,  $P$  is the power, dimensions: height $\times$ width $\times$ length.

types is less than 16 °C. The total thermal power released on the dipole magnets of the two rings is 2475 kW.

### 1.11.2 Quadrupole lenses

All the quadrupole lenses have an inscribed radius of the core  $\varnothing 76$  mm. In the lens aperture the vacuum chamber has a regular cross section (see p. 1.10, Fig. 1.52). Figure 1.57 presents 1/4 of the cross section of the quadrupole lens.

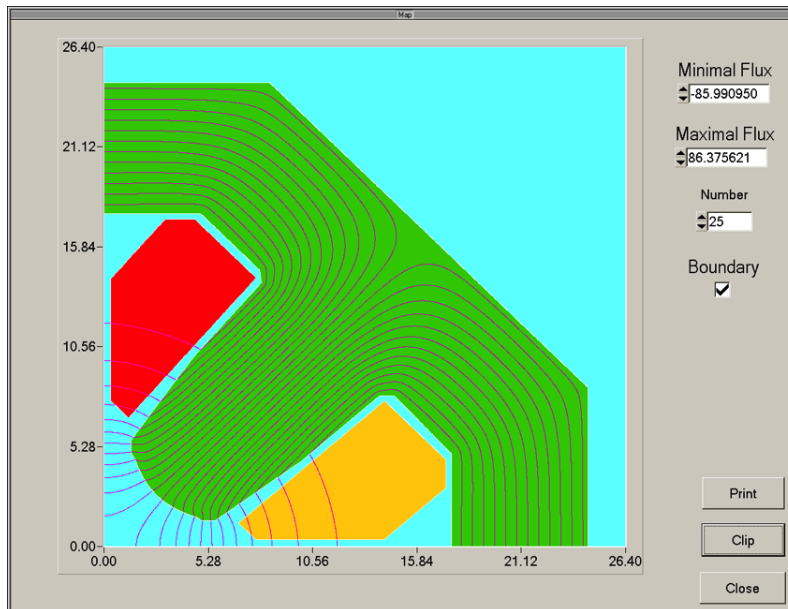


Figure 1.57. Cross section of 1/4 quadrupole lens.

Quadrupoles of the types 1 and 2 have an additional gradient correction. The other types of quadrupoles are fed individually and do not have any correction. In all quadrupoles, the coils are wound of a hollow copper conductor with a  $6.35 \times 6.35 \times \varnothing 3.15$  mm cross section. The cross-section is chosen such that the voltage of the power supply on the families is less than 1000 V. The number of turns in quadrupoles with different gradients is different.

Figure 1.58 shows the field distribution along the axis  $x$  ( $y = 0$ ) for different gradient levels. The field quality  $\Delta B_1/B_1$  is better than  $\pm 1 \cdot 10^{-3}$  in the area within  $\pm 30$  mm. The shape of the core meets the requirements to the field quality.

Table 1.17 lists the parameters of the quadrupole lenses.

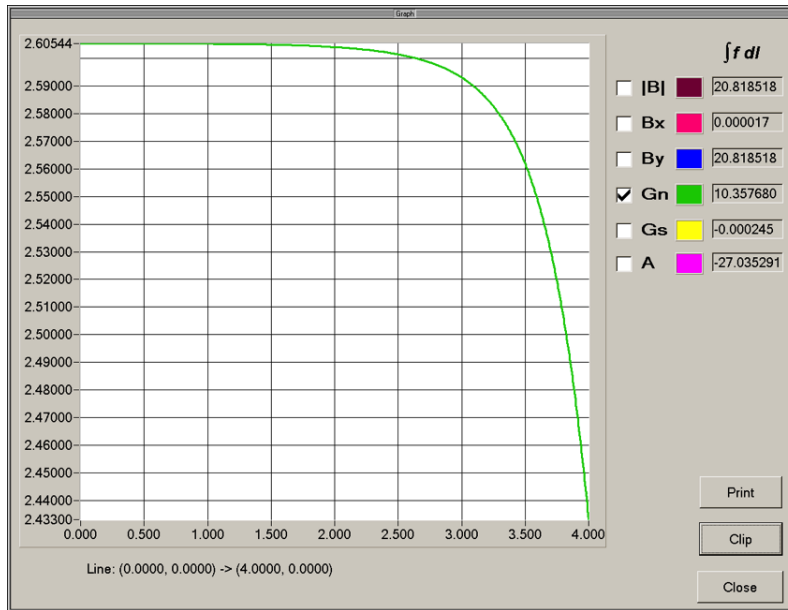


Figure 1.58. Field distribution in quadrupole lens.

Table 1.17. Parameters of quadrupole lenses.

Type	Q-ty	$L$ , cm	$B_1$ , kG/cm	$I$ , A	$U$ , A	$P$ , kW	Dimensions, m	Weight, t
1	41	25	1.2	113	12	1.4	$0.7 \times 0.7 \times 0.40$	0.32
2	130	30	2.2	120	27	3.2	$0.7 \times 0.7 \times 0.50$	0.43
3	60	40	2.6	113	48	6.4	$0.7 \times 0.7 \times 0.60$	0.61
4	97	50	2.6	133	60	8.0	$0.7 \times 0.7 \times 0.70$	0.76
5	84	65	2.6	133	77	10.2	$0.7 \times 0.7 \times 0.85$	0.97

Notation:  $L$  is the magnetic length,  $B_1$  is the maximum gradient,  $I$  is the current in the coil,  $U$  is the voltage drop on one magnet,  $P$  is the power, dimensions: height  $\times$  width  $\times$  length.

### 1.11.3 Sextupole lenses

All the sextupole lenses have the same radius of the inscribed circle,  $\varnothing 76$  mm. The vacuum chamber in the aperture of the sextupole lens has an irregular shape (see p. 1.10, Fig. 1.53). Figure 1.59 shows a 1/4 cross section of sextupole.

All types of the sextupoles are fed individually and have no correction coils. The coil is made of a copper hollow conductor with a  $6.35 \times 6.35 \times \varnothing 3.15$  mm cross-section.

Creating a sextupole gradient of more than  $1.4 \text{ kG/cm}^2$  is problematic. The maximum saturation occurs in the neck of the core in a distance of  $7 \div 8$  cm from the midpoint. Varying the shape of the pole, the closing yoke, or the coils does not change the situation.

Figure 1.60 shows the distribution of the field and the gradient  $B_2$  in the area within  $\pm 27.5$  mm along the radius at  $1.4 \text{ kG/cm}$ .

Table 1.18 lists parameters of the sextupole lenses.

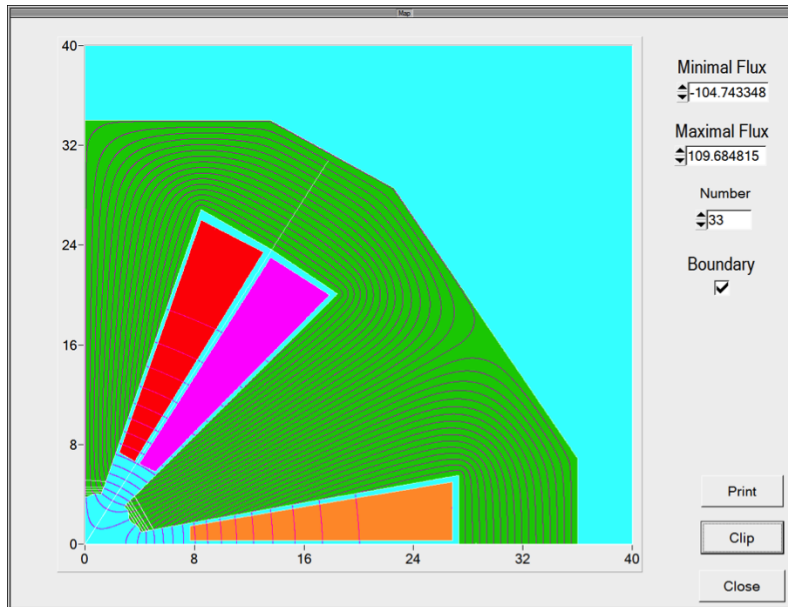


Figure 1.59. Cross section of 1/4 sextupole lens.

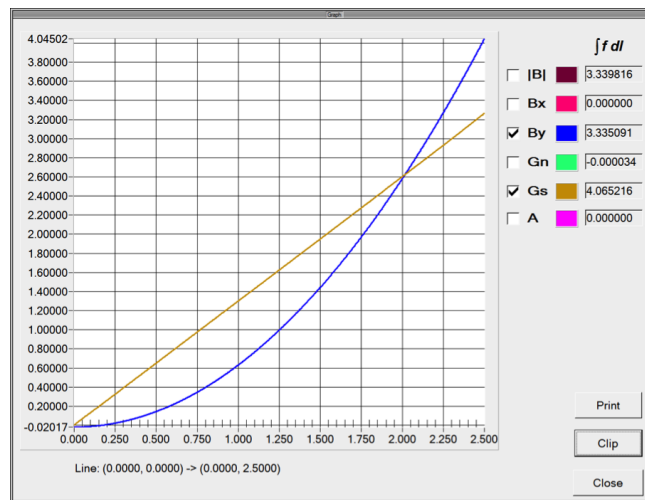


Figure 1.60. Field and gradient of sextupole lens.

Table 1.18. Parameters of sextupole lenses.

Type	Q-ty	$L$ , cm	$B_2$ , kG/cm <sup>2</sup>	$I$ , A	$U$ , A	$P$ , kW	Dimensions, m	Weight, t
1	14	20	1.3	108	40	4.3	$0.7 \times 0.76 \times 0.33$	0.64
2	90	30	1.3	108	48	5.2	$0.7 \times 0.76 \times 0.43$	0.90
3	14	40	1.3	108	57	6.2	$0.7 \times 0.76 \times 0.53$	1.17

Notation:  $L$  is the magnetic length,  $B_1$  is the maximum sextupole gradient,  $I$  is the current in the coil,  $U$  is the voltage drop on one magnet,  $P$  is the power, dimensions: height×width×length.

## 1.12 Power Supply System

The magnetic elements of the Super Charm–Tau factory (see Table 1.15) are fed by power supplies (PSs): some of the dipole and quadrupole magnets are fed in series from one PS and make groups or families of magnets; the rest, as well as all the sextupole lenses, are fed individually. The magnets powered in families have low-current correction coils, which are fed individually. The parameters of PSs are listed in Table 1.19.

Table 1.19. Currents and voltages of magnetic elements of collider.

Magnet	PS	$N_{\text{PS}}$	$N_{\text{M}}$	$I$ , A	$U$ , V	$P$ , kW	$\Delta I/I$
Type 1 dipole	DPS1	1	144	1060	900	954	1 ppm
Type 1 dipole	DPS2	4	4	1140	27	31	1 ppm
Type 2 dipole	DPS2	18	1	1300	7	9	1 ppm
Type 1 quadrupole	QSP2	1	18	113	216	24	100 ppm
Type 1 quadrupole	QSP2	1	15	113	180	20	100 ppm
Type 1 quadrupole	QSP3	4	2	113	24	3	100 ppm
Type 2 quadrupole	QSP1	2	35	120	930	112	10 ppm
Type 2 quadrupole	QSP1	2	30	120	800	96	10 ppm
Type 3 quadrupole	QSP2	60	1	133	48	6	100 ppm
Type 4 quadrupole	QSP2	97	1	133	60	8	100 ppm
Type 1 quadrupole	QSP2	84	1	133	77	10	100 ppm
Type 1 sextupole	SPS1	14	1	108	40	4.3	100 ppm
Type 2 sextupole	SPS1	90	1	108	48	5.2	100 ppm
Type 3 sextupole	SPS1	14	1	108	57	6.2	100 ppm

Notation: PS is power supply name,  $N_{\text{PS}}$  is number of PSs,  $N_{\text{M}}$  is number of magnets connected to one PS,  $I$  is output current of PS,  $U$  is output voltage of PS,  $\Delta I/I$  is instability of output current of PS,  $P$  is output power of PS.

### 1.12.1 Power supplies for dipole magnets

As follows from Table 1.19, the dipole magnets of the Super Charm–Tau factory are fed by 5 power supplies of two types. A schematic structure of the PSs is shown in Fig. 1.61. Both types of the PSs are made based on a dual step-down transformer with delta-wye connection, a 12-pulse thyristor rectifier, and an active ripple suppression filter. The principle of the design of the system for the output current stabilization using the active pulsation suppression filter is shown in Fig. 1.62.

The difference in the set and measured output current goes to the error amplifier. Then its output signal is used in two control loops: in the first circuit the system controls the output voltage of the thyristor rectifier; in the second circuit the signal is fed to the high-pass filter with a 1 Hz fringe area and then to the active filter amplifier. Such a scheme allows suppressing the 600 Hz rectified voltage ripples present at the output of the passive 12-pulse thyristor rectifier filter and thus provides the required level of ripple and instability of the output current of  $10^{-6}$ . In general, the schemes of the source of the two types are similar, but because of the differences in the power

and the output voltage, in the DPS1 source the input step-down transformer is supplied with three-phase 380 V and in the DPS2 source with 10 kV.

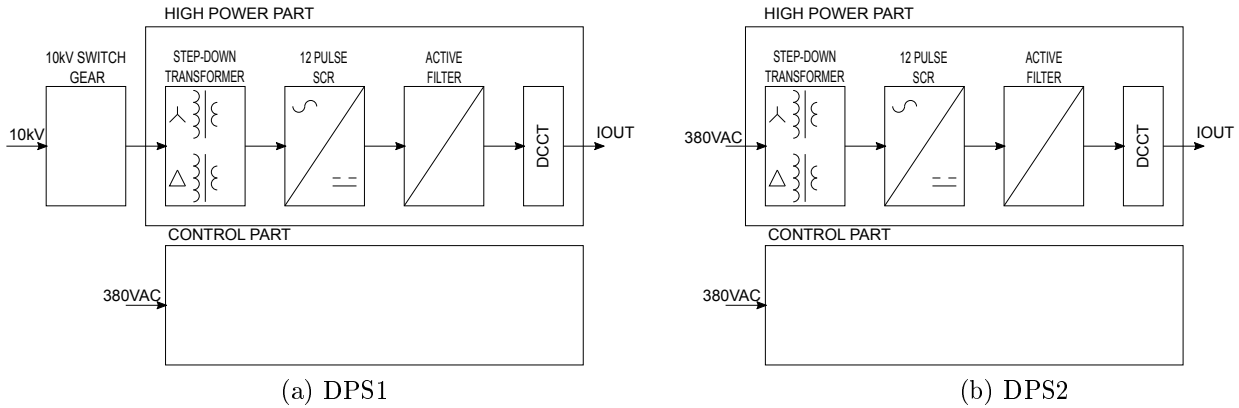


Figure 1.61. Block diagram of power supplies of dipole magnets.

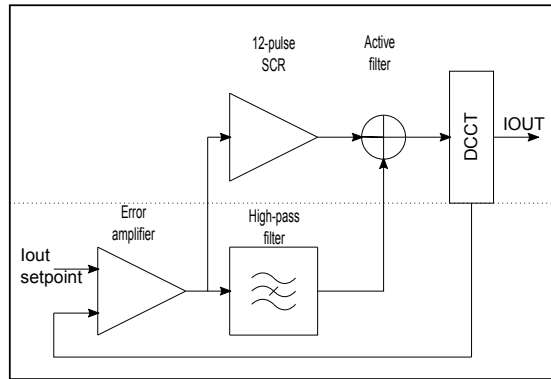


Figure 1.62. Block diagram of current stabilization system with active filter.

### 1.12.2 Power supplies for quadrupole lenses

There are three types of power sources to feed the quadrupole lenses (see Table 1.19). The block diagram of the QPS1 quadrupole sources is shown in Fig. 1.63, a). The source consists of the step-up transformer powered from three-phase 380 V mains, the rectifier, the voltage regulator made by the scheme of asymmetric (skew) bridge, the output filter, and the non-contact precision output current transducer.

QPS2 (Fig. 1.63, b)) consists of the step-down transformer and the rectifier, which are common for 9 sources and individual for each voltage regulator source, the asymmetric (skew) bridge, the output filter and the non-contact precision output current transducer. QPS3 (Fig. 1.63, c)) consists of the AC-DC converter with an output voltage of 12 V and a power of 1.5 kW (such converters are widely available in the market and are manufactured, for example, by MeanWell), the voltage regulator designed as an asymmetric (skew) bridge, the output filter, and the non-contact precision output current transducer.

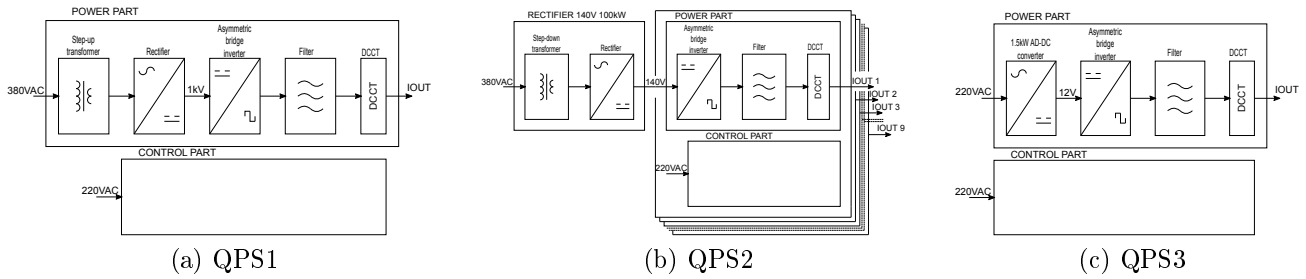


Figure 1.63. Block diagrams of power supplies of quadrupole lenses.

### 1.12.3 Power supplies of sextupole lenses

Each sextupole lens is powered by its own power source. One SPS1 source is used, the parameters of which are similar to the QPS2 source. For this reason, it is similarly designed, with a step-down transformer common for 9 sources and a rectifier (see Fig. 1.64).

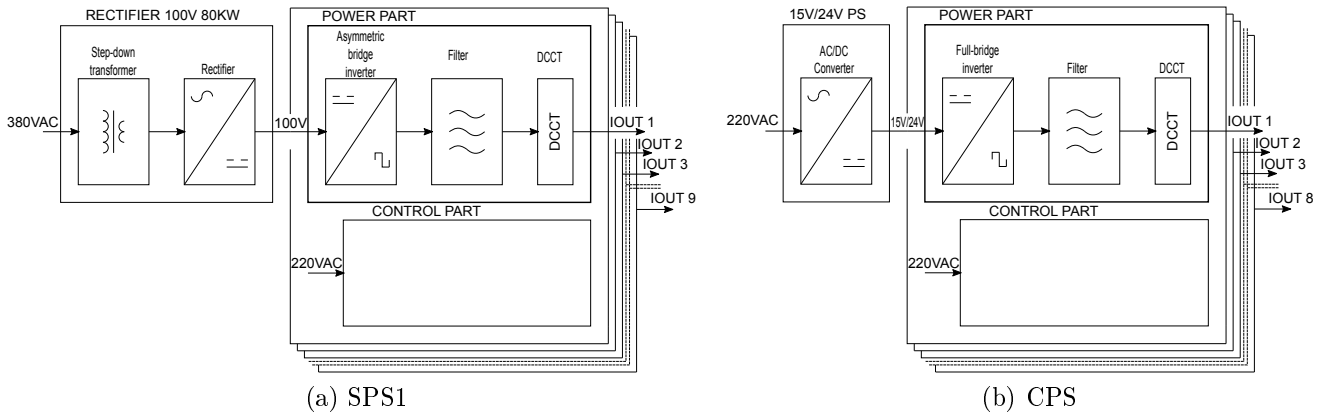


Figure 1.64. Block diagram of power supplies of sextupole lenses and correction.

### 1.12.4 Power supplies of correctors

Dipole and quadrupole magnets connected to the same power source have correction coils, which are fed individually. The block diagram of the sources is shown in Fig. 1.64. An AC-DC converter with an output voltage of 15 V (DCPS1) or 24 V (DCPS2, QCPS1) with a power of 1.5 kW/2 kW, common for 8 sources, is used. The sources themselves, consisting of the bridge four-quadrant voltage regulator, output filter, and non-contact current transducer, are fed from the AC-DC converter.

## 1.13 Superconducting magnets

### 1.13.1 Final focus

The final focus system is to focus beams at the interaction point (see p. 1.3.1). It consists of two units of superconducting magnets in one cryostat. They are placed on the opposite sides of the IP

inside the main detector. Each cryostat includes a compensating solenoid, two shielding solenoids, two quadrupole lenses of the final focus, a set of corrective windings, and other equipment. The section near the interaction point has a vacuum chamber common to both rings; the chamber diverges into two chambers inside each of the cryostats.

### Cryostat

The cryostat covers a solid angle of  $15^\circ$ . A three-layer cryostat will be used, consisting of the two copper shields with temperatures of 20 K (the first) and of 70 K (the second) and the outer casing made of stainless steel, of ambient temperature. Between the shields there is a vacuum isolating gap. It is 1 mm thick in the vacuum chamber area, 8 mm thick in the area of the vertex detector, and 20 mm thick from the opposite side. For cooling of the shields it is supposed to use two cryo-coolers placed on the cryostat end far from the IP. The superconducting magnets will be cooled by means of helium channels laid in the winding.

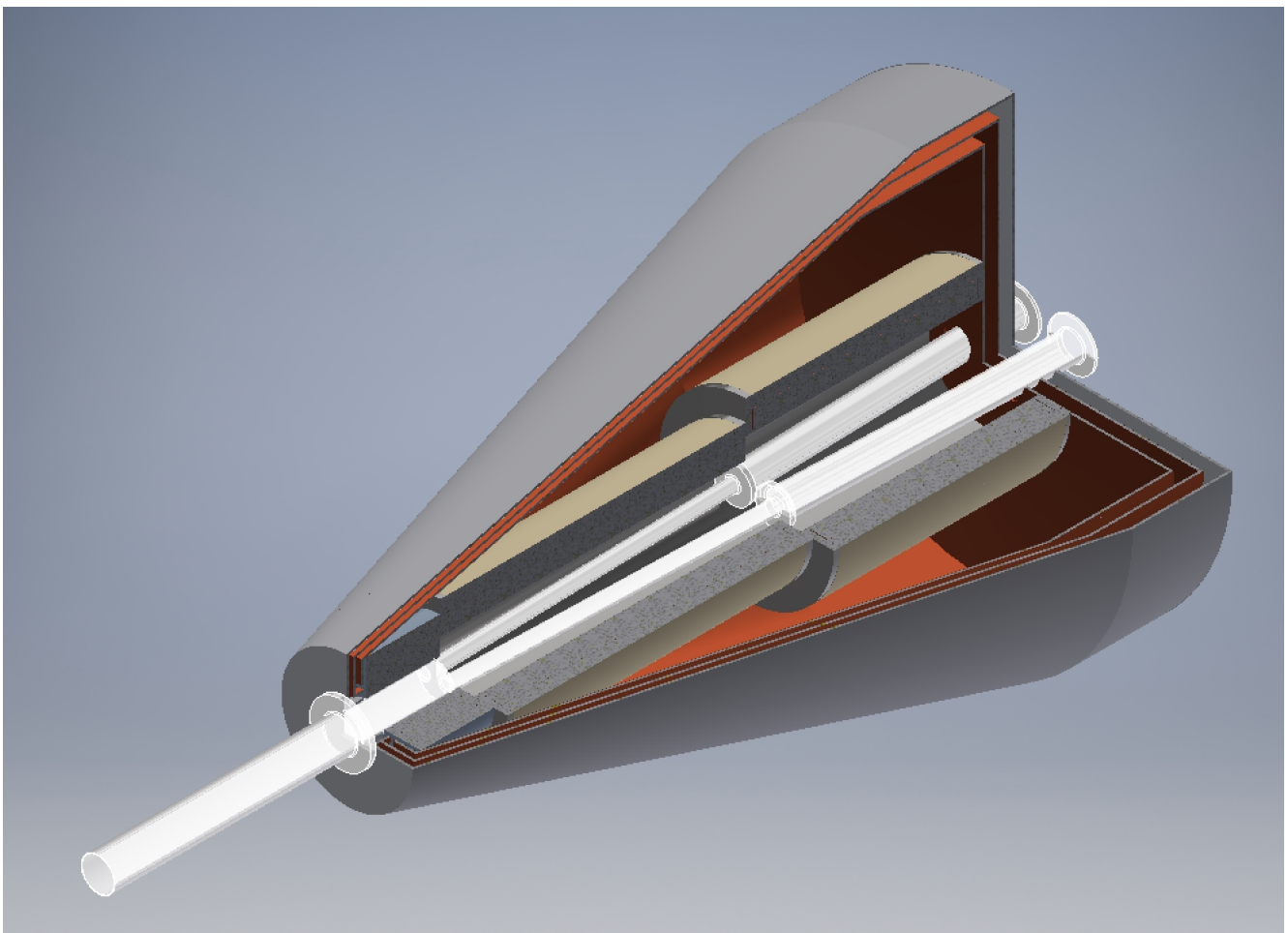


Figure 1.65. General view of cryostat.

### Vacuum chamber

The vacuum chamber of the final focus (the vertex detector section) is a beryllium cylinder with an outer diameter of about 55 mm and a length of 800 mm. Next is the vacuum tube of the compensating solenoid, of 170 mm in length and 55 mm in outer diameter. It is placed in a

cryostat. On one side, the chamber has a cylinder with a diameter of 55 mm, a thickness of at least 1 mm, and a length of 170 mm. Then the chamber branches into two chambers of 22 mm in diameter with a wall thickness of 1 mm and a length of 520 mm. The chamber ends with a flange connection. The next section has a length of about 470 mm, an outer diameter of 44 mm, and a thickness of 2 mm.

The vacuum chamber should be “warm”, but the transition to the superconducting state should be as compact as possible, that is, one nitrogen shield of a temperature of 20 K and vacuum gap of 1 mm for the first defocusing lens.

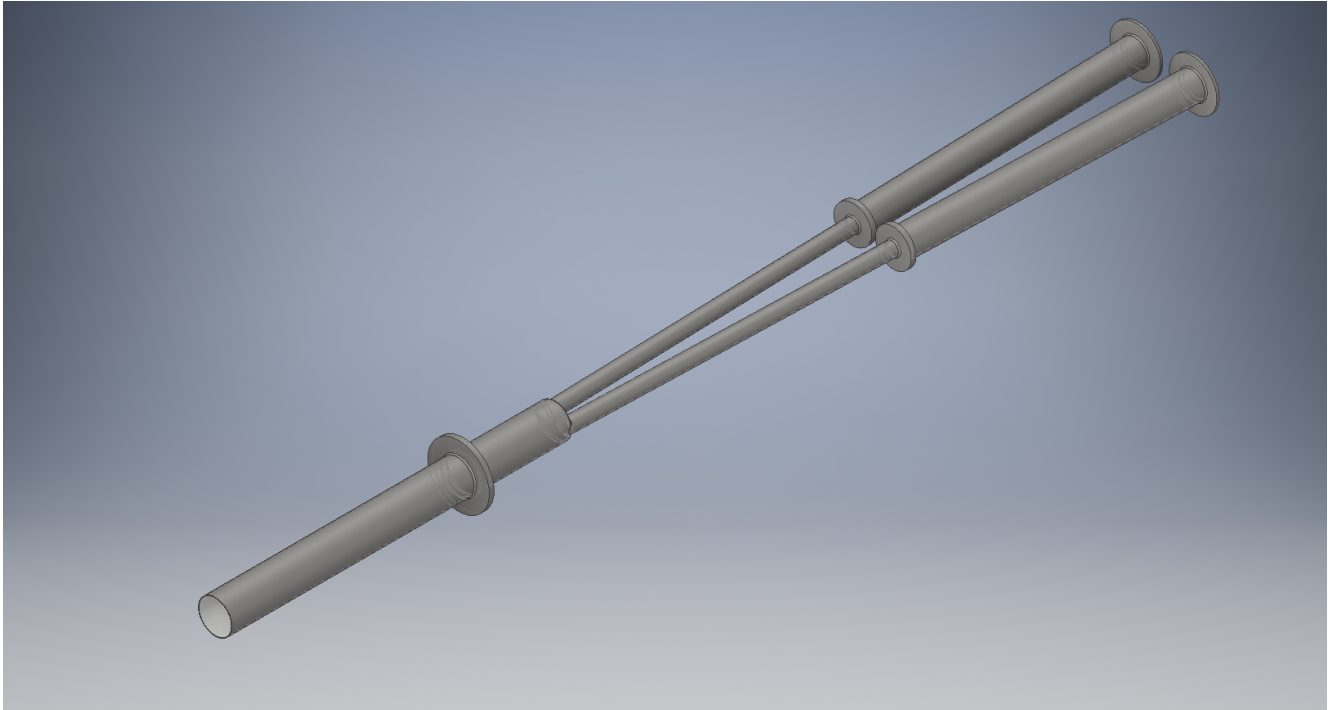


Figure 1.66. Vacuum chamber of crossing section.

### Compensating solenoid

The magnetic field strength in the compensating solenoid must be 5.5 T at least. The length of the solenoid is 100 mm. It begins in 450 mm from the IP. The field of the main solenoid of the detector is 1 T. From simple estimates it follows that to compensate for the effect of the main detector of the solenoid on the beam, the maximum field of the compensating solenoid must be  $\sim 5.8$  T, because of the design of the solenoid itself and the influence of shielding solenoid. The coils of the solenoid will be wound of NbTi cable with a diameter of 0.92 mm. The operating current is 600 A.

### Shielding solenoids

In addition to the compensating solenoid, the cryostat contains 2 shielding solenoids. Their number is determined by limitation on the transverse dimensions of the cryostat and the dimensions of the superconducting lenses. The inner diameter of the first shielding solenoid is 110 mm; the length is 500 mm. The second shielding solenoid has a diameter of 180 mm and a length of 400 mm. The maximum value of the magnetic field induction in the compensating solenoids is 1.2 T, to compensate for the effects from the main solenoid and yokes of the magnetic lenses of the final

Table 1.20. Parameters of available SC cable.

Parameter	Value
External diameter	0.92 ÷ 0.93 mm
Diameter without insulation	0.87 mm
Density per meter	4.79 g/m
NbTi/Cu ratio	1/1.42
Number of conductors	8910
RRR of copper matrix	115
Current (at 5 T, 4.2 K)	630 A
Current (at 7 T 4.2 K)	370 A

focus. These solenoids will be produced of the superconducting cable, its parameters are shown in Table 1.20.

### Lenses of the final focus

The lenses of the final focus are the lens prototypes developed at BINP SB RAS as a modification of the Panofsky lens. The parameters of the lenses are given in Table 1.2 (parameters of the final focus magnets). Figure 1.67 presents the general view and the drawing of the first lens of the final focus. The winding of the lens is made of a  $0.8 \times 1.4$  mm rectangular superconducting wire. The maximum current obtained in the prototype tests is 1150 A, which corresponds to a gradient of 10.9 kGs/cm.

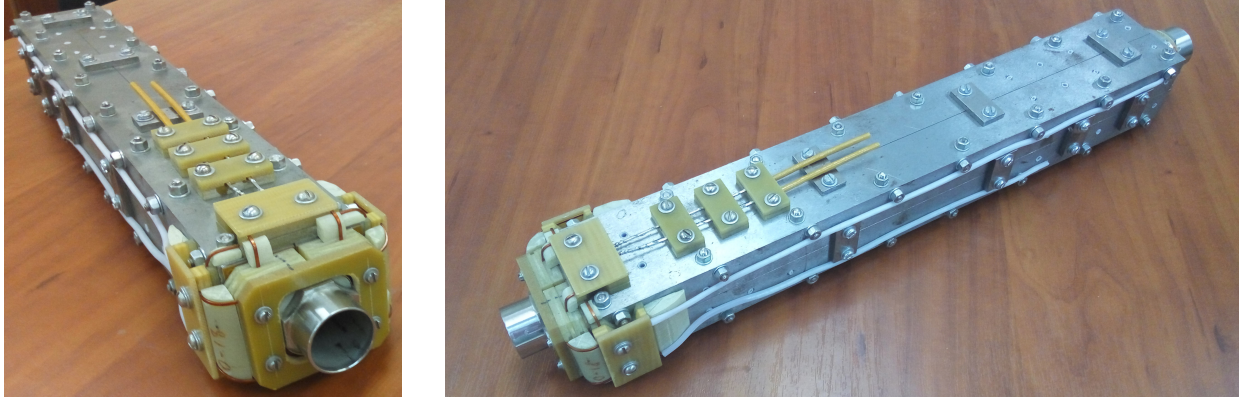


Figure 1.67. Prototype of defocusing lens of final focus.

Table 1.21. Parameters of superconducting Nb-Ti wire for final focus lenses.

Parameter	Value
Size with insulation	$1.28 \times 0.83$ mm
Sizes without insulation	$1.20 \times 0.75$ mm
Cu/Sc	1.35:1
RRR	over 70
Critical current (at 7 T)	510 A

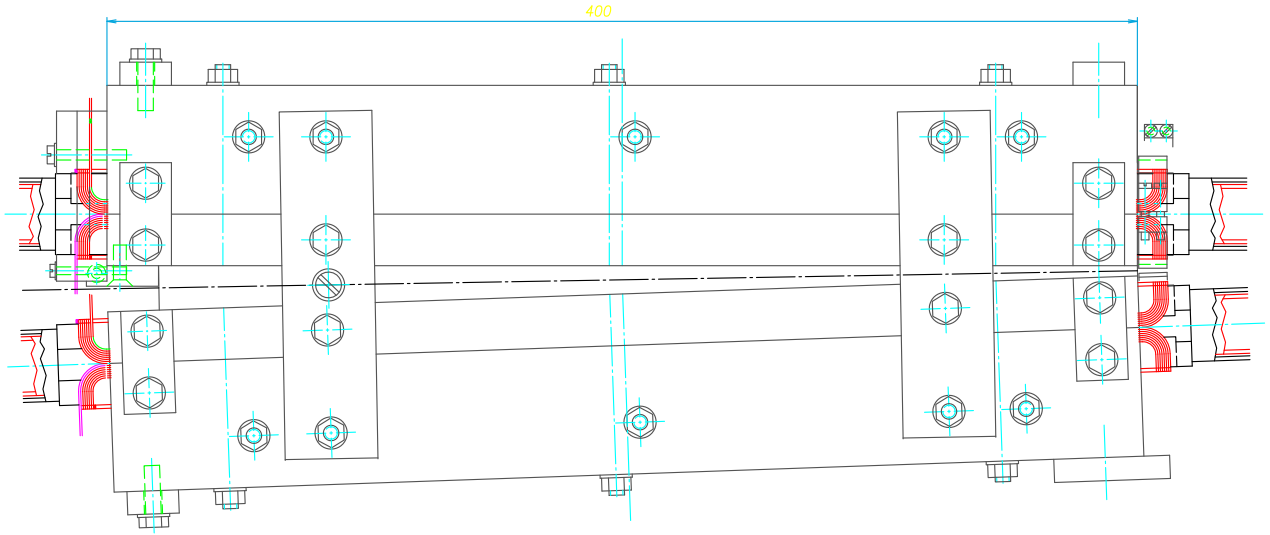


Figure 1.68. Drawing of defocusing lens of final focus (top view).

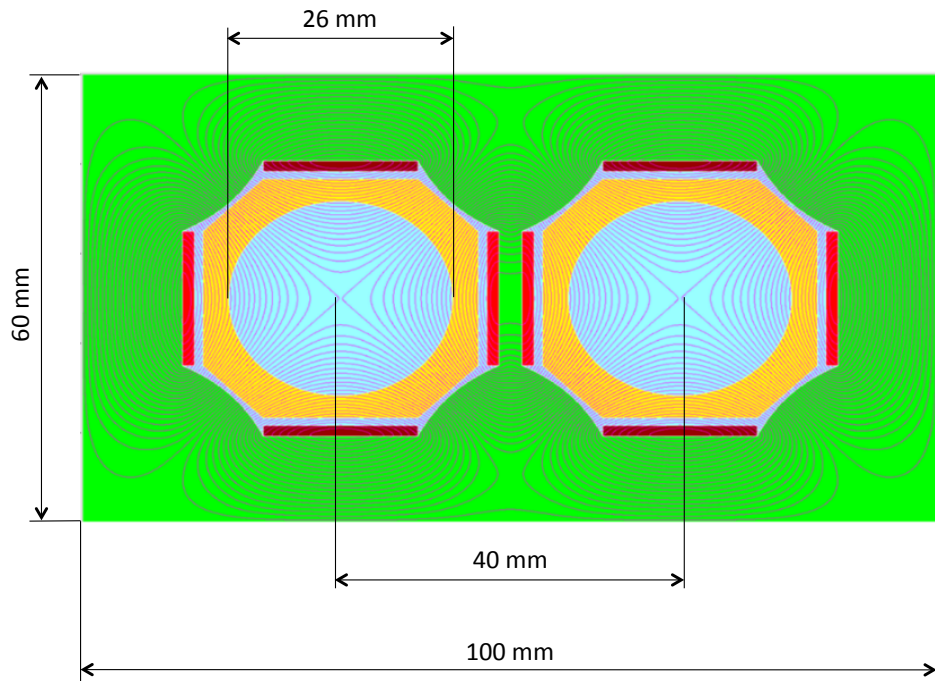


Figure 1.69. Calculation of magnetic field of defocusing lens of final focus in program MERMAID (transverse section).

## 1.13.2 Damping wiggler

### Magnetic system of wiggler

The magnetic system of a superconducting wiggler is a sequence of alternating dipole magnets along the beam trajectory. The main requirement to the magnetic field of the wiggler is that the first and second integrals of the wiggler field along the trajectory must be equal to zero:

$$I_1^x(s) = \int_{-L/2}^s ds' B_y(s') = 0, \quad I_2^x(s) = \int_{-L/2}^s ds' \int_{-L/2}^{s'} ds'' B_y(s'') = 0. \quad (1.67)$$

If conditions (1.67) are fulfilled, the orbit in the storage ring outside the wiggler remains practically unperturbed by the wiggler field. Conditions (1.67) are provided by 4 special magnets installed on the ends of the wiggler, with field integrals equal to 1/4 and 3/4 of those of the main magnets. The main parameters of the wiggler are given in Table 1.22.

Table 1.22. Basic parameters of wiggler.

Parameter	Value
Max Field	5.1 T
Period	250 mm
Total length of magnet	1.875 m
Structure of magnets	+1/4, -3/4, +1, -1, ..., +1, -3/4, +1/4
Number of main poles	11
Number of 3/4 poles	2
Number of 1/4 poles	2
Main winding 1st section	12 layers $\times$ 40 turns
Main winding 2nd section	12 layers $\times$ 40 turns
Winding of 3/4 pole	24 layers $\times$ 40 turns
Winding of 1/4 pole	8 layers $\times$ 40 turns
Current $I_1$	255 A
Current $I_2$	300 A

For the manufacture of a wiggler with the parameters indicated in Table 1.22, it is necessary to use a superconducting (SC) cable with the parameters specified in Table 1.23.

Table 1.23. Superconducting cable parameters.

Parameter	Value
Cable diameter without insulation	0.85 mm
Diameter of cable with insulation	0.91 mm
NbTi/Cu ratio	0.43
Critical current	over 370 A at 7 T
Number of fibers in cable	8600

The main poles of the wiggler are made in the form of 2-section “race-track” windings, wound on a core of magneto-soft iron of the Armco type. The number of layers in the windings and the height of the windings are optimized so as to obtain the maximum field in the orbit subject to the parameters of the SC cable. Figure 1.70 presents the critical curve of the SC cable in the current-field coordinates. The figure shows points of the load curves of the outer and inner sections of the wiggler windings in the maximum field of the windings in the maximum operating mode and at a winding temperature of 4.2 K. The current margin to the critical curve is  $\sim 10\%$ , which is sufficient for reliable operation of the magnet.

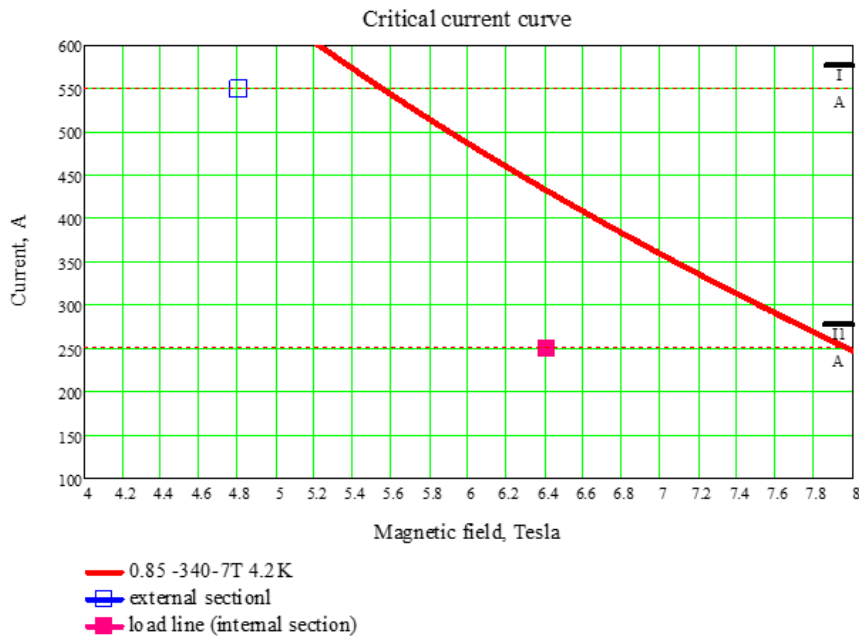


Figure 1.70. Behavior of critical curve of SC cable with NbTi/Cu = 0.43 (red curve). Dots: maximum fields in sections at operating currents.

To optimize the maximum luminosity at different beam energies, it is necessary to vary the amplitude of the wiggler magnetic field after a change in the beam energy. The maximum amplitude of the field in the wiggler of 5 T is set at energies of 1 GeV to 1.5 GeV. When the beam energy is increased, the amplitude of the magnetic field is set in accordance with Table 1.1. The dependence of the magnetic field  $B_y$  in the wiggler on the longitudinal coordinate at different beam energies (1, 1.5, 2, and 2.5 GeV) is shown in Fig. 1.71. The largest influence of the wiggler on the beam dynamics occurs at the maximum field and the minimum energy of 1 GeV particles, planned for the project. Under these conditions, the orbit inside the wiggler will be equal to the maximum amplitudes of changes in the inclination angles and in the deviation of the trajectory relative to the wiggler axis (see Fig. 1.72).

Wiggler is a high-power synchrotron radiation generator in a wide range of photon energies, from visible light to hard X-rays of  $\sim 100$  keV (Fig. 1.74). The total radiation power from a single wiggler in dependence on the energy of the beams at a beam current of 2 A is shown in Fig. 1.73. The maximum radiation power is achieved at 1.6 GeV. The spectral characteristics of radiation vary insignificantly when the energy of the beams changes. The angular distribution of the total power at beam energies of 1, 1.5, 2, and 2.5 GeV is shown in Fig. 1.75. The maximum horizontal

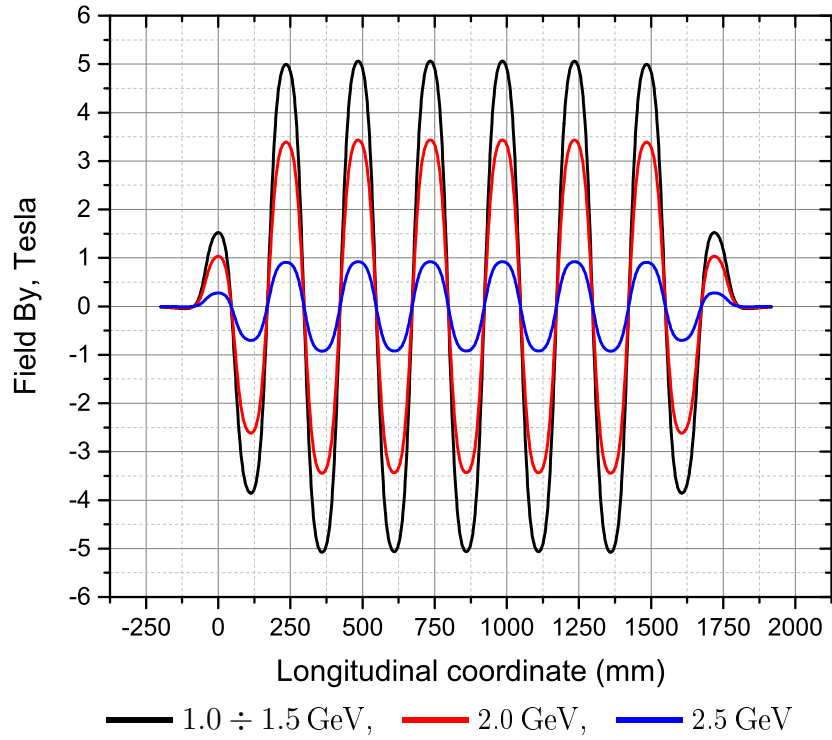


Figure 1.71. Behavior of wiggler magnetic field in longitudinal direction at different beam energies.

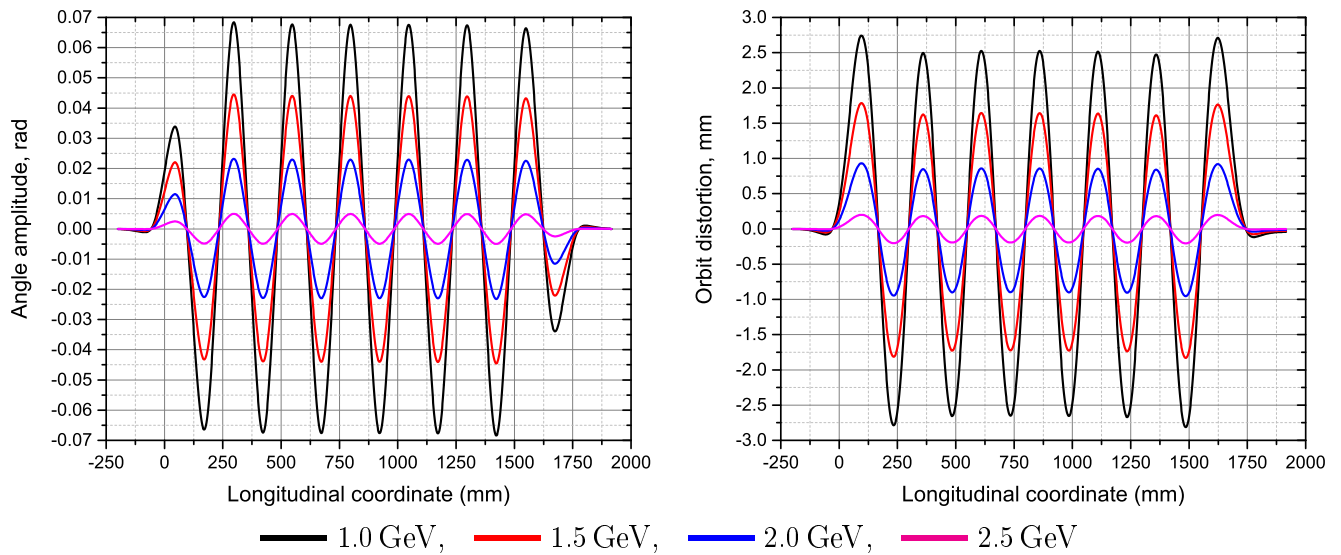


Figure 1.72. Behavior of angle and coordinates of beam trajectory inside wiggler at beam energies.

angle into which radiation is transmitted is  $\pm 70$  mrad at a particle energy of 1 GeV and the field in a wiggler of 5 T. The size of the synchrotron radiation beam from the wiggler for beam energies of 1, 1.5, 2, and 2.5 GeV is shown in Fig. 1.76 in distances from the beginning of the wiggler magnet of 1750 mm and 2400 mm, which correspond to the end of the magnet inside the cryostat and outside the cryostat, respectively. The angular and coordinate distribution of the radiation power must be taken into account when designing the storage ring vacuum chamber, which will be discussed below.

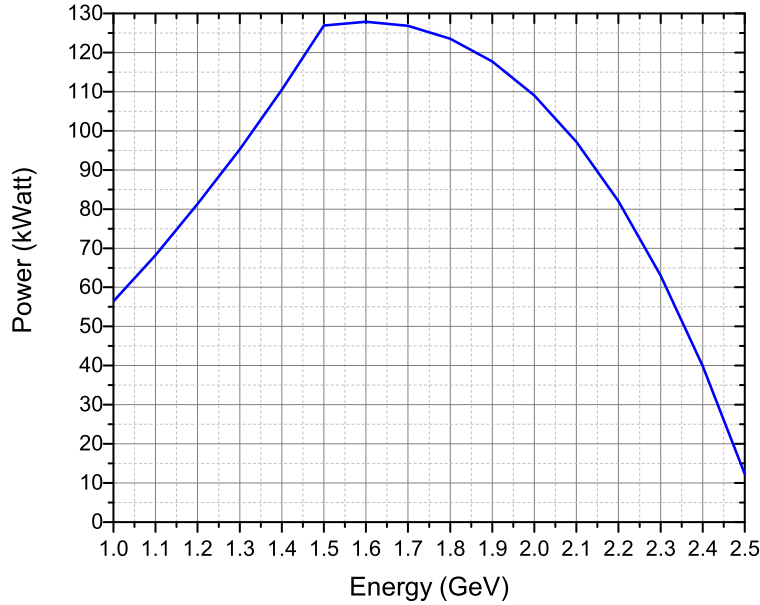


Figure 1.73. Radiation power from wiggler vs. beam energy (beam current of 2 A).

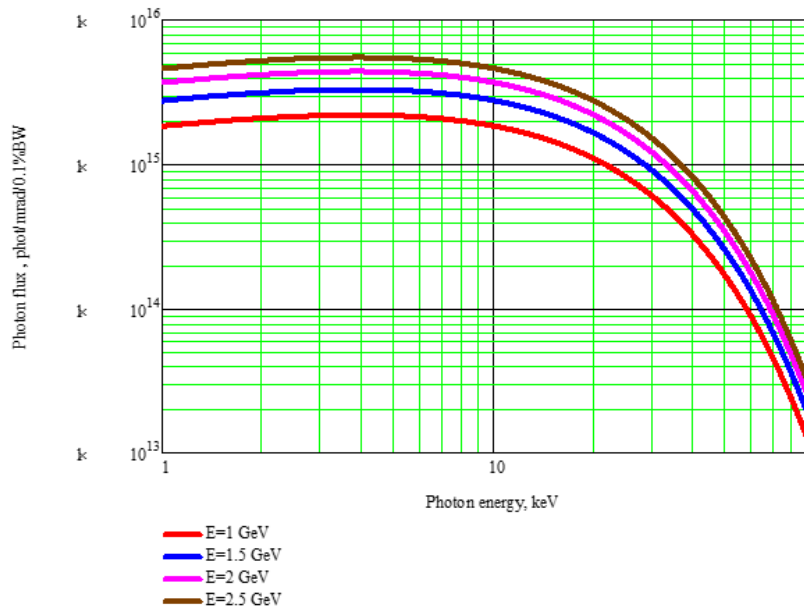


Figure 1.74. Radiation spectra at zero angle to wiggler axis at different beam energies (beam current of 2 A).

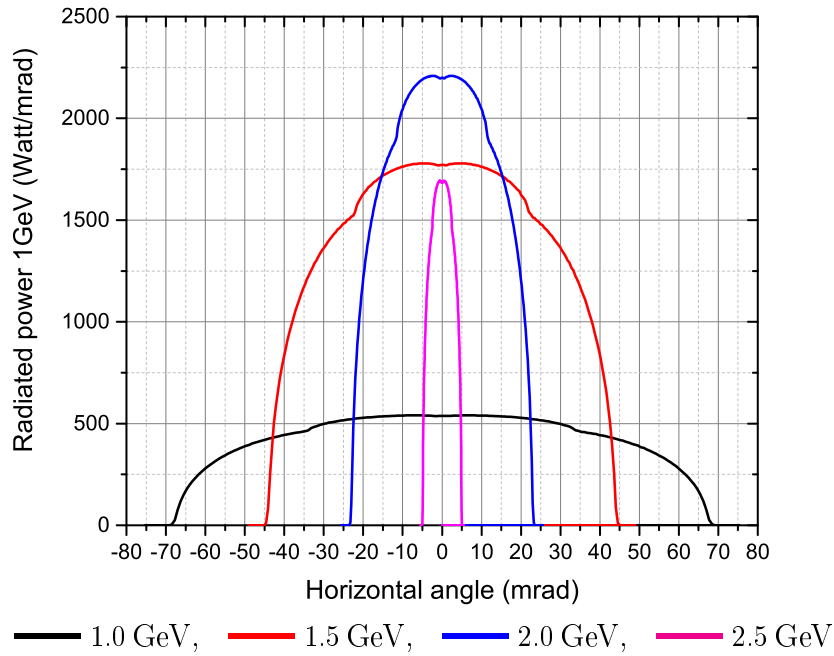


Figure 1.75. Angular distribution of radiation power from wiggler at different beam energies (beam current of 2 A).

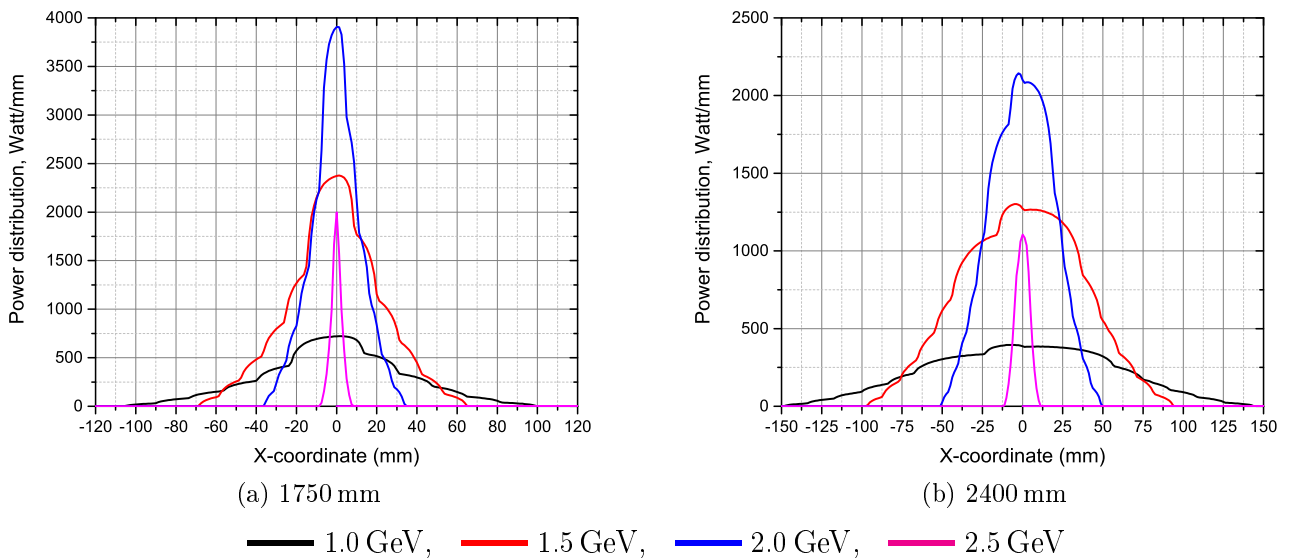


Figure 1.76. Distribution of power emitted by wiggler vs. horizontal coordinate at end of magnet (from beginning of magnet inside the cryostat) for different beam energies (beam current of 2 A).

From the distribution of wiggler radiation power over the horizontal transverse coordinate at a particle energy of 1 GeV and a maximum operating field of 5 T it can be concluded that the horizontal aperture of the storage ring vacuum chamber at the exit of the wiggler cryostat (2400 mm from the magnet beginning) is more than 180 mm for extraction of radiation without touching the vacuum chamber. Inside the cryostat, the maximum size of the photon beam is 140 mm at the end of the magnet.

## Cryogenic system of superconducting multi-pole wiggler

The cryogenic temperature on the superconducting windings is maintained due to the cooling of the magnet by liquid helium. The concept of the cryogenic system is based on the use of industrially produced cryocoolers and consists in application of the refrigeration stages of the cryocoolers for recondensation of already evaporated helium and for complete prevention of its evaporation due to sequential interception of all channels of heat influx at a cryocooler stage with appropriate temperatures. This makes it possible to use the power of cryocoolers not only to reduce the consumption of liquid helium to zero, but also to create a lower relative atmospheric pressure in the helium vessel, with respective lowering of the boiling point of liquid helium to  $\sim 3$  K. This cryostat, whose appearance is shown in Fig. 1.77, is able to operate autonomously on a charged particle accelerator for a few years under conditions of limited access without consumption of liquid helium in spite of the additional thermal load generated by the electron or positron beam and by a current of up to  $\sim 1000$  A applied to power the magnet. The design of the cryostat and its functional diagram are shown in Fig. 1.78 and in Fig. 1.79, respectively.



Figure 1.77. Appearance of cryostat of superconducting damping wiggler.

The cryostat consists of the external vacuum casing, two heat shields with temperatures of 60 K and 20 K, surrounding the helium vessel with the magnet inside, the central neck for connecting the helium vessel with the upper flange, helium filling and diagnostics, and the vacuum chamber for passing the beam. Figure 1.80 shows the longitudinal and transverse cross sections of the cryostat.

The cryostat elements are cooled by a system of copper heat conductors, which intercept heat fluxes at all critical points and divert them to the heads of four SUMITOMO cryocoolers, operating in the Gifford-McMahon cycle. In this case, one pair of SRDK-415D cryocoolers with 4 K and 60 K temperatures is used to cool the current input elements and re-condense the liquid helium, and the second pair of SRDK-408S2 cryocoolers with temperatures of 20 K and 60 K to cool the shields and the vacuum chamber. The characteristics of the cryocoolers used are presented in

Table 1.24 and in Figs. 1.81 and 1.82.

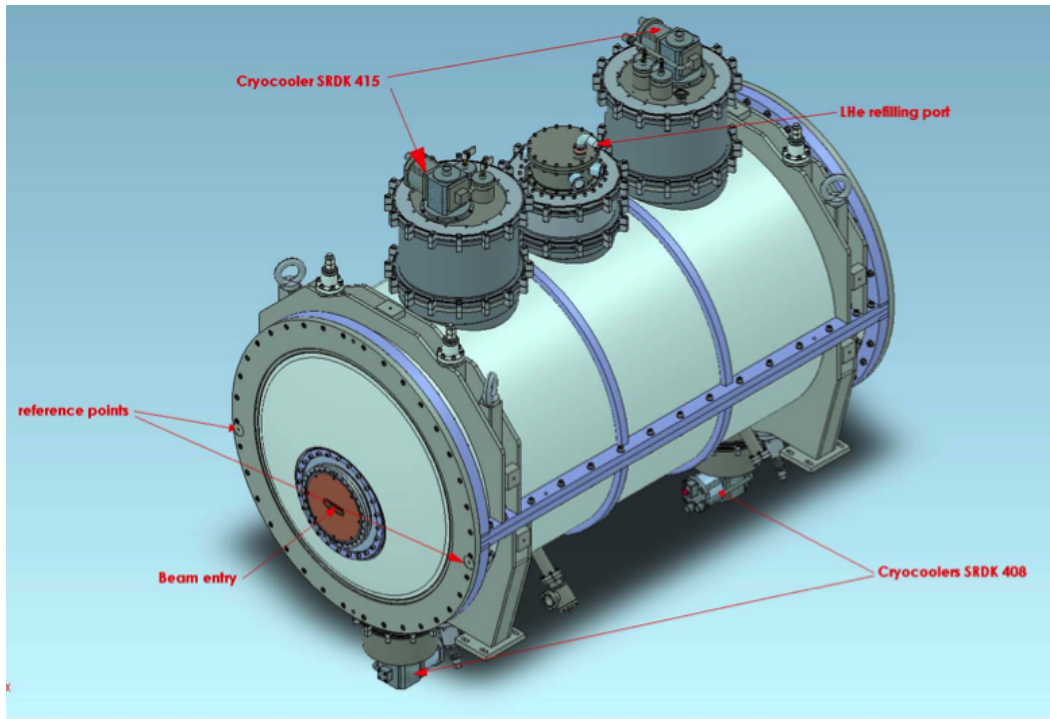


Figure 1.78. Cryostat of superconducting wiggler (3D model).

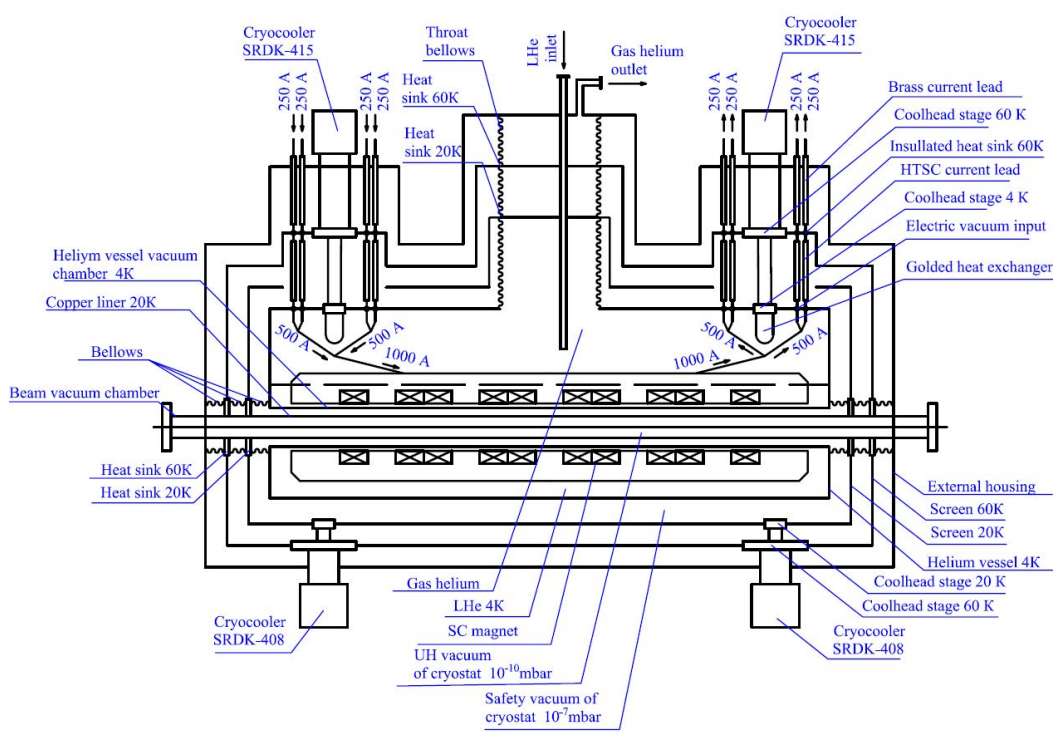


Figure 1.79. Functional scheme of cryostat of superconducting multipole wiggler on zero helium consumption cryocoolers.

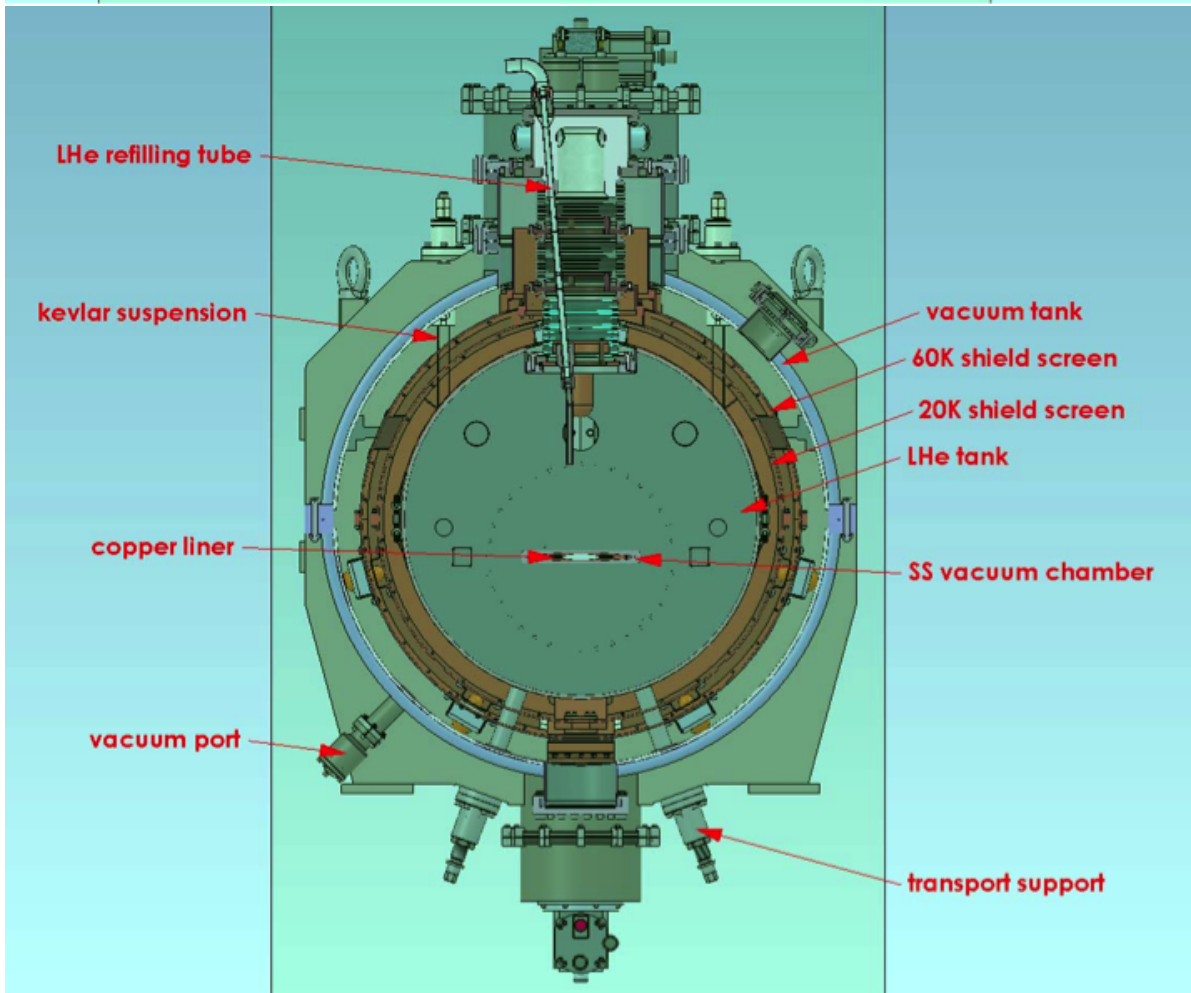
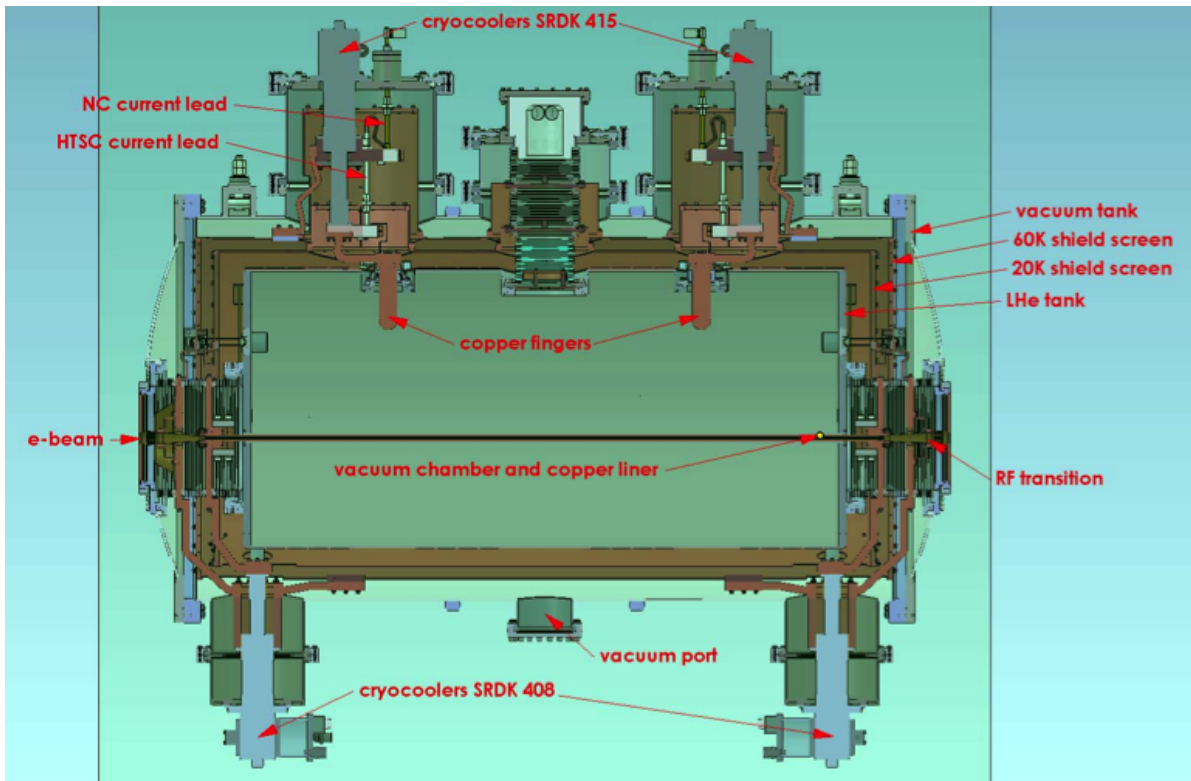


Figure 1.80. Longitudinal and cross sections of cryostat (3D model).

Table 1.24. Main characteristics of SUMITOMO cryocoolers.

Model name	SRDK-415D			SRDK-408S2		
Cooling capacity:	60 Hz	50 Hz		60 Hz	50 Hz	
First stage	50 K	45 W	35 W	45 K	45 W	35 W
Second stage	4.2 K	1.5 W	1.5 W	10 K	6.3 W	5.4 W
Minimum temperature:						
First stage	30 K			30 K		
Second stage	2.8 K			7 K		
Weight	18.5 kg			17.2 kg		
Compressor	CSW-71C			CSW-71C		
Service	14 months			14 months		

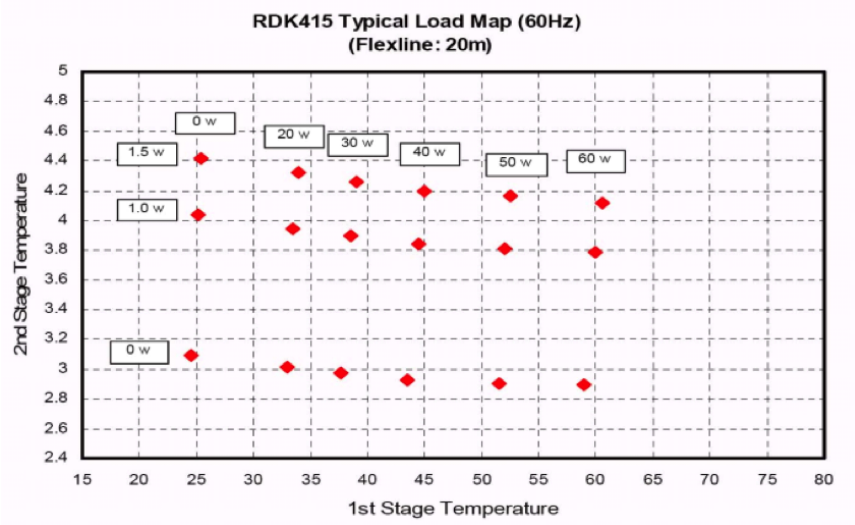


Figure 1.81. Power characteristics of SRDK-415D cryocooler.

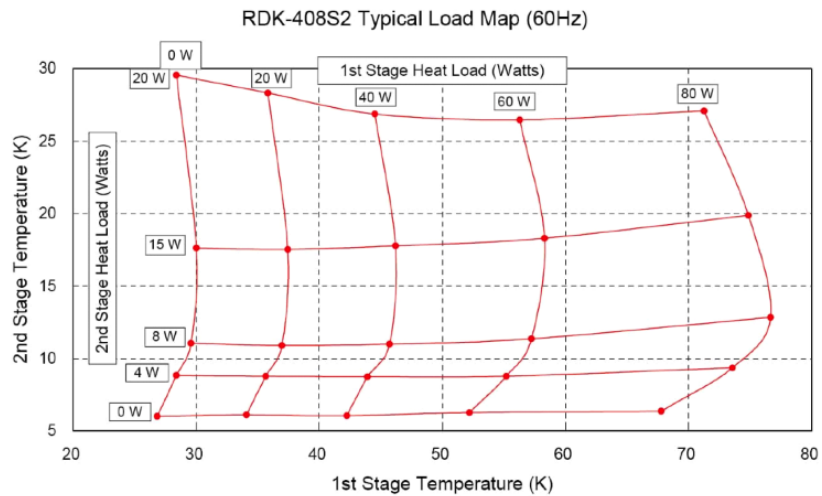


Figure 1.82. Power characteristics of cryocooler SRDK-408S2.

The external thermal shield and the helium vessel are covered with 30-layer and 10-layer cryogenic super-insulation, which improves the efficiency of protection against external thermal radiation. With this shielding, the thermal radiation heat influx into the helium does not exceed 0.01 mW. Figures 1.83 and 1.84 show the appearance of the outer 60 K and internal 20 K shields, respectively. Figures 1.85 and 1.86 show the model of the helium vessel with connected cryocoolers and the appearance of the helium vessel, respectively.

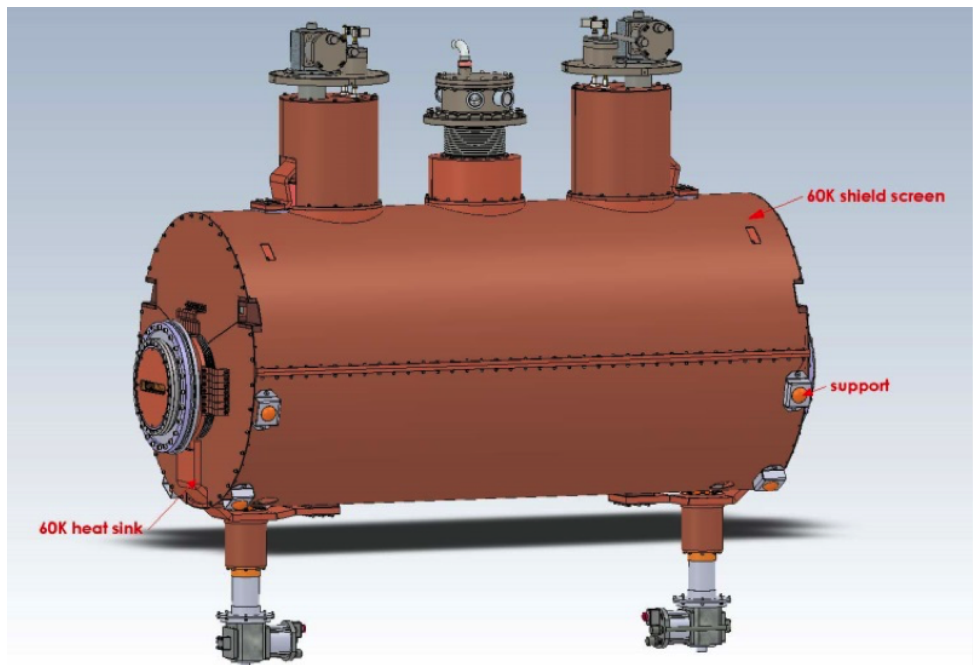


Figure 1.83. Appearance of outer 60 K thermal shield (3D model).

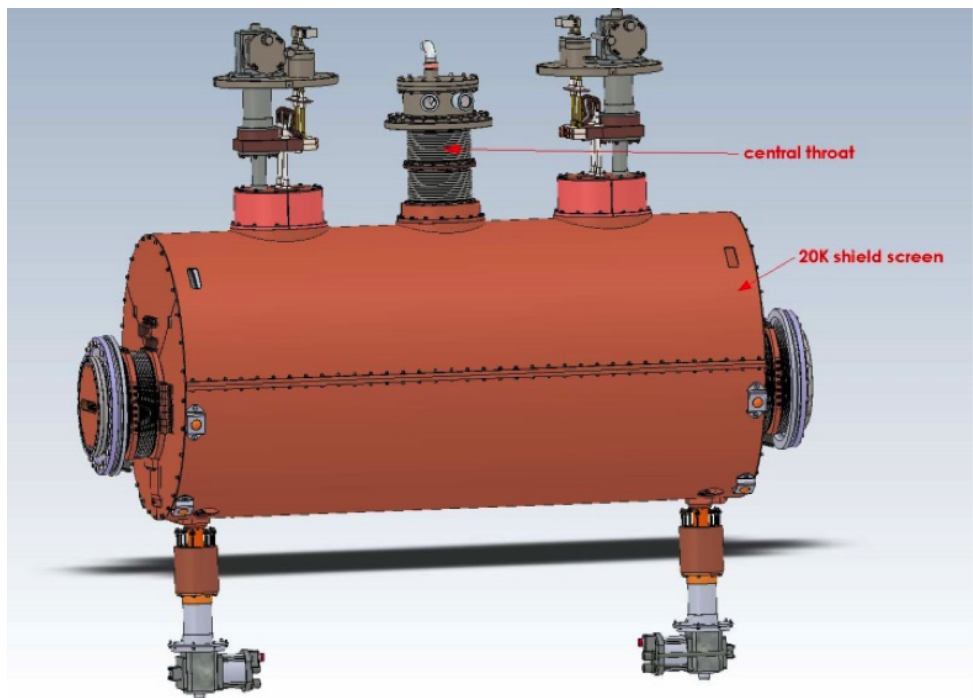


Figure 1.84. Appearance of internal 20 K thermal shield (3D model).

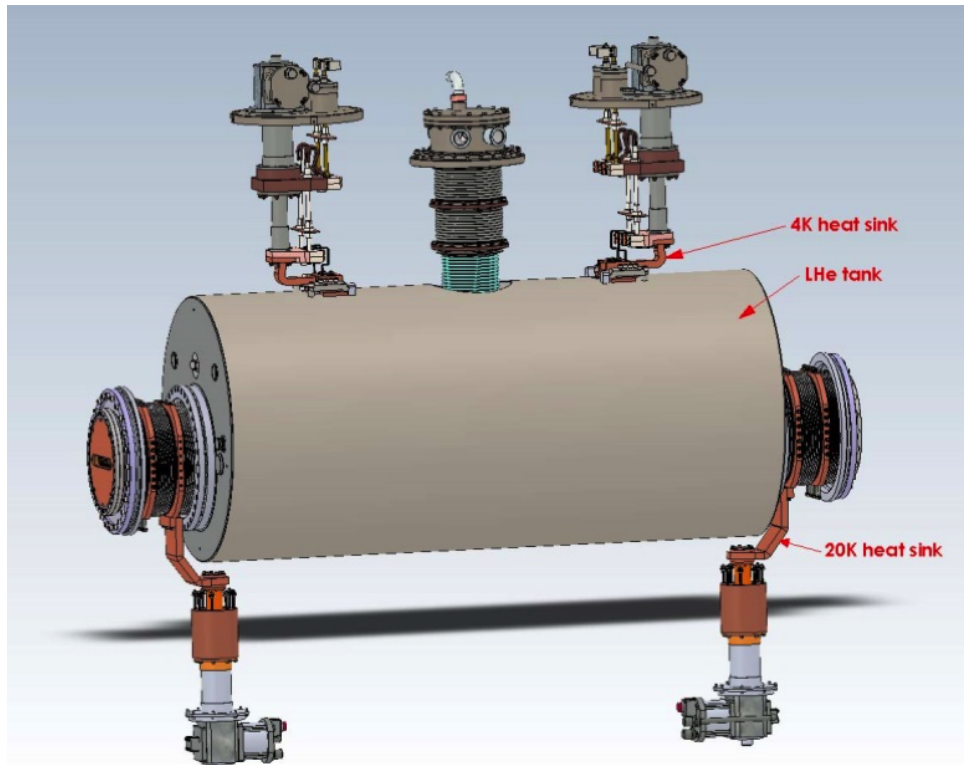


Figure 1.85. Appearance of helium vessel with connected cryocoolers (3D model).



Figure 1.86. Helium vessel assembly.

The space between the helium vessel and the outer casing serves as vacuum insulation, preventing heating of the cryostat elements from heat influx through the molecules of the residual gas. The protective vacuum is evacuated to a residual pressure not exceeding  $10^{-7} \div 10^{-8}$  mbar. In addition, the cold surfaces of the cryostat work like vacuum cryogenic pumps, and thus the heat transfer into the helium through the residual gas can be considered negligible. The superconducting magnet is fixed by special protrusions in the median plane of the magnet, which are inserted into the grooves on the end flanges inside the helium vessel. The helium vessel with the magnet is suspended to the outer casing of the cryostat by means of four vertical Kevlar tapes passing

through both thermal shields and fixed to suspension assemblies, which enables fine adjustment of the magnet position from outside the cryostat without violating the vacuum of the cryostat. Adjustment of the position of the magnet in the horizontal plane is performed by means of four Kevlar horizontal stretches. The appearance of the adjustment assemblies and Kevlar suspensions is shown in Fig. 1.87, and Fig. 1.88 presents the appearance of the suspension system during the assembly of the cryostat. The use of Kevlar, which has a very low thermal conductivity and high mechanical strength, can radically reduce the cross section of the suspensions and reduce the flow of heat into the helium through the suspension system to 0.01 W.



Figure 1.87. External view of adjustment assemblies and Kevlar suspensions.

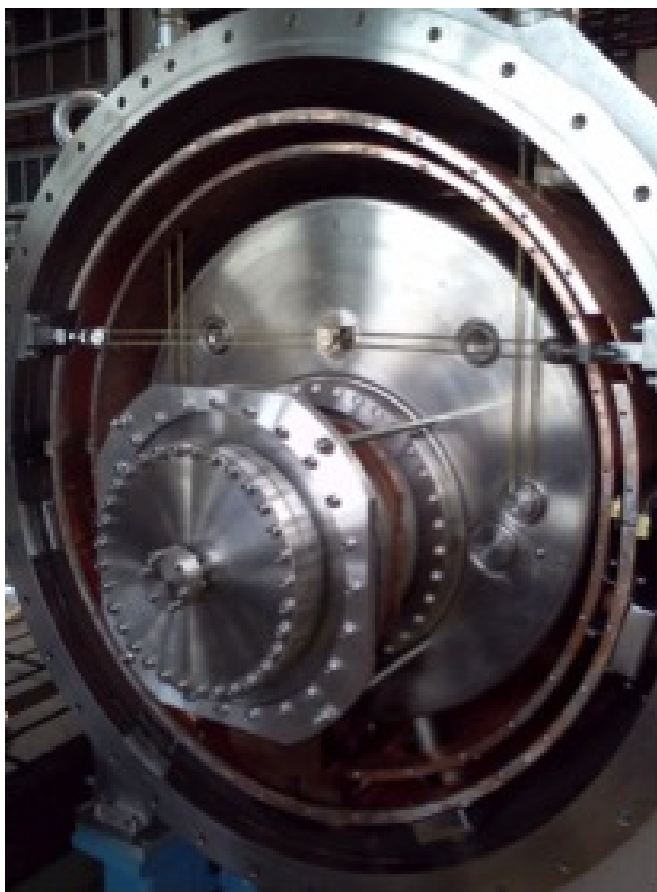


Figure 1.88. External view of suspension system during assembly of cryostat.

The helium vessel is connected with the external atmosphere through the central throat of the cryostat, shown in Fig. 1.89, which also serves for feeding liquid helium, discharge of the helium gas, and output of the diagnostic wires. The total calculated heat input into the helium through the bellows of the central throat does not exceed 0.06 W.

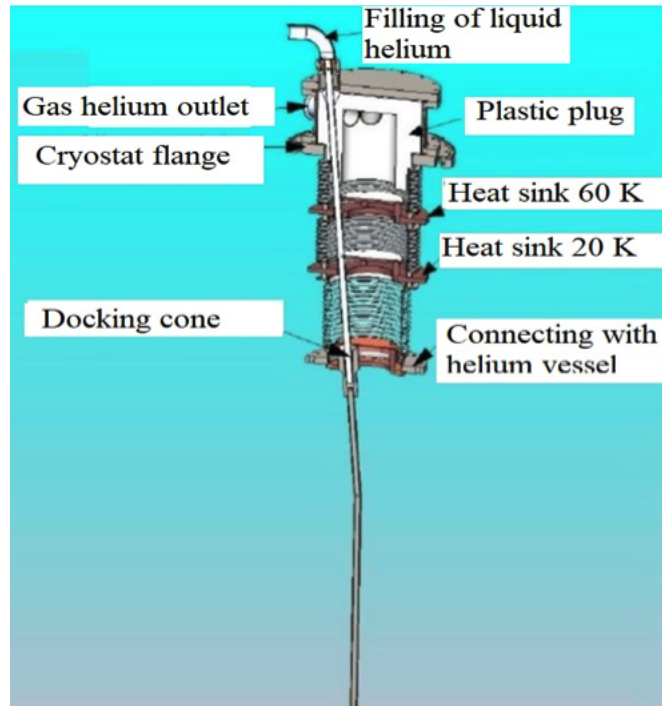


Figure 1.89. Central throat for connection to upper flange (3D model).

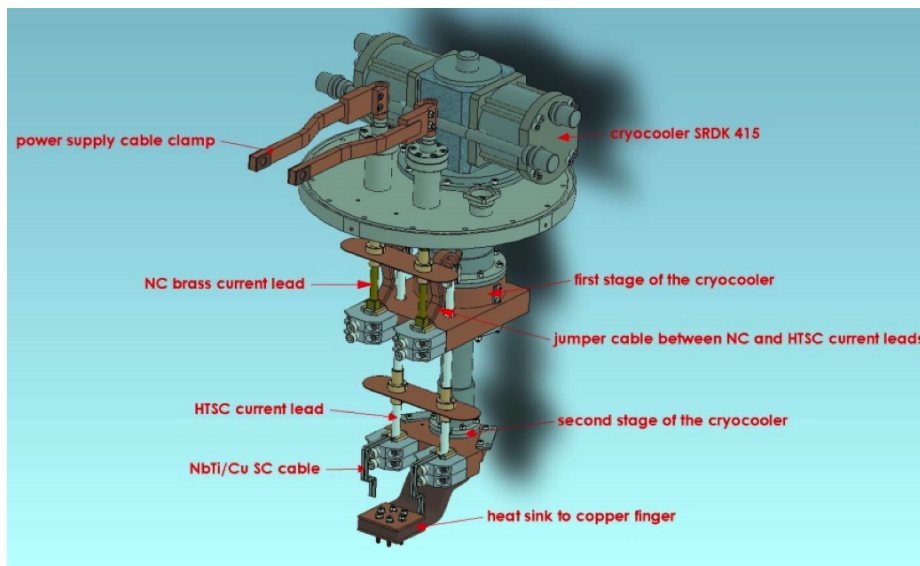


Figure 1.90. Appearance of current input assembly (3D model).

All four stages of the cryocoolers with a temperature of 60 K and a total power of  $\sim 180$  W are used for cooling of the external heat shield from external radiation and interception of heat from the vacuum chamber of the storage ring. The SRDK-415D cryocoolers are the basis of two current lead assemblies (see Fig. 1.90), consisting of external brass current leads connected to

internal high-temperature superconducting HTSC current leads. The stages of the SRKK-415D cryocoolers with a temperature of 60 K are also used for intercepting the heat coming from the outside along the brass current leads and the Joule heat released in these current leads when a total current of  $\sim 300$  A flows in each. Two stages with a temperature of 4 K and a power of 1.5 W each intercept the heat from the HTSC current leads and also cool the liquid helium in the vessel using a special gold-plated copper heat exchanger, shown in Fig. 1.91. The rated heat flux to the helium over all the current leads does not exceed 0.3 W with no current, and a heat input of no more than 0.3 W is added with current. The maximum temperature level on the upper ends of the HTSC current leads, which defines the safety margin of this unit, does not exceed the safe  $\sim 48$  K in stationary operation with the maximum current and falls to  $\sim 38$  K when the current is turned off. Figure 1.92 presents a model of arrangement of the current lead assemblies in the cryostat.



Figure 1.91. Appearance of gold-plated copper heat exchanger.

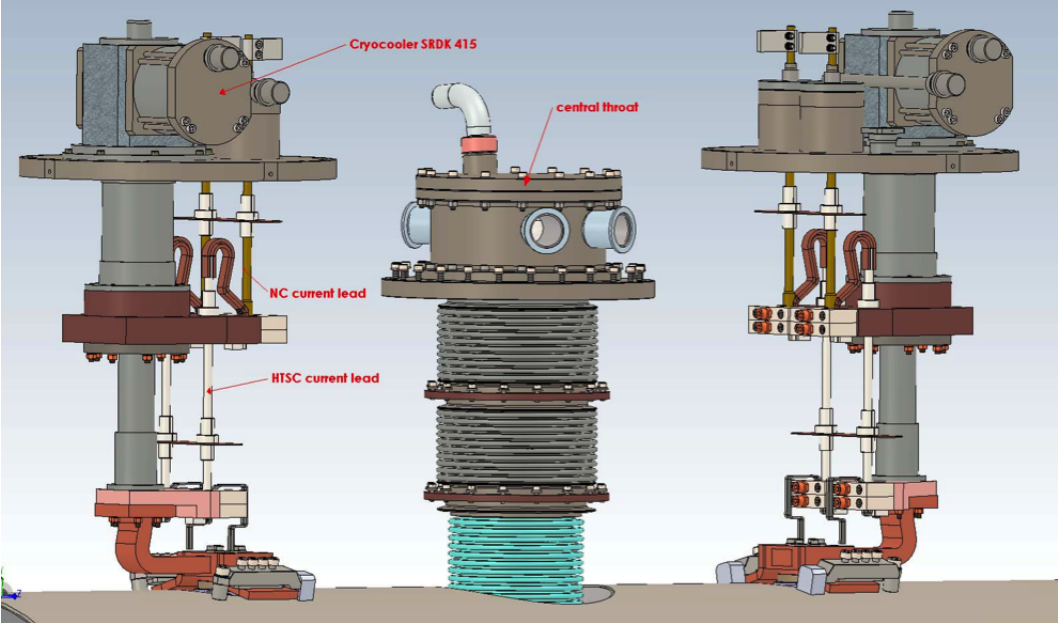


Figure 1.92. Arrangement of current lead assemblies in cryostat (3D model).

The room-temperature stainless steel vacuum chamber for beam pass is inserted into the pole gap of the superconducting magnet. So is the intermediate copper chamber cooled by the stages of the SRDK-408S2 cryocoolers at a temperature of 20 K. The latter chamber is used to protect the liquid helium volume from heating both by the synchrotron beam radiation and by the currents induced by the beam of the storage ring. The mechanical clearance between the copper chamber and the liquid helium vessel along the entire length of the wiggler is ensured by distal gaskets. They are made of a material with low thermal conductivity (ULTEM 2100) to reduce the influx of heat into liquid helium. The calculated heat input into the helium through the mechanical supports of the copper liner does not exceed 0.2 W. The cross section of the vacuum chamber is shown in Fig. 1.93.

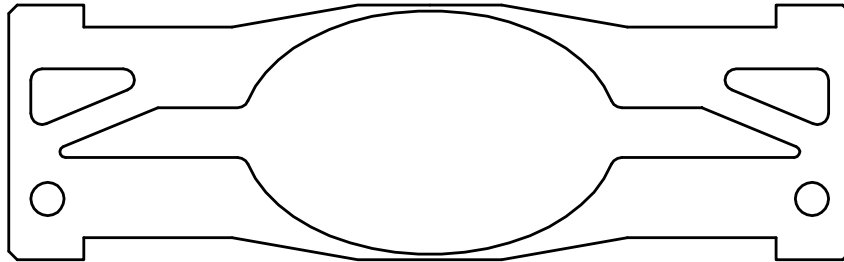


Figure 1.93. Cross-section of pole gap with vacuum chamber and liner.

The protective vacuum is separated from the ultrahigh vacuum chamber of the beam by bellows units. The total calculated heat input into the helium from these bellows does not exceed 0.04 W. The appearance of the output flange for connection with the storage ring is shown in Fig. 1.94.



Figure 1.94. Appearance of output flange for connection with storage ring.

The total calculated heat balance in the cryostat is presented in Table 1.25, from which it can be concluded that the cooling capacity of the cryocoolers at all stages clearly exceeds the corresponding heat influxes, which not only significantly improves the reliability of the cryogenic system, especially in operation in the accelerator, but also makes the life of the cryocoolers longer. It can be noted that the total cooling capacity of the 4 K stages exceeds the heat release  $\sim 3$  times, and the excess power goes to the supercooling of the helium vessel with the magnet inside and lowering the pressure in the vessel. This enables improvement of the reliability of the work of the magnet, as well as increase in the level of the magnetic field due to better current characteristics of the superconductor.

Table 1.25. Balance of heat inflows into cryostat with zero helium consumption.

Screen	Outer	Inner	Helium	
Temperature	60 K	20 K	4 K	
Thermal radiation	8.0	0.05	0.0002	W
Central throat	2.5	0.30	0.06	W
Vacuum chamber bellows	5.3	0.25	0.04	W
System of suspensions	0.5	0.10	0.01	W
Current leads (thermal conductivity)	50.0	0.00	0.30	W
Heating of current leads by current	50.0	0.00	0.30	W
Sensing wires	5.0	0.10	0.01	W
Copper chamber	10.0	10.00	0.20	W
Total inflow	131.3	10.80	0.92	W
Power of cryocoolers	180 (at 50 K)	15 (at 20 K)	3 (at 4.2 K)	W

The process of cooling the cryostat with a cold mass of  $\sim 1000$  kg from room temperature to the operating state with a temperature of 4 K takes not more than 2 days (including pre-cooling with liquid nitrogen). The cooling rate is significantly increased due to pre-cooling of the heat shields and other cryostat elements by cryocoolers with a large reserve of cooling power. The concept of the wiggler control system is based on an autonomous controller, which processes diagnostic signals (temperature, pressure, and interlocks), and also controls the currents of the sources feeding the superconducting magnet, the operation mode of the cryocooler compressors, etc. The data exchange with the external system is also performed through the wiggler controller. Figure 1.95 shows a typical temperature map at the main operating points of such cryostat in stationary mode operation.

### Power supply of superconducting magnets

The superconducting magnets are powered from a precision bipolar current source VCH500-10-2Q. In terms of load characteristics, the coils of the superconducting magnets are a purely inductive load, in operation with which standard power supplies tend to instability and excitation. The VCH500-10-2Q power supply is specially designed and tuned for stable operation with a purely inductive load and is most suitable for operation of a superconducting wiggler having an inductance of up to 10 G at a low field level. A general view is presented in Fig. 1.96.

Figure 1.97 presents a simplified block diagram of the current source. The three-phase mains voltage is rectified by diode rectifier D1. IGBT transistors T1÷T4 form an inverter based on the complete bridge scheme with controlled phase shift between the half-bridges. The inverter converts

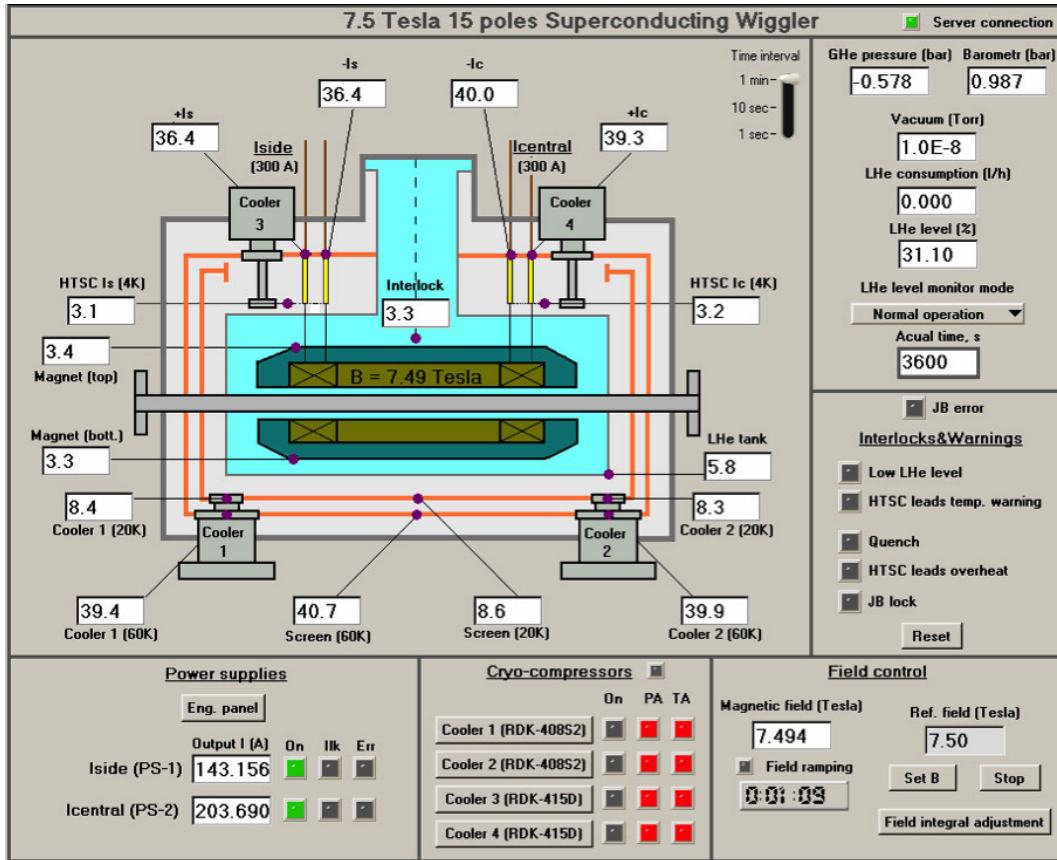


Figure 1.95. Typical temperature map at main operating points of cryostat when operating in stationary mode (screenshot).



Figure 1.96. Appearance of current source VCH500-10-2Q.

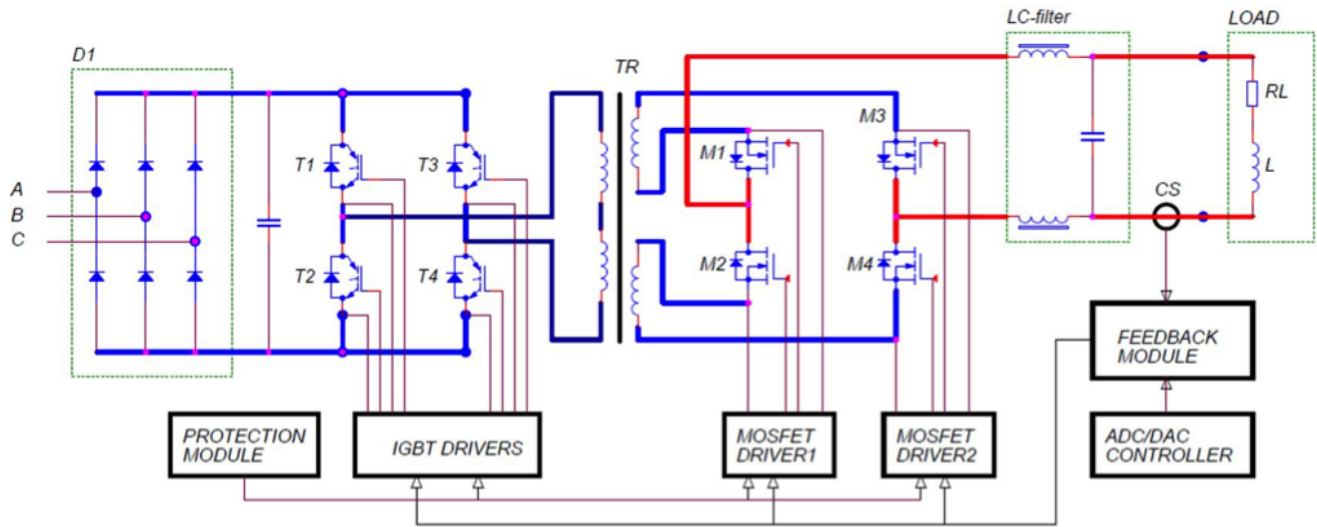


Figure 1.97. Block diagram of current source VCH500-10-2Q.

the rectified voltage of the mains into an alternating voltage of 550 V at a frequency of 40 kHz. The transformer (Tp) performs potential isolation and lowers the input voltage. The voltage from the output of the transformer is fed to the synchronous rectifier on MOSFET transistors M1÷M4. With positive output voltage, transistors M1 and M2 are commuted alternately, and transistors M3 and M4 are constantly open. With negative output voltage, M3 and M4 work, while M1 and M2 are in the open state. With such a topology of output rectification it is possible to obtain an output current of either direct or reverse polarity. After synchronous rectification, the voltage is smoothed by the output LC filter and fed into the load. The main characteristics of the source are presented in Table 1.26.

Table 1.26. Main characteristics of current source VCH500-10-2Q.

Parameter	Value
Rated output power	5000 W
Rated output voltage	$\pm 10$ V
Rated output current	$\pm 500$ A
Stability class	$\pm 0.01\%$ of $I_{nom}$ (8 hours)
Output ripple and noise, R.M.S.	less than 10 mV @ $0 \div 300$ Hz less than 300 mV @ $0 \div 40$ kHz
Supply parameters	400 V $\pm 10\%$ , 50 Hz
Cooling water requirements	4 l/min ( $< 35^\circ\text{C}$ )
Dimensions	$547 \times 550 \times 133$ mm
Weight	$\sim 20$ kg

### 1.13.3 Solenoid of Siberian Snake

To control the electron spin direction in the electron ring of the Super Charm–Tau factory, it is planned to install five Siberian snakes (see p. 1.6), each containing two 2 superconducting

solenoids. The magnetic length of solenoid is 1.85 m; the magnetic field is 2.8 T to 7.1 T; the outer diameter of the warm vacuum chamber is 76 mm. The chamber can be heated up to 220°C.

The superconducting solenoid is placed in a separate cryostat. In the very first approach, the cryostat is planned to be cooled by two cryocoolers. The solenoid is in a warm cylindrical casing with an outer diameter of less than 500 mm and a length of about 2500 mm. The cryocoolers will look like towers on this cylinder; their diameter will be about 300 mm, and they can be placed anywhere on the surface of the cylinder.

The magnetic field is in a linear dependence on the current. The distribution of the magnetic field in the solenoid is shown in Fig. 1.98; the on-axis field of the solenoid is shown in Fig. 1.99.

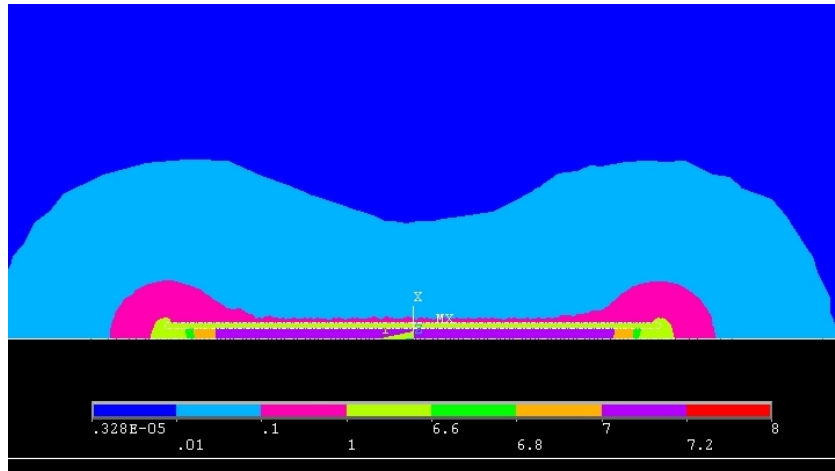


Figure 1.98. Distribution of magnetic field in solenoid at current of 220 A. Maximum field on winding is 7.12 T.

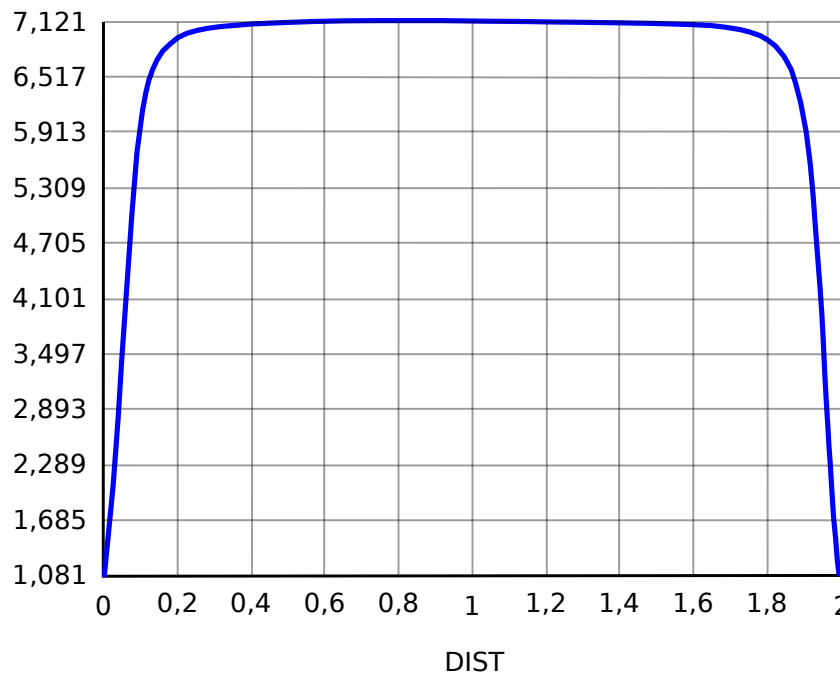


Figure 1.99. Distribution of magnetic field and integral of magnetic field along axis of solenoid over length of  $\pm 1.05$  m from center.

The solenoid consists of four sections, which are joined together along the axis. The length of section is about 0.5 m. The sections are wound of NbTi superconducting cable. The winding process is dry. Then each section is impregnated with epoxy compound. The parameters of the solenoid are given in Table 1.27. Table 1.28 lists the cable parameters in the first approximation.

In the future, it will be necessary to optimize the parameters in order to reduce the inductance of the solenoid and to study in detail the overall design of all the superconducting devices.

Table 1.27. Solenoid parameters.

Parameter	Value
Inner diameter of winding	100 mm
Outer radius of winding	148 mm
Winding length (four sections)	1900 mm
Number of turns	50000
Current	220 A
Maximum magnetic field on winding	7.12 T
Inductivity ( $2E/I^2$ )	16.1 T
On-axis magnetic field	7.1 T
Integral over 2.1 m along axis	13.4 T·m
Stored energy	390 kJ

Table 1.28. Parameters of available SC cable.

Parameter	Value
Outer diameter	0.92 ÷ 0.93 mm
Diameter without insulation	0.87 mm
Linear density	4.79 g/m
NbTi/Cu ratio	1/1.42
Number of conductors	8910
RRR of copper matrix	115
Current (at 5 T, 4.2 K)	630 A
Current (at 7 T, 4.2 K)	370 A
Current (at 8 T, 4.2 K)*	~ 220 A
Current (at 9 T, 4.2 K)*	~ 120 A

\* as recalculated.

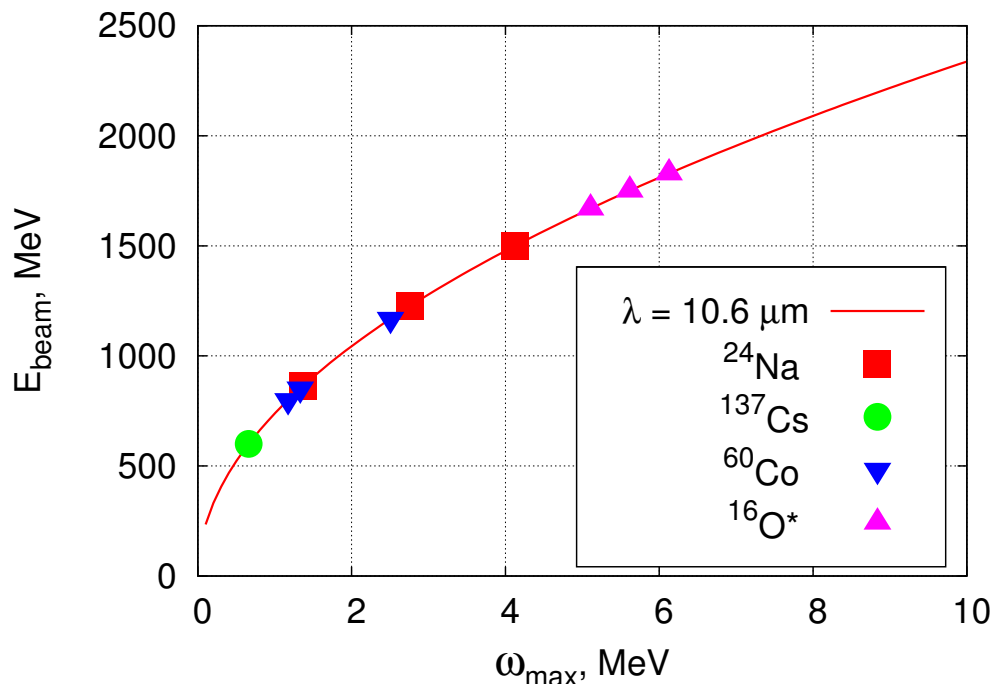
Power supply parameters: current of 300 A, voltage of up to 10 V, stability of  $5 \cdot 10^{-5}$ .

## 1.14 Beam Diagnostics

### 1.14.1 Beam Energy Measurement Systems

#### Energy spectrum of backscattered laser radiation

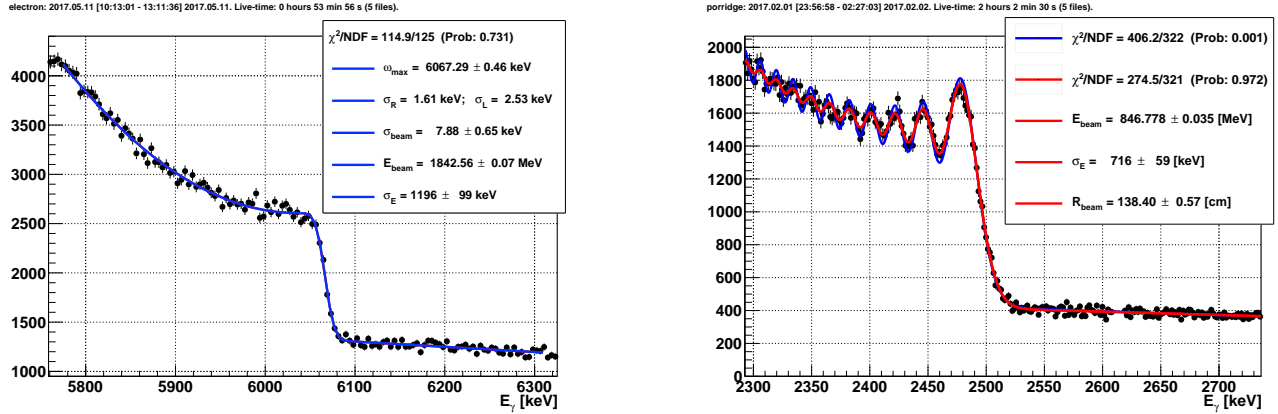
Currently, BINP SB RAS has accumulated considerable experience in measuring beam energy by the method of Compton backscattering of monochromatic laser radiation. The systems for the centre-of-mass energy calibration were created and successfully operated at colliders VEPP-4M [79], BEPC-II [80], and VEPP-2000 [81]. The essence of the applied method is the absolute measurement of the energies of scattered laser photons, which makes it possible to measure the average gamma factor of the beam electrons. To obtain the high accuracy of such measurements (the best achieved relative accuracy is  $20 \div 30$  ppm), it is necessary to obtain gamma quanta in the energy range from 0.5 MeV to 7 MeV and to register their energy spectrum with a High Purity Germanium detector (HPGe). In this range of energies, HPGe detectors have sufficient registration efficiency (several percent), and in addition, photons with energies from 0.5 MeV are easily removed from the vacuum chamber of the collider [82, 83, 84]. The upper limit of the energy range is due to a significant drop in the registration efficiency and, more importantly, no possibility to perform an absolute calibration of the energy scale by means of gamma-active nuclear radiation sources (Fig. 1.100). At electron beam energies from 100 MeV to 2 GeV, all these requirements are met with the lasers operating from visible to infrared spectrum range, which practically ends with a  $10.6 \mu\text{m}$  wavelength of carbon dioxide laser. However, when the beam energy is above 2 GeV, the accuracy and speed of such measurements decrease rapidly. Unfortunately, there are no affordable and sufficiently powerful monochromatic sources of more infrared radiation.



The points show sources for absolute calibration of the energy scale.

Figure 1.100. Dependence of the electron beam energy on the maximum energy of gamma quanta produced by the Compton backscattering of  $\text{CO}_2$  laser radiation.

The beam energy measurement system for the Super Charm–Tau factory will provide simultaneous independent energy measurements in both electron and positron rings. After approval of the magnetic structure of the collider, the location of the two systems will be selected, allowing, in addition to the average energy, measurement of the energy spread of the beam with accuracy of about 10%. In accordance with the unique experience of the VEPP-2000 collider (see Fig. 1.101), it is possible to organize the interaction of laser and electron beams in a curvilinear portion of the orbit, for example, in one of the magnetic poles of the damping wiggler. Such a scheme is more preferable from the point of view of absolute calibration of the scale, and in addition, it enables measurement of the magnetic field directly in the beam orbit, with an accuracy of about 0.1%.



(a) BEPC-II. The measurement was performed by recording the scattered photon spectrum from the CO<sub>2</sub> laser (wavelength of radiation in vacuum  $\lambda = 10.591035 \mu\text{m}$ ) on the electron beam in the absence of a magnetic field.

(b) VEPP-2000. The result was obtained by scattering CO laser radiation (wavelength  $\lambda = 5.426463 \mu\text{m}$ ) on electrons with an orbit radius  $R = 140 \text{ cm}$ .

Figure 1.101. The results of single measurements of the beam energy obtained on the colliders BEPC-II and VEPP-2000.

## Spectrometer with laser calibration

Since the Super Charm–Tau factory will be able to work with a polarized electron beam, we suggest trying a recently proposed method of simultaneous measurement of polarization and beam energy. For this purpose it is required to measure 2D coordinate distributions of scattered photons and scattered electrons after the dipole magnet. Analysis of the distribution of scattered electrons makes it possible to carry out precision calibration of the magnetic field integral in the spectrometer magnet and, in presence of polarization in the electron beam, to measure its direction and degree. The measured integral of the magnetic field enables determination of the average electron energy with high accuracy by measuring the beam bending angle using BPMs and, independently, by joint analysis of the coordinate distributions of scattered photons and electrons. The basic principles of such measurements are described in [85]. The measurement scheme is shown in Fig. 1.102, from which it follows that the absolute energy of the beam electrons is determined by the ratio of the bending angles of the scattered electrons and the main beam in a spectrometric dipole.

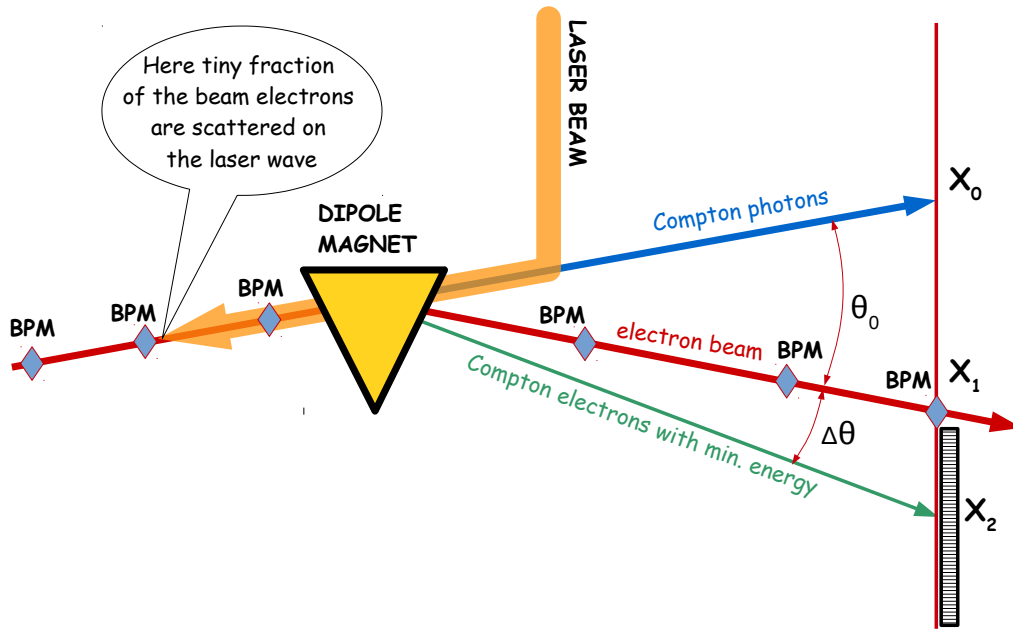


Figure 1.102. A sketch of the measurements.

## 1.14.2 Beam position system

### Beam position monitor

It is proposed to use electrostatic beam position monitors (pickups) to measure the beam position and to ensure the operation of the beam-stability system. Two types of pickups are required: for a regular vacuum chamber of  $\varnothing 68$  mm with an anti-chamber in the bending arcs and for a  $\varnothing 68$  mm vacuum chamber without an anti-chamber in the straight sections (see Fig. 1.103) An anti-chamber does not have a significant effect on the pickup parameters.

The electrodes are round button electrodes with a diameter of  $20 \div 25$  mm, connected to the vacuum feed-through (see Fig. 1.104). The vacuum feed-through is a commercial product with an SMA connector for cable connection.

### Processing signals from position monitor (pickup station)

Electronics for processing signals from a pickup (pickup station) is a U1 eurocard standard unit, located in a rack in a room for electronics. Four cables connect the measurement electronics with a pickup. Assuming that the electronics are placed in four rooms located along the perimeter of the ring, the average length of the route will be  $800/4/2/2 \times 2 = 100$  m.

Signals from the pickups can be divided into two classes: signals from pickups in the arcs, where particles of one type move in one direction, and signals from pickups located near the IP, where particles of both types move in different directions. In the first case, a narrow-band version of pickup station will be used. This option enables more accurate measurement of the beam position ( $\sim 0.5 \mu\text{m}$ ), but it has a worse time resolution. In the second case, a broadband version of pickup station will be used. This version has a somewhat lower accuracy of position measurement ( $\sim 10 \mu\text{m}$ ), but it enables separation of bunches of particles near the IPs. In other respects, both versions perform the same types of measurements. Parameters of narrow-band pick-up station are given in Table 1.29 and of broadband one in Table 1.30.

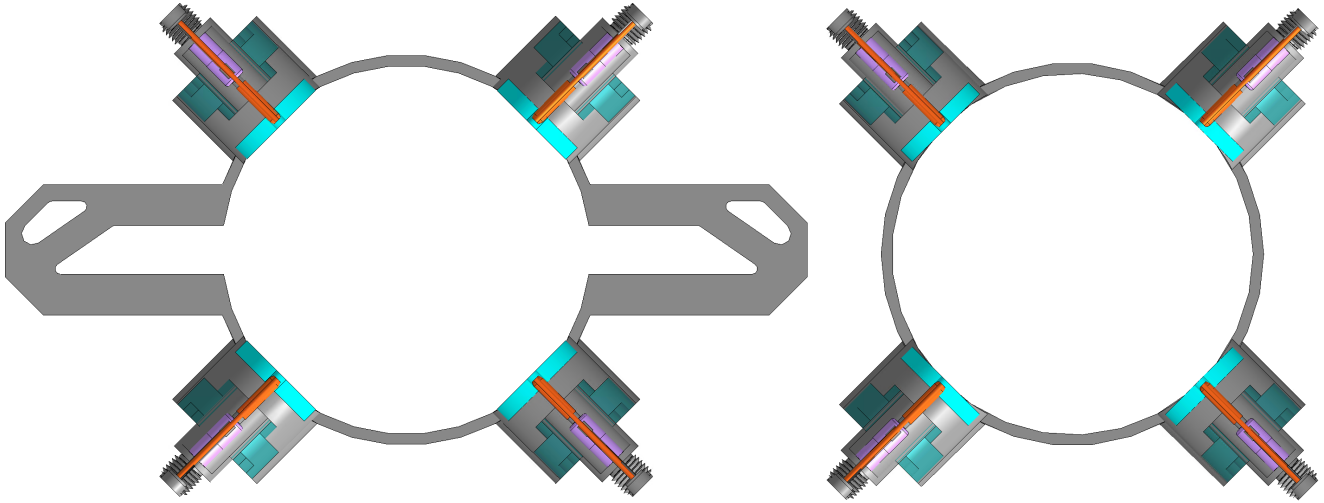


Figure 1.103. Cross-section of beam position monitors.

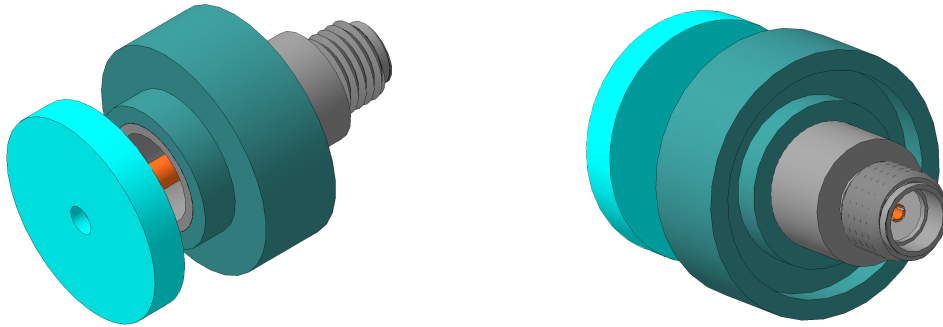


Figure 1.104. Electrode in pickup.

Table 1.29. Narrow-band pickup station parameters.

Parameter	Value
Resolution in band of 10 Hz	50 nm
Resolution in band of 10 kHz	100 nm
Resolution of turn-by-turn measurements	2 $\mu\text{m}$
Dependence on temperature	less than 200 nm/ $^{\circ}\text{C}$
Dependence on current	less than 1 $\mu\text{m}$
Interface	1 GigE
Feedback	1 Gig

Table 1.30. Broadband pickup station parameters.

Parameter	Value
Resolution of turn-by-turn measurements	10 $\mu\text{m}$
Distance between bunches	more than 20 ns
Cross-effect of bunches	less than 1%
Interface	1 GigE
Feedback	1 Gig

The measurement electronics measure the equilibrium orbit and the beam position in the 10 kHz band. The measurement electronics also perform turn-by-turn measurements. The electronics are equipped with a Gigabit Ethernet for control and accepting measurement results. Dedicated digital interfaces are provided for fast real-time feedback. Besides that, operation of the electronics requires synchronization signals. These signals are passed through optical communication channels.

A digital synchronization system is used; the transmission is carried out through optical channels. The synchronization system enables generation of reference signals tied to the phase of the revolution frequency with a discreteness of 10 ns; the jitter of reference pulses is not worse than 10 ps. The reference generator is a dedicated oscillator with the possibility of tuning the frequency from an external source. The pickup stations receive a synchronization signal in digital form and independently generate all necessary types of synchronization.

### 1.14.3 The optical diagnostics

The optical diagnostics is traditionally applied to measurement of radial, vertical and longitudinal beam sizes  $\sigma_x, \sigma_y, \sigma_z$  with acquisition of synchrotron radiation (SR) of the beams. The SR arrives from bending magnets of accelerator. It is desirable, if possible, to choose an observation point within an area with the maximum value of the vertical beta function  $\beta_y$ , which allows avoiding or mitigating the restrictions of spatial resolution determined by the diffraction limit.

It also seems reasonable to provide the possibilities for X-ray diagnostics, say, pinhole or interferometry.

Following these approaches, we propose choosing the positions of the optical diagnostics in the experimental area for acquisition of SR from the weak-field bending magnets. The diagnostics can be placed symmetrically for the electron and positron directions (Fig. 1.105). Computed values for magnet structure and beam dimensions at the proposed observation point for the electron/positron rings are presented in Table. 1.31.

Table 1.31. Design parameters of the magnet lattice and beam dimensions at observation points.

Parameter	Value
Beam energy	1.0 ÷ 2.5 GeV
Bending radius	100 m
Radial beta function, $\beta_x$	10 m
Vertical beta function, $\beta_y$	66 m
Radial beam size, $\sigma_x$	260 $\mu\text{m}$
Vertical beam size, $\sigma_y$	46 $\mu\text{m}$
Longitudinal beam size, $\sigma_z$	2.5 cm

### Parameters of synchrotron radiation at observation points

The spectra of synchrotron radiation in the radial plane at observation points at beam energies  $E_b = 1 \text{ GeV}$  and  $E_b = 2.5 \text{ GeV}$  are presented in Fig. 1.106. The arrow denotes the conditional boundary of the transmission of berillium foil. The optical area of the spectrum is shaded.

Figure. 1.107 represents the angular divergence of the SR for the X-ray (56 nm) and optical areas (500 nm) of the spectrum,  $E_b = 1 \text{ GeV}$ .

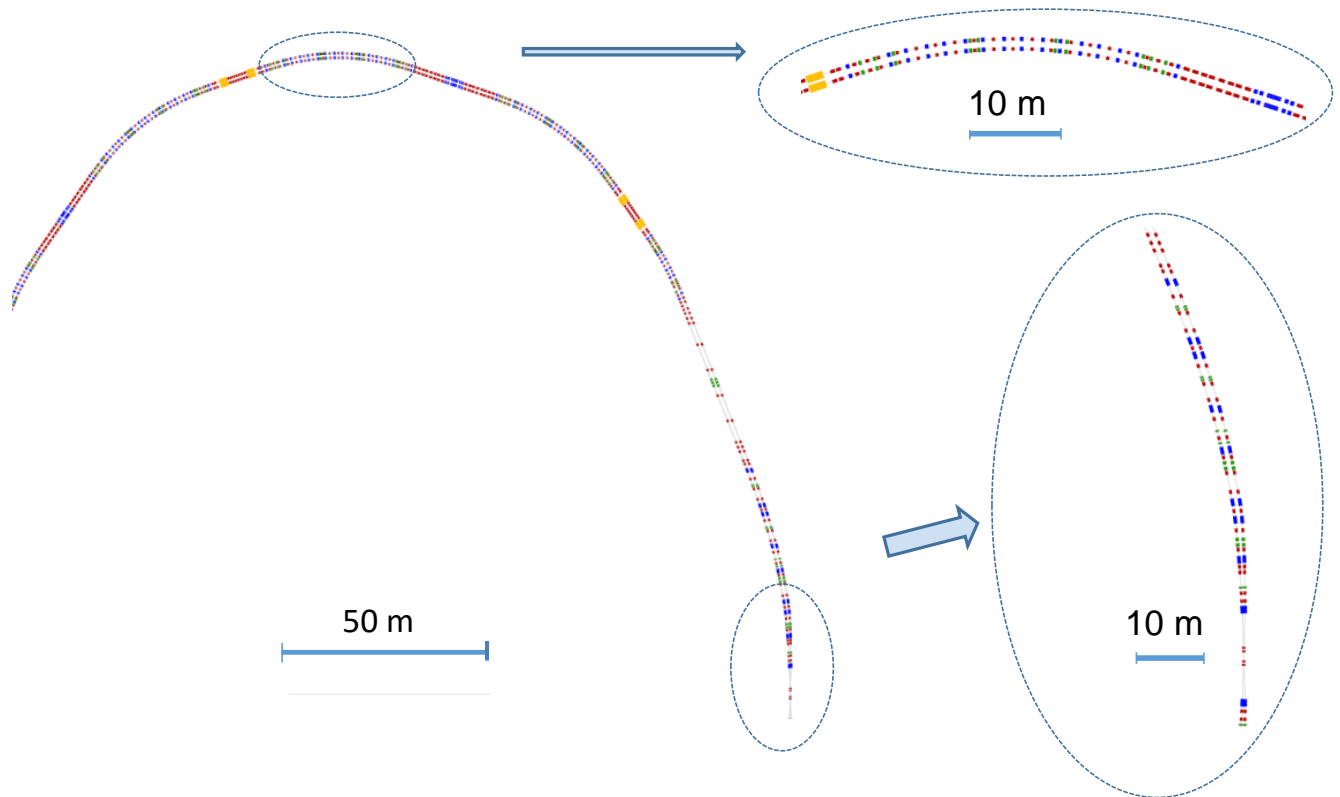


Figure 1.105. Scheme of optical diagnostics.

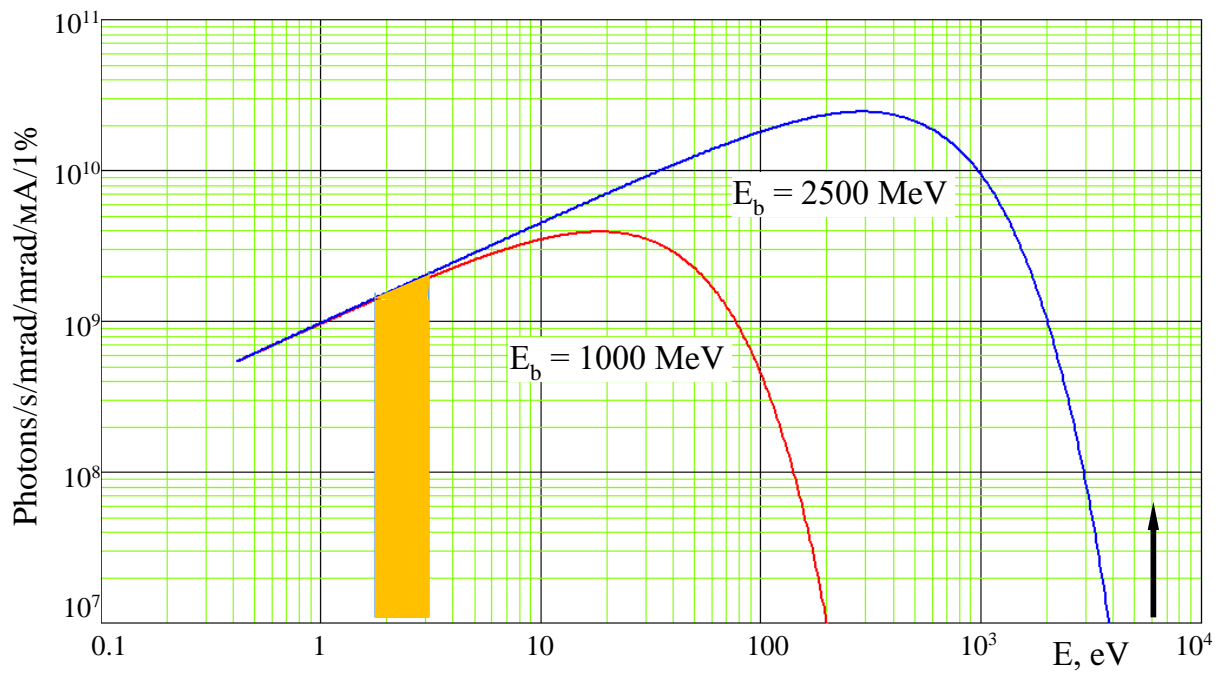


Figure 1.106. Spectrum of synchrotron radiation from bending magnet corresponding to bending radius  $R = 100$  m.

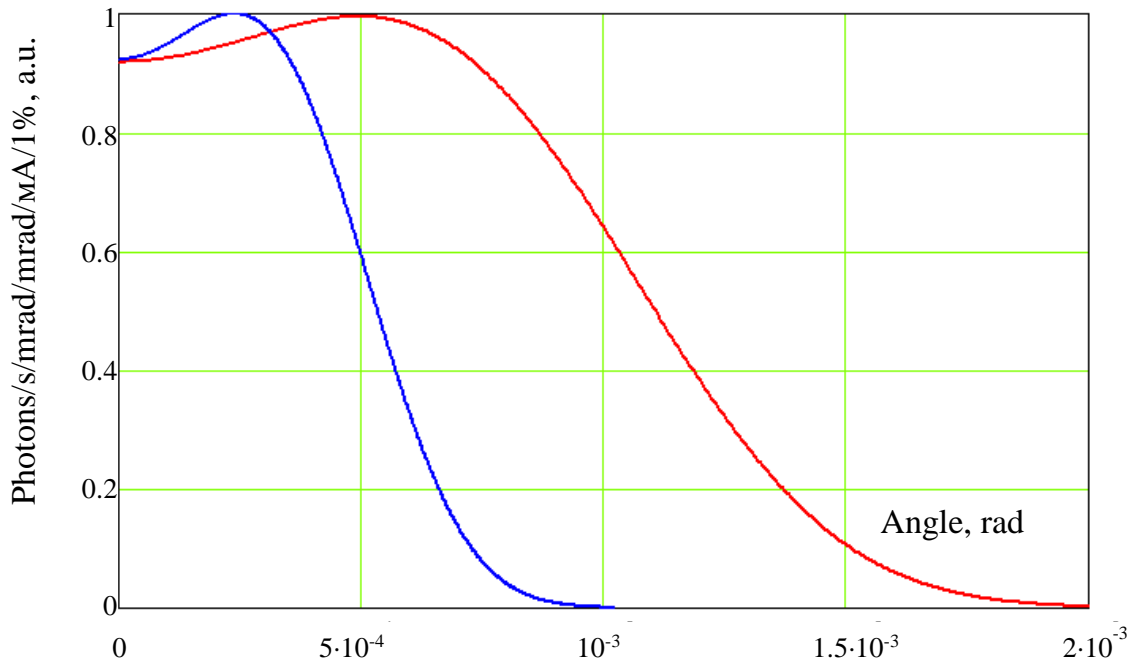


Figure 1.107. Vertical angular divergence of SR from weak-field bending magnet.

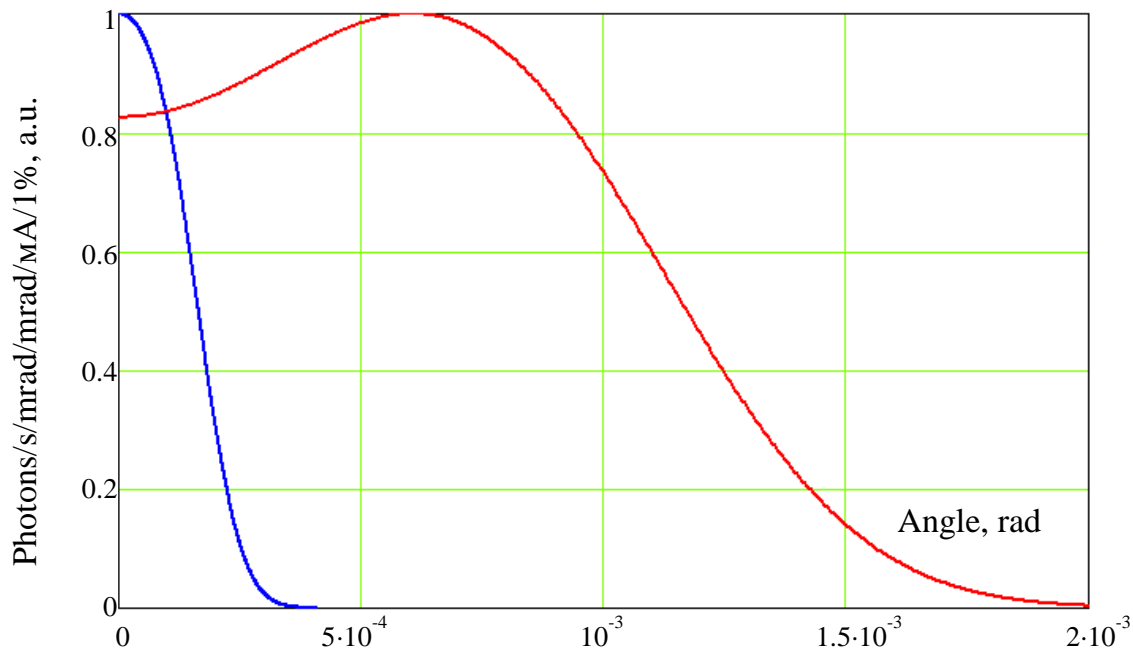
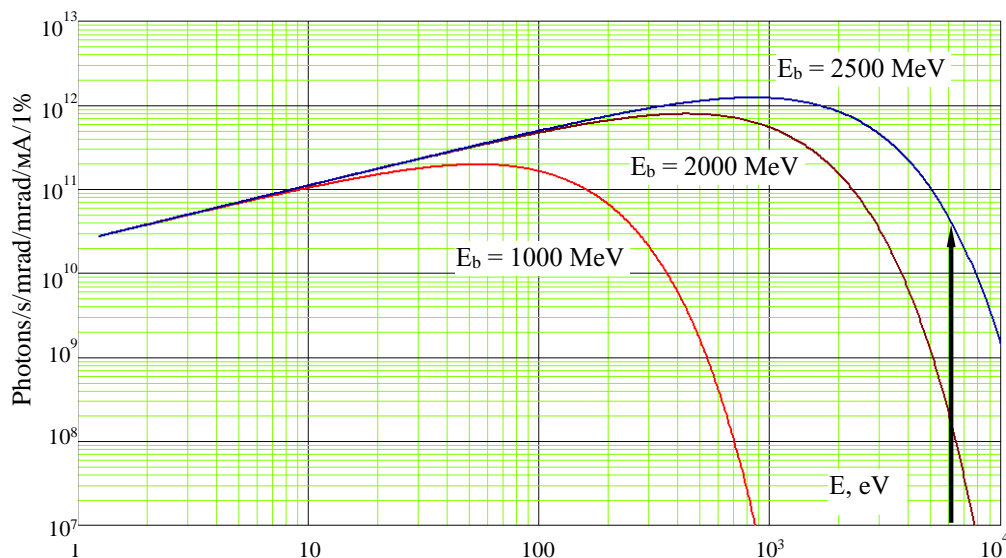


Figure 1.108. Vertical angular divergence of SR from weak-field bending magnet.

The same data are presented in Fig. 1.108 for  $E_b = 2.5$  GeV.

The crucial energy in the SR spectrum is about 1 keV even for  $E_b = 2.5$  GeV. These X-ray photons are strongly absorbed by the berillim foil. So, the application of X-ray diagnostics for weak-field bending magnets is unreasonable.

The spectrum of the SR from the strong-field bending magnets has a crucial energy about several keV for beam energy of  $E_b = 1, 2, 2.5$  GeV. It allows us to use the X-ray area of the spetrum for beam dignostics, Fig. 1.109.



The arrow denotes the conditional boundary of the transmission of berillium foil.

Figure 1.109. Spectrum of synchrotron radiation from strong-field bending magnet for beam energy  $E_b = 1, 2, 2.5$  GeV.

The average power  $P_{SR}$  of SR from a weak-field bending magnet within 1 mrad of solid angle is about 9 mW for a beam current of 1 mA and a beam energy of 2.5 GeV. The total power for a design beam current  $I_b = 1.7$  A is 6.3 W. It corresponds to a power density  $P_d = 10^3 P_{SR} (L\theta)^2 \approx 24$  W/cm<sup>2</sup> for a vertical angular divergence  $\theta \approx 3.2 \cdot 10^{-4}$  rad at a distance of 10 m from the observation point (Fig. 1.109). The area heated by the X-ray part of the SR will have the width of 3.5 mm, whereas the optical part of SR will diverge to a size of 25 mm. It is likely that the central part of a mirror reflecting the optical SR outward of the vacuum chamber of the acclerator has to be protected by a thin receiver of the SR. It will decrease the heat load on the mirror and allow us to avoid aberration of the mirror. That is also an additional argument against application of optical diagnostics based on strong-field bending magnets.

## Restrictions for measurements of the transverse beam sizes

The minimum vertical and radial beam sizes determined by the angular divergency of the SR and bending radius at the observation point are:

$$\sigma_d \approx \left( \frac{\lambda^2 R}{12\pi^2} \right)^{\frac{1}{3}} \approx 60 \mu\text{m},$$

$$\sigma_R \approx \frac{R\psi^2}{2} \approx 70 \mu\text{m},$$

where  $\lambda = 500 \text{ nm}$  is the wavelength of the light,  $R = 100 \text{ m}$  is the bending radius,  $\psi = 1.2 \cdot 10^{-3} \text{ rad}$  is the divergency of the SR. Thus, the projection optics does not allow us to determine the transverse beam sizes.

## The design and set of the optical diagnostics

The proposed design of the optical diagnostics is based on the similar system developed for the SIBERIA-2 storage ring (Fig. 1.110, 1.111). The Super Charm–Tau factory should have two diagnostics for the electron and positron rings.

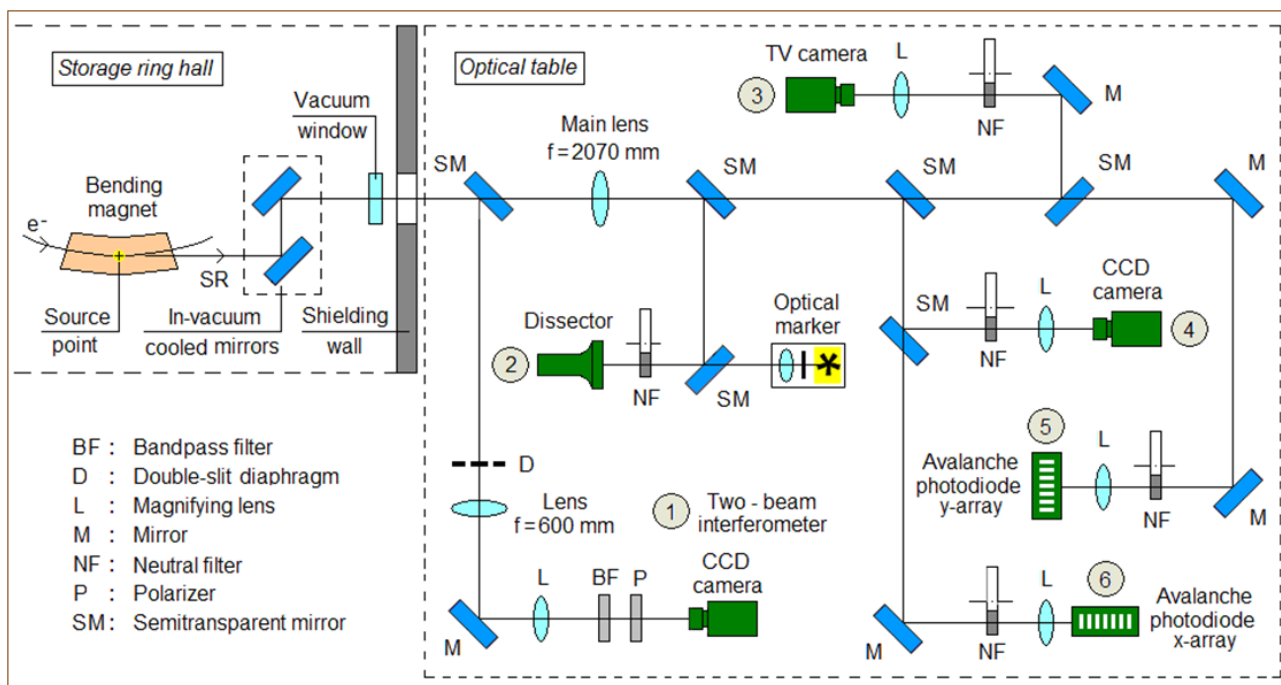


Figure 1.110. Optical scheme of optical diagnostics of SIBERIA-2 storage ring.

The optical diagnostics commissioned in 2013 on SIBERIA-2 controls the beam position at the observation point and measures the transverse beam dimensions. The light from the bending magnet is accepted. The SR parameters on SIBERIA-2 are similar to those at the Super Charm–Tau factory and we can expect that the heat load on the first cooled mirror placed inside the vacuum chamber will not significantly distort its surface. Nevertheless, some protection of the central area of the mirror is desirable.

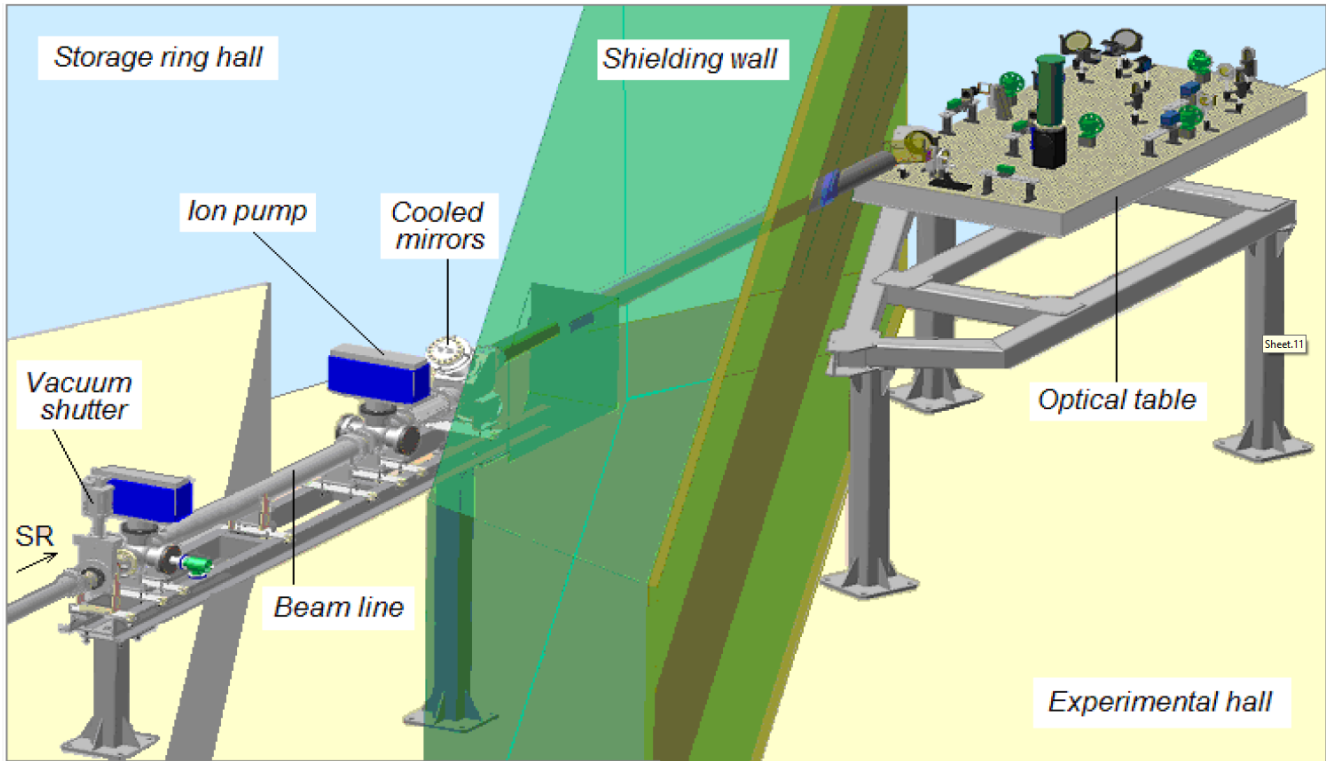


Figure 1.111. Layout of optical diagnostics.

The design of the optical diagnostics of SIBERIA-2 is as follows. The optical part of the SR spectrum reflected from the cooled mirror passes through the biological shield and is distributed between the six channels of the diagnostics, which are placed on the optical table (Fig. 1.111). The main lens and adapting lenses create a beam image on the detectors. The dynamic range of the detectors is expanded by switchable neutral filters.

The cooled mirror is placed at a distance of 6 m from the observation point. The silica window of the SR output is placed after the second mirror. The optical channel after the output passes through the biological shield to the optical table with the channels of the diagnostics.

### The set of the detectors of the optical diagnostics

The optical diagnostics contain six independent channels (Fig. 1.110).

(1) **The double-slit interferometer** is intended to measure of the vertical size of the beam with an accuracy of about 1  $\mu\text{m}$ .

RMS  $\sigma_x$  of the beam is devoted via RMS  $\sigma_\gamma$  of the spatial coherence  $\gamma$ ,

$$\sigma_x = \frac{\lambda L}{\pi D} \sqrt{\frac{1}{2} \ln \frac{1}{\sigma_\gamma}},$$

where  $L$  is the distance between the observation point and the slits, and  $D$  is the separation of the slits.

The intensity distribution of the interferometric pattern is devoted as

$$I(y) = I_0 \frac{\sin \alpha}{\alpha} \left( 1 + \exp \left( -\frac{2(\pi D \sigma_x)^2}{(\lambda L)^2} \right) \cos \left( \frac{2\pi D}{\lambda R} y \right) \right),$$

where  $\alpha = 2\pi a y / \lambda R$ , and  $a$  is the halfwidth of the slit.

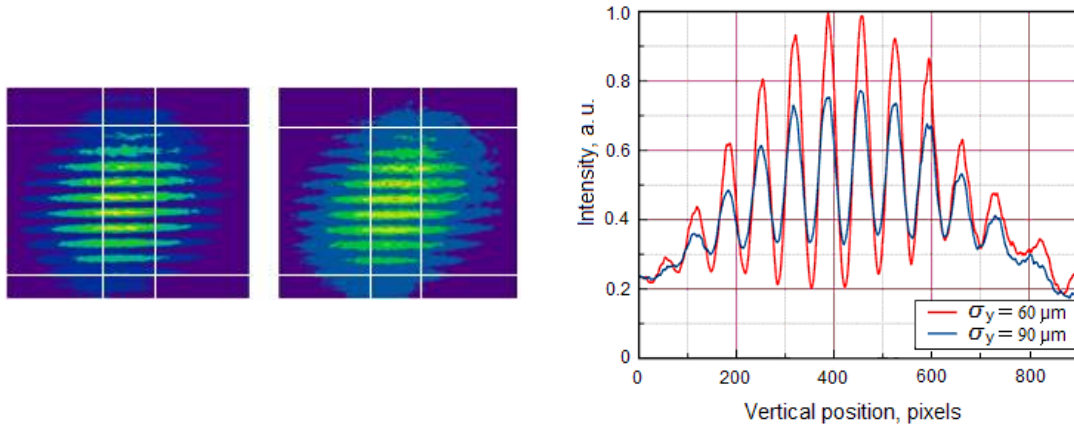


Figure 1.112. Left: interferometry patterns corresponding to vertical beam sizes of 60 and 90  $\mu\text{m}$ . Right: cross-section of patterns. The intensity distribution is integrated within the area restricted by the vertical lines.

The spatial resolution of the double-slit interferometer achieved on SIBERIA-2 is about 5  $\mu\text{m}$ . It is several fold worse than the declared accuracy of this method [89, 90, 91]. It is very likely that we have to replace the lenses in the optical layout of the interferometer on the mirrors to avoid the aberration caused by the dispersion.

**(2) The electron-optical dissector.** The main details of the operation principle of the device are described in [92, 93, 94] (Fig. 1.113, 1.114, 1.115, 1.116).

The temporal resolution of the dissector is about 3.5 ps [94], which allows us to measure the length of the beam with a precision of several percents.

The traditional streak camera [95, 96] can also be applied to some kinds of experiments.

**(3) The TV camera** is used for qualitative control of the beam transverse behaviour.

**(4) The CCD camera** (Prosilica GC 1290) with  $1280 \times 960$  pixels is used for acquisition of the transverse beam profile (Fig. 1.117). It is possible to measure the transverse beam sizes.

**(5, 6) The linear array of avalanched photodiodes** is intended for turn-by-turn measurement of the vertical and radial beam profiles (Fig. 1.118). This detector allows us to study the instabilities and non-linear dynamics of the beam [88].

This diagnostics set was well-proven on the electron-positron collider VEPP-4M [97] and synchrotron light source SIBERIA-2 [88] during several years. The experience obtained on these installations allowed us to declare that acquisition of an optical SR can reliably measure the transverse and longitudinal beam dimensions.

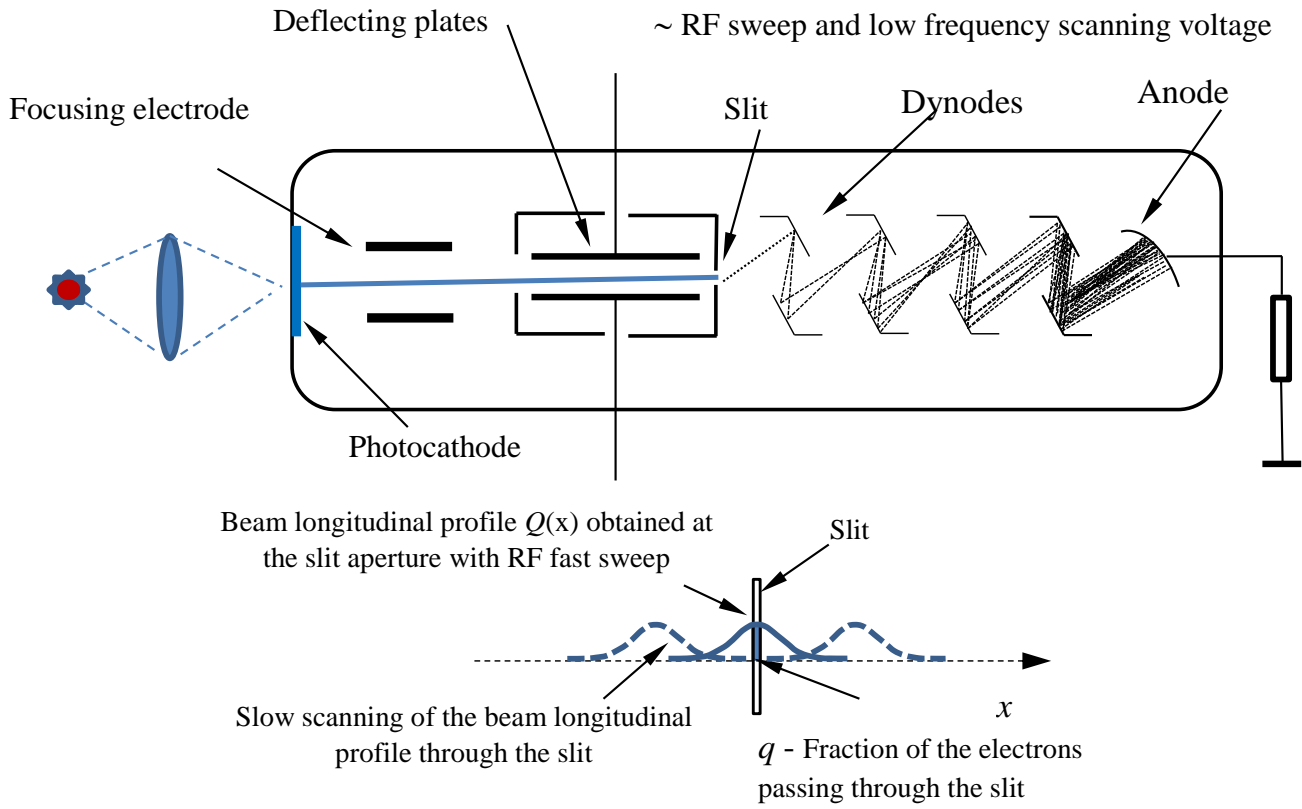


Figure 1.113. Simplified layout of dissector operation principle.

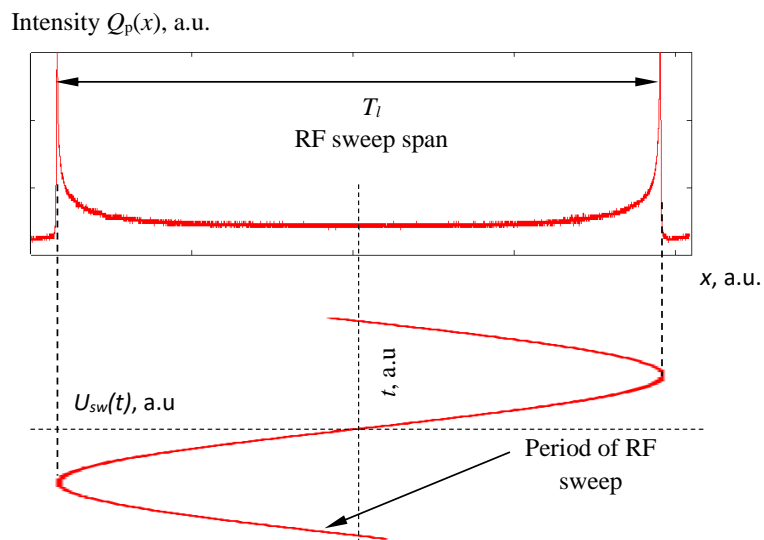


Figure 1.114. Calibration of temporal scale of dissector with permanent light source.

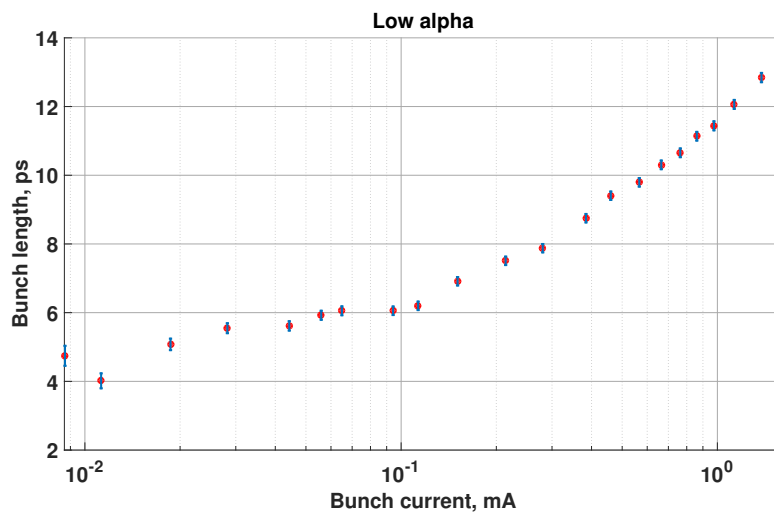


Figure 1.115. The current dependence of the beam length in low- $\alpha$  mode measured with the dissector on the MLS storage ring.

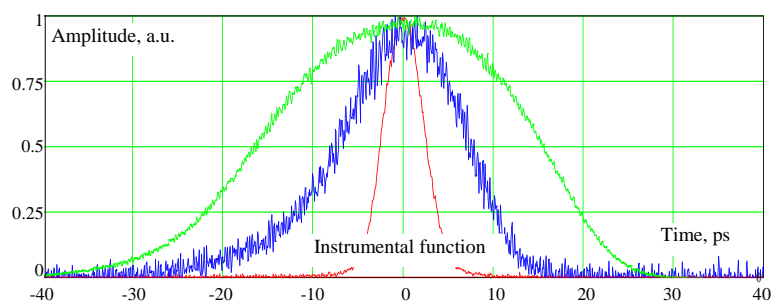


Figure 1.116. Longitudinal beam profile from the MLS storage ring accepted by the dissector.

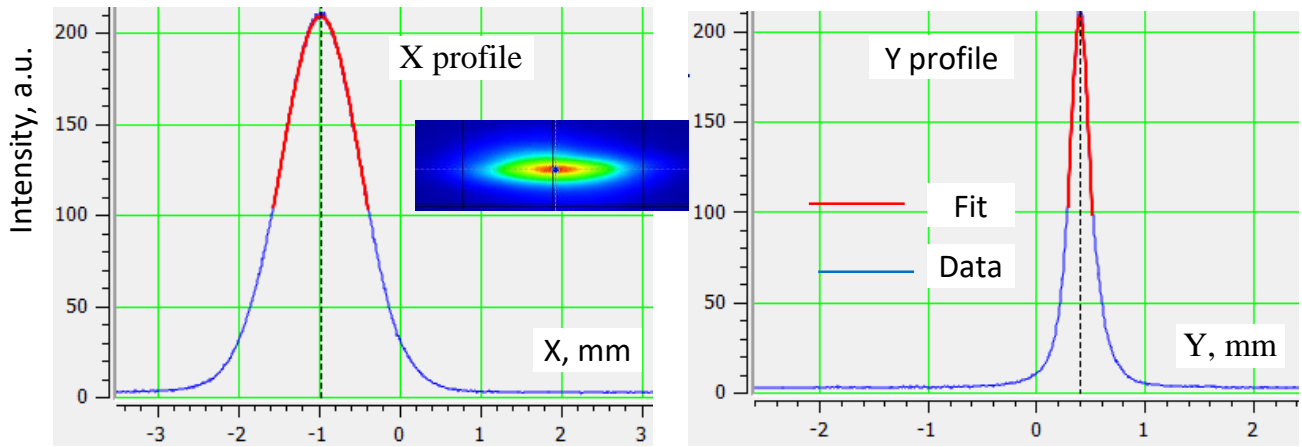


Figure 1.117. Beam image obtained with CCD camera and fitted by Gaussian distribution.

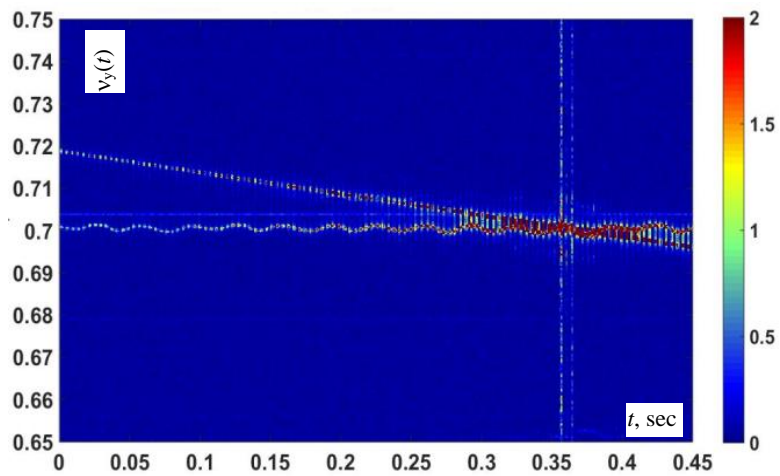


Figure 1.118. Measurement of vertical betatron tune by excitation with help of linear photodiode array (the vertical beam size is acquired) [88].

# Bibliography

- [1] P. Raimondi, “Status of the SuperB Effort”, presentation at the 2nd Workshop on SuperB Factory, LNF-INFN, Frascati, March 2006.
- [2] D. V. Pestrikov, NIM Phys. Res., Sect. A 336, 427, 1993.
- [3] K. Ohmi et al., Phys. Rev. ST Accel. Beams 7, 104401, 2004.
- [4] P. Raimondi, D. Shatilov, M. Zobov, “Beam-Beam Issues for Colliding Schemes with Large Piwinski Angle and Crabbed Waist”, LNF-07-003-IR, 2007, e-Print: physics/0702033.
- [5] P. Raimondi, D. Shatilov, M. Zobov, “Suppression of beam-beam resonances in Crab Waist collisions”, EPAC08-WEPP045, Proc. of EPAC-2008, Genoa, Italy, 23–27 June 2008.
- [6] D. Shatilov, E. Levichev, E. Simonov, M. Zobov, “Application of Frequency Map Analysis to Beam-Beam Effects Study in Crab Waist Collision Scheme”, Phys. Rev. ST Accel. Beams 14, 014001, 2011.
- [7] M. Zobov for DAFNE Collaboration Team, “DAFNE Operation Experience with Crab Waist Collision”, arXiv:0810.2211v1.
- [8] M. Zobov et al., “Test of crab-waist collisions at DAFNE Phi factory”, Phys.Rev.Lett.104:174801, 2010.
- [9] <http://www.lnf.infn.it/acceleratori/status/upto.html>.
- [10] P. Raimondi, M. Zobov, LNF INFN Technical Note G-58, 2003.
- [11] D. Shatilov, M. Zobov, ICFA Beam Dyn. Newslett. 37, 99, 2005.
- [12] A. Bogomyagkov, S. Glukhov, E. Levichev and P. Piminov, “Effect of the Sextupole Finite Length on Dynamic Aperture in the Collider Final Focus”, arXiv:0909.4872.
- [13] K. Brown, R. Servranckx, “First- and second-order charged particle optics”, SLAC-PUB-3381, 1984.
- [14] E. Levichev, N. Vinokurov, “Undulators and wigglers for production of radiation and other application”, Phys. Usp. 58 850–871, 2015.
- [15] R. Helm et al., “Evaluation of Synchrotron Radiation Integrals”, PAC-1973-0900, 1973.
- [16] J. Hagel, “Analytic Calculation of the Off Momentum Closed Orbit in Storage Rings with Insertions and Sextupoles”, CERN-LEP-TH-84-18.
- [17] D. Shatilov, Part. Accel. 52, 65, 1996.

- [18] K. Ohmi et al., "Coherent Beam-Beam Instability in Collisions with a Large Crossing Angle", *Phys. Rev. Lett.* 119, 134801, 2017.
- [19] D. Shatilov, "FCC-ee Parameters Optimization", *ICFA Beam Dyn. Newslett.* 72, 2017.
- [20] Ya. Derbenev et al., "Radiative Polarization: Obtaining, Control, Using", *Part. Accel.* vol. 8, 1978, pp. 115-126.
- [21] I. Koop et al, "Spin transparent Siberian snake and spin rotator with solenoids", *AIP Conf. Proc.*, vol. 915, 2007, pp. 948-954.
- [22] A. A. Zholents, V.N. Litvinenko, "On The Compensation of Solenoid Field Effects by Quadrupole Lenses", *DESY-L-TRANS-289*, 984.
- [23] V. Ptitsyn, PhD., BINP SB RAS, Novosibirsk, 1997.
- [24] V. Ptitsyn, Ya. Shatunov, S. Mane, "Spin response formalism in circular accelerators", *Nucl. Instrum. Meth. A608* (2009) pp. 225–233.
- [25] Ya. Derbenev, A. Kondratenko, "Polarization kinematics of particles in storage rings", *Sov. Phys. JETP*, vol. 37, 1973, pp. 968-973.
- [26] A. Chao, "Physics of Collective Beam Instabilities", Wiley, New York, 1993.
- [27] B. W. Zotter, S. A. Kheifets, "Impedances and Wakes in High-Energy Particle Accelerator", World Scientific, Singapore, 1998.
- [28] N. S. Dikansky, D. V. Pestrikov, "The Physics of Intense Beams and Storage Rings", AIP Press, 1994.
- [29] B. Zotter, "Potential-Well Bunch Lengthening", *CERN SPS/81-14 (DI)*, Geneva, Switzerland, 1981.
- [30] F. Sacherer, *IEEE Trans. Nucl. Sci*, NS-24 (1977) p. 1393.
- [31] E. Keil, W. Schnell, *CERN ISR-TH-RF 69/48*, 1969.
- [32] D. Boussard, "Observation of Microwave Longitudinal Instabilities in the SPS", *CERN-Lab II/RF/75-2*, 1975.
- [33] J. A. Clarke, "Bunch Lengthening Thresholds on the Daresbury SRS", *Proc. of PAC-95, Dallas, 1995 (WAC23)*.
- [34] J. M. Byrd, J. N. Corlett, T. Renner, "Single Bunch Collective Effects in the ALS", *Proc. of PAC-95, Dallas, 1995 (WXE06)*.
- [35] Y.-C. Chae et al., "Measurement of the Longitudinal Microwave Instability in the APS Storage Ring", in *Proc. of PAC-2001, Chicago, 2001 (TPPH068)*.
- [36] G. De Ninno et al., "Longitudinal Single-Bunch Instabilities for Different Operation Energies at ELETTRA", in *Proc. of PAC-2003, Portland, 2003 (WPAG018)*.
- [37] W.K.H. Panofsky, W. A. Wenzel, "Some considerations concerning the transverse deflection of charged particles in radio-frequency fields", *Rev. Sci. Instrum.* 27 (1956), p. 967.

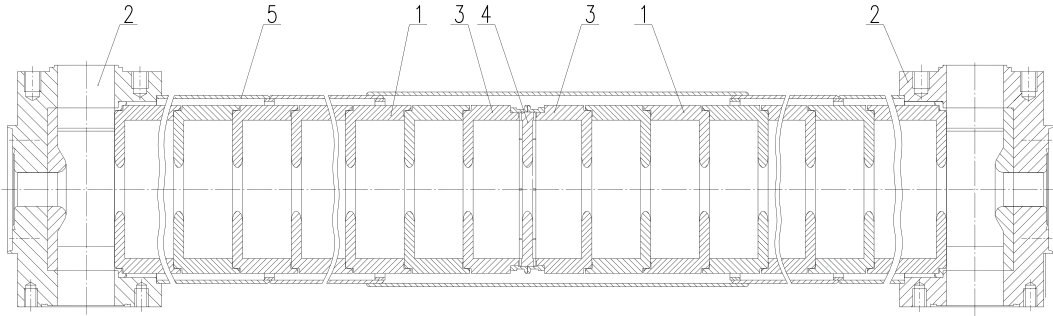
- [38] Y. Cai et al., “Potential-well distortion, microwave instability, and their effects with colliding beams at KEKB”, *Phys. Rev. ST Accel. Beams*, Vol. 12, 061002 (2009).
- [39] A. Novokhatski, M. Sullivan, “Loss Factor of the PEP-II Rings”, in *Proc. of EPAC-2008, Genoa, 2008 (TUPP055)*.
- [40] T. Ieiri et al., “Impedance Measurements in the KEKB”, in *Proc. of EPAC-2000, Vienna, 2000 (TUP4A12)*.
- [41] F.-J. Decker et al., “Tune Feed-Forward for PEP-II”, in *Proc. of PAC-2001, Chicago, 2001 (RPPH136)*.
- [42] H. Wiedemann, “Particle Accelerator Physics II”, Berlin, Springer, 1999.
- [43] F. Sacherer, CERN/MPS-BR/73-3, Geneva, Switzerland, 1973.
- [44] A. Fabris, C. Pasotti, M. Svandrik, “Coupled Bunch Instability Calculations for the ANKA Storage Ring”, *Proc. of EPAC-1998, Stockholm, 1998*.
- [45] F. Sacherer, CERN/PS/BR 76-21, Geneva, Switzerland, 1976.
- [46] Y. Baconnier, G. Brianti, “The Stability of Ions in Bunched Beam Machines”, CERN/SPS/80-2(DI), Geneva, Switzerland, 1980.
- [47] Y. Ohnishi et al., “Study of Fast Ion Instability at KEKB Electron Ring”, *Proc. of EPAC-2000, Vienna, Austria, 2000*.
- [48] T. O. Raubenheimer, F. Zimmermann, “Fast Beam-ion Instability I. Linear Theory and Simulations”, *Phys. Rev. E* 52, 5487 (1995).
- [49] G. V. Stupakov, T. O. Raubenheimer, F. Zimmermann, “Fast Beam-ion Instability II. Effect of ion decoherence”, *Phys. Rev. E* 52, 5499 (1995).
- [50] P. Emma, T. Raubenheimer, F. Zimmermann, “Emittance Dilution by Ions in the SLC Arcs”, *Proc. of EPAC-1994, London, 1994*.
- [51] K. Ohmi, F. Zimmermann, “Head-Tail Instability Caused by Electron Clouds in Positron Storage Rings”, *Phys. Rev. Lett.* Vol. 85 No. 18, 2000.
- [52] K. Ohmi, “Beam-photoelectron Instability at KEKB”, KEK Prepr. 98-17, 1998.
- [53] K. Ohmi, S. Matsumoto, “Beam-photoelectron Instability at KEKB: Applying a magnetic field”, KEK Prepr. 98-37, 1998.
- [54] K. Ohmi, “Beam-Photoelectron Interactions in Positron Storage Rings”, *Phys. Rev. Lett.* Vol. 75 No. 8, 1995.
- [55] E. Perevedentsev, “Head-Tail Instability Caused by Electron Cloud”, *Proc. of ELOUD-2002, CERN-2002-001, Geneva, 2002*, p. 171–194.
- [56] D. Bulfone, “Overview of Fast Beam Position Feedback Systems”, *Proc. of EPAC 2008, Genoa, 2008*.
- [57] V. Smaluk et al., “Feedback for suppression of single-bunch transverse instability in electron-positron storage rings”, *Journal of Instrumentation* 7 (2012) P01007.

- [58] “Present status of KEKB project”, Shin-ichi Kurokawa, Proceedings of APAC-1998.
- [59] J. M. Dorfan, “PEP-II status report”, SLAC-PUB-7919, June 1998.
- [60] T. Kageyama et al, “The ARES cavity for KEKB”, Proceedings of APAC-1998.
- [61] Y. Morita, “KEKB superconducting accelerating cavities and beam studies for Suser-KEKB”, Proceedings of IPAC-2010.
- [62] R. Rimmer et al, “High-power RF cavity R&D for the PEP-II B factory”, Proceedings of EPAC-1994.
- [63] P. Corredoura, “Architecture and performance of the PEP-II Low-Level RF system”, Proceedings of PAC-1999.
- [64] T. Furuya, “Recent status of the superconducting cavities for KEKB”, Proceedings of the 1999 Workshop on RF Superconductivity, La Fonda Hotel, Santa Fe, New Mexico, USA.
- [65] D. Teytelman, “Beam-loading compensation for Super B-factories”, Proceedings of PAC-2005.
- [66] V. V. Anashin et al, “An installation for magnetron deposition of getter coatings in narrow-aperture chambers”, *Instrum Exp Tech*, 2009, 52, 882.
- [67] C. Benvenuti et al, “Vacuum properties of TiZrV non-evaporable getter films”, *Vacuum*, vol. 60, p. 57, 2001.
- [68] I. R. Collins et al, “A photodesorption study of a TiZrV coated stainless steel vacuum chamber”, EPAC-2002, Paris, France, June 2002, Proc. of EPAC-2002, pp. 2550-2552.
- [69] V. V. Anashin et al, “Investigation of photo-desorption in a vacuum chamber with deposited TiZrV getter film”, Proceeding of SR-2002 conference, 15-19 July 2002, BINP, Novosibirsk, Russia.
- [70] B. Henrist et al, “The Secondary Electron Yield of TiZr and TiZrV Non-Evaporable Getter Thin Film Coatings”, *Applied Surface Science* Volume 172, Issues 1-2, 1 March 2001, pp. 95-102.
- [71] Y. Suetsugu et al, “First experimental and simulation study on the secondary electron and photoelectron yield of NEG materials (Ti-Zr-V) coating under intense photon irradiation”, *Nuclear Instruments and Methods in Physics Research Section A: Accelerators, Spectrometers, Detectors and Associated Equipment*, vol. 554, Issues 1-3, 1 December 2005, pp. 92-113.
- [72] K. Ohmi, F. Zimmermann, E. Perevedentsev, “Wake-field and fast head-tail instability caused by an electron cloud”, *Phys. Rev. E* 65, 016502, 2002.
- [73] B. Henrist et al, “Secondary electron emission data for the simulation of electron cloud”, Proc. Mini Workshop on Electron Cloud Simulations for Proton and Positron Beams (E-CLOUD’02), Geneva, 15-18 April 2002, pp. 75-78, CERN Report: CERN-2002-001, 2002.
- [74] R. Cimino, I. Collins, V. Baglin, “VUV photoemission studies of candidate Large Hadron Collider vacuum chamber materials”, *Physical review special topics – accelerator and beams*, v.2, 063201, 1999.

- [75] V. V. Anashin et al, “Magnetic and electric field effects on the photoelectron emission from LHC beam screen material”, Vacuum, ISSN 0042207X, p. 255-260, vol. 60, N 1-2, January-February 2001.
- [76] M. Taborelli et al, “Nine years of carbon coating development for the SPS upgrade: achievements and heritage”, CERN-ACC-2016-0010.
- [77] S. Calatroni et al, “First accelerator test of vacuum components with laser-engineered surfaces for electron-cloud mitigation”, PHYSICAL REVIEW ACCELERATORS AND BEAMS 20, 113201, 2017.
- [78] M. Green, B. Strauss, “The cost of superconducting magnets as a function of stored energy and design magnetic induction times the field volume”, IEEE Trans. on Appl. Supercond, vol. 18, no. 2, 2008, pp. 248–251.
- [79] O. V. Anchugov et al., “Experiments on the physics of charged particle beams at the VEPP-4M electron-positron collider”, J. Exp. Theor. Phys., vol. 109, pp. 590–601, 2009. Zh. Eksp. Teor. Fiz. 136, 690 (2009).
- [80] Q. Qing et al., ““Beam dynamics studies on BEPC-II storage rings at the commissioning stage””, Chinese Physics C, vol. 33, no. S2, pp. 65–70, 2009.
- [81] D. E. Berkaev et al., ““The VEPP-2000 electron-positron collider: First experiments””, J. Exp. Theor. Phys., vol. 113, no. 2, pp. 213–220, 2011.
- [82] V. E. Blinov et al., “Beam energy and energy spread measurement by Compton backscattering of laser radiation at the VEPP-4M collider”, ICFA Beam Dyn. Newslett., vol. 48, pp. 195–207, 2009.
- [83] E. Abakumova et al., “The beam energy measurement system for the Beijing electron-positron collider”, Nucl. Instr. Meth. Phys. Res. A, vol. 659, no. 1, pp. 21–29, 2011.
- [84] E. Abakumova et al., “A system of beam energy measurement based on the Compton backscattered laser photons for the VEPP-2000 electron-positron collider”, Nucl. Instr. Meth. Phys. Res. A, vol. 744, pp. 35–40, 2014.
- [85] N. Muchnoi, “Measurement of beam polarisation and beam energy in one device”, in 58th ICFA Advanced Beam Dynamics Workshop on High Luminosity Circular  $e^+e^-$  Colliders, 2016.
- [86] A. N. Skrinskii and Yu. M. Shatunov, “Precision measurements of masses of elementary particles using storage rings with polarized beams”, Soviet Physics Uspekhi, vol. 32, no. 6, pp. 548–554, 1989.
- [87] V. Blinov et al., “Review of beam energy measurements at VEPP-4M collider””, Nucl. Instr. Meth. Phys. Res. A, vol. 598, no. 1, pp. 23–30, 2009.
- [88] O. Meshkov et al, “A new station for optical observation of electron beam parameters at electron storage ring SIBERIA-2”, Journal of Instrumentation 12/2016; 11(12):P12015-P12015., DOI:10.1088/1748-0221/11/12/P12015.
- [89] T. Mitsuhashi, “Beam size measurement by use of SR interferometers”, Proc. of BIW 2004, Knoxville, p. 3, 2004.

- [90] T. Mitsuhashi, “Beam Profile and Size Measurement by SR Interferometer in Beam measurement”, Ed. By S. Kurokawa et al., pp. 399-427, World Scientific (1999).
- [91] T. Naito and T. Mitsuhashi, “Very Small Beam-Size Measurement by a Reflective Synchrotron Radiation Interferometer”, *Phys. Rev. ST Accel. Beams*, V. 9, No. 12, p. 122802, 2006.
- [92] E.I. Zinin et al, “Stroboscopic method of electro-optical picosecond-resolution chronography and its application in synchrotron radiation experiments”, *Nucl. Instrum. Meth.* 208 (1983) 439.
- [93] E.I. Zinin and O.I. Meshkov, *JINST*, 2015 1748-0221 10 P10024, doi:10.1088/1748-0221/10/10/P10024.
- [94] E.I. Zinin et al, “Direct temporal-resolution calibration of new-generation dissector”, *Journal of Instrumentation* 03/2016, 11(03), T03001-T03001, DOI:10.1088/1748-0221/11/03/T03001.
- [95] N.S. Vorobev et al, “Recording Vavilov–Cherenkov radiation in a linear accelerator using a picosecond streak camera”, *Quantum Electronics* 09/2016, 46(9):860-862, DOI:10.1070/QEL16080.
- [96] A.K. Vereshchagin et al, “Recording the synchrotron radiation by a picosecond streak camera for bunch diagnostics in cyclic accelerators”, *Quantum Electronics* 01/2016; 42:185-188.
- [97] P.A. Piminov et al, “Synchrotron radiation research and application at VEPP-4”, *Physics Procedia* 12/2016, 84, DOI:10.1016/j.phpro.2016.11.005.
- [98] R.M. Klein, G. Ulm, “The Metrology Light Source – an electron storage ring dedicated to metrology”, *Proceedings of EPAC2006, THPLS019*, Edinburg, Scotland.





Notation: 1 is regular acceleration cell, 2 is wave-type transformer, 3 is transition (connection) acceleration cell, 4 is connecting diaphragm, 5 is cooling jacket

Figure 2.2. Acceleration structure.

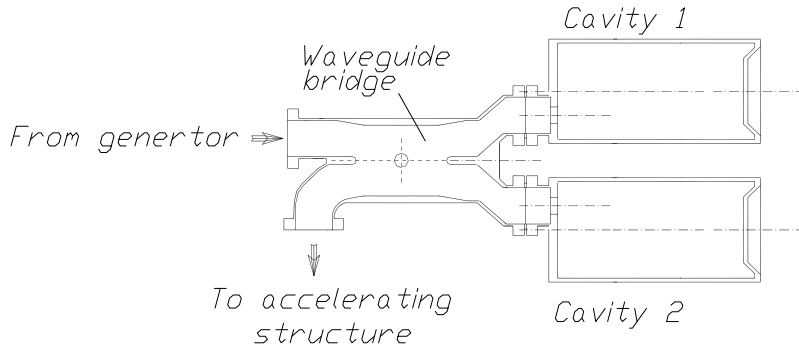


Figure 2.3. Scheme of SLED power multiplication system.

Table 2.1. Main parameters of klystron.

Parameter	Value
Operating frequency	2856 MHz
Repetition rate	up to 50 Hz
Peak power	50 MW
Pulse duration	5 $\mu$ s

Table 2.2. Min parameters of SLED power multiplication system.

Parameter	Value
Diameter, $D$	196 mm
Height, $H$	346.9 mm
Operating frequency, $f_0$	2856 MHz
Oscillation type	H <sub>015</sub>
Q factor, $Q_0$	80000
Coupling, $\beta$	3.6
Power multiplication factor, $K_P$	5

Table 2.3. Main parameters of acceleration structure.

Parameter	Value
Operating frequency, $f_0$	2856 MHz
Inner cell diameter, $2b$	83.75 mm
Iris aperture diameter, $2a$	25.9 mm
Thickness of diaphragm, $t$	6 mm
Period, $D$	34.99 mm
Oscillation type, $\theta$	$2\pi/3$
Relative phase velocity, $\beta_{ph}$	1
Relative group velocity, $\beta_{gr}$	0.021
Section length, $L$	2.93 m
Total number of cells	85
Unloaded Q factor, $Q_0$	13200
Shunt impedance, $R_{sh}$	51 MOhm/m
Unloaded time, $\tau_{0a} = 2Q_0/\omega_0$	1.471 $\mu$ s
Attenuation parameter, $\alpha_e = 1/\tau_{0a}V_{gr}$	0.108 $m^{-1}$
Filling time, $T_f = L/V_{gr}$	0.465 $\mu$ s

The acceleration structure is a diaphragm-type waveguide with a  $2\pi/3$  oscillation mode. Due to the selected parameters of the SLED power multiplication system, the structure can operate in the quasi-uniform acceleration field distribution mode. Figure 2.4 shows the distribution of reflected power from the SLED system. The distribution of the amplitude of the electric field along the accelerating structure is demonstrated in Fig. 2.5. In this case, half of the power of the SLED system arrives at the input.

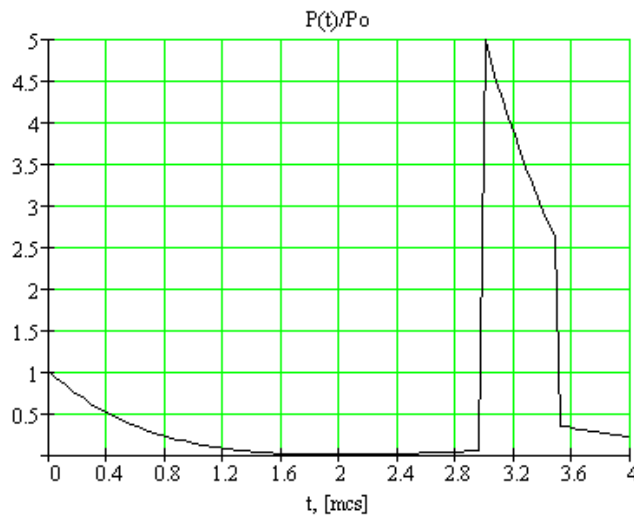
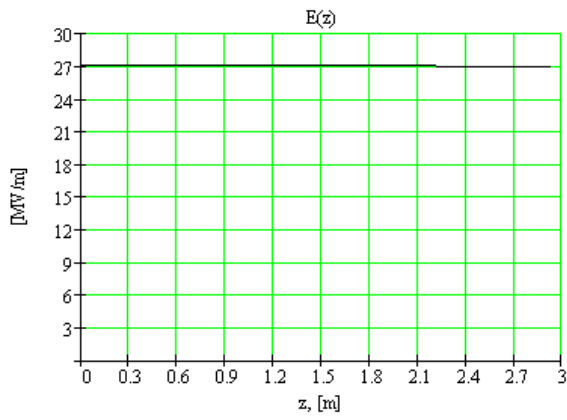
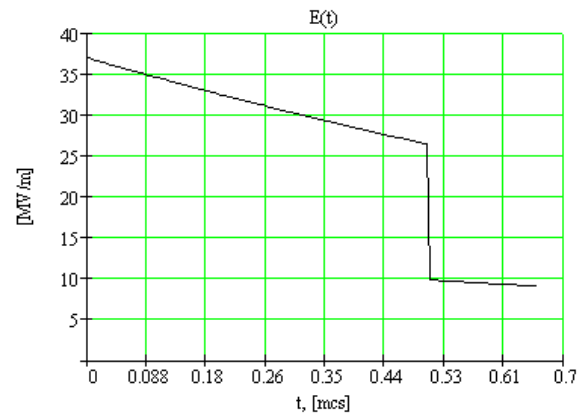


Figure 2.4. Reflected power from SLED system.



(a) distribution along structure



(b) initial value

Figure 2.5. Amplitude of electric field in acceleration structure.

As can be seen in Fig. 2.5, the amplitude of the electric field along the acceleration structure is 27 MV/m. The maximum acceleration rate is 27 MeV/m, and the beam energy gain after the passage of the acceleration structure is 81 MeV. With reserve, of 15%, an acceleration rate of 23 MeV/m and an energy gain of 67 MeV can be considered as operating values. With the above parameters, the injector circuit can be represented as in Fig. 2.6; parameters of the regular acceleration module are given in Table 2.4.

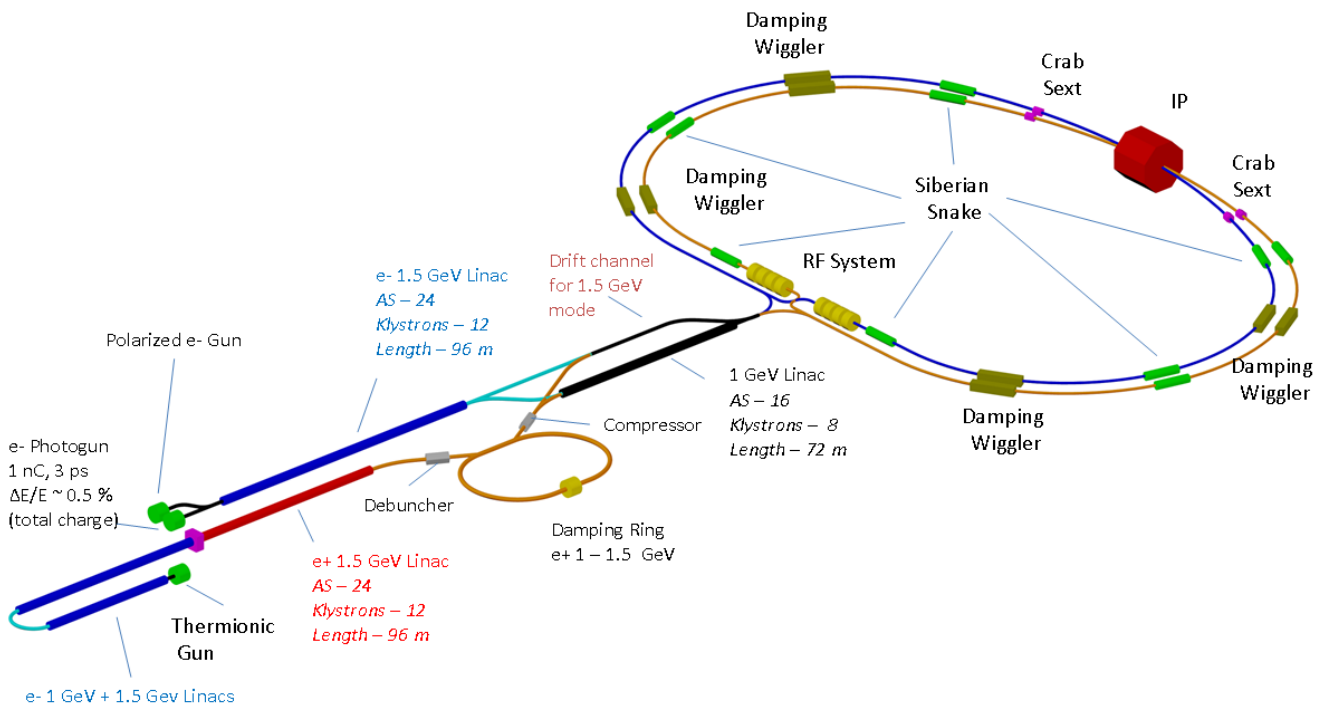


Figure 2.6. Scheme of injector of Super Charm – Tau factory.

Table 2.4. Acceleration module parameters.

Parameter	Value
Number of klystrons	1
Operating frequency, $f_0$	2856 MHz
Repetition rate	up to 50 Hz
Peak power of klystron	50 MW
Pulse duration	3.5 $\mu$ s
Number of SLED-type power multiplication systems	1
Power multiplication factor	5
SLED output power	250 MW
Number of acceleration structures	2
Input power of acceleration structure	125 MW
Acceleration rate	23 MeV/m
Energy gain per module	134 MeV

## 2.2 Source of operation electrons

The main parameters of the injected electron beam are given in Table 2.5. To attain the given values, the electron source must produce beams with emittance less than 10 nm and length of no more than  $\sigma_z = 1$  mm. Such small emittance is necessary since it can increase at the initial stages of acceleration because of various aberration effects and Coulomb fields. With a minimum injection energy of 1.5 GeV, the normalized emittance should be less than 30 mm  $\cdot$  rad. The beam length is one of the factors that determine the energy spread. When  $\sigma_z = 1$  mm, the nonlinearity of the accelerating field leads to a value  $\delta W/W = \pm(1 - \cos(\pi\sigma_z/\lambda_0)) = \pm 0.05\%$ , where  $\lambda_0 = 105$  mm is the wavelength of the accelerating field at a frequency  $f_0 = 2856$  MHz. In actual practice, various phase instabilities can occur during acceleration, which will lead to increase in the energy spread in the beam. For their effect to be smaller, the beam should not have a large length.

Table 2.5. Parameters of injected beam.

Parameter	Value
Number of particles per bunch	$2 \cdot 10^{11}$
Energy	1.5 $\div$ 2.5 GeV
Emittance	10 nm
Root-mean-square energy spread	0.1%

It is suggested that the electron source should be a microwave photo gun based on an acceleration structure with parallel coupling, a scheme of which is depicted in Fig. 2.7. The microwave power from the klystron goes into the common cavity, from which the accelerating cavities are excited. The magnetic field performs coupling of the excitation cavity with the accelerating cavities through the coupling holes. The focusing axially-symmetric alternating magnetic field on the beam axis is created by permanent magnets with radial magnetization, which are inserted into the iron yoke. The copper pins are to adjust the eigenfrequency of the exciting cavity [1].

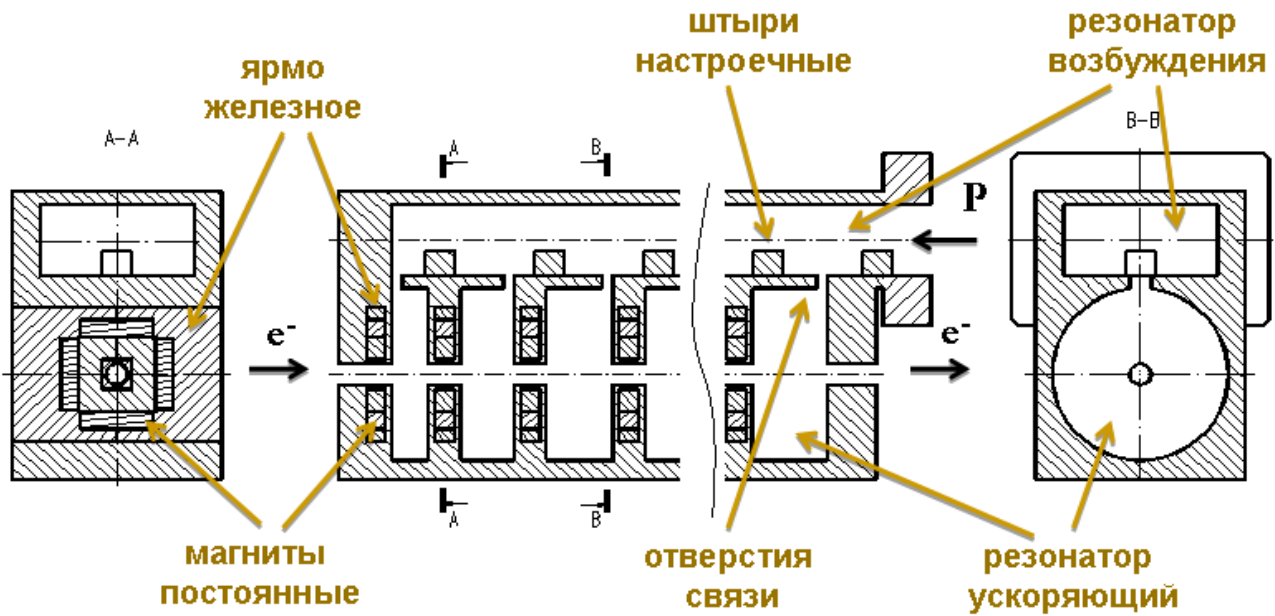


Figure 2.7. Scheme of acceleration structure with parallel coupling.

It is proposed to use in electron sources an indium seal between the accelerating cells of the structure [2]. The photocathode must be part of the wall of the flange of the first accelerating cavity. Such a system will have the following properties:

- The accelerating cavities are easily calculated and optimized, which enables detailed calculation and selection of individual cavity parameters necessary for obtaining a high-quality beam.
- The lengths of the cavities can be varied with keeping a  $\pi$  oscillation mode, which provides a high effective shunt impedance.
- Among the known structures, this structure has the smallest apertures for excitation and flight of beam, which enables compensation for the non-linear and transverse components of the electromagnetic field, which may increase the beam emittance.
- As focusing elements, one can use permanent magnets placed directly between the accelerating cavities, and thus keep a small- dimension beam near the axis.
- Any distribution of field amplitudes in the cavities can be set via optimization of the process of beam acceleration.
- The variant with indium sealing and a small number of cavities enables multiple tuning and optimization procedures and thus precise settings.

The particle dynamics were modeled using  $3 + 1/2$  accelerating cavities of the structure with parallel coupling, a fly-hole diameter of 10 mm, and permanent focusing magnets. Figure 2.8 shows the distributions of the longitudinal components of the electric and magnetic fields along the cavity axis. At the output of the electron source there was a matching solenoid. The initial beam parameters used in the modeling are given in Table 2.6.

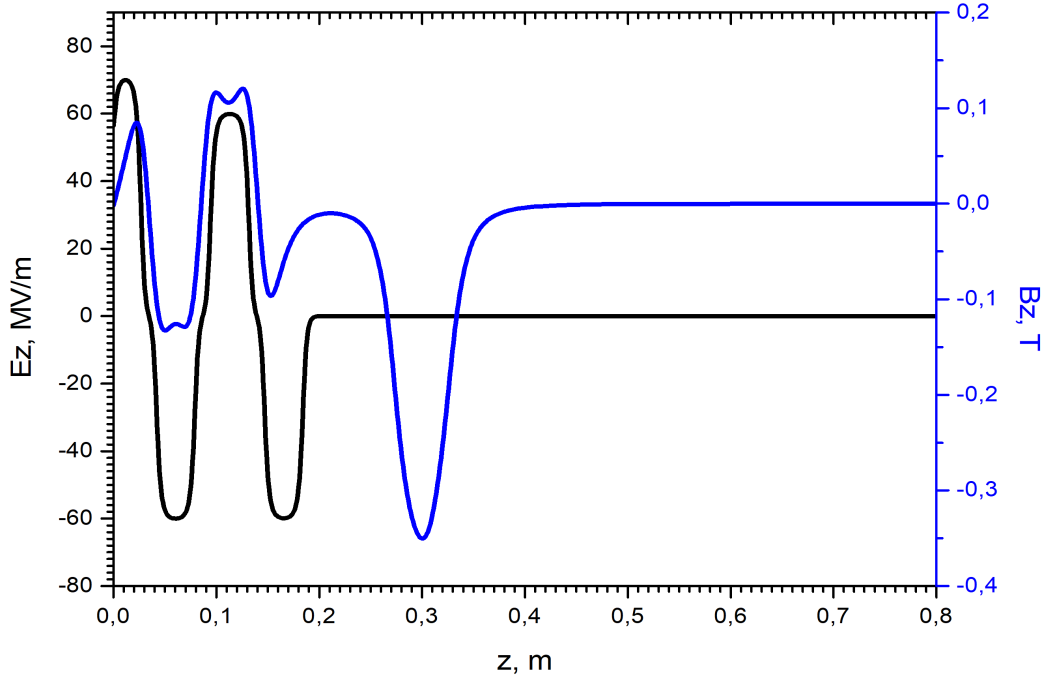


Figure 2.8. Distributions of longitudinal components of electric and magnetic fields along cavity axis.

Table 2.6. Initial beam parameters used in modeling of particle dynamics.

Parameter	Value
Initial emittance	0.4 mm · mrad
Initial kinetic energy	0.6 eV
Beam charge	1.5 nC
Operation frequency	25 Hz
Size of laser spot on cathode	5 mm
Laser pulse duration	7 ps
Magnetic field on cathode	0 T
Electric field on cathode	70 MV/m
Input microwave power	10 MW

The modeling of the particle dynamics using the **ASTRA** code [3] gave the envelope of the transverse beam size, shown in Fig. 2.9. The resulting output parameters are given in Table 2.7.

Table 2.7. Beam parameters at output of microwave photo gun.

Parameter	Value
Beam charge	1.5 nC
RMS beam length	1 mm
Normalized emittance	3 mm · mrad
Energy	6.5 MeV

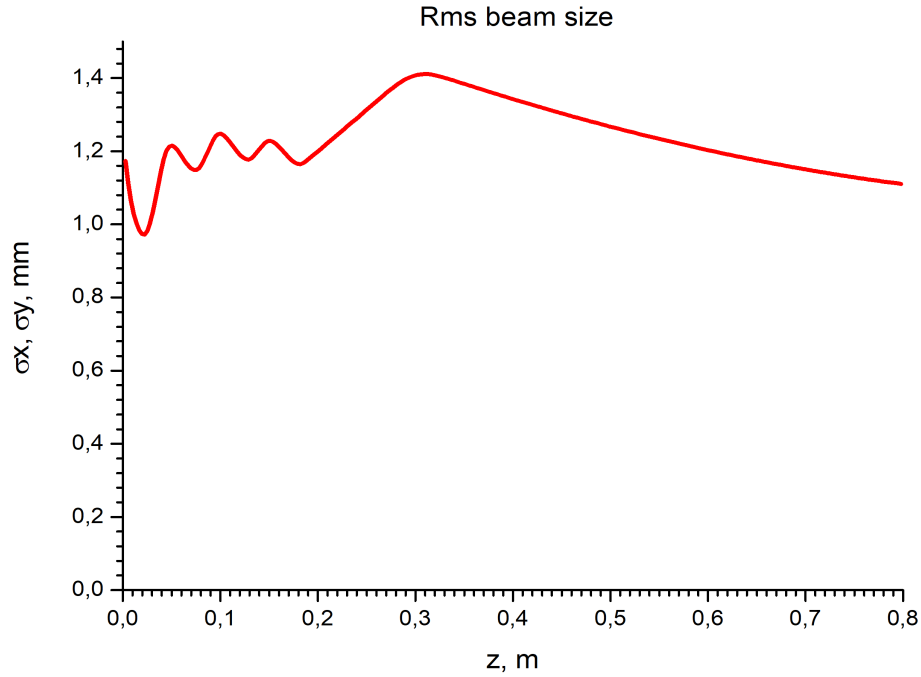
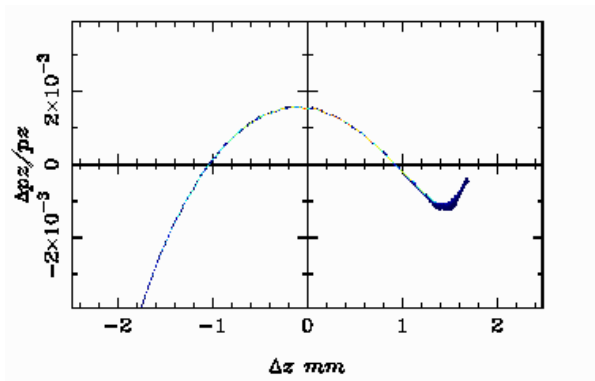
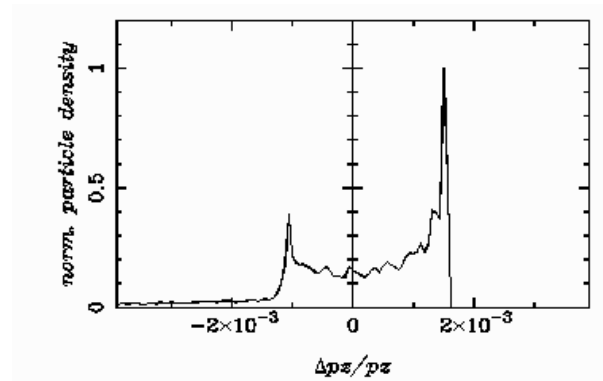


Figure 2.9. Root-mean-square deviation of transverse beam size.

The energy of the beam produced is insufficient to completely compensate the Coulomb field of the beam; so it must be accelerated in the regular accelerating sections. The results of calculating the beam dynamics at the output of the first two acceleration structures (one accelerating module) are shown in Figs. 2.10–2.12 and in Table 2.8. The beam length and the normalized emittance are completely steady-state parameters, and thus we can assume that they are the same at the end of the injector accelerator.

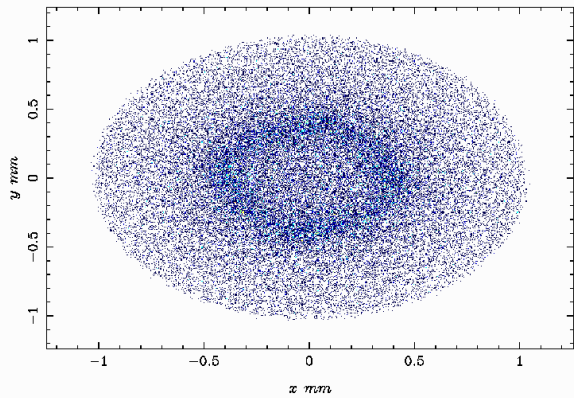


(a) Spread of longitudinal pulses vs. longitudinal coordinate of particles.

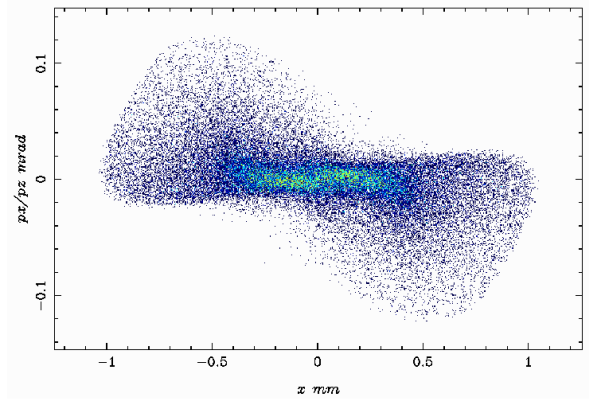


(b) Density of particles vs. spread of longitudinal pulses.

Figure 2.10. Longitudinal characteristics of beam.



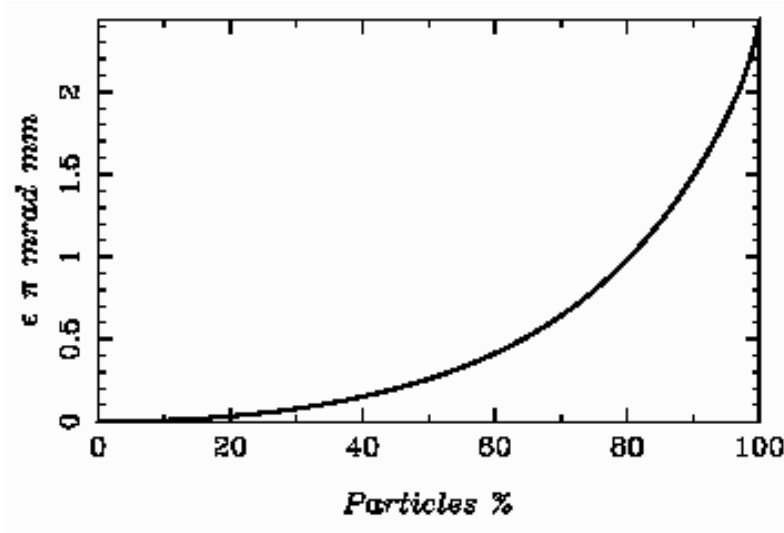
(a) Transverse coordinates of particles.



(b) Phase plane.

(because of axial symmetry of beam, phase planes are the same for both coordinates)

Figure 2.11. Transverse characteristics of beam.



(because of axial symmetry of beam, the phase planes are the same for both coordinates)

Figure 2.12. RMS normalized emittance vs. number of beam particles taken into account.

Table 2.8. Beam parameters after the first accelerating module.

Parameter	Value
Beam charge	1.5 nC
RMS beam length	1 mm
Total beam length	4 mm
RMS energy spread	0.1%
Normalized emittance for 100% of particles	2.5 mm · rad
Energy	115 MeV

### 2.2.1 Laser system

The laser system needed for work with an electron source based on the microwave photo gun should have the following parameters.

1. Pulse duration of 10 ps at most.
2. Wavelength within  $263 \div 267$  nm.
3. Pulse energy of up to 1 mJ.
4. Repetition rate of 25 Hz at least.
5. The laser must be synchronized with the microwave power system.
6. Transverse laser spot size of  $0.5 \div 5$  mm.
7. Displacement of the laser spot on the photocathode from shot to shot of 0.5 mm at most.
8. Stability in energy from laser pulse to pulse not worse than 2%.
9. Longitudinal pulse shape of the “flat-top” type (constant rectangular pulse).

### 2.2.2 Photocathode

As described above, the extracted beam charge should be 1.5 nC, which imposes certain conditions on the properties of the photocathode: a long lifetime and resistance to pulsed loads of laser radiation of high energy density. We suggest Ir<sub>5</sub>Ce as the photocathode material. It is widely used as a high-temperature thermal cathode and has a record emission current density, as well as a long lifetime. The maximum extracted charge for a similar photocathode was 5 nC at a laser energy of 10 mJ. Another advantage of this photocathode is the low operating vacuum level ( $10^{-9}$  Torr) and the possibility of opening to the atmosphere without loss of photocathode properties. The parameters of the cathode are given in Table 2.9.

Table 2.9. Parameters of Ir<sub>5</sub>Ce photocathode.

Parameter	Value
Operating wavelength, $\lambda$	266 nm
Quantum efficiency, QE	$10^{-4}$ (for wavelength of 266 nm)
Lifetime	over 1000 h
Working vacuum	$10^{-9}$ Torr
Response time	less than 1 ps
Permissible value of accelerating field	less than 120 MV/m
Work function	2.69 eV (for 1800 K)

## 2.3 Injection of positrons

Table 2.10 presents parameters of the injected positrons. The main issues of their injection are as follows:

1. factor of conversion of electron beam into positron beam;
2. capture of positron beam into acceleration mode;
3. compensation for emittance of positrons accepted;
4. compensation for energy spread of positrons accepted.

The general scheme of the positron injector depends on the methods of solving these issues.

Table 2.10. Parameters of injected beam.

Parameter	Value
Number of particles in bunch	$2 \cdot 10^{11}$
Energy	$1.5 \div 2.5$ GeV
Emittance	10 nm
Root-mean-square energy spread	0.1%

To increase the factor of conversion of electrons into positrons, it is planned to use an electron energy of 2.5 GeV. In this case, we can expect up to 40% of positrons in the head of the resulting beam with a length of  $\pm 10^\circ$  from the electron beam incident on the conversion target.

To match the positron beam with the acceleration-focusing line of the linear accelerator, we apply a special matching device with decreasing longitudinal magnetic field. A pulsed flow concentrator is the best technical implementation of this type of device. The flow concentrator is able to form a maximum magnetic field of  $50 \div 80$  kGs and handle  $(2 \div 3) \cdot 10^9$  pulses in this case. A semi-sinusoidal current pulse is used for electrical supply of the flow concentrator. The duration of the pulse current depends on the components of the power generator. A power generator made on the basis of high-current thyristors generates a current pulse of a predetermined shape with a duration of  $25 \div 30$   $\mu$ s.

For increase in the coefficient of positron capture, several first accelerating sections are placed in the field of the tracking solenoid. The arrangement of the elements of the positron system is shown in Fig. 2.13. Usually, the solenoidal focusing is used at an average positron bunch energy of less than  $200 \div 250$  MeV. With further energy acquisition by the bunch, the focusing by the solenoid becomes less and less effective, and it is worth switching to focusing using a regular FODO structure. Usually, the value of the magnetic field of the solenoid is  $5 \div 6$  kGs and can be easily achieved, from the technical point of view, using solenoids with a constant current. Therefore, when choosing the parameters of the magnetic field of the positron system, one should target this value. Additional coils placed around the flow concentrator compensate for the drop of the magnetic field between the concentrator and the tracking solenoid, and also enable creation of long adiabatically decreasing magnetic field of the matching device.

Electron-positron conversion is performed using refractory heavy metals with a large atomic number, for example, the  $W_{74}RE_{26}$  alloy. Conversion calculations for an electron bunch energy of 2.5 GeV show that this value is approximately 6.2 positrons per electron (the number of positrons exiting from the conversion target). The thickness of the target should be about  $4X_0$ , or 14 mm (where  $X_0$  is the radiation thickness of the target material).

As a result of the passage of charged particles through the conversion target, some of their energy is released into the target as heat. This is the so-called thermal losses in the target material, which amount to approximately 16% of the total energy of the electron bunch for a

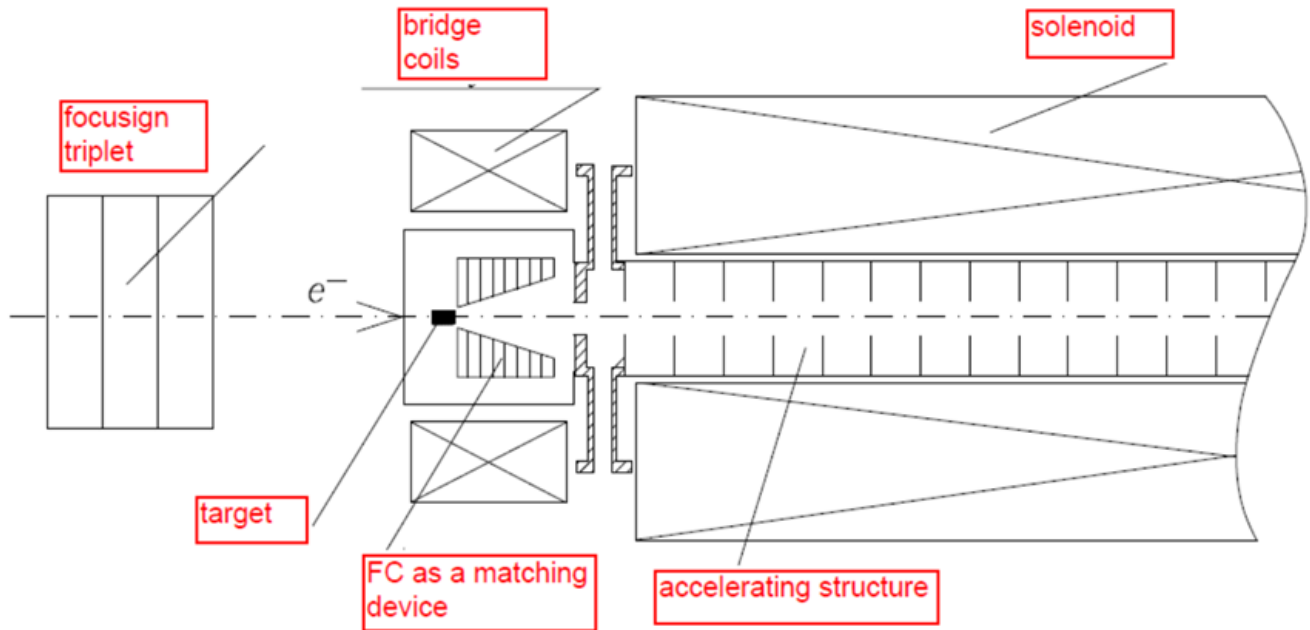


Figure 2.13. Arrangement of elements of positron system.

given conversion energy and target thickness. If the number of particles in the electron bunch is approximately equal to  $1.9 \cdot 10^{10}$  (3 nC), then the total energy release in the target is 380 W at a linac repetition rate of 50 Hz. In principle, this value is not too high, which makes it possible to apply a stationary target with water cooling channels. The target may be slightly smaller than that used for SuperKEKB. A stationary target can be located closer to the flow concentrator than a rotating one, which allows placing the rear end of the target in the higher field of the concentrator and increasing the capture of positrons.

The size of electron bunch focused on the target is limited by the maximum energy release density. With the  $W_{74}RE_{26}$  alloy, this value must not exceed 35 J/g per electron bunch. With a bunch size  $\sigma = 0.5$  mm, the maximum energy release density is 7.7 J/g; with  $\sigma = 0.2$  mm it is approximately 25.7 J/g; in both cases it is below the threshold value. Therefore, the size value can be chosen from considerations of technical implementation.

The flow concentrator in use on the existing injection complex has proved itself to be highly reliable in operation. So, it makes sense to use it again with minor modifications. For example, it is necessary to increase the minimum aperture of the concentrator from 6.6 mm to 8 mm and make the capacitive battery of the pulse generator approximately 2 times bigger.

The emittance compensation is to occur in the ring of the cooler (the damping ring). It will be described separately.

The energy spread of positrons should be compensated for before the cooling ring subject to its energy acceptance. For these purposes, it is necessary to apply a monochromator section, which is based on the accelerating structure. The beam in it must fly not in the accelerating phase of the electric field but in a phase providing a zero increase in the average energy. Before this, the beam must acquire a correlated energy spread in the magnetic lattice of the debuncher.

Since the electric field inside the monochromator has a cosine phase dependence, we should compensate for the beam energy spread using only the field part representing the most linear region. This leads to a restriction on the beam length. At an operating frequency of 2856 MHz, the wavelength of the electric field with the most linear part is approximately  $\Delta\varphi \approx 80^\circ$ . If

we use a field amplitude of 30 MW/m, then a phase  $\Delta\varphi/2 \approx \pm 40^\circ$  will provide an amplitude  $30 \cdot \cos(-\pi/2 \pm \Delta\varphi/2) = \pm 20$  MV/m. To compensate for the energy spread, it makes sense to use only one section of the monochromator. Otherwise it will be necessary to realize phase matching between the sections, which can be quite a difficult task and lead to additional errors, which in turn increases the energy spread of the particles. The maximum length of the section produced at BINP SB RAS is 3 m. With this and the field amplitude taken into account, the maximum energy spread that can be compensated for will be  $\Delta W = \pm 57$  MeV. At a total average energy  $W_0 = 1.5$  GeV, this will correspond to  $\Delta W/W_0 = \pm 3.8\%$ . Thus, there is a restriction on the resulting positron beam before the cooler ring: its length after the magnetic debuncher must not exceed  $80^\circ$  or 23 mm, and the energy spread must not exceed  $\pm 3.8\%$  at an average energy of 1.5 GeV.

Figure 2.14 shows longitudinal phase planes of positron beams that were captured in the acceleration regime and acquired an average energy of about 200 MeV. The diagrams are built for different lengths of the electron beam arriving at the conversion target. The electron beam is assumed to have a normal distribution.

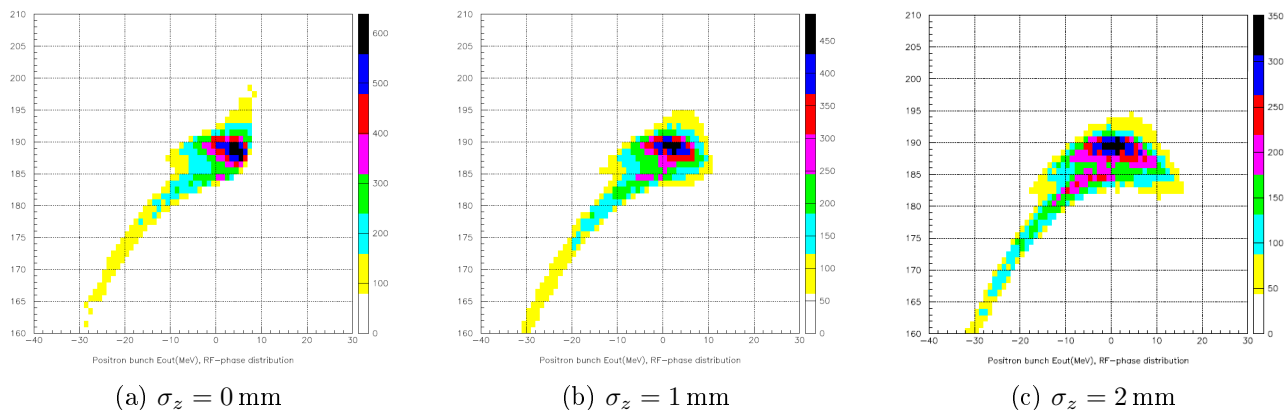
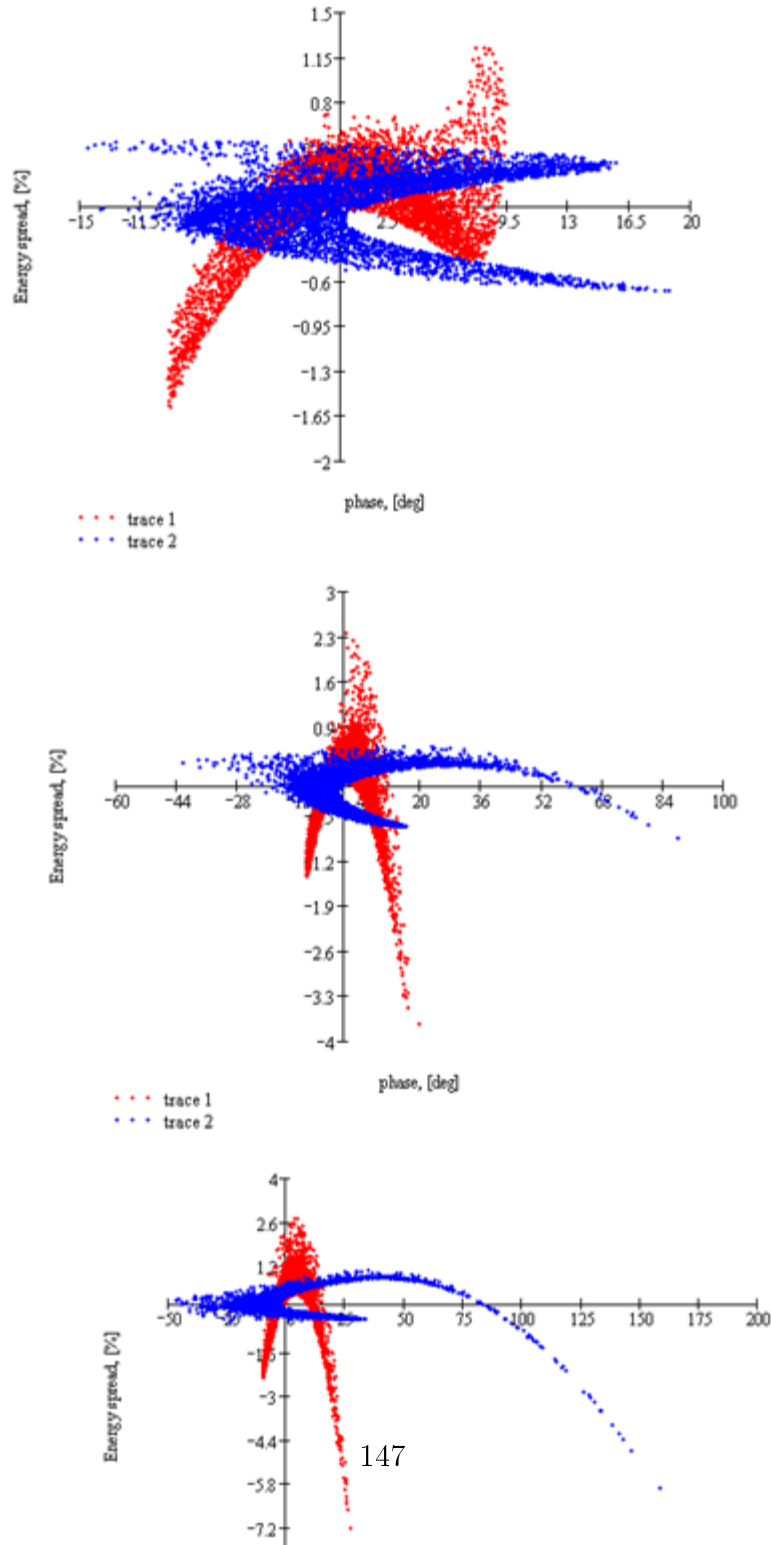


Figure 2.14. Longitudinal phase planes of positrons at different lengths of electron beam with normal distribution.

If we consider the head of a positron beam with a length of  $\pm 10^\circ$ , which contains approximately 40% of the electron beam, then after acceleration up to 1.5 GeV and the debuncher-monochromator, ideally it is possible to achieve the energy spreads shown in Table 2.11. The longitudinal phase planes of the beams after acceleration and the debuncher-monochromator are shown in Fig. 2.15.

Table 2.11. Energy spreads in beams after acceleration up to 1.5 GeV and debuncher-monochromator.

Length of electron beam from which positrons are produced	Energy spread after acceleration to 1.5 GeV (for particles within $6\sigma$ )	Energy spread after acceleration to 1.5 GeV and debuncher-monochromator (for particles within $6\sigma$ )
$\sigma_z = 0$ mm	$\pm 1.2\%$	$\pm 0.8\%$
$\sigma_z = 1$ mm	$\pm 1.8\%$	$\pm 0.8\%$
$\sigma_z = 2$ mm	$\pm 3\%$	$\pm 1.3\%$



From the obtained data it follows that the optimal size of the electron beam at the entry to the conversion target should be  $\sigma_z = 1$  mm. Taking into account the operation frequency of the particle sources of 25 Hz and the amount required for injection into the collider (see Table 2.10), we find that the charge of operational positron bunch should be 1.3 nC. Based on the factor of conversion of the electron beam to the positron beam of 40%, we have that the electron source should yield 3.2 nC at least. The parameters of electron source are given in Table 2.12.

Table 2.12. Parameters of injected beam.

Parameter	Value
Bunch charge	3.5 nC
Length	$\sigma_z = 1$ mm (normal distribution)
Repetition rate	25 Hz
Emittance	any
Root-mean-square energy spread	any

Table 2.13. Parameters of RF gun and electron source

Parameter	Value
Type of acceleration structure	diaphragm-type waveguide
Length	$\sigma_z = 1$ mm (normal distribution)
Repetition rate	25 Hz
Emittance	any
Root-mean-square energy spread	any
Beam energy	10 MeV
Amplitude of field on cathode	not less than 100 MeV/m
RF pulse duration	less than 1 $\mu$ s

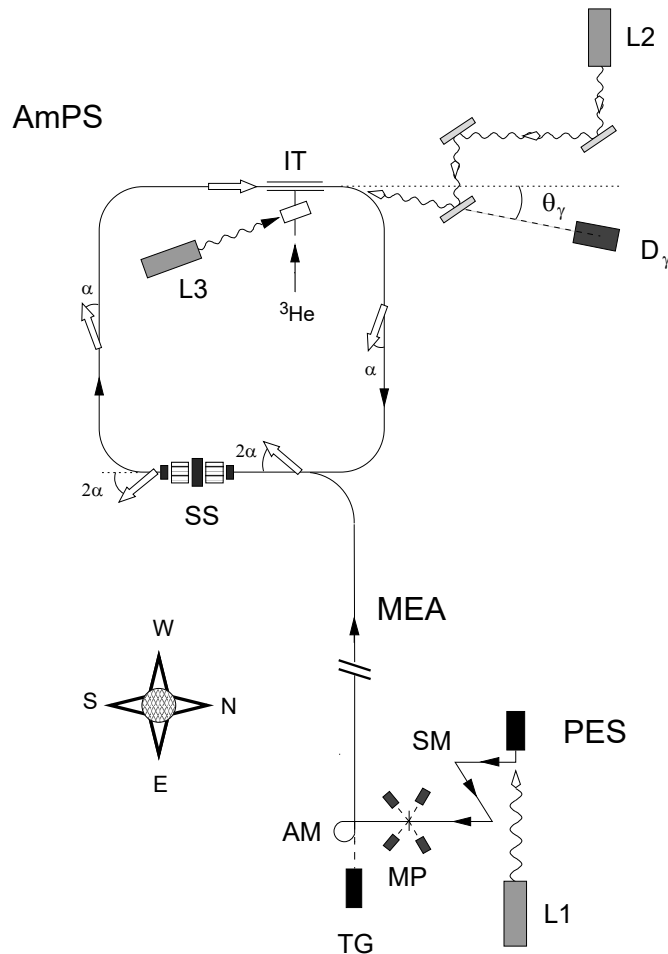
### 2.3.1 Electron source

The main difficulty associated with the source of electrons for the conversion of positrons is the beam high charge and small length. An RF microwave gun with a photocathode can be used here, but to obtain a 3.5 nC charge it will be necessary to have an accelerating field of about 100 MV/m on the cathode. Then the characteristic length of the resulting beam will be  $\sigma_z = 1.5$  mm. That is, to reduce the beam length, it is necessary to use a magnetic buncher.

Since the quality of electron beam is not critical for the production of positrons, it is proposed to use an RF gun based on a diaphragm-type waveguide with high internal coupling. This will reduce the filling time of the accelerating cavities and enable work with RF pulse with durations less than 1  $\mu$ s, which is necessary to achieve high values of the accelerating field. The energy of the particles should be about 10 MeV, which will compensate for the effect of space charge. In view of the foregoing, below are presented possible final parameters of the electron gun of the electron source for obtaining positrons.

## 2.4 Source of polarized electrons

The project of the polarized electron source (PES) for the Novosibirsk Super Charm–Tau factory is largely based on the positive experience of work with such a source created in the 90s at BINP SB RAS in close cooperation with ISP SB RAS and NIKHEF (Amsterdam) [4, 5, 6, 7, 8]. The Amsterdam source (Fig. 2.16) was involved in experiments to study the internal structure of polarized nuclei by the method of scattering of polarized electrons on the nuclei of inner target in the AmPS storage ring. In the source for AmPS the laser irradiated the photocathode with a relatively long electron pulse with the following parameters: duration of  $2.1\ \mu\text{s}$ , current of  $15 \div 50\ \text{mA}$ , repetition frequency of 1 Hz, polarization level of up to 80%, and energy output of the PES of  $70 \div 100\ \text{keV}$ . Unlike it, in the new source it is required to accelerate a single bunch of electrons with a duration not exceeding 2 ns and a repetition frequency of 50 Hz. In the future, an electron current pulse will be compressed into an even shorter bunch, suitable for direct acceleration in an  $S$ -range pulsed linear accelerator up to an energy of 2.5 GeV.



Notation: L1 is the titanium-sapphire laser, PES is the source of polarized electrons with energies of up to 100 keV, SM is the spin manipulator, MP is the Mott polarimeter, TG is the thermo-emission gun for experiments with unpolarized electrons, AM is the alpha-magnet for beam injection into the linear accelerator, MEA is the 700 MeV linear accelerator, SS is superconducting solenoids (a spin rotator of the Siberian snake type), IT is the internal target of the Aamps synchrotron.

Figure 2.16. General view of AmPS accelerator complex in Amsterdam.

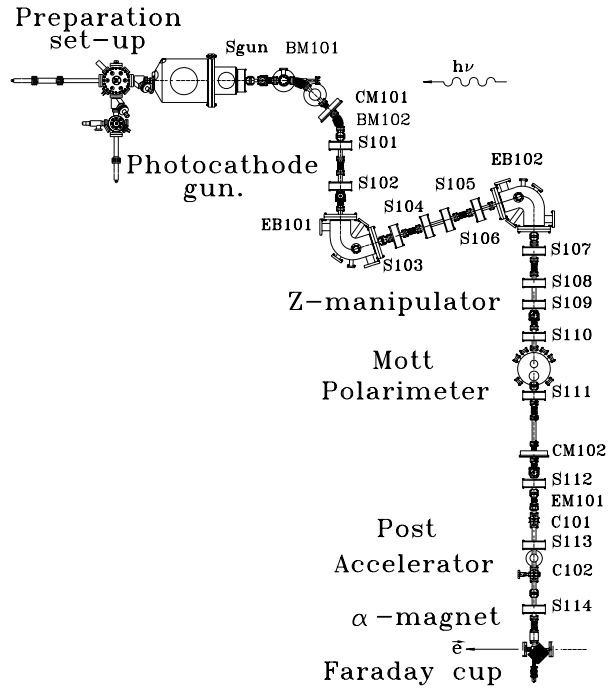


Figure 2.17. Straight-line diagram of AmPS source of polarized electrons.

Despite some differences in the problems to address, the overall layout of the source for the Super Charm–Tau factory almost completely repeats the scheme of the source for AmPS. Figure 2.16 shows the scheme of the AmPS complex, and Fig. 2.17 the scheme of the source of polarized electrons of this complex. The latter figure depicts two *S*-range cavities, C101 and C102, which perform grouping and additional acceleration of the beam to an intermediate energy of 400 keV, i. e., the energy of the beam from the thermo-emission gun before the entry to the chopper of the main linac.

Let us proceed to discussion of the most important units and problems of the future source.

### 2.4.1 Photocathode

In the source created for NIKHEF, the photocathodes were a structure of InGaAsP and GaAs crystal layers [4]. According to our measurements, the polarization level was 80% in the best samples. The cathodes, the system of their preparation, and the laser optical system were designed and manufactured at the Institute of Semiconductor Physics of the Siberian Branch of the Russian Academy of Sciences, at a laboratory headed by Professor A.S. Terekhov.

In recent years, significant progress has been made in the technology of creating GaAs photocathodes, which are used for production of polarized electron beams [9]. Almost all their parameters have been improved, see Table 2.14. For example, the polarization level of electrons in the best photocathodes is as high as 92% and the possibility of its further increase up to 97% is being discussed. The quantum efficiency of photocathodes reached 0.85%. Currently, the best photocathodes are produced in St. Petersburg by a scientific team headed by Professor Yu. Mamaev. These photocathodes have been thoroughly tested at the SLAC laboratory at Stanford. They showed a high polarization level and good quantum efficiency and also demonstrated a quite acceptable lifetime. The project of the source for ILC is also being developed on their basis.

The modern photocathode is a multilayer semiconductor structure with alternating periods of a crystal lattice grown on a relatively thick base of GaAs. The mechanical stress produced

Table 2.14. Comparative characteristics of best photocathodes [9].

Sample	Composition	$P_{\max}$	$QE(\omega_{\max})$	Group
SLSP 16	GaAs(3.2 nm)/ GaAs <sub>0.68</sub> P <sub>0.34</sub> (3.2 nm)	92%	0.5%	Nagoya University, 2005
SL5-777	GaAs(1.5 nm)/ In <sub>0.2</sub> Al <sub>0.23</sub> Ga <sub>0.57</sub> As(3.6 nm)	91%	0.14%	SPbSPU, 2005
SL7-307	Al <sub>0.4</sub> Ga <sub>0.6</sub> As(2.1 nm)/ In <sub>0.19</sub> Al <sub>0.2</sub> Ga <sub>0.57</sub> As(5.4 nm)	92%	0.85%	SPbSPU, 2007

via doping the alternating layers of the main semiconductor with indium, aluminum, and other elements creates a sufficiently large splitting of the energy levels of electrons with different spin directions in the valence band. This splitting of the levels  $J = 3/2$ ,  $m = -3/2$  and  $J = 3/2$ ,  $m = -1/2$  exceeds 60 MeV in the best samples, which enables quite selective emission of electrons with only one spin direction into the conduction band, see Fig. 2.18 [10].

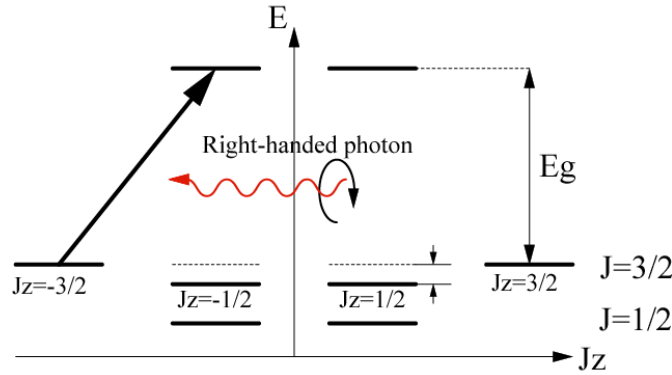


Figure 2.18. Splitting of levels of valence band and scheme of transitions to conduction band.

Details of the technology of preparation of photocathodes are beyond the scope of this review. We are mainly interested in the consumer qualities of this product. The graph in Fig. 2.19 shows the curves of the dependence of the quantum yield and polarization on the light wavelength [9]. As can be seen from the presented data, a maximum polarization level of 92% is reached at 825 nm.

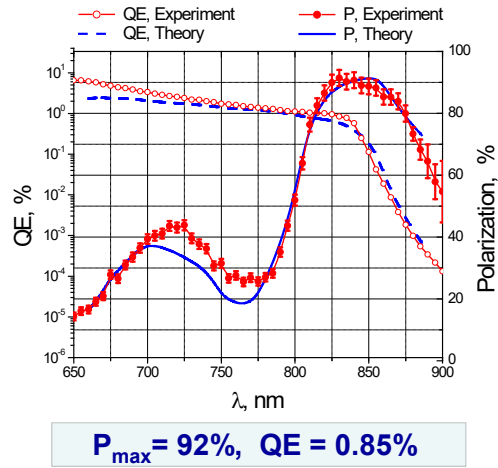
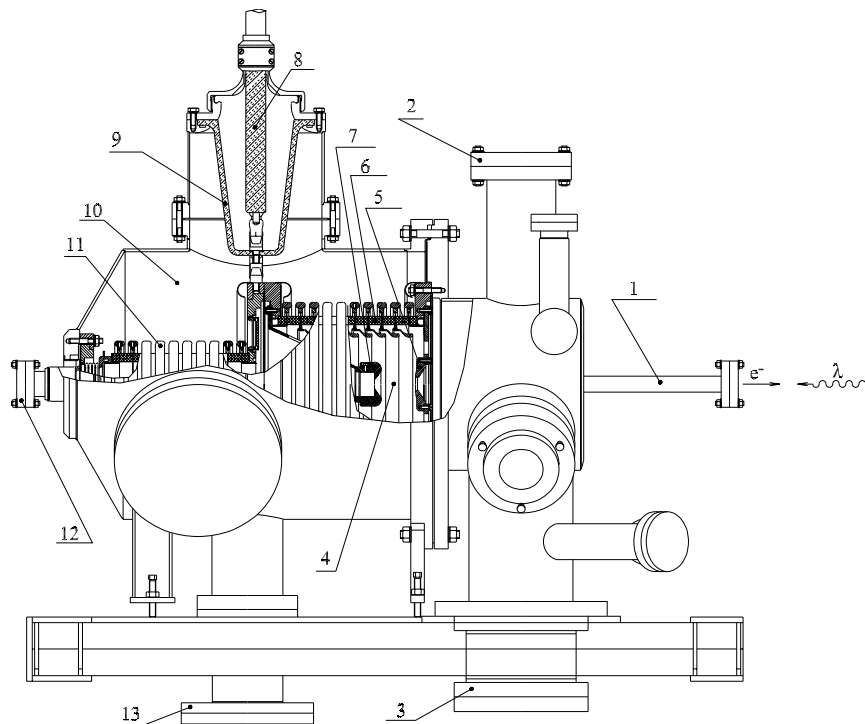


Figure 2.19. Level of polarization and quantum yield vs. light wavelength.

### 2.4.2 High-voltage unit

The main requirement to the high-voltage volume of the photo gun is that it must provide ultra-high vacuum, at a level of  $10^{-11}$  mbar. An idea of using a double vacuum volume with an insulating vacuum of  $10^{-8}$  mbar surrounding the accelerator tube insulators was successfully tested on the Amsterdam source. Figure 2.20 presents the scheme of such a double vacuum volume.



Notation: 1 is extraction line and laser input window; 2, 3, 13 are vacuum pump ports; 4 is acceleration gap; 5 is anode; 8 is high-voltage cable; 6 is insulator of accelerator tube; 11 is second insulator of accelerator tube; 10 is protective vacuum casing; 12 is flange for interfacing the preparation and loading chambers with the unit.

Figure 2.20. Photo gun.

A negative voltage pulse of  $-100\text{ kV}$  with a duration of about  $500\ \mu\text{s}$  in base was applied to the accelerating tube. The beam pulse duration was determined by the light flash duration. For the source of the Super Charm–Tau factory the light pulse duration should be less than  $2\text{ ns}$  in base.

The low pulse rate of the accelerating voltage reduced the time of bombing the photocathode with dark currents, which are always present in high voltage devices, by more than three orders of magnitude. That made it possible to increase the lifetime of the cathodes to one month, whereas with a constant voltage on the accelerating gap the lifetime of cathode was  $2 \div 3$  days at most.

The accelerating gap of the gun for AmPS was  $65\text{ mm}$ . The maximum field strength in the cathode surface did not exceed  $17\text{ kV/cm}$ . The diameter of the photocathode was  $12\text{ mm}$ , and the size of the light spot was varied from  $1$  to  $7\text{ mm}$ .

Generation of a shorter beam pulse in the source of the Super Charm–Tau factory will obviously require using a significantly higher rate of acceleration as compared with the source for AmPS. For instance, at the source being developed under the ILC project at the Nagoya University, the acceleration rate was brought to  $29.7\text{ kV/cm}$  on the photocathode surface [10]. In this case, a constant accelerating voltage of  $-200\text{ kV}$  is applied to a very small gap of  $35\text{ mm}$ , see Figs. 2.20–2.22. In this source, the dark currents were suppressed due to molybdenum as the material for the cathode electrodes and titanium as the anode material. Studies that were conducted at the Nagoya University show attainability of field strengths of up to  $1300\text{ kV/cm}$  on combined molybdenum-titanium electrodes [11]. In general, the high-voltage unit for the Nagoya University in assembly with the preparation and charging chambers is built on the same principles that were used earlier in the source for AmPS. However, the unit for the Nagoya University has better shielding of the cathode against weak electrical discharges occurring along the ceramic insulators. In addition, the magnetic lens with a longitudinal magnetic field is placed maximally close to the photocathode. This improves the matching of the beam emittance with the electron-optical path. All these innovations, as well as the new photocathodes produced in St. Petersburg, are expected to be used in the project of the source for the Super Charm–Tau factory.

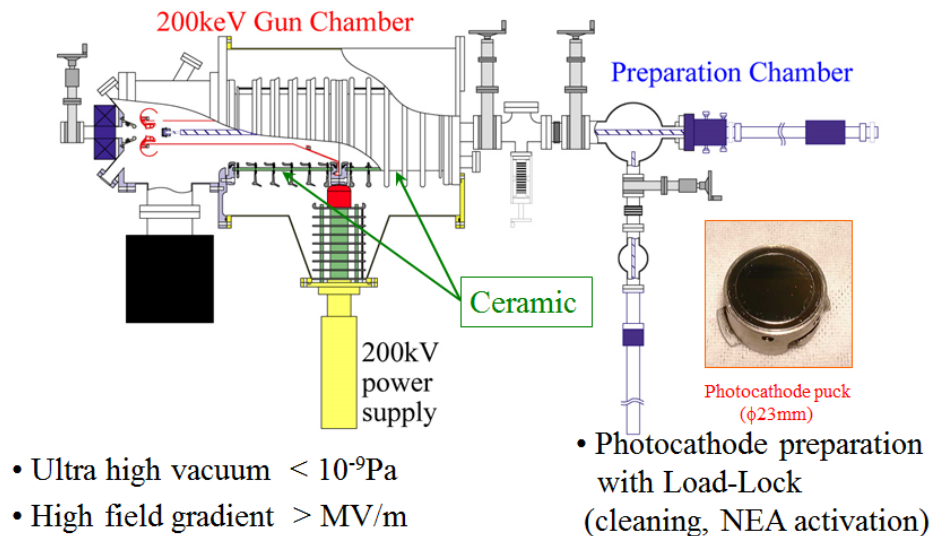


Figure 2.21. Scheme of high-voltage unit of polarized electron source of Nagoya University, Japan [10].

## Electrode Design & Fabrication (Nagoya U.)

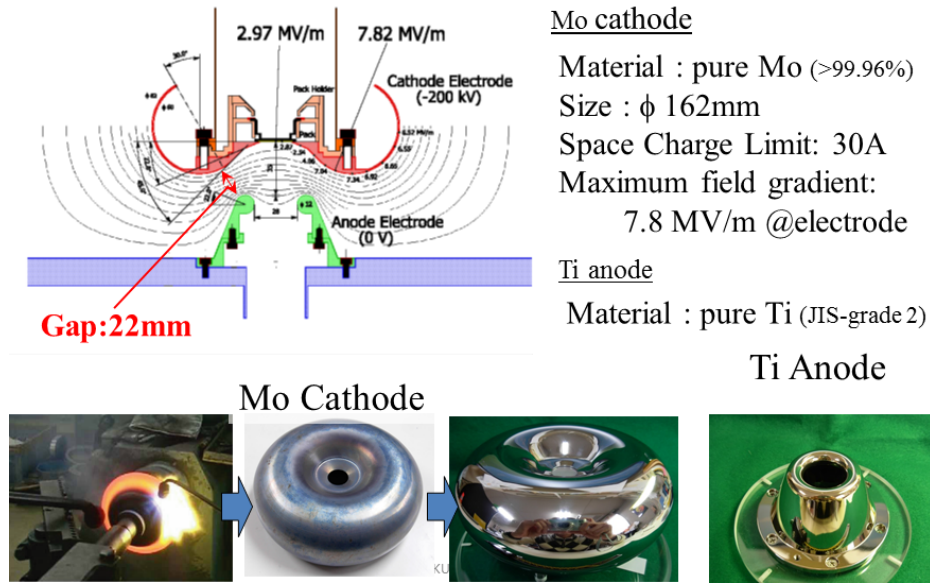


Figure 2.22. Geometry of acceleration gap of source of Nagoya University [10].

### 2.4.3 Activation of photocathodes

The cathode is subjected to chemical etching in hydrochloric acid ( $15 \div 20$  s) in nitrogen atmosphere in a fume hood. This is followed by washing with methanol and drying. After that, the cathodes are inserted into frames and placed in a special sealed container in the top part of the hood. The container can hold up to three cathodes at a time. The container with the cathodes is filled with nitrogen and then transferred to the upper part of the loading chamber, also filled with pure nitrogen. Further, the loading chamber with the cathodes in it is pumped to  $10^{-8}$  mbar, using oil-free turbo-pumps and magnet-discharge pumps. After that, the cathodes are transferred through the sluice into the preparation chamber. In the latter chamber, the photocathodes are placed on a carousel, where up to four cathodes can be placed simultaneously. All the movements of the cathodes are made using magnetic manipulators. The chambers are separated by a gate with a metal seal.

The procedure of activation of the photocathode takes place in the preparatory chamber under a vacuum of  $10^{-11}$  mbar, maintained by an ion pump with a titanium getter and NEG tape. The carousel is rotated, and the cathode in the frame is moved to the position opposite the heater plate. The infrared radiation of the heater gradually heats the cathode to  $600^\circ\text{C}$ . In so doing, the pressure must not rise above  $10^{-8}$  mbar. The temperature of  $600^\circ\text{C}$  is maintained for one hour to evaporate the contaminated surface layer of various arsenic compounds. After that, the cathode slowly cools down to room temperature.

Further, alternate sputtering of cesium and oxygen atoms is performed in order to relax the potential barrier for electrons to escape. It was called the “Yo-Yo” procedure. The thickness of each elementary layer is about 0.1 monolayer. Cesium is sprayed first.  $12 \div 15$  pairs of layers are applied, till the saturation of the photocurrent collected on a special collector. In the process of cesium application, the cathode is continuously illuminated by the halogen lamp light.

After the activation, the quantum yield is measured using a helium-neon laser at several power levels. A good InGaAsP cathode typically shows a yield of  $10 \div 14\%$  at the wavelength of this laser.

The old cathode is removed and put on the carousel for subsequent reactivation. Usually  $2 \div 3$  reactivations slightly reduce the quality of cathode. The new cathode is placed in the cathode unit and is tested at several wavelengths of the titanium-sapphire laser.

#### 2.4.4 Magneto-optical system. Spin rotator

A lens with an axially symmetric longitudinal magnetic field is placed directly on the exit from the gun. The configuration of the lens field is chosen subject to the influence of the space charge effect on the electron trajectory. For an intense nanosecond bunch, this effect must be taken into account and, if possible, compensated for. According to the results of the modeling and measurements of normalized emittance at the Nagoya University [10], its value does not exceed  $\varepsilon_{x,y} = 10\pi \text{ mm} \cdot \text{mrad}$ . These measurements were made for a charge with a bunch duration of 1 ns.

Then the magnetic field bends the beam by  $90^\circ$  or a slightly smaller angle, for separation of the light and electron beams. In principle, it seems to be possible to inject the laser beam by an oblique trajectory, and then no magnetic bending is required. The latter option requires further elaboration. Note that magnetic bends of a nonrelativistic electron beam practically do not affect the spin, i. e., the spin rotates in exactly the same way as the velocity vector.

Then there are two possibilities to turn the spin perpendicular to the velocity vector. In the Amsterdam source we used an **electric** field to bend the beam by  $110^\circ$ . In so doing, the spin almost did not rotate in the laboratory coordinate system (since, due to the smallness of the beam velocity, the magnetic field in the co-moving particle coordinate system is very small) and turned out to be exactly perpendicular to the velocity. Then the solenoid rotated the spin around the longitudinal axis into the vertical direction, and the spin remained vertical after the reverse rotation by the electric field. If, however, in a configuration with a zero integral of the longitudinal field the solenoids were switched on between the rotations, then two electric rotations compensated for each other, and the spin remained longitudinal. Adjusting the value of the longitudinal field integral, we were able to obtain any desired spin orientation. This type of spin rotator was called the *Z*-shape manipulator because of its shape in plan.

The other option is to use the so-called Wien filter. It is a straight interval with crossed magnetic and electric fields. Their actions on the rotation of the velocity vector are mutually compensated for, and the spin rotates around the direction of the magnetic field by an angle proportional to the integral of the magnetic field. The main advantage of using the Wien filter is the absence of linkage with a strictly defined electron energy. The main disadvantage of such a spin rotator is the significant chromaticity of the rotation of particles with different energies.

Below we discuss in some detail a new approach to constructing spin rotators for nonrelativistic energies. This approach originated during the work on the project of the muon ( $g - 2$ ) experiment [12]. The idea is that in crossed electric and magnetic fields, choosing a certain ratio of the values of these fields, one can eliminate dependence of the radius of particle bend on its velocity. Acting in this way, we can make all the beam bends perfectly achromatic.

Equation of the motion of a particle in transverse  $\mathbf{E}$  and  $\mathbf{B}$  fields is as follows:

$$\mathbf{p} = \gamma\beta mc, \quad \frac{d\mathbf{p}}{dt} = e(\mathbf{E} + \boldsymbol{\beta} \times \mathbf{B}) \quad \rightarrow \quad B + \frac{E}{\beta} = -\frac{pc}{er}. \quad (2.1)$$

The requirement of independence of the bending radius on the momentum will determine the ratio of the fields:

$$\frac{d}{dp} \left( \frac{B}{p} + \frac{E}{p^2} \sqrt{1+p^2} \right) = 0 \quad \rightarrow \quad B = -E \frac{\gamma^2 + 1}{\beta\gamma^2}, \quad E = -B \frac{\beta\gamma^2}{\gamma^2 + 1}. \quad (2.2)$$

Substituting (2.2) in (2.1) results in the following:

$$B = -\frac{pc}{er}(\gamma^2 + 1), \quad E = \frac{pc}{er}\beta\gamma^2. \quad (2.3)$$

In the nonrelativistic case  $\gamma \simeq 1$ . Realizing this passage to the limit, we have that

$$E = -\frac{\beta}{2}B, \quad B = -2\frac{pc}{er}, \quad E = \frac{pc}{er}\beta. \quad (2.4)$$

It is seen from these expressions that to make the dispersion zero, the field to bend the beam should be twice as strong as that in a purely magnetic bend, which compensates for half of the excess Lorentz force due to a weak radial electric field directed away from the center.

Let us now consider the question of spin rotation in such a hybrid magnet. In the laboratory coordinate system, the angular frequency of the precession of the spin is

$$\boldsymbol{\Omega} = -\frac{e}{mc} \left[ \left( a + \frac{1}{\gamma} \right) \mathbf{B} - \left( a + \frac{1}{\gamma + 1} \right) \boldsymbol{\beta} \times \mathbf{E} \right],$$

or, subject to (2.3) and the fact that  $\Omega_0 = \beta c/r$ ,  $\beta^2\gamma^2 = \gamma^2 - 1$ :

$$\begin{aligned} \Omega &= -\frac{e}{mc} \left[ \left( a + \frac{1}{\gamma} \right) B + \left( a + \frac{1}{\gamma + 1} \right) \beta E \right] = \\ &= \frac{\beta c}{r} \left[ \left( a + \frac{1}{\gamma} \right) (\gamma^2 + 1) - \left( a + \frac{1}{\gamma + 1} \right) \beta^2 \gamma^2 \right] = \Omega_0 (2a\gamma + \gamma + 1). \end{aligned} \quad (2.5)$$

Respectively, the relative frequency of precession in an accelerating coordinate system rotating with a frequency  $\Omega_0$  is

$$\nu = \frac{\Omega - \Omega_0}{\Omega_0} = \gamma(2a + 1). \quad (2.6)$$

We see that the spin of a strongly nonrelativistic electron or muon rotates in the same direction as the velocity vector, with the tune  $\nu = 1$  in the accelerating coordinate system.

The correction for the difference of the gamma-factor from unity leads to the fact that at an electron energy  $E = 100$  keV, for the spin to turn by  $90^\circ$  it is enough to rotate the velocity vector only through  $75.1^\circ$ . Figure 2.23 shows a possible configuration of spin rotator with two such hybrid magnets with a radial electric field. Changing the mutual polarity of the fields in the pairs of solenoids between the achromatic bends and at the end of the structure, it is possible to freely control the spin direction at the output of the entire device.

The focusing properties of the achromatic bend that are discussed here are determined by the choice of the field index of the electric and magnetic fields [13]:

$$\begin{aligned} B &\sim 1/r^{n_B}, \quad E \sim 1/r^{(n_E+1)} \\ \nu_x^2 &= (1 - n_B)(\gamma^2 + 1) + n_E\gamma^2 \\ \nu_z^2 &= n_B(\gamma^2 + 1) - n_E\gamma^2 \\ \nu_x^2 + \nu_z^2 &= \gamma^2 + 1 \\ \nu_x &= \nu_z \quad \text{for } n_E = 0, n_B = 0.5. \end{aligned} \quad (2.7)$$

It is also useful to give here the expression for the bend radius chromaticity in the second and third orders with respect to the difference of the particle momentum from the equilibrium momentum:

$$\left. \frac{r_0}{\rho} \right|_{r=r_0} = 1 - \left( \frac{3}{2} - \frac{1}{2\gamma^2} \right) \delta^2 + \left( \frac{7}{2} - \frac{2}{\gamma^2} + \frac{1}{2\gamma^4} \right) \delta^3, \quad \delta = \frac{\Delta p}{p}. \quad (2.8)$$

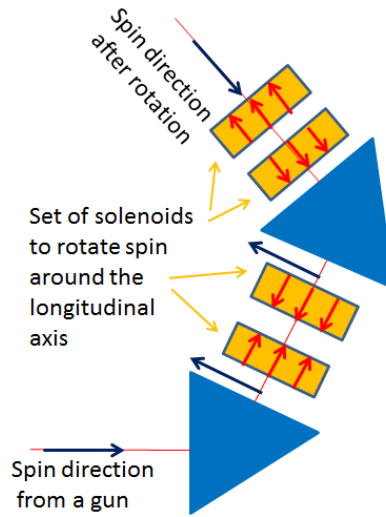


Figure 2.23. Proposed scheme of achromatic spin rotator analogous in all other properties to  $Z$ -manipulator in project for AmPS.

These corrections to the bend radius do not exceed 0.002 at  $|\delta| < 0.04$ . Trial magnet parameters for a  $90^\circ$  spin rotation are given in Table 2.15.

Table 2.15. Magnet parameters.

Parameter	Value
Beam energy in source of polarized electrons	$E = 100 \text{ keV}$
Lorentz factors	$\beta = 0.54822, \gamma = 1.195695$
Spin tune	$\nu = 1.198468$
Velocity/spin rotation angle	$\phi = 75.1^\circ/90^\circ$
Bend radius	$\rho = 25 \text{ cm}$
Vertical magnetic field	$B = 108.6 \text{ Gs}$
Radial electric field	$E = -10.5 \text{ kV/cm}$
Magnetic field exponent	$n_B = 0.5$
Electric field exponent	$n_E = 0$
Betatron tunes	$\nu_x = \nu_z = 1.1022$

## 2.4.5 Mott Polarimeter

Having passed the spin rotator, the beam has a spin orientation perpendicular to the velocity, for example, it is vertical, see Fig. 2.17. Its scattering on gold atoms has a noticeable angle asymmetry, which is usually applied in measurement of the polarization degree. The details of the polarimeter structure and the features of its operation can be found in [5, 7].

## 2.4.6 Beam bunching, pre-acceleration, and injection of beam into linac

At the AmPS source, the beam was bunched and then accelerated to 400 keV by means of two cavities fed by part of the power of the 1st klystron of the large linac [6]. Then the beam was

injected onto the axis of the linac due to a  $270^\circ$  magnetic bend by the so-called alpha magnet. Such a bend has a number of advantages as compared with a  $90^\circ$  simple bend. It can be made achromatic and focusing with respect to both transverse coordinates. In addition, it has a certain bunching effect, opposite in sign to the drift. In operation with an unpolarized electron source, the alpha magnet was switched off, letting the beam from the forward direction pass.

### 2.4.7 Conclusion

In conclusion, we list the main subsystems of the source of polarized electrons.

- Fume hood for etching of the photocathode.
- Loading chamber.
- Preparation chamber.
- Magnetic manipulators.
- Photo gun and 100 kV pulsed power supply (pulse of 0.2 ms, 50 Hz).
- Ultra-high vacuum system (pumps, heaters, NEG, and sensors):  
 $P < 10^{-11}$  mbar.
- Titanium-sapphire laser and optics.
- Spin Z-manipulator.
- 100 keV beam transport line.
- Mott polarimeter.
- Subharmonic pre-buncher and pre-accelerator.
- Alpha magnet.
- Faraday cup.

The basic design parameters of the polarized electron source for the Super Charm–Tau factory are given in Table 2.16. It should be noted that many characteristics of the beam are determined not so much by the quality of the photo gun itself, but by its subsequent transformations in the process of bunching and acceleration. In particular, the emittance value still cannot be predicted reliably.

Table 2.16. Parameters of polarized electron source for Super Charm – Tau factory.

Parameter	Value
Beam polarization	80 ÷ 90%
Lifetime of polarization in ring	3000 ÷ 4500 s
Voltage on cathode (pulsed, 0.2 ms, 50 Hz)	–100 kV
Photocathode type (provisionally)	AlInGaAS/AlGaAS SL with strained QW
Laser type	Ti-Sapphire
Laser wavelength	700 ÷ 850 nm
Laser energy in pulse	10 μJ
Pulse duration	2 ns
Repetition rate	50 Hz
Number of electrons in pulse	$3 \cdot 10^{10}$ (5 nC)
Normalized beam emittance(RMS)	10 ÷ 30 mm · mrad
Quantum efficiency of photocathode	to 0.5%
Time of photocathode reactivation	200 ÷ 600 h*

\* depending on the power of the laser and vacuum.

# Bibliography

- [1] Yu.D. Chernousov et al, “Parallel-Coupled Accelerating Structure: Invention patent № RU2472244C1”, (in Russian).
- [2] A. Levichev et al, “Experience of Operation of the Electron Linear Accelerator Based on Parallel Coupled Accelerating Structure”, Proceedings, 27th Linear Accelerator Conference, LINAC2014: Geneva, Switzerland, August 31-September 5, 2014. 2014, THPP123.
- [3] <http://www.desy.de/~mpyf10/>
- [4] Yu.B. Bolkhovityanov et al, “An investigation of strained InGaAsP photocathode properties with the polarized electron source at NIKHEF”, High-energy spin physics. Proceedings, 12th International Symposium, SPIN 96, Amsterdam, Netherlands, September 10–14, 1996 p. 700–702.
- [5] B.L. Militsyn, “A pulsed polarized electron source for nuclear physics experiments”, PhD thesis, Eindhoven, Universiteit Eindhoven, 1998.
- [6] I. Koop et al, “Polarized electrons in AmPS”, Nucl. Instrum. Meth. 1999 vol. A427 p. 36–40.
- [7] B. Militsyn et al., “Beam optical system of the polarized electron source of the Amsterdam pulse stretcher AmPS”, Nucl. Instrum. Meth. 1999 vol. A427 p. 46–50.
- [8] I.A. Koop, “Longitudinally Polarized Electrons in AmPS Storage Ring: Doctoral dissertation”, BINP SB RAS, Novosibirsk, 2000 (in Russian).
- [9] L. Gerchikov, “Optimization of Semiconductor Superlattice for Spin-Polarized Electron Source”, Proceedings, PESP2008—Workshop on Sources of Polarized Electrons and High Brightness Electron Beams, CEBAF Center, Jefferson Lab, Newport News, VA, USA, Oct 1–3, 2008. 2009. p. 1017–1021.
- [10] M. Yamamoto, “High polarization and low emittance electron source for ILC”, Proceedings, CCAST workshop on TeV physics and the LHC, Beijing, China, Nov 6–10, 2006.
- [11] F. Furuta et al, “Reduction of field emission dark current for high-field gradient electron gun by using a molybdenum cathode and titanium anode”, Nucl. Instrum. Meth. 2005 vol. A538 p. 33–44.
- [12] I.A. Koop et al, “Two examples of in-flight spin flippers”, Phys. Part. Nucl. 2014. Vol. 45. P. 279–282.
- [13] S.R. Mane, “Orbital and spin motion in a storage ring with static electric and magnetic fields”, Nucl. Instrum. Meth. 2012 vol. A687 p. 40–50.